

DISSERTATION

---

4D Microprinting Based on  
Liquid Crystalline Elastomers

---

Li-Yun Hsu

**2023**



# DISSERTATION

zur  
Erlangung der Doktorwürde (Dr. rer. nat.)  
der  
Gesamtfakultät für Mathematik, Ingenieur- und Naturwissenschaften  
der  
Ruprechts-Karls-Universität Heidelberg

vorgelegt von

Li-Yun Hsu

aus Taipei

Tag der mündlichen Prüfung  
**30. JUNI 2023**



---

# 4D Microprinting Based on Liquid Crystalline Elastomers

---

Gutachter  
Prof. Dr. Eva Blasco  
Prof. Dr. Christine Selhuber-Unkel



# ACKNOWLEDGEMENTS

This thesis not only concludes my doctoral research but also includes the immense support, guidance, advice, and kindness extended by numerous individuals who have played a significant role in this remarkable journey.

First and foremost, I would like to express my deepest gratitude to Prof. Dr. Eva Blasco, my supervisor. I am deeply thankful for the opportunity she provided me to be a starting member of her phenomenal research group. I truly appreciate her invaluable support and the freedom she has granted me to explore the world of 3D/4D printing. Witnessing the substantial growth of the group over these few years, she has been a role model, imparting invaluable lessons on conducting research and building a successful career as a researcher.

I would also like to extend my thanks to Prof. Dr. Christine Selhuber-Unkel for kindly agreeing to be the second reviewer of this thesis and participating in the upcoming examination. Furthermore, I express my gratitude to the mentors in my mentoring committees, Prof. Dr. Christopher Barner-Kowollik, Prof. Dr. Kerstin Göpfrich, Dr. Enrico Lemma, and Dr. Jan Freudenberg, for their valuable and motivating feedback, which has greatly supported my progress.

My sincere appreciation goes to all the members of the Blasco group. I would like to first thank Dr. Joel Monti for his constant support and enthusiasm since my first day in the group. I will forever cherish the memories of his introduction through the confusing KIT Campus North and our fume hood sharing experience. Super big thank you to the other "originals" of the group, Dr. Christoph Spiegel. Throughout these years, we have encountered numerous transitional phases together, from the initial confusion regarding the direction of our projects to the anxieties and depression before our first publications. His kind support and encouraging words have always cheered me up from the depths of my heart. I will never complain about LED ordering again, and I eagerly anticipate the possibility of sharing an office with him in the future. I would also like to thank Britta Weidinger, the first copolymer master in our group. From the DASA copolymer, the thrilling lab moving, and the lab setup in Heidelberg, she has always been the person who has resolved challenges rationally and efficiently. I would like to thank my first office buddy Samantha Catt for her great companionship both in and outside

of work and her helpful tips and guidelines for survival in Germany. Her independence and efficient multitasking skills have been a true inspiration. I extend my appreciation to Clara Vazquez-Martel, who is like the Canary sunshine of the group. She has always been warm, caring, and treating others' needs like hers. Many thanks to Philipp Mainik, my first supervised student and a great partner in the interesting field of LCE. He has amazed me with his first synthesis on day one and his enthusiasm in every discussion since then. I would also like to thank Marcus Dodds for his kind support. Your suggestion and tips have rescued me as a Heidelberg rookie several times. I am also immensely grateful to all my colleagues and every member of the Blasco group, including Dr. Guangda Zhu, Dr. Or Eivgi, Niklas Schwegler, Jan Hobich, Finn Kröger, Viktoria Bothe, Pia Klee, Hoang Bao Duc Tran, Ann-Kathrin Bergmann, Michael Kutek, and many others, for creating a harmonious and motivating working environment that I have truly enjoyed. Additionally, special thanks go to Dr. Christoph Spiegel for supporting the German abstract, as well as to Samantha Catt, Philipp Mainik, and Marcus Dodds for their generous assistance in proofreading parts of this thesis.

I would like to acknowledge and express my gratitude to my collaborators for their contributions to making the projects presented in this thesis possible. First, I like to thank Prof. Dr. Martin Wegener and his group at KIT. Special thanks to Dr. Alexander Münchinger for introducing me to the world of liquid crystal and offering invaluable guidance during the initial stages of my project. I would also like to thank Dr. Liang Yang for being a supportive colleague in KIT Campus North, Dr. Marc Hippler for introducing me to the Nanoscribe PPGT microprinter, and Pascal Kiefer and Sebastian Kalt for their incredible skills in supporting me with 3D modeling in Blender. Profound thanks also go to Prof. Rasmus R. Schröder, Dr. Irene Wacker, and Ernest Ronald Curticean for their assistance with microscopy imaging, Dr. Tanja Schmitt for making my azobenzenes and DASA molecules shine through transient absorption spectroscopy, Sebastian Lindenthal for his support with Raman spectroscopy, and Tobias Spratte for the assistance with the nanoindenter, even on the day before Christmas Eve.

I would like to thank my friends and family back in Taiwan for their endless support of my decision to pursue this degree in Germany and their understanding of my absence during family events. To my most important soul mate and best partner, Kevin, I cannot thank him enough for his unwavering support, warmth, and acceptance of my negative emotions during this challenging time. Furthermore, I would like to express my heartfelt appreciation to his family, Elisabeth, Doris, and Marcel, for embracing me as part of their own and providing

incredible warmth and support, especially during the difficult times of not being able to be with my own family for almost three years due to the pandemic.

In the end, I would also like to thank myself for having the courage to step out of my comfort zone and pursue my dream in a foreign country four years ago, and for never giving up until the completion of this thesis, which I am incredibly proud of.



# ABSTRACT

Two-photon laser printing (2PLP) is a disruptive three-dimensional (3D) printing technique that can afford structural fabrication at the submicrometer scale. Apart from constructing static 3D structures, research in fabricating dynamic ones, known as "4D printing", is becoming a burgeoning field. 4D printed structures exhibit adaptability or tunability towards their environment through the control of an external stimulus. In contrast to the rapid growth in macroscale fabrication, progress in microprinted actuators has only been scarcely reported. Liquid crystal elastomer (LCE) stands out among the promising classes of smart materials for fabricating microrobotics or microactuators due to its distinct anisotropic property, which enables the printed structures to exhibit automated reversible movements upon exposure to stimuli without environmental limitations. Nevertheless, the use of 2PLP for the manufacture of 4D printed LCE microstructures with high versatility and complexity have presented some challenges, limiting their implementation in final applications. This thesis aims to overcome two main obstacles faced in this regard: first, the limitation of two-photon printable stimuli-responsive materials; and second, the lack of a facile approach for aligning liquid crystal (LC) within three dimensions.

The first part of this thesis aims on expanding the library of materials used for implementing light responsiveness into LC microstructures, as light provides a higher degree of temporal and spatial control compared to other stimuli. The initial approach has involved incorporation of acrylate-functionalized photoresponsive molecules, such as azobenzene and the donor-acceptor Stenhouse adduct (DASA), into a LC ink using a conventional synthetic method. However, several challenges, such as compatibility with the LC ink, have prevented the achievement of 4D printing via 2PLP. The second approach is based on post-modifying printed LC structures and successfully fabricated microactuators with five different photoresponsive features by individually incorporating each light-absorbing molecule. Furthermore, LC microactuators that exhibit distinct actuation patterns under different colors of light were fabricated by simultaneously implementing orthogonal photoresponsive molecules.

The second project presented in this thesis focuses on developing a new strategy to induce alignment domains in a more flexible manner, with the aim of spatially tailoring the LC topology of the 3D printed microstructures. This is achieved by microprinting 3D scaffolds

based on polydimethylsiloxane (PDMS) to manipulate the alignment directions of LC molecules. Taking advantage of 2PLP to fabricate arbitrary scaffolds, LC alignments, including planar and radial patterns, could be introduced freely and simultaneously in three-dimensional space with varying degrees of complexity. The applicability of this alignment approach was demonstrated by fabricating responsive LC microstructures within different PDMS environments, and distinct actuation patterns were observed.

Overall, these two breakthroughs have unveiled a wide array of new potentials for the utilization of responsive LC microsystems with tunable functionalities and customizable actuation responses, that can be applied across various domains and applications.

# KURZFASSUNG

Der Zwei-Photonen-Laserdruck (2PLP) ist eine bahnbrechende dreidimensionale (3D) Drucktechnik, die die Herstellung von Strukturen im Submikrometerbereich ermöglicht. Neben der Fabrikation statischer 3D-Strukturen wird die Forschung hin zur Fertigung dynamischer Strukturen, dem so genannten "4D-Druck", zu einem immer wichtigeren Gebiet. Gedruckte 4D-Strukturen weisen hierbei eine Anpassungsfähigkeit oder Abstimbarkeit gegenüber ihrer Umgebung auf, indem sie durch einen externen Stimulus gesteuert werden. Im Gegensatz zu den rasanten Fortschritten bei der Herstellung im Makromaßstab, wurden bisher kaum Fortschritte bei mikrogedruckten Aktoren erzielt. Flüssigkristall-Elastomere (LCE) gehören zu den vielversprechenden Klassen intelligenter Materialien für die Herstellung von Mikrorobotern oder Mikroaktoren. Dies ist auf ihre ausgeprägte anisotrope Eigenschaft zurückzuführen, die es den gedruckten Strukturen ermöglicht, automatisierte reversible Bewegungen auszuführen, wenn sie Stimuli ausgesetzt werden, ohne dass sie durch die Umwelt eingeschränkt werden. Die Verwendung von 2PLP für die Herstellung von 4D-gedruckten LCE-Mikrostrukturen mit hoher Vielseitigkeit und Komplexität hat jedoch einige Herausforderungen mit sich gebracht, die ihre Umsetzung in Endanwendungen einschränkt. Diese Arbeit zielt darauf ab, in dieser Hinsicht zwei Haupthindernisse zu überwinden: erstens die Beschränkung der mit zwei Photonen druckbaren, auf Stimuli reagierenden Materialien und zweitens das Fehlen eines einfachen Verfahrens für die LC-Ausrichtung in drei Dimensionen.

Der erste Teil dieser Arbeit zielt darauf ab, die Bibliothek der Materialien zu erweitern, die für die Implementierung von Licht-Responsivität in LC-Mikrostrukturen verwendet werden, da Licht im Vergleich zu anderen Reizen ein höheres Maß an zeitlicher und räumlicher Kontrolle bietet. Der erste Ansatz bestand darin, Acrylat-funktionalisierte lichtresponsive Moleküle wie Azobenzol und das Donor-Akzeptor-Stenhouse-Addukt (DASA) mit Hilfe einer herkömmlichen synthetischen Methode in eine LC-Tinte einzubauen. Verschiedene Hürden, wie z. B. die Kompatibilität mit der LC-Tinte, haben jedoch das Erreichen des 4D-Drucks mittels 2PLP verhindert. Der zweite Ansatz basiert auf der Post-Modifikation gedruckter LC-Strukturen und hat erfolgreich die Herstellung von Mikroaktoren mit fünf verschiedenen photoresponsiven Eigenschaften ermöglicht, indem in diese lichtabsorbierende Moleküle eingebaut wurden, die

die jeweilige Eigenschaft ausdrücken. Darüber hinaus wurden LC-Mikroaktuatoren, die bei verschiedenen Lichtfarben unterschiedliche Aktuierungsmuster aufweisen, durch gleichzeitige Implementierung orthogonaler photoresponsiver Moleküle hergestellt.

Das zweite in dieser Arbeit vorgestellte Projekt konzentriert sich auf die Entwicklung einer Strategie zur flexiblen Erzeugung von Ausrichtungsdomänen mit dem Ziel, die LC-Topologie der gedruckten Mikrostrukturen räumlich anzupassen. Dies wird durch den Mikrodruck von 3D-Gerüsten auf der Basis von Polydimethylsiloxan (PDMS) erreicht, wodurch die Ausrichtungsrichtung von LC-Molekülen manipuliert werden kann. Unter Ausnutzung der Vorteile von 2PLP zur Herstellung beliebiger Gerüste konnten LC-Ausrichtungen, einschließlich planarer und radialer Muster, frei und gleichzeitig im dreidimensionalen Raum mit unterschiedlichem Komplexitätsgrad realisiert werden. Die Anwendbarkeit dieses Ausrichtungsansatzes wurde durch die Herstellung responsiver LC-Mikrostrukturen in verschiedenen PDMS-Umgebungen demonstriert, wobei unterschiedliche Aktuierungsmuster beobachtet wurden.

Mit diesen beiden Durchbrüchen wurde ein breites Spektrum an neuen Möglichkeiten für die Nutzung responsiver LC-Mikrosysteme mit abstimmbaren Funktionalitäten und anpassbaren Aktuierungsreaktionen eröffnet, die in verschiedenen Bereichen und Anwendungen eingesetzt werden können.

---

# ABBREVIATIONS

2PI	two-photon initiator
1PA	one-photon absorption
1PP	one-photon polymerization
2PA	two-photon absorption
2PLP	two-photon laser printing
2PP	two-photon polymerization
3D	three dimensional
4D	four dimensional
Azo	azobenzene
BAPO	phenylbis (2,4,6-trimethylbenzoyl)phosphine oxide
BSA	bovine serum albumin
BTPOS	bis(2,2,6,6-tetramethyl-4-piperidyl-1-oxyl) sebacate
cat.	catalytic amount
CNT	carbon nanotubes
Cw	continuous wave
DASA	donor-acceptor Stenhouse adduct
DETC	diethylamino-3-thenoyl coumarin
DI	deionized
DIW	direct ink writing
DLP	digital light processing
DLW	direct laser writing
DMAc	dimethylacetamide
DMAP	4-dimethylaminopyridine
DMF	dimethyl formamide
DMSO	dimethyl sulfoxide
DOC	double bond conversion
DPGDA	dipropylene glycol diacrylate
DSC	differential scanning calorimetry
FW	fabrication window
IPA	isopropyl alcohol
LAP	lithium phenyl-2,4,6-trimethylbenzoylphosphinate
LC	liquid crystal
LCE	liquid crystalline elastomer
LCST	lower critical solution temperature
LM	light microscope

---

MEMS	microelectromechanical systems
MC	merocyanie
NIR	near-infrared
NMP	nitroxide-mediated polymerization
NMR	nuclear magnetic resonance
OD	optical density
PDMS	polydimethylsiloxane
PEGDA	poly(ethylene glycol) diacrylate
PETA	pentaerythritol tetraacrylate
PETG	polyethylene terephthalate glycol
PI	photoinitiator
pNIPAM	poly( <i>N</i> -isopropylacrylamide)
POM	polarized optical microscope
PVA	polyvinyl alcohol
RM	reactive mesogen
SBII	sudan Blue II
SEM	scanning electron microscopy
SLA	stereolithography
SME	shape memory effect
SMP	shape memory polymer
SP	spirothiopyran
STED	stimulated emission depletion
TAEI	tris[2-(acryloyl)ethyl] isocyanurate
TBAF	tetrabutylammonium fluoride
TEMPO	2,2,6,6-tetramethylpiperidine 1-oxyl
$T_g$	glass transition temperature
$T_{trans}$	transition temperature
$T_m$	melting temperature
TGA	thermogravimetric analysis
$T_m$	melting point /temperature
TMPTA	trimethylolpropane triacrylate
ToF-SIMS	time of flight-secondary ion mass spectrometry
TPA	two-photon absorption
TPO	diphenyl(2,4,6-trimethylbenzoyl)phosphine oxide
TPP	two-photon polymerization
UV	ultraviolet
VIS	visible

---

---

# CONTENTS

ACKNOWLEDGEMENTS .....	I
ABSTRACT .....	V
KURZFASSUNG.....	VII
ABBREVIATIONS .....	IX
CONTENTS.....	XI
LIST OF PUBLICATIONS AND CONFERENCE CONTRIBUTIONS.....	XIII
<b>1. Introduction</b>	<b>1</b>
<b>2. General and Theoretical Background</b>	<b>5</b>
2.1 3D Printing.....	6
2.1.1 Vat photopolymerization.....	8
2.1.2 Ink components and curing mechanisms.....	11
2.2 Two-photon laser printing (2PLP).....	16
2.2.1 Two-photon absorption (2PA).....	16
2.2.2 Resolution and Feature Size .....	17
2.2.3 Ink requirements for 2PLP .....	20
2.2.4 Current progress and challenges.....	21
2.3 4D microprinting .....	25
2.3.1 Stimuli responsive hydrogels.....	25
2.3.2 Shape memory polymers:.....	28
2.4 Liquid crystalline elastomers.....	32
2.4.1 Alignment method of liquid crystals .....	35
2.4.2 Surface alignment.....	37
2.4.3 Mechanical alignment.....	41
2.4.4 Electromagnetic alignment .....	42
2.4.5 Rheological alignment.....	43
2.5 Stimuli-responsive properties toward 4D microprinted LCE.....	44
<b>3. 4D Microprinting of Multi-Photoresponsive Liquid Crystalline Actuators</b>	<b>47</b>

---

3.1 Motivation and aims .....	48
3.2 Results and discussion .....	51
3.2.1 Synthesis of photoabsorbers.....	51
3.2.2 Incorporation of the dyes in the LC ink.....	56
3.2.3 From conventional approach to post-modification approach: demonstration with photoresponsive LCE films .....	58
3.2.4 2PLP of LCE microstructures .....	60
3.2.5 Implementation of photoresponsive properties into LCE microstructures.....	62
3.2.6 Two-photo laser printing of light-driven LCE microstructures.....	69
3.3 Summary .....	75
<b>4. Tailoring Liquid Crystalline Alignment of 4D Microstructures via PDMS Confinement</b>	<b>79</b>
4.1 Motivation and aims .....	80
4.2 Results and discussion .....	82
4.2.1 Fabrication of PDMS microcavities.....	82
4.2.2 LC alignment based on PDMS confinement.....	82
4.2.3 Alignment modulation along Z-axis.....	88
4.2.4 Tailoring alignment profile for LC microstructures .....	89
4.2.5 Investigating actuation behaviors based on PDMS induced alignment.....	94
4.2.6 Selective removal of PDMS scaffold .....	99
4.3 Summary .....	104
<b>5. Experimental Section</b>	<b>107</b>
5.1 Materials.....	108
5.2 Methods and procedures.....	108
5.3 Synthesis.....	118
5.4 NMR spectra .....	128
<b>6. Conclusions and outlook</b>	<b>139</b>
BIBLIOGRAPHY .....	145

---

---

# List of Publications and Conference Contributions

The results described in this thesis were partially published in scientific journals and presented at conferences. Publications, conference contributions and additional related works are listed in the following:

## *Peer-reviewed articles*

- **L.-Y. Hsu**, P. Mainik, A. Münchinger, S. Lindenthal, T. Spratte, A. Welle, J. Zaumseil, C. Selhuber-Unkel, M. Wegener, E. Blasco. "A Facile Approach for 4D Microprinting of Multi-Photoresponsive Actuators." *Adv. Mater. Technol.* **2023**, 8, 2200801.
- Münchinger, **L.-Y. Hsu**, F. Fürniß, E. Blasco, M. Wegener. "3D optomechanical metamaterials." *Materials Today*, **2022**, 59, 9.
- T. Schmitt, **L.-Y. Hsu**, N. Oberhof, D. Rana, A. Dreuw, E. Blasco, P. Tegeder. "Ultrafast Excited States Dynamics of Orthogonal Photoswitches and The Influence of the Environment." *Adv. Funct. Mater.* **2023**, 2300863.
- T. Spratte, S. Geiger, F. Colombo, A. Mishra, M. Taale, **L.-Y. Hsu**, E. Blasco, C. Selhuber-Unkel. "Increasing the Efficiency of Thermoresponsive Actuation at the Microscale by Direct Laser Writing of pNIPAM." *Adv. Mater. Technol.*, **2023**, 8, 2200714.
- P. Mainik, **L.-Y. Hsu**, C. W. Zimmer, D. Fauser, H. Steeb and E. Blasco. "DLP 4D Printing of Multi-responsive Bilayered Structures." *Adv. Mater. Technol.* **2023**, *submitted*.
- R. Eichelmann, J. Monti, **L.-Y. Hsu**, J. Ballmann, E. Blasco, L. H. Gade. „Two-Photon Microprinting of 3D Emissive Structures Using Tetraazaperylene-Derived Fluorophores." *ACS Appl. Mater. Interfaces.*, **2023**, *submitted*.
- **L.-Y. Hsu**, C. Vazquez-Martel, E. R. Curticean, I. Wacker, R. R. Schröder, E. Blasco, "Tailoring Liquid Crystalline Alignment of 4D Microstructures via PDMS Confinement." *manuscript in preparation*.

---

*Book Chapter*

- **L. Y. Hsu**, C. A. Spiegel, E. Blasco, 4D printing Principles and Fabrication, Smart Materials in Additive Manufacturing (Eds.: M. Bodaghi, A. Zolfagharian), Vol. 1, Elsevier, Amsterdam, the Netherlands **2022**, pp. 231 – 263.

*Conferences*

- **L.-Y. Hsu**, E. Blasco, "4D Microprinting of Liquid Crystalline Elastomers.", The 3DMM20 Conference 2022–3D Nano- and Micro-Manufacturing: Technology and Technical Applications, April 2022. Awarded with the Best Poster Award.
- **L.-Y. Hsu**, E. Blasco, "A Facile Approach for 4D Microprinting of Multi-Photoresponsive Actuators." GDCh Makro Molekulare Chemie 2022, September 2022. Awarded with the Best Poster Award.
- E. Blasco, C. A. Spiegel, **L.-Y. Hsu**, "4D microprinting of programmable polymers: towards "living" behaviours." SPIE Photonic West 2023, January 2023. Awarded with the 3D Printing Best Paper Award.

# **Chapter 1.**

## **Introduction**

Disruptive technologies, including the inventions of the light bulb, steam engine, aircraft, and internet, have had an unparalleled impact on human history. Additive manufacturing (AM), commonly known as 3D printing, is widely considered to have the potential to become another revolutionary technology. It not only transforms traditional manufacturing processes into more cost-efficient and productive ones but also enables the construction of complex structures that were previously unfeasible. Over the years, the range of materials used in manufacturing has expanded significantly, now including not only polymers but also metals, concrete, ceramics, glass, food components, and even cells. Additionally, the dimensions of 3D printing have scaled up to meters, allowing for the building of infrastructure or spacecraft, and meanwhile have scaled down to submicrometer levels, enabling the fabrication of microelectronic devices or microoptics.

As the common perception of 3D printing has been centered around the fabrication process and the intricately designed products, in recent decades, there has been a growing interest in integrating sensitivity to environmental impact into the printed structures across all sectors. This innovative approach, known as 4D printing, renders structures not with a fixed set of features but with adaptivity that allows properties or configurations to change dynamically over time according to the surroundings, exhibiting responses such as self-assembly, self-repair, or shape morphing. This has led to the creation of advanced smart systems that respond to varying external stimuli with different responding behaviors, which is attractive to multiple fields in both academic and industrial sectors, such as smart devices,<sup>[1]</sup> smart packages,<sup>[2]</sup> metamaterials, biomedicine,<sup>[3]</sup> and biomimetics.<sup>[4]</sup> Along with the development of emerging printing techniques, 4D printing at the microscale has generated significant interest, since microprinting not only fits into the manufacturing trend of miniaturization, but also paves the way to achieve applications that are not feasible with other fabrication techniques. Despite the availability of a wide variety of stimuli-responsive materials for macroscale fabrication, the investigation into the customization of smart microsystems remains in its early stages. In fact, merely three classes of promising materials, namely responsive hydrogels, shape memory polymers, and liquid crystalline elastomers (LCE), have been reported to achieve 4D microprinting. Among these, LCE has shown great potential in the development of autonomous smart systems, such as soft artificial muscles or actuators that can perform remote tasks. However, most published results are based on the same printing material and fabrication approach, which limits to the use of only one type of stimulus and exhibits only one responding behavior, thus impeding further advancement in this material sector of 4D

---

microprinting. Therefore, exploring emerging materials and approaches is mandatory to facilitate the development of such LCE based smart microsystems.

In the scope of this thesis, solutions to overcome underlying challenges will be discussed from two different perspectives. First, new functional materials are presented to expand the stimuli-responsive properties of the liquid crystal (LC) system. Second, a new fabrication approach is developed to enhance the complexity of the stimuli response of the LC material. The thesis comprises six chapters, and the topics and highlights of each chapter are outlined below.

Chapter 2 provides the reader with the fundamental knowledge necessary for understanding the work presented in this thesis. The chapter begins with a brief overview of the history of 3D printing technology and provides a more detailed description of the microfabrication technique, two-photon laser printing, employed in this research. As the primary class of material used in this thesis, Liquid Crystalline Elastomers (LCEs) are explained in detail, including their theory and the approach used in designing smart systems. The chapter also includes a summary of state-of-the-art examples related to 4D microprinted LCEs.

In Chapter 3, "4D Microprinting of Multi-Photoresponsive Liquid Crystalline Actuators", new materials for fabricating light-responsive LC microstructures were investigated. The chapter begins by discussing the challenges associated with developing new functional LC materials using conventional methods. In response, an emerging approach based on post-functionalization of the printed structures was developed to overcome limitations. The success of the approach was demonstrated with the fabrication of photoresponsive LC actuators, which can exhibit either single or dual responses under different irradiating conditions on demand.

Chapter 4, entitled "Tailoring Liquid Crystalline Alignment of 4D Microstructures via PDMS Confinement", presents a new approach to the tailoring of the LC alignment pattern, which is a crucial factor determining the behavior of the printed structure in response to stimuli. The new approach was based on the utilization of PDMS confining microscaffolds to redirect the LC three-dimensionally, enabling the implementation of distinct actuating patterns into the simultaneously printed structures.

Chapter 5 provides comprehensive details on all experimental procedures and techniques employed in Chapters 3 and 4, including characterization methods, fabrication design, and evaluation of the 4D systems and their stimuli-responsive behaviors.

Finally, Chapter 6, summarizes the discussion and results of this thesis. The chapter also provides an outlook for the future of 4D printing and potential applications derived from this thesis.

**Chapter 2.**

**General and Theoretical  
Background**

The development of emerging materials for 4D printed structures is a highly intricate process that requires the investigation of various aspects, including 3D printing technologies, the chemistry involved in the printing process, mechanisms for implementing the "4th" dimension, and approaches for pursuing innovation. This chapter aims to provide readers with a comprehensive understanding of the concepts and terms used in these topics, with a primary focus on two core foundations of this thesis: the applied printing technique "two-photon laser printing" and the material "liquid crystal elastomer". Prior to introducing the research in Chapters 3 and 4, the state of the art in relevant topics within this thesis will be discussed, with a scope on technical concepts and material perspectives. Additionally, the challenges encountered in the fabrication of stimuli-responsive liquid crystalline microstructures will be addressed.

## 2.1 3D Printing

3D printing, also known as additive manufacturing (AM), is a process of creating a three-dimensional object from a digital file or computer-aided design (CAD) model by stacking or fusing multiple layers of material to produce the final object. Traditional manufacturing processes generally involve excessive waste of material and time, such as subtractive techniques or formative techniques, which rely on the subtraction of material from a larger block or the additional material on fabricating molds, respectively, and often have limitations such as the need for expensive tooling and human labor. In contrast, 3D printing builds up parts layer by layer without additional tools, which enables unprecedented design freedom, reduced costs and lead times, and the improvement on environmental efficiencies.

This emerging technology wasn't evident until the late 1980s, at which time several patents were filed in parallel and multiple companies were founded. Initially, the technique was developed for creating prototypes, but as 3D printing technology has intensively progressed, various 3D printing methods were developed, and the technology was rapidly commercialized by the early 1990s. Due to its capabilities, it is often used in not only prototyping but also creating lightweight geometries in the engineering industry, including automotive, aerospace, healthcare, and consumer goods. To date, 3D printers have become smaller and affordable for under US\$500, making this technology more accessible to small companies for desktop fabrication of 3D objects, thus more systems, materials, applications, services, and ancillaries emerged. The prosperity associated with 3D printing, involving either the products developed

from 3D printing or the commercialization of the technology itself, has continuously accelerated the market growth across the globe and is estimated to achieve a market size of US\$ 87.2 billion at 2030, according to a new forecast report from Acumen Research and Consulting.<sup>[5]</sup>

The process of 3D printing commences with the creation of a 3D model with a CAD software or 3D scanning of a physical object.<sup>[6]</sup> The resulting model is then converted into the standard triangulation language (STL) format, which has been the most widely used format for preparing data for AM since 1987. The STL format contains the information about the surface geometry of the 3D model, represented by groups of connected triangles of varying sizes according to the required resolution. When the size of the triangles is smaller, the designed surface of a mesh is more accurately represented, yielding a smoother surface of the object to be printed. A preprocessing stage is responsible for preparing the mesh model before the start of the 3D printing process. The mesh model is subjected to a "slicing process" along the Z direction to determine the layer thickness based on the printer, AM technology, and quality requirements. The sliced model is then transmitted to the printer at the second stage to commence the 3D printing. The mesh is fabricated in a layer by layer fashion as defined previously. Following the completion of printing, the printed structure is removed from the platform, and additional technical processing procedures are employed to the printed object in a stage known as "development" or "postprocessing". In the case of photopolymerization, the solidified parts are rinsed with a solution, such as isopropyl alcohol (IPA), to remove the unpolymerized ink. Afterwards, in order to enhance the mechanical characteristics, post-curing treatment of these printed structures with UV or ambient light is commonly applied. Additionally, other techniques like removing support structures, grinding, sealing, gluing, polishing, painting, varnishing, coating, sterilizing, inspecting and measuring are utilized as well. Notably, the mechanical properties of the finished parts are influenced by the rinsing time, temperature, and duration of the curing process.

With a growing number of techniques being employed in the field of AM, various AM processes have been developed to meet their demands. Classifying various AM process based on various criteria such as application or physical principle of solidification, seven defined terms were listed in the following.<sup>[7]</sup>

- **Material extrusion:** Selective dispensing of flowable material through a nozzle is involved, including fused deposition modeling (FDM), fused filament fabrication (FFF), 3D dispensing, and 3D bioplotting.
- **Material jetting:** Selective deposition of droplets of build material, such as photopolymer or thermoplastic materials is involved. Inkjet-printing systems are examples of this type of process.
- **Binder jetting:** A process which involves the use of a liquid bonding agent through a nozzle to selectively join powder materials.
- **Sheet lamination:** Sheets of material are bonded together and selectively cut by laser to form an object.
- **Vat photopolymerization:** A vat is used to contain liquid photopolymer where light is used for selective curing by photopolymerization. Lithography-based AM approaches such as two-photon polymerization (2PP), digital light processing (DLP), and stereolithography (SLA) fall into this category.
- **Powder bed fusion:** Thermal energy provided by a laser or an electron beam is used to selectively fuse regions of a powder bed. Selective laser sintering (SLS) and electron beam machining (EBM) are examples of this category, which can be used for metals or polymers.
- **Directed energy deposition:** Focused thermal energy, like laser or plasma, is used to selectively fuse materials as they are being deposited. This process is currently only available metals currently only for metals.

These AM processes differ from each other in the terms of curing process, the type of materials, and the application purpose. In this thesis, attention is paid to vat photopolymerization-derived AM technology, particularly the one based on 2PP.

### 2.1.1 Vat photopolymerization

As described by the terminology, vat photopolymerization is a polymerization process involving the use of a “vat” and a “light” source. The vat contains a photocurable polymer, often also describe as an “ink”. The concept of the ink used in 3D printing was adapted from the negative photoresist, meaning solidification occurs at the part of the ink that is irradiated with a light source, either LEDs or laser beam, and it becomes insoluble in the solvent tank during the development.<sup>[7c, 8]</sup> Generally, a transitional stage is equipped within this type of 3D printer to afford local illumination three-dimensionally for fabricating the 3D structures. Vat polymerizing techniques can be classified into one-photon polymerization (1PP) and two-photon polymerization (2PP), which are namely differentiated by the number of photons used to reach the excited state for initiating the polymerization process. In the following sections,

some common 3D printing techniques based on 1PP will be introduced, sequentially followed by 2PP which is the focus of this thesis.

### **Stereolithography (SLA)**

The first commercialized AM devices, termed as "stereolithography" (SLA), were established by Chuck Hull's patent filed in United States in 1984.<sup>[7a, 9]</sup> The process involves a platform that is immersed in a tank filled with ink where a laser beam traces the construction area according to a sliced STL template (Figure 2.1A). The lateral position of the laser scanning is typically controlled by a pair of mirrors within a galvanoscanner to crosslink the plane on the surface of the photosensitive material, giving a print speed typically in the range of 10–20 mm h<sup>-1</sup>. The 3D model is created with layer-by-layer lithographic fabrication by lowering or raising the platform in the Z direction by a constant height of a single layer, ranging from 12 to 150 μm<sup>[8b]</sup>. The vertical resolution is defined by the curing depth, which is highly dependent on the exposure dose of the laser and the ink properties. The advantages of using a laser as the curing light source is that it offers high spatial resolution due to the spot size of the focused laser beam. Besides, grayscale patterning can be achieved if layer exposure dose for every pixel is adjusted individually by controlling the laser intensity, however it is not typically utilized in practice, likely because of the dependence of the curing depth on the exposure dose.

### **Digital Light Processing (DLP)**

Similar to SLA, DLP is also a 3D printing technique that utilizes light to selectively crosslink a photocurable ink in a layer-by-layer fashion to create a 3D object.<sup>[8b]</sup> Instead of exposing each point of the layer individually with the laser beam, the whole layer is projected with a sliced pattern of light through the transparent window at once (Figure 2.1B). The process utilizes a digital micromirror device (DMD), a micromirror array, which can tilt each mirror individually at high speeds to either reflect light or direct it away from the resin. The lateral resolution of DLP is therefore dependent on the pixels/mirrors provided by the DMD. The pixelated nature of the curing process can result in smoother surfaces and finer details than SLA technology. Light-emitting diodes (LED) are used as light sources in DLP covering a wavelength range from deep ultraviolet (UV) to visible. Importantly, since each layer is produced in one exposure step, the build time of DLP is considerably shorter than SLA. However, DLP printers may struggle

with certain geometries and overhangs due to the way that the light is projected onto the surface of the resin.

### Continuous Liquid Interface Production (CLIP).

Soon after the development of DLP, the novel CLIP system was introduced to enhance these techniques. A CLIP device is modified from a DLP device, implemented with a UV and oxygen permeable window at the bottom of the vat (Figure 2.1C). The window is used to supply oxygen to the liquid interface, creating an oxygen-enriched "dead" zone by quenching the radical resin-curing process derived from the digital light projector. With this, polymerization at the surface close to the UV source is prevented. This modification allows the ink be continuously pushed into the gap by suction force generated by the stage with the printed component moving away from the window. Therefore, without excessive stage movement, CLIP can afford printing rate of  $30 \text{ cm h}^{-1}$  at z-axis by dynamically varying each printed layer thickness ranging from 25-200  $\mu\text{m}$ , which is significantly faster than the traditional DLP printing.<sup>[8b, 10]</sup>

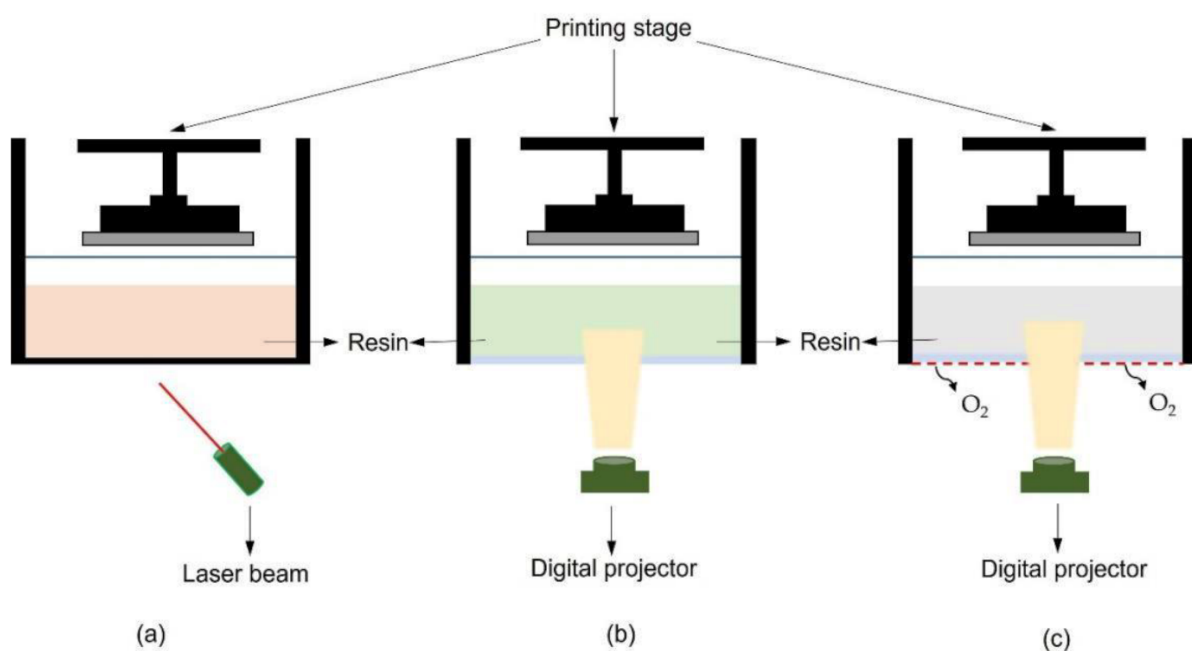


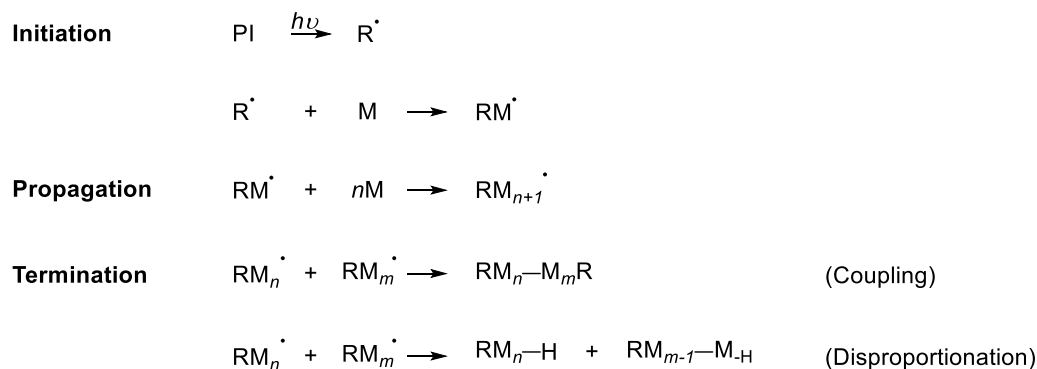
Figure 2.1 Schematic illustration of 3D printing techniques based on vat photopolymerization: (A) SLA printer (B) bottom-up DLP printer, and (C) CLIP printer. Figure adapted from reference [11]. Permission by MDPI.

### 2.1.2 Ink components and curing mechanisms

To conduct photopolymerization, the conventional ink typically consists of a photoinitiator (PI) and monomers functionalized with polymerizable group.<sup>[12]</sup> Two types of photocurable ink suitable for vat photopolymerization have been commonly employed in AM processes.<sup>[8a, 13]</sup> They vary in the type of photoinitiator and photopolymerizable moiety that determine the mechanism of polymerization and the mechanical/functional properties of the final 3D printed product. The first is cationic systems, in which the polymerization is a chain growth process initiated by a proton offered by a photoacid generator. A common epoxy-based ink, SU-8, belongs to this category.<sup>[14]</sup> The second exemplary class belongs to the radical system, which employs monomers with acryl/methacryl- or vinyl- functional groups. Particularly for the formulation based on acrylate-functionalized monomers, fast and high conversion of polymerization gives prominent performance in 3D printing. Therefore, the main discussion and development of the ink in this thesis focuses on this type of ink composition.

In the radical systems, crosslinking of a mixture of functionalized oligomers or monomers is carried out via free radical polymerization.<sup>[12, 14-15]</sup> This process involves several stages as outlined in Scheme 2.1.<sup>[14-15, 16]</sup> First, upon irradiation, light absorbed by a PI creates the initiating radicals  $R^*$ , which subsequently react with monomer  $M$  to form the first macroradical. The chain-growth proceeds through propagation by reacting with the double bond of monomer units to the growing macroradical. Last, for the formation of polymers at the final stage is the mono- or bimolecular termination reaction, which is dependent on the experimental conditions. Monomolecular termination involves the recombination of two chain pieces by coupling radicals into a carbon-carbon single bond. This is often the case for chains with a small steric effect, particularly when the ink becomes too viscous or rigid to allow diffusion of the remaining monomer near the reactive centers. On the other hand, bimolecular termination takes place through the disproportionation of two polymer chains which causes an atom (typically hydrogen) transferring from one radical chain to another ending up with two polymeric chains. This mechanism can be observed by following the conversion of monomer double bonds which results in an S-shaped conversion–time curve.<sup>[15b]</sup> This curve can be divided into three regimes attributed to the corresponding stage: (1) In the initial stage, the excited PI and reactive species react with inhibitors such as oxygen and stabilizers, leading to an induction period during which polymerization hardly begins. (2) Next, reactive species react with the monomer to form macroradicals after all inhibitors are consumed, which

propagate rapidly to reach a maximum value. (3) Last, a plateau is reached for the conversion when the medium becomes more solid.



Scheme 2.1 General mechanism of radical photopolymerization, including steps of initiation, propagation, and termination.

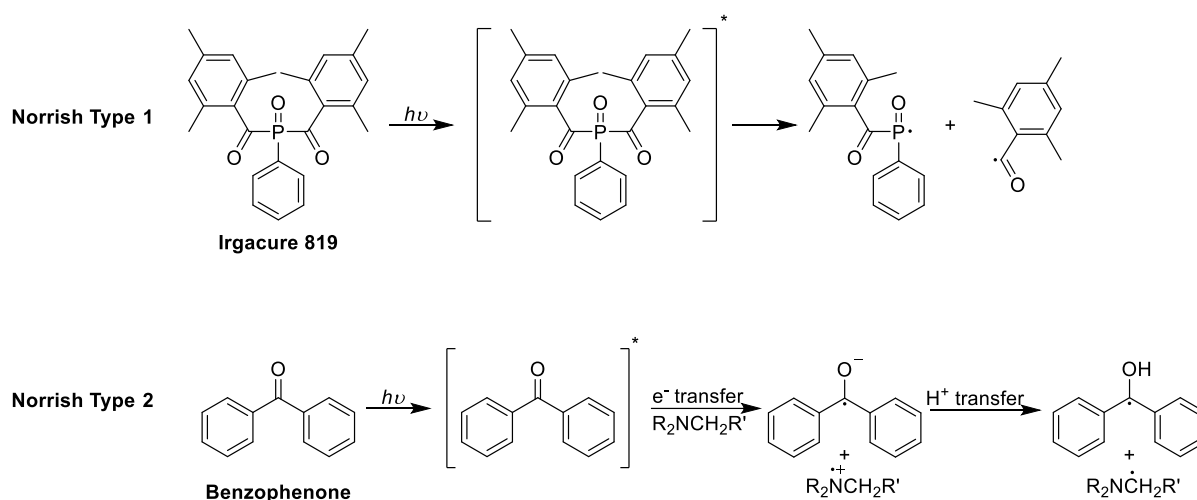
To accomplish this entire polymerization during the AM process, a few components which are essential in the ink composition are listed and discussed in the following section.

### Radical Photoinitiators (PIs)

A PI in the radical system converts the photolytic energy into reactive species at the beginning initiation stage of the polymerization. Therefore, the first consideration when selecting a PI is that the absorption region is favorable for the chosen AM process.

Typical radical PIs are classified into two types: Norrish Type I or Type II.<sup>[8a, 13-14]</sup> Norrish Type I PIs are single molecules which cleave into radical fragments after absorbing light as depicted in Scheme 2.2. Commonly used initiators that belongs to this category include Darocur 1173, Irgacure 184, Irgacure 651, and Irgacure 369, Irgacure 819 and TPO (diphenyl(2,4,6-trimethylbenzoyl)phosphine oxide). For those belonging to acyl phosphine oxides, such as Irgacure 819, a lower  $n \rightarrow \pi^*$  transition energy is needed due to the presence of a phosphorus atom adjacent to the carbonyl group which lowers the energy level of the  $\pi^*$  state, resulting in a more red-shifted absorption maximum than that of benzil ketals around 400 nm.<sup>[7a]</sup> Norrish Type II photoinitiation proceeds through a two component system including a light-absorbing molecule (or sensitizer) and a co-initiator (or synergist). Upon irradiation, the initiating radical is generated by the proton transferring from the synergist to the excited sensitizer, acting as

a rate determining step of the initiation. Benzophenone and isopropylthioxanthone are typical examples used as Type II sensitizers and tertiary amines are often employed as Type II co-initiators. However, it is worth mentioning that amine synergists would suppress the cationic-based system therefore it is not favorable for inks that involve mixed systems.



Scheme 2.2 Photoinitiation mechanisms of Norrish type I (above) and type II (below) photoinitiators.<sup>[7a]</sup>

## Monomers

Acrylate-functionalized monomers have been typically employed in vat photopolymerization-based AM process, owing to their faster reaction time.<sup>[8a, 12, 14-15]</sup> However, distortions and severe shrinkage of the printed objects are the major drawbacks of acrylate inks, particularly in layer-by-layer fabrication, which has to be considered while using acrylates. Various strategies exist to mitigate the issue of polymerization shrinkage. One intuitive method is the incorporation of other types of photopolymerizable monomers, such as methacrylate or vinyl monomers, which have slower curing kinetics. On the other hand, the addition of monomers with dual- or even multifunctionalized monomers not only ensures rapid crosslinking but also enhances the mechanical stability of the printed structures. Dipropylene glycol diacrylate (DPGDA) or pentaerythritol tetraacrylate (PETA), for example, are often incorporated to serve this purpose (Figure 2.1). In addition, the degree of shrinkage is also influenced by the molecular structure of the monomers, where the ones with cycloaliphatic and aromatic acrylates, e.g., tris[2-(acryloyl)ethyl] isocyanurate (TAEI), shrink less than aliphatic ones. Using preorganized acrylate monomers or oligomeric acrylates with higher molecular weight (e.g.,

PEGDA (poly(ethylene glycol) diacrylate),  $M_n=700$ ) has also been explored as an alternative approach to reduce shrinkage stress (Figure 2.2).

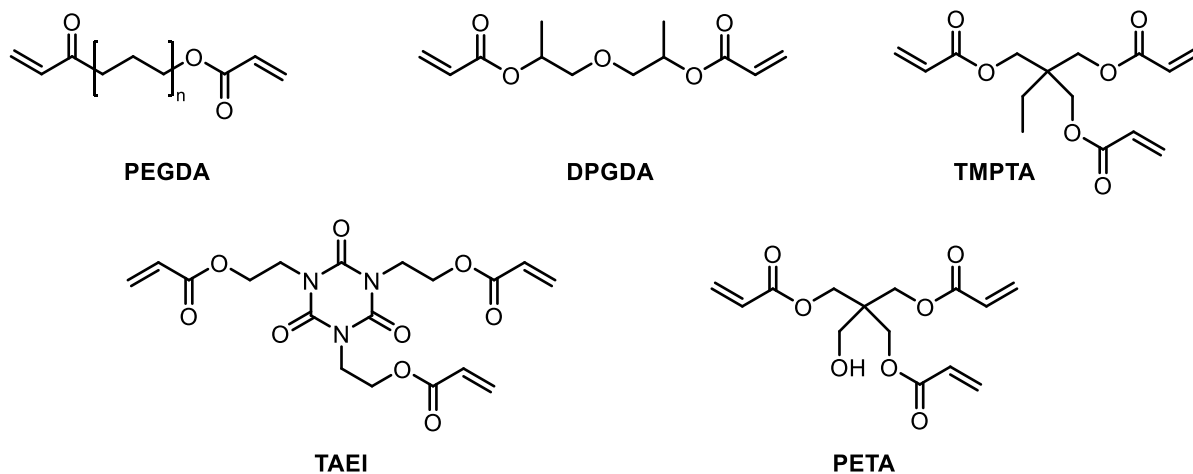


Figure 2.2 Chemical structures of acrylate functionalized crosslinkers.

On top of the (meth)acrylate monomers mentioned, “thiol–ene” chemistry has also been explored in the radical system.<sup>[7a, 17]</sup> Structures printed with thiol–ene-or thiol–yne based formulations were observed to have less polymerization shrinkage and were less brittle compared to acrylate-based ones. This is attributed to the shorter kinetic chain length resulting from the step growth kinetics of thiol–ene systems, allowing a more efficient dissipation of stress.<sup>[18]</sup> Therefore, thiol-based monomers were commonly combined with acrylates or other double bond species to afford the optimal mechanical properties of the printed structures.

In certain instances, multifunctionalized monomers are too viscous to be processed directly on their own by AM and require thinning with a lower viscosity reactive diluent. Additionally, in the presence of the PI, insolubility or inhomogeneity are also often observed in the ink mixture, causing obstacles for the AM process. Therefore, the addition of nonreactive additives or solvents may be necessary not only for decreasing the viscosity of the formulation but also ensuring complete dissolution of the monomers, PI, or additional additives.<sup>[19]</sup> However, adding a solvent to the ink is generally not advantageous in 3D printing for several reasons and a few aspects have to be carefully considered. Firstly, the addition of a solvent leads to the dilution of polymerizable components within the ink, leading to poor or insufficient curing during the printing/polymerization process and thus unsatisfactory printing outcomes.<sup>[15a, 19a,</sup>

<sup>20]</sup> Even for high boiling point solvents, volatility may cause inconsistency of the formulation especially under the circumstances where stage movement is involved in the printing process. Subsequently, since solvent within the 3D printed object will be removed together with unpolymerized monomers during the development step, the resulting voids might weaken the mechanical stability or lead to structural shrinkage, distortion or surface cracking. Thirdly, solvent molecules can potentially cause chain transfer during the polymerization process, where the consequent early termination of chain propagation might lead to poor polymerization and printing outcomes.<sup>[15a, 21]</sup> As a result, solvent-free formulations are generally preferable to avoid the potential issues arising from solvent use. To overcome the dissolution problem mentioned, a reactive diluent may be used as an alternative.<sup>[19b]</sup> This refers to those monomers which have low viscosity that allows for dissolution and viscosity reduction.

In addition to the main components mentioned, a photoabsorber (e.g., Sudan I), an organic dye that has the ability to absorb light within the range of the applied photoinitiating wavelength, is often utilized in inks used in macroscale vat photopolymerization methods to reduce the curing depth of each layer leading to the enhancement of resolution along the Z-axis. On the other hand, functional additives can be incorporated into a liquid ink to incorporate additional properties to the 3D printed structures.<sup>[12]</sup> Such composite formulations have been created by including magnetic nanoparticles, piezoelectric barium titanate nanoparticles, quantum dots, carbon nanotubes, proteins, and biological cells, among other things. This presents an opportunity to fine tune or implement corresponding functionalities such as magnetism, conductivity, electrochromism, thermoresponsivity, photoresponsivity, or biodegradability into the 3D printed structures.<sup>[22]</sup>

## 2.2 Two-photon laser printing (2PLP)

Two-photon laser printing (2PLP), also known as direct laser writing (DLW), is an advanced vat polymerization 3D printing technique. Different from other techniques mentioned earlier in which the photopolymerization is a one-photon absorption (1PA) process, 2PLP is based on two-photon polymerization (2PP), which involves the use of a femtosecond pulsed laser focusing inside an ink to fabricate 3D structures with submicrometer resolution.<sup>[13]</sup> The utilization of two-photon absorption allows the printing resolution to surpass the limitations of other 3D printing methods. Its potential in a wide range of applications, including in the fields of optics, photonics, tissue and cellular engineering, has garnered significant attention.<sup>[23]</sup>

### 2.2.1 Two-photon absorption (2PA)

The theoretical analysis of the simultaneous absorption of two photons by a single molecule was initially proposed in 1931 by Maria Göppert-Mayer in her doctoral thesis.<sup>[24]</sup> The first experimental demonstration of two-photon absorption (2PA) was reported in 1961 by Kaiser and Garrett, shortly after the invention of the laser.<sup>[25]</sup> The advent of sub-picosecond pulsed lasers, such as the Ti:sapphire laser, in the 1990s made it easier to investigate two-photon absorption. The invention of two-photon fluorescence microscopy by Webb and colleagues,<sup>[26]</sup> and its rapid adoption by confocal microscope manufacturers, spurred interest in all types of multiphoton processes.<sup>[27]</sup> Until 1997, 3D fabrication using two-photon laser lithography was pioneered by Kawata.<sup>[28]</sup>

The key distinction between 1PA and 2PA lies in the fact that the exposure dose ( $D_{exp}$ ) of the latter is a nonlinear process. This involves the simultaneous absorption of two photons and increases proportionally to the square of the light intensity ( $D_{exp} \propto I^2$ ) (Figure 2.3). In contrast, 1PA is linearly dependent on the local intensity ( $D_{exp} \propto I$ ). As a result, 2PA is only observed in highly intense laser beams generated by focused pulsed lasers that give a very high instantaneous photon density. As depicted in the Jablonski diagram (Figure 2.3), the polymerization process of 2PP occurs upon the excitation of the initiating species to a singlet excited state through a virtual intermediate state with lifetimes in the femtosecond range, followed by intersystem crossing to a triplet excited state and decaying through the cleavage

of bonds to form radical species in the case of radical polymerizations. However, this is a competing process among all the deactivation pathways, such as fluorescence, phosphorescence, and initiator and radical quenching. The control over the propagation process aids in the polymerization occurring within small volumes, allowing access to fabrication with fine feature resolution.<sup>[29]</sup>

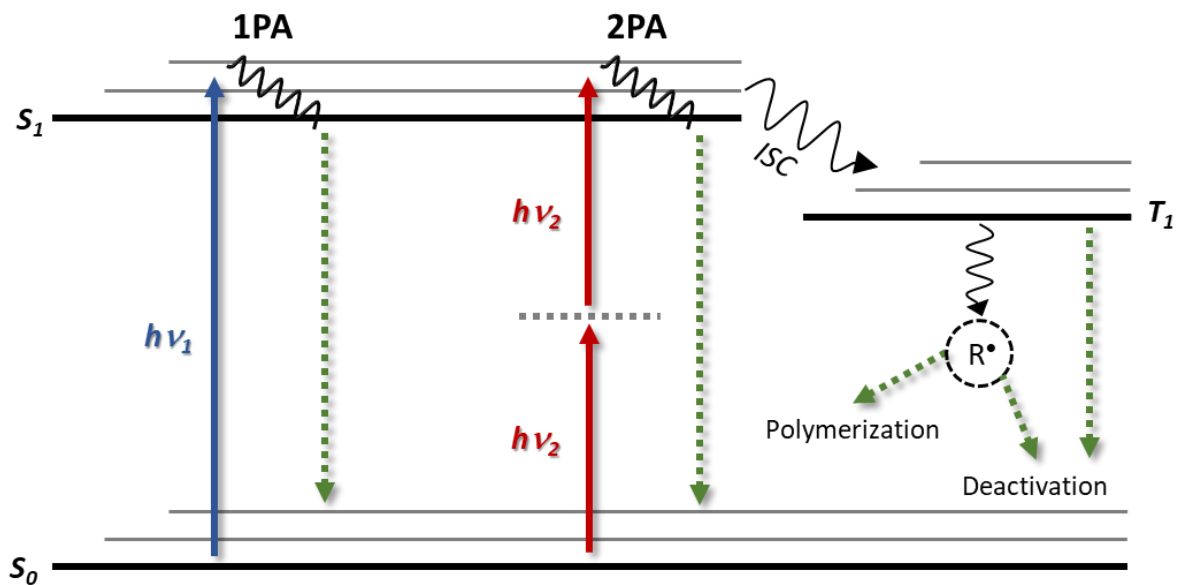


Figure 2.3 Jablonski diagram of photopolymerization based on one-photon absorption (1PA) and two-photon absorption (2PA), where the latter leads the excited electron through a virtual intermediate state before reaching the  $S_1$  excited state.

### 2.2.2 Resolution and Feature Size

The minimum volume which can be achieved by 2PP is known as a voxel, analogous to a pixel in 2D images. The size of a voxel is optimized by dosing the ink only fractionally above the polymerization threshold while using high numerical aperture optics to focus the beam into a smaller excitation volume.<sup>[30]</sup> In general, single-photon polymerizations are limited to feature sizes of half the wavelength of the incident light. In contrast, 2PP can achieve feature sizes below 100 nm using a 780 nm source because its nonlinear intensity decreases steeply moving away from the voxel center. Although the underlying processes during the ink

photopolymerization are not yet fully comprehended,<sup>[31]</sup> most observed effects in experiments can be explained using the threshold model and the accumulation model.<sup>[29]</sup>

**Threshold model:** The threshold model states that the local exposure dose within the ink should exceed a certain dose threshold to achieve sufficient crosslinking and remain intact after development. If the exposure dose falls below the threshold dose, the material is not adequately crosslinked and will be washed out during the development stage. For this case, the printed width from a single exposure is determined by the dose profile, with a width corresponding to the peak above the threshold value. With this model alone, it is possible to fabricate small features arbitrarily close together, independent of whether the absorption process is linear or nonlinear.<sup>[30, 32]</sup>

**The accumulation model:** The accumulation model involves the integration of two or more point exposures that the ink experiences at the same or different locations — regardless of whether they are above or below the threshold. The total exposure dose is then evaluated using the threshold model to determine whether a stable polymer network has formed. On this basis, even if the first exposure alone is below the threshold, it still contributes to the shape of the polymerized feature when the subsequent adjacent exposure occurs. Additionally, the minimum separation between adjacent separated features is determined by the two-photon Sparrow criterion<sup>[30]</sup> of the accumulated exposure doses. This model infers that two doses which are spatially separated above the threshold could possibly lead to undistinguishable polymeric features. However, within the accumulation model, it is not feasible to print arbitrary complex 3D architectures using 1PA, while 2PA or multiphoton absorption enables this possibility.

The advantage of the nonlinearity of 2PA against the linearity of 1PA is significant while considering the proximity effect, i.e., the accumulation of exposure dose.<sup>[33]</sup> A precise comparison was reported by Wegener and coworkers with a modeled 3D object printed with voxels for both one-photon and two-photon absorption, shown in Figure 2.4.<sup>[29]</sup> The printing of table-like structures was simulated with the total exposure dose being the accumulated individual exposure dose by laser focus scanning. For 1PA, the table plate becomes thicker in the middle, with a rapid increase in thickness as the exposure dose increases. This leads to a prominent overexposed region in the upper row of Figure 2.4 for a 333% dose. For 2PA, a thickening of the plate along with increasing dose is also observed in the lower row, but the

thickness of the plate remains roughly constant throughout the area, showing superior performance of two-photon in terms of structural fidelity.

Achieving efficient polymerization by 2PP processes requires the optimization of several combined system parameters, including laser power, writing speed, objective lens and ink. As the width at the threshold value of the dose profile is dependent on the intensity of the incident light, the voxel size is variable depending on the laser writing conditions. Generally, fine features can be achieved with lower powers and higher writing speed by having a minimum laser dose above the threshold. On the contrary, higher laser power or lower writing speed results a wider written line. The optimization of these two printing parameters offers a fabrication window (FW) with a lower limit of surpassing the polymerization threshold and an upper limit of over exposure.

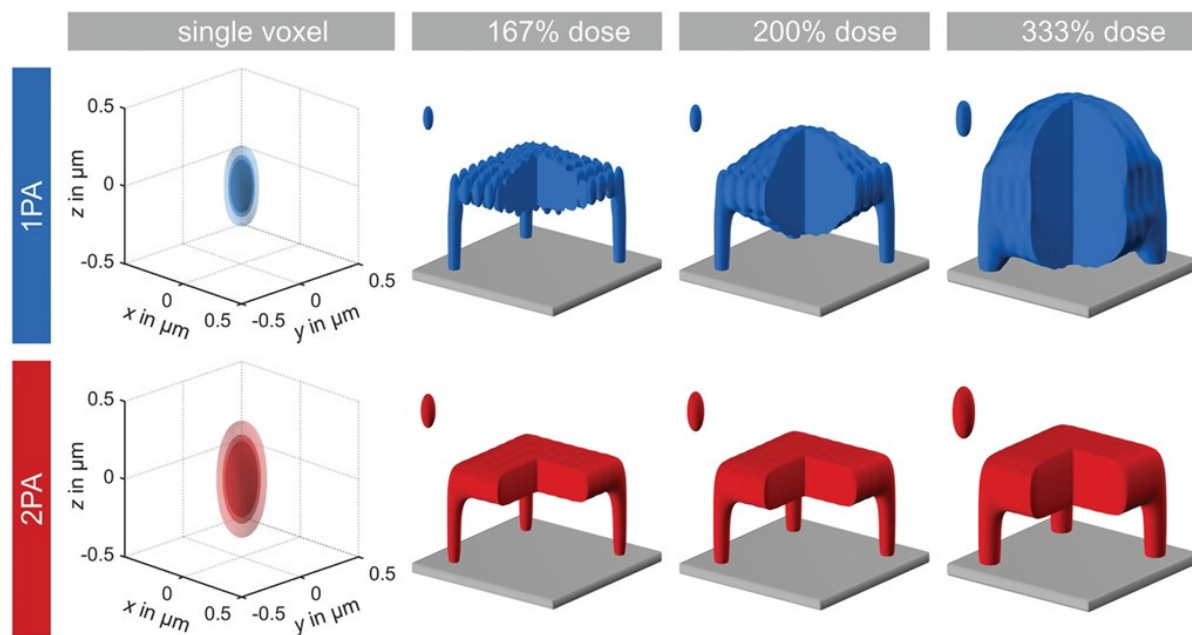


Figure 2.4 Illustrations of 3D laser nanoprinting varied in 1PA and 2PA. Herein, the simulation was based on an objective with numerical aperture of  $NA = 1.4$  and printing wavelength at  $400\text{ nm}$  was considered for 1PA ( $D_{exp} \propto I$ ) and  $800\text{ nm}$  for 2PA ( $D_{exp} \propto I^2$ ). Their single-voxels were defined by the threshold model and the resulting printed structure by increasing the exposure dose to 167%, 200%, and 333% with the assumption of accumulation model are displayed. (slicing =  $0.2\text{ }\mu\text{m}$ ) Figure adapted from reference [29]. Permission by Wiley-VCH.

### 2.2.3 Ink requirements for 2PLP

Similar to other vat polymerization-based AM process relying on one-photon absorption, the inks used in this approach consist of monomers, crosslinkers, PIs, and a suitable solvent such as water or polar solvents. However, as the probability of the 2PP occurrence is much lower than 1PP, higher density of crosslinkable groups in the ink is necessary to facilitate the 2PLP process. Therefore, the content of crosslinkers in an ink for 2PLP is generally higher than for one-photon printing.<sup>[13, 22, 34]</sup> In particular, aside from bifunctionalized crosslinkers, multifunctional ones, such as PETA or TMPTA (Trimethylolpropane triacrylate), are also commonly included to ensure high printing velocities and efficient network formation.<sup>[35]</sup> Moreover, despite other polymerization processes, such as crosslinking epoxide moieties based on cationic polymerization, which have been applied in 2PLP, acrylate-based monomers and crosslinkers are most commonly published due to their fast reaction kinetics.<sup>[7a, 13, 23a, 29, 34]</sup>

The selection of PI is more critical in this case compared to one-photon printing, owing to the requirement of prominent two-photon sensitivity that highly restricts the selection into a narrower range.<sup>[36]</sup> The evaluation of two-photon initiators (2PIs) often involves one crucial parameter that is the two-photon cross-section ( $\sigma_{2PA}$ ), which represents a molecule's ability to undergo the 2PA process. The unit of this parameter is Göppert-Mayer value (GM), where one GM value represents  $10^{-50} \text{ cm}^4 \text{ s photon}^{-1}$ .<sup>[36]</sup> Two standardized methods are utilized to determine the value of  $\sigma_{2PA}$ : the Z-scan<sup>[37]</sup> and the two-photon excited fluorescence.<sup>[38]</sup> These measurement methods have been described in detail in reference <sup>[36]</sup>. A wide range of commercially available PIs have been reported with their  $\sigma_{2PA}$  value.<sup>[36]</sup> Conventionally, a high  $\sigma_{2PA}$  was considered to be indicative of high efficiency in the polymerization process. However, in the field of two-photon polymerization, the effectiveness of a PI depends on various conjugated factors, including the concentration of the 2PI, fluorescence quantum yield ( $\Phi_{fl}$ ), intersystem crossing efficiency, solubility, monomer composition, laser intensity and viscosity, which also play crucial roles in fabricating structures. Usually, additional fabrication tests using different laser intensities and writing speeds to evaluate the fabrication window (FW) are required to assess the potential of a 2PI. As a result, while it is possible to compare initiators within a single study, there is a lack of a standardized approach to compare initiators across multiple reports. Kiefer *et al.* have addressed this challenge by comparing over 70 photoresists from the literature in terms of various relevant factors such as writing speed, polymerization threshold, laser wavelength, pulse duration, repetition rate, numerical aperture, and 2PI

concentration, and established a figure of merit to enable the comparison of different inks.<sup>[29]</sup> Among all the commercially available ink systems, DETC (7-diethylamino-3-thenoylcoumarin) has shown high two-photon sensitivity with high figure of merit value at large focus velocities while having PETA as crosslinker.

For inks with composite materials or poorly soluble PI, the use of solvent is particularly necessary despite several potential issues as mentioned in the previous section. This is owed to the fact that inhomogeneity in inks often leads to unpredictable microexplosions (microbubbling) under such highly powered laser focus hindering the fabrication process. High boiling point solvents with no absorption at the curing wavelength, such as DMSO, DMF or DMAc, are the typical choices to prevent evaporation.<sup>[7a, 19a]</sup>

### 2.2.4 Current progress and challenges

Since the commercialization of 2PLP in 2007, tremendous growth of this technology in terms of technical aspects, the library of printable materials, and applications, has been witnessed over many disciplines in both academia and industry.<sup>[13, 23a]</sup> Overall, 2PLP is still a relatively young technology. To further enhance the potential of this technology for future applications, three development challenges are described as "finer, faster, more".<sup>[39]</sup> Current developments of this technology in these three aspects will be addressed in the following section.

#### **Super-resolution printing**

As 2PLP is in the field of micro- to nano-scale 3D fabrication, intensive works have aimed at achieving finer features or smaller voxel sizes, which ultimately leads to better spatial resolution. The major challenge is to transcend the diffraction limit.<sup>[30]</sup> Printing stable 3D structures, particularly conductive ones, with a line width written below the diffraction limit of around 10 nm at high writing speeds would represent a significant advancement, with the capacity to transform an entire industry. Optics-based approaches play a significant role in this ongoing challenge.

Several successful attempts have been made in this regard. One of them is the utilization of the principle of stimulated-emission depletion (STED) to further improve the possible minimal feature size of fabricable 3D microstructures. STED is a principle introduced by Stefan Hell and

used in fluorescence microscopy to confine the volume of photoexcited fluorescent molecules by deactivating them with a second laser with a doughnut focus shape.<sup>[40]</sup> Translating this principle to 2PLP, the second laser is employed for depleting the polymerization. For example, Müller *et al.* have demonstrated STED lithography using methacrylate copolymers equipped with side groups of photochromic spirothiopyran, which is able to undergo photoisomerization from a closed form (SP) to an opened merocyanine form (MC) that can activate crosslinked network formation via supramolecular interaction between the chromophores upon the 2PA at 820 nm. The photoswitching is reversible under irradiation of a 640 nm laser, which was employed with a half-space phase mask for depleting the peripheral polymerization of the focused center. The result was a reduced linewidth to 31 nm, which is almost a factor of 2 compared to that of its diffraction limited conventional approach.<sup>[41]</sup>

Recently, apart from utilizing the conventional simultaneous 2PA for 3D microfabrication, multiple “(1 + 1)-photon absorption” processes, including upconversion luminescence, two-step absorption, and triplet-triplet annihilation, were also explored by Hahn *et al.*<sup>[42]</sup> In particular, a similar optical nonlinearity as 2PA was presented with a novel approach of employing sequential two-step absorption for the radical initiation process using benzil<sup>[43]</sup> as a photoinitiator.<sup>[44]</sup> Under the optimized conditions, a PETA-based ink consisting of BTPOS (bis(2,2,6,6-tetramethyl-4-piperidyl-1-oxyl) sebacate) as a scavenger was employed to print structures with outstanding resolution of minimum grating periods below 150 nm. In this approach, the use of a continuous-wave (cw) laser with sub-milliwatt optical output at 405 nm wavelength has reduced equipment costs, enabling highly efficient and precise microstructure fabrication. These advantages have overcome the limitations of conventional 2PA, including high costs of femtosecond pulsed lasers, poor reliability, and spacious size of the microprinting systems.

### **Towards fast and scalable 2PLP**

Increasing the fabrication speed, referring to number of 3D printed voxels per second, is the key to improve 3D microgeometry output and make this technology scalable. This aim could be approached through various methods, such as increasing the scanning speed of a single focused laser,<sup>[29]</sup> adapting to multiple foci,<sup>[45]</sup> or using projection-based methods to print several units in parallel without scanning in the focal plane.<sup>[46]</sup> As demonstrated by coworkers from the Wegener group in 2020, a method that enables the parallelization of microstructure

fabrication was developed, allowing for the simultaneous printing of microstructures in a  $3 \times 3$  array with a total voxel printing rate of  $10^7$  voxels  $s^{-1}$  by separating one focus into nine single spots. This multi-focus approach was demonstrated by fabricating a 3D structure constructed by 108000 unit cells with a total volume of  $2.4 \times 2.4 \times 9.6$  mm<sup>3</sup>, manifesting the advantages of this method.<sup>[45c]</sup> Recently the same group has presented a new generation multi-focus printing technique which prints ten times faster than the previous generation, where the laser beam was split up into a  $7 \times 7$  foci array with equivalent laser intensity by implementing a multi-lens array to overcome the angular dispersion problem.<sup>[47]</sup>

Another novel approach under development to overcome the speed limitations of 3D printing is inspired by light-sheet optical microscopy, which involves the use of two different wavelengths to create a 2D image.<sup>[39]</sup> Such light-sheet 3D printing, also called xolography<sup>[48]</sup>, requires an "AND-photoresist" that will polymerize only if lights of both wavelengths are present in a certain volume element. The light-sheet 3D-printing approach uses two successive one-photon absorption processes, rather than two-photon absorption, which can be induced by two different continuous-wave lasers or two different light-emitting diodes. In the "two-color two-step absorption" approach reported by Hahn *et al.*, fabrication was conducted by projecting images with two colors (440 nm and 660 nm) of light sheets to facilitate the two-step absorption of the PI, biacetyl (2,3-butanedione).<sup>[46a]</sup> Together with the mixture of multifunctional acrylates and TEMPO (2,2,6,6-tetramethylpiperidine 1-oxyl) as a scavenger, fabrications of various complex 3D microstructures were demonstrated, having a peak printing speed of  $7 \times 10^6$  voxels  $s^{-1}$  with a voxel volume of  $0.55$   $\mu\text{m}^3$ .

### New functionalities

To date, the majority of conventional fabrications via 2PLP have employed only a single material, resulting the printed structures with a fixed set of characteristics. In particular, most structures reported have been passive ones, meaning that there is no adaptability or tunability of the material properties. To transcend the "more" challenge, various aspects have been pursued by researchers as addressed in the following chapters.<sup>[22, 34]</sup>

In terms of material aspects, much progress has been made from expanding the library of two-photon printable materials, such as adaptive, biocompatible, metallic, ceramic, and semiconductor ink formulations.<sup>[22, 34]</sup> This affords accessibility to fabricate not only 3D

microstructures with higher variance of material features, but also the possibility to fabricate multimaterial architectures with enhanced functionality via step-wise printing.<sup>[49]</sup> For example, recently Yang *et al.* reported microelectronics with minimum feature sizes below 1  $\mu\text{m}$ .<sup>[50]</sup> This was achieved by the utilization of three different inks in combination with both femtosecond laser (780 nm) and continuous-wave laser (532 nm) to carry out a photochemical reaction of each ink selectively, to create a device comprised of three materials of semiconductor ZnO, and metals Pt and Ag. Another example of multimaterial printing with more sophisticated features was based on the integration of a microfluidic system containing multiple ink cartridges to the printer.<sup>[51]</sup> After writing a 3D micro-architecture with a first photoresist, the structure was autonomously developed on site, followed by the injection of a second resist and the corresponding writing job. This allowed the fabrication of complex multimaterial structures, demonstrated by 3D microstructures with intricate security features, which were printed with four fluorescent inks doped with various semiconductor CdSSe core-shell quantum dots or dye molecules and a non-fluorescent ink.

Instead of relying on the particular ink to afford one single property, in recent years much more attention has been paid on the development of printing dynamic, adaptive, or “living” materials, meaning that structures from a single ink are able to show multiple material properties, achieved by either expanding, cleaving or degrading the printed network, or the incorporation of stimuli-responsive features. One approach to achieve this is the incorporation of dynamic covalent chemistry<sup>[52]</sup> into the 3D printed microstructures that allows bond cleavage or formation autonomously or upon stimulus<sup>[52b, 53]</sup>, leading to the possibility of extending and cleaving the polymer network.<sup>[54]</sup> One example that belongs to this category is the dynamic alkoxyamine bond which offers accessibility of modulation from nitroxide exchange reaction (NER) as well as nitroxide mediated polymerization (NMP).<sup>[53a]</sup> As reported by our group, the covalent adaptable microstructures incorporated with alkoxyamine bonds showed dynamic and adaptable size and mechanical properties on demand.<sup>[19a]</sup> The other approach of incorporating stimuli-responsive properties in the 3D printed structures is often described as “4D printing”. This topic will be discussed in detail in the following sections.

## 2.3 4D microprinting

As the technique of 3D printing has evolved, innovations in printing materials have aimed to expand the functionality of the printed structures. The integration of environmental impact into 3D printing was first proposed by Skylar Tibbits at 2013, introducing the concept of 4D printing. This emerging approach highlights the adaptive behavior of a printed 3D structure that can transform from one shape to another in response to external forces.<sup>[7c, 55]</sup> Therefore, "time" serves as the fourth dimension. After intensive development of this topic within the past few years, the term "4D printing" has evolved to refer to controllable shape or property changes of a 3D printed object upon exposure to an external stimulus, such as temperature, humidity, solvent, light, pH, or magnetic and electric fields. With this idea began the conception of incorporating "life" into a static object that show biomimetic response to environments.<sup>[4, 7c]</sup> Evolving over time, 4D printing has attracted great research interest into a much larger interdisciplinary scope, including the fields of chemistry, physics, biology, medicine, and material science, paving the way for its potential in multidirectional applications.<sup>[7a, 56]</sup> To date, while 4D printing of macroscopic objects has been prosperously developed in both scientific research and industry, the demand for precise micro- and nanostructures with adaptable properties has increased in innovative areas such as biomedicine, microoptics, microfluidics, microsensors and microrobotics.<sup>[22]</sup> 2PLP offers a novel approach for manufacturing on a nanometer scale with high precision, however, the development of the library for printable functional materials to achieve the "fourth dimension" that show great printability via 2PP and adaptiveness is still in its early stages.<sup>[57]</sup>

The following sections will summarize the current state-of-the-art materials for 4D printing at the microscale along with their challenges and potential applications.<sup>[57g, 57h]</sup> The stimuli-responsive materials which have shown promising performance for 4D microprinting include hydrogels, shape memory polymers, and liquid crystal elastomers. Particular attention and details will be given to liquid crystal elastomers (LCEs), which is the main focus of this thesis.

### 2.3.1 Stimuli responsive hydrogels

Hydrogels, which are hydrophilic 3D crosslinked polymer networks, are a fascinating category of soft stimuli-responsive materials. This is due to the dependency of the water content to their environment, leading to significant volume changes by the alteration of stimuli such as

temperature, solvent, pH value, or enzymes. This property makes hydrogels ideal candidates for the creation of 3D soft actuators<sup>[58]</sup>, including artificial arms<sup>[59]</sup> and smart grippers<sup>[60]</sup>, using 3D printing at the macro- and mesoscales.<sup>[61]</sup>

Transferring these remarkable stimuli-responsive features to microprinting with the utilization of 2PLP has been an auspicious approach to achieve 4D microstructures. For fabricating hydrogel microstructures with 2PP, the ink contains monomers and crosslinkers, which are commonly equipped with photopolymerizable groups like acrylates or acrylamides, polar solvents such as water, and a soluble photoinitiator. To obtain the desired stimuli-responsiveness, specific functionalized monomers are included in the formulation. For example, poly(*N*-isopropylacrylamide) (pNIPAM) is often used to generate thermoresponsive structures. pNIPAM exhibits a low critical solution temperature (LCST) of 32-34°C, resulting in the substantial collapse and shrinkage of the network, and consequently the printed structure, at temperatures beyond this range.<sup>[62]</sup> Moreover, pH sensitivity can be achieved by adding monomers containing acrylic acid functional groups or by using protein hydrogels. For this case, the swelling behavior is attributed to the robust electrostatic repulsion when the isoelectric group is deprotonated/protonated due to a change in pH. Furthermore, multi-responsive structures can be attained by combining two or more functional monomers such as NIPAM and acrylic acid in the ink. The addition of a crosslinker is crucial for fabricating microstructures with good mechanical stability due to the soft nature of hydrogels. Since the stiffness of the hydrogel network is highly dependent on the presence of crosslinkers and their ratio between the monomers within the formulation, it requires careful optimization because high crosslinking density might also diminish the actuating behavior at the same time. Choosing the right photoinitiator can also be a challenge, as it needs to have a high two-photon cross-section ( $\sigma_{2PA}$ ) and photoinitiation efficiency, and must be adaptable to the highly polar environment. While a few water-soluble photoinitiators have been reported, their complex preparation and limited accessibility remain a drawback.<sup>[36, 63]</sup> This limits the selection of water/bio-compatible initiators to only few options, such as the commonly used LAP (lithium phenyl-2,4,6-trimethylbenzoylphosphinate). Considering the solubility of these components, water is usually used as solvent in the case of macroprinting,<sup>[23c, 64]</sup> however, in the case of 2PLP, high boiling point polar solvents, e.g., ethylene glycol, are preferable to limit solvent evaporation and microexplosions.

For fabricating microactuators based on the shape changes of active hydrogels under external stimuli, 2PLP is an exquisite method as it offers a versatile approach for tuning various parameters during the fabrication process to optimize the resulting structures. Printing parameters, such as power intensity, writing speed, and writing distance, play a crucial role in determining the crosslinking density of the hydrogel network, thereby affecting the final properties of the structures. Gray-tone lithography, which modulates the exposure dosage of femtosecond laser pulses, has been widely used to study the effect of crosslinking density on the responsiveness of hydrogel-based microstructures.<sup>[64c, 65]</sup> This method has been demonstrated in a collaborative work of our group,<sup>[64c]</sup> by using gray-tone lithography to fabricate heterogeneous bimaterial beams based on pNIPAM with differing degrees of crosslinking. These structures exhibited reversible bending effects with large amplitudes that were modulated by changing the temperature between 45 °C and 20 °C. In addition, by combining this with a nonresponsive ink (PETA), a photothermal actuation caused by two-photon absorption was observed while the heterostructure was irradiated with a near-infrared (NIR) light beam. This observation allows for the spatial control of thermally triggered smart hydrogel systems in a more precise manner. Such combination of responsive and nonresponsive materials is often employed in structural designs of actuators, leading to amplified deformation upon stimulation. For instance, a highly repeatable (over 10,000) microcantilever<sup>[66]</sup> and solvent-driven micropump system<sup>[67]</sup> have been demonstrated.

Hydrogels are not only distinguished by their adjustable stiffness, but also biodegradability and low cytotoxicity,<sup>[68]</sup> making them one of the most ubiquitously desirable materials in the biomedical field. With the utilization of 2PLP, hydrogel microstructures provide new opportunities in the field of biology. This allows the creation of biocompatible smart microsystems that mimic the adaptable environment of living organisms based on cells' requirements<sup>[69]</sup> and the study of the biophysical properties of single cells through the use of controllable hydrogel cell scaffolds. In another collaborative work of our group, novel composite microscaffolds were fabricated for the investigation of tracking the biophysical behavior of living cells in dynamic physiological environments. The composite scaffold consisted of protein-repellent and protein-adhesive parts, including a hydrogel block where the size can be modulated reversibly via host-guest interaction. After embedding the cell into the scaffold, the initial traction force was found to be ~80 nN.<sup>[23c]</sup>

Another interesting class of active hydrogels for microstructure fabrication are proteins, which are sensitive to changes in pH. For example, bovine serum albumin (BSA) has been used in fabricating controllable microgrippers for grabbing and releasing microobjects<sup>[70]</sup> and also has been explored for cell confinement and release studies. Additionally, light-responsive properties can be induced by incorporating photosensitizers, which lead to a swelling effect of the 3D printed protein hydrogels via a photochemical mechanism under illumination. By using microchambers composed of different sensitizers/proteins and printing conditions, it is possible to sequentially trigger morphological changes in each chamber to corral and release bacterial populations within picoliter volumes.<sup>[71]</sup>

### 2.3.2 Shape memory polymers:

Shape memory polymers (SMPs) are one of the promising classes of stimuli-responsive materials which were successfully employed for 4D printing soon after this concept was first proposed. The 4D behavior of SMPs is attributed to their exquisite so-called shape memory effect (SME), meaning that the shape deformation after programming can be recovered upon reheating the network beyond a certain transition temperature ( $T_{trans}$ ). To enable the programming process, the polymers must first be deformed under external stress while heating above  $T_{trans}$ . For amorphous SMPs, heating above glass transition temperature ( $T_g$ ),  $T_{trans}$  in these cases, results in a glassy to rubbery state transition. If the SMP network contains crystalline domains, transition from hard-to-soft relies on their melting temperature ( $T_m$ ). As the temperature increases, the mobility of molecules within a polymer also increases, allowing the polymer chains to be stretchable and alignable under application of an external force resulting in a reduction in the polymer's entropy. After deforming the polymer into the desired temporary shape, the programming process is followed by a shape fixation step induced by lowering temperature below  $T_{trans}$ . While the temperature decreases without any alteration of the applied external force, the polymer loses its thermoviscoelasticity due to a weakening in molecular motion. As a result, stress is stored within the polymer chains in the form of elastic potential energy during this process. The temporary shape is obtained and will not change even when the external stress is removed.<sup>[72]</sup> Once the temperature increases again, the polymer chains regain their thermoviscoelasticity, which leads to the release of the previously stored elastic potential energy and therefore the SMP recovers back to its energetically lower initial shape.<sup>[73]</sup> Beside thermal activation, other stimuli such as light, magnetism, electricity,

etc. can also be used for SMPs, by incorporating the corresponding functionality into the switching domain.<sup>[73]</sup>

SMPs have garnered significant attention as a highly useful and promising class of smart materials among functional polymer engineers, in both academic and industrial fields. In particular, the unique SME effect of SMPs offer various advantages compared to other classes of stimuli-responsive material like hydrogels or liquid crystal elastomers (see section 2.4) especially in view of applicability. For example, the programming steps afford the programmed shapes to be versatile and reformable based on the alteration of the approach of applying external force for multiple times. In contrast the stimuli response of hydrogels solely relies on the volumetric difference between swelling and shrinkage, and the one displayed by liquid crystal elastomers is restricted to the preprogramming of alignment. In addition, SMPs also have the flexibility on tailoring the desired mechanical properties by offering Young's moduli ranging from MPa to GPa.<sup>[73-74]</sup> Contrary, the moduli of liquid crystal elastomer only cover the range of few MPa and the ones of hydrogels are generally located in the range of kPa. Moreover, SMPs are compatible with dry and vacuum conditions in addition to wet environments, giving them greater versatility in their application in various fields,<sup>[73-74]</sup> such as aerospace technology,<sup>[75]</sup> biomedical devices,<sup>[76]</sup> flexible electronics,<sup>[77]</sup> and soft robotics to name a few.<sup>[78]</sup>

Along with an increasing interest in SMP research, scientists exploit their fascinating properties in fabricating 3D geometries. Several printable SMPs at the macroscale have been developed for stereolithography and extrusion-based printing techniques.<sup>[79]</sup> However, despite their potential, SMP microprinting remains a rather unexplored area. Scaling down the SME to the microscale is not a straightforward process.<sup>[57g, 57h]</sup> In order to achieve efficient printability via 2PLP, it is necessary to develop new photoresist formulations that can establish a sufficient number of crosslinks within the short time period of laser irradiation of the voxel volume. To accomplish this, materials that contain a high density of crosslinkable functional groups and undergo rapid crosslinking via radical polymerization, such as multifunctional acrylates and methacrylates, are commonly used. However, to ensure an adequate SME, it is important to have a polymer network with a high content of monofunctional polymerized chains, which are able to undergo a glass transition. The search for an ink formulation that balances the proportion of monofunctional monomer and crosslinker is challenging, as a high concentration of crosslinker can result in a nondynamic structure. Additionally, programming,

evaluating and proving the SME at the microscale presents an additional challenge for researchers. As a result, in contrast to the prosperous progress at the macroscale, 4D microprinting of SMP based on 2PLP still remains a challenge and only a handful of examples are reported.

One of the first examples of 4D-printed SMP microstructures was published by Elliott *et al.* in 2020.<sup>[80]</sup> They developed a photoresist composed of two kinds of methacrylated chain builder, which are benzyl methacrylate (BMA) and an amine-functionalized methacrylate, as well as modified PETA acting as a crosslinker. Long chains of each component were employed to tailor the desired mechanical characteristics in the printed product. This ink successfully allowed printing of complex 3D microstructures, which showed SME by programming the structures employing a nanoindenter above their  $T_g$  of 60°C. In another SMP system, an elastomeric ink for microprinting based on Vero Clear, a commercially available photoresin producing transparent thermosetting polymers, was reported by Zhang *et al.* The fabricated 3D submicron grid showed a color filtering effect caused by preferential transmission of certain wavelengths of incident light depending on the geometric parameters of the structure. The color of the structure disappeared and turned into transparent while the structure was programmed into a compressed shape and subsequently reappeared upon heating to 80°C due to initial shape recovery.<sup>[81]</sup> Despite the development of SMP in microprinting has a young history, much effort has been put in expanding the printable SMP library<sup>[82]</sup> and their characterization methods<sup>[83]</sup>. Our group has recently reported a novel system which can achieve 4D printing at both, the macro- and micro- scale.<sup>[20]</sup> The photoresist was based on the combination of monofunctional isobornyl acrylate, and poly(ethylene glycol) diacrylate (average  $M_n = 575 \text{ g mol}^{-1}$ , PEGDA 575) as well as tricyclo[5.2.1.0<sup>2,6</sup>] decanedimethanol diacrylate (TcddA) as soft and hard crosslinkers. The balance between both crosslinkers allowed finetuning of the printability and mechanical properties to achieve the optimal SME depending of the printing technologies used for macro- or micro-printing. Apart from excellent shape morphing behaviors of the DLP printed structures, a micrometric smart box printed by 2PLP was also demonstrated enabling controlled trapping and release of microobjects.

Currently, most reported 4D printed SMPs, particularly within the field of microprinting, belong to the class of one-way shape memory polymers. In fact, there exists numerous types of different shape memory polymers, which also includes two-way, and multiple shape memory

polymers.<sup>[73]</sup> Two-way SMPs, also known as reversible SMPs, have the unique property of autonomously deforming at high temperatures and reverting at low temperatures between two desired shapes after one programming step. The development of two-way SMPs with good mechanical properties and shape memory performance has the potential to replace irreversible one-way SMPs to avoid the required external force necessary for each programming step in the future. Moreover, multiple SMPs have been developed, which are capable of storing/memorizing more than one temporary shape by the copolymerization of one-way SMPs with diverse transition temperatures. This allows the polymer to switch into a set of shapes through the relevant programming process. A comprehensive understanding of these shape memory phenomena could bring novel application opportunities with advanced properties

## 2.4 Liquid crystalline elastomers

Liquid crystals (LCs) are materials that exhibit properties of both, liquids and crystalline solids. They possess an orientational order like crystalline solids, while also showing fluidity. These properties are attributed to the chemical structure of the molecules forming the LC phases. They consist of an essential highly rigid mesogen core for defining their shape and possible intermolecular interactions, as well as some flexible side chains for enhanced fluidity in a liquid crystal mesophase. Depending on their molecular shapes and individual properties, mesogens exhibit varying levels of mesophase organization and therefore, they are typically categorized as calamitic (rod-shaped), discotic, bent-shaped, or cholesteric.

Among these different mesogen types, the nematic liquid crystal is one of the most common calamitic LC phase. These LC molecules self-assemble along a long-range direction, resulting in an anisotropic nematic phase. The orientation of the LC molecules is described by the director, which represents the vector of such alignment. Due to their thermotropic behavior, the alignment will be disrupted upon heating and turn into disordered isotropic states. This is a first order transition which happened within a range of few degrees Kelvin. Such transition can be observed optically with polarized optical microscope (POM) accompanied with a loss of birefringence or thermoanalytically via differential scanning calorimetry (DSC).

Liquid crystal elastomers (LCEs) are crosslinked liquid crystalline polymer networks. They are synthesized by polymerizing mesogens which equipped with functional groups, such as acrylates, thiols, or epoxides. Based on the position of the functional group on the mesogens, they are either integrated within the main chain, side chain, or as side-on pendants of the network (Figure 2.5A). Despite the polymerization, LCEs combine the mechanical and molecular properties of elastomers and LC by having elastic moduli typically in the MPa range and self-organized liquid crystalline behaviors. These properties were retained by intermolecular interactions including  $\pi$ -stacking and dipole-dipole interactions. These mesogen-mesogen interactions lead to the introduction of local order, however, such morphology of LCEs is generally localized within micrometer-sized domains (polydomain), meaning the directors are not aligned at the macroscopic level. By enforcing alignment, nematic LCEs can become monodomain, wherein the mesogens in the polymer network are oriented according to a common director (Figure 2.5B). This not only can substantially amplify the amplitude of deformation (possibly with strains up to 400%<sup>[84]</sup>) but also navigate the

direction of that. Such deformations are often nonlinear processes displaying fast response, great repeatability, and high mechanical loading. Since LCEs do not require external loads or aqueous environments, these exquisite properties make them an ideal candidate for various 4D printing applications, including robotics, optics, and biomedical devices.<sup>[85]</sup>

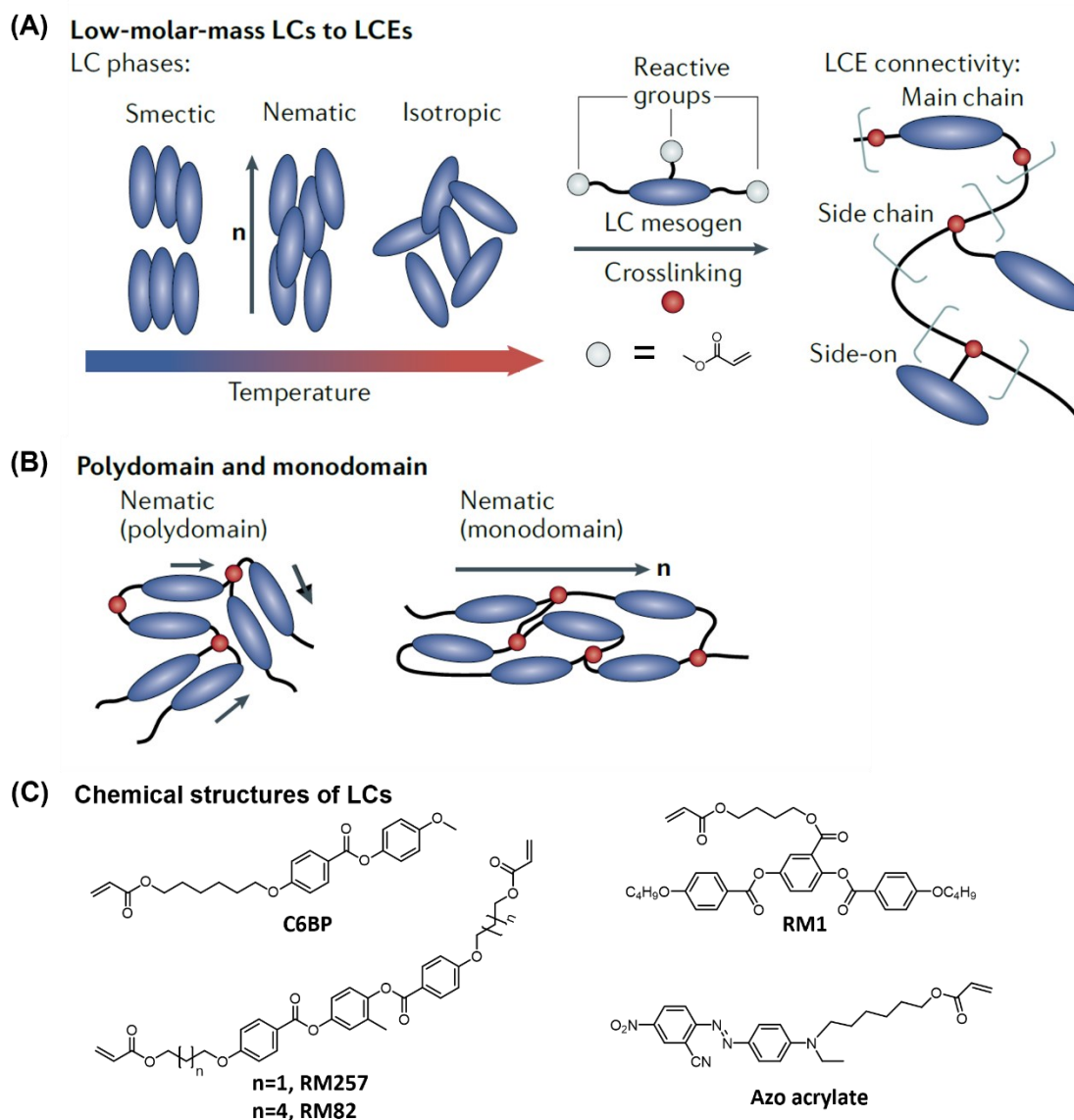


Figure 2.5 Schematic illustrations of (A) synthesis towards LCE of calamitic mesogens in varied liquid crystalline states, (B) and the orientational difference between the polydomain and monodomain LCEs. (C) Chemical structures of commonly used monofunctional LC monomer, side-chain LC monomer, bifunctionalized reactive mesogens (RMs), and the photoresponsive acrylate-functionalized azobenzene. Figure adapted from reference [86]. Permission by Springer Nature.

Due to their flexible and reconfigurable physical properties in terms of the shape, color, size, and response to the environment, in particular LCEs have a leading position in 4D printing applications and have been extensively explored for microactuator fabrications. The fabrication of LCE-based microstructures is commonly achieved via photopolymerization using 2PLP due to its ability to generate high-resolution 3D patterns. A typical formulation comprises a reactive monoacrylated reactive mesogen (RM), diacrylate functionalized RMs as crosslinkers and a two-photon photoinitiator. Functional dopants, such as azobenzene monoacrylate or photothermal nanoparticles were occasionally incorporated into the ink to endow the 2PP printed LCEs with remote optical response behavior (Figure 2.5C).

The configuration for 2PLP of LCEs is similar to printing of other materials, except of the substrate preparation. Unlike most of other two-photon polymerizable inks which can be printed directly with an opened resin vat, the use of a sandwich glass cell as depicted in Figure 2.6, composed of two modified surfaces or conductive substrates, is often necessary to predetermine the mesogen alignment. During 2PLP, a laser beam is focused on a 3D volume (voxel) within the cell, and the LC ink is polymerized with the programmed director retained via simultaneous absorption of two photons.<sup>[87]</sup>

The printing parameters, such as writing speed, writing energy, and writing temperature, significantly influence the print quality of the final objects and also the level of anisotropy of the polymerized LCE. The focal volume of the laser determines the theoretical resolution of the 2PLP. For the fabrication of LCEs, structures in few micrometer-scale could be achieved by using a high magnification lens. However, when pursuing high resolution 3D printing with nanoscale precision in LCE, it turns particularly challenging due to their birefringent nature.<sup>[88]</sup> It was found that, at the interface of the substrate and the birefringent media, the refraction of the laser light path refracted into an ordinary wave and an extraordinary wave, resulting to two spatially separated foci and the consequent polymerization conducted by two voxels simultaneously. Generally, the distance between the two split foci increases along the focal depth with a linear dependency, which is specifically unfavorable for fabricating high resolution photonic structures. One way to bypass the distorted focus is adapting the printing configuration to an inverted approach, by inverting the z-axis and starting the fabrication from the top plat of the cell to minimize the focus depth.<sup>[88a]</sup> Another way is the optical approach, by using a suitable polarization of the laser to suppress the extraordinary wave leading to a

confined laser focus. But the type of polarization depends on the kind of alignment which the LC ink is programmed for.<sup>[88b]</sup>

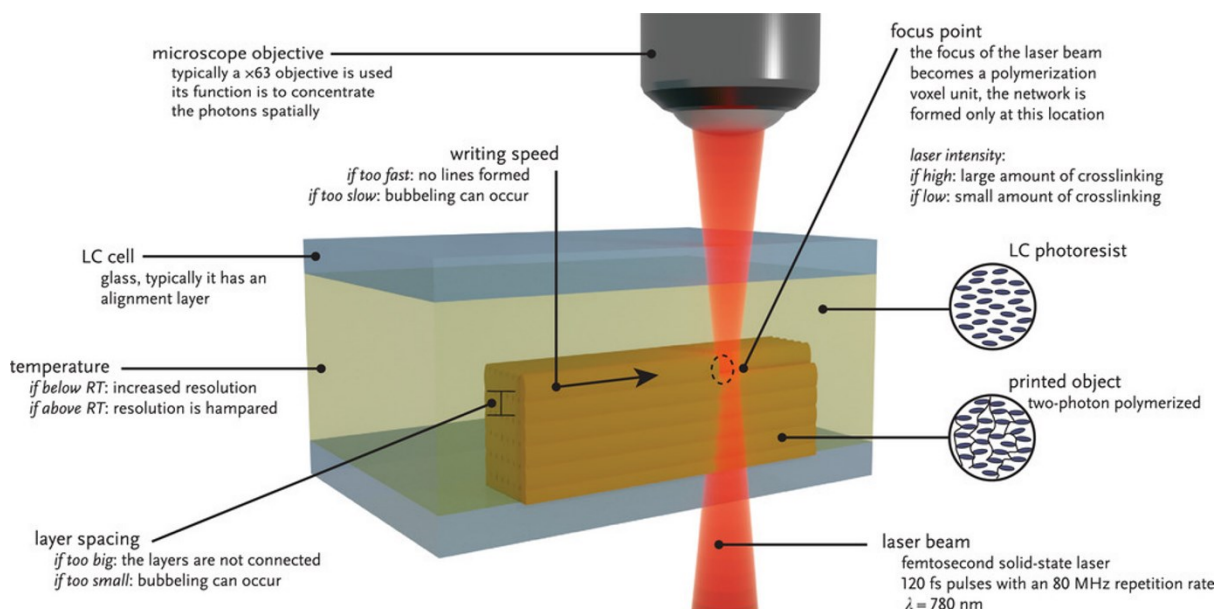


Figure 2.6 Schematic representation for 2PLP of LCs, in which LC ink is filled inside the alignment glass cell and a femtosecond laser was used to fabricate LCE microstructure with the programmed alignment retained. Variable printing parameters are highlighted. Figure adapted from reference [89] Permission by Wiley-VCH.

### 2.4.1 Alignment method of liquid crystals

To achieve significant deformation of LCEs, it is crucial to pre-/program a global alignment in LCEs to induce a collective reorientation of the liquid crystalline segments within the polymer network by external stimulus, as proposed theoretically by de Gennes in 1975.<sup>[90]</sup> There are various alignment methods for this purpose have been intensively developed. However, employing 3D printing technologies for fabrication of arbitrary geometries makes LC alignment one of the biggest challenges while developing the production process, since there are three important factors which must be considered: (1) The alignment setup is compatible to the 3D printer. (2) The possibility to vary the LC director orientation spatially. (3) The scale of the chosen alignment method is within the same range with the 3D printing technique applied.

In the following sections, the discussion is structured around the introduction of the advanced alignment methods, as schematically illustrated in Figure 2.7, including surface

functionalization, mechanical, electromagnetic, or rheological alignment. The focus will be put on the uses of these techniques applied on thermotropic, calamitic LCs at nematic phase, which has shown their leading position as stimuli-responsive materials in 4D printing. Current challenges of applying these methods to 3D printing, particularly to 2PLP, are also discussed.

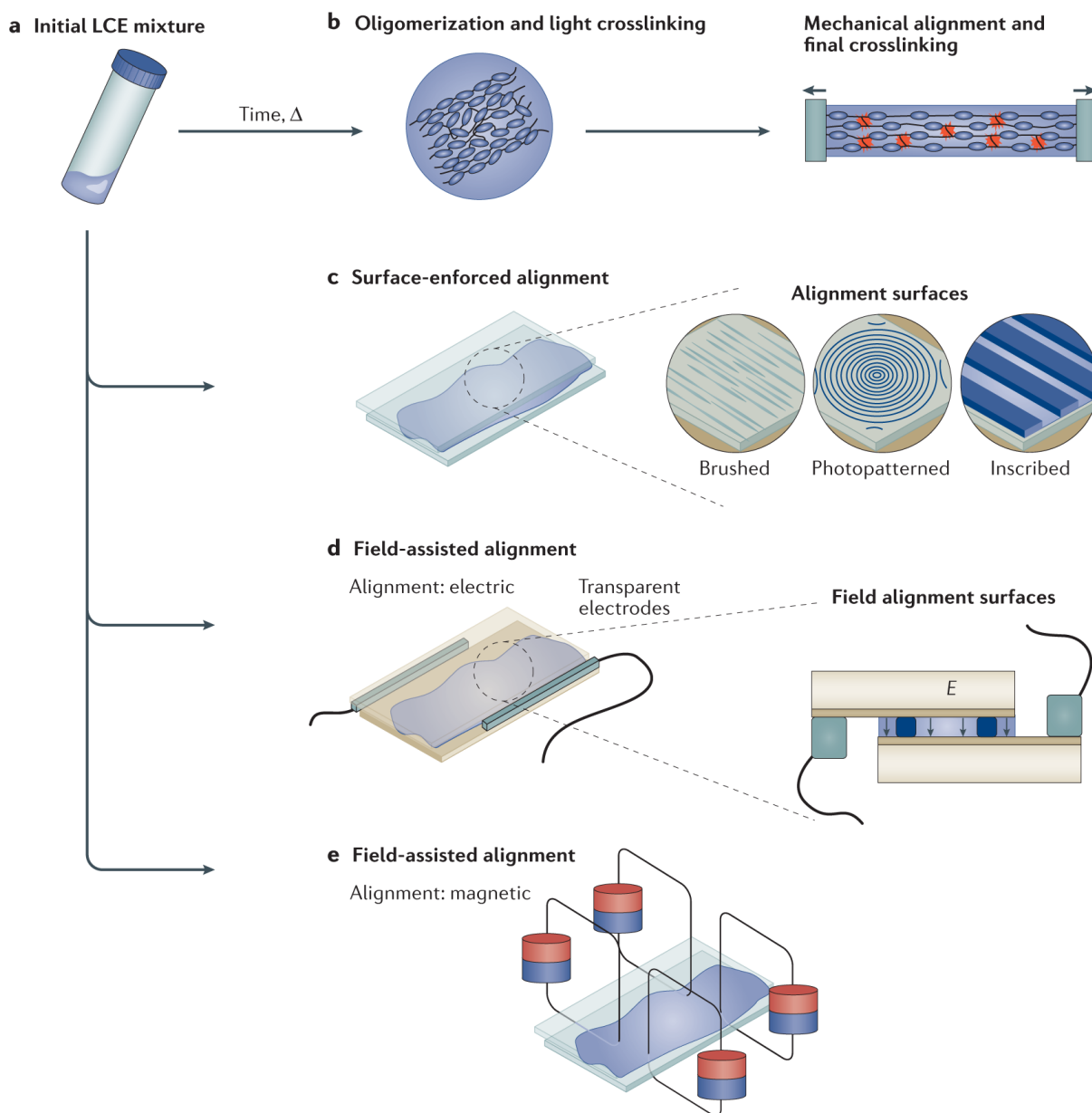


Figure 2.7 Alignment methods of (A) liquid crystalline elastomers, including (B) mechanical alignment, (C) surface alignment, (D) electro and (E) magnetic field alignment. Figure adapted from reference [86] reference. Permission by Springer Nature.

### 2.4.2 Surface alignment

Using chemical surface treatments to create alignment layers is one of the pioneer methods which has been commonly applied to date. It is proceeded by filling LC molecules into a sandwich glass cell wherein the top and bottom surfaces are functionalized, patterned, or coated with alignment layers. Through a realignment process, by heating the cell with the infiltrated LC above the isotropic state and gradually cooling down to LC state, the orientation of the perturbed mesogens would propagate through the entire glass cell by undergoing self-organization based on their intermolecular interaction and the boundary conditions imposed by the alignment layers. As a result, the anisotropic distribution of mesogens within the cell can be organized in multiple ways corresponding to the selected top and bottom alignment surfaces, which could be same type or in combination with varied anchoring effect (i.e., homeotropic or planar alignment layers) or directing orientation (parallel or perpendicular). Examples for typical alignment includes planar, homeotropic, splay, or twisted, alignment (Figure 2.8). Due to the ease of mass productivity and the small volume of a sandwich glass cell, this approach has been most commonly applied in 2PLP to program the LC alignment. Material and methods used for fabricating these alignment surfaces are summarized in the following.

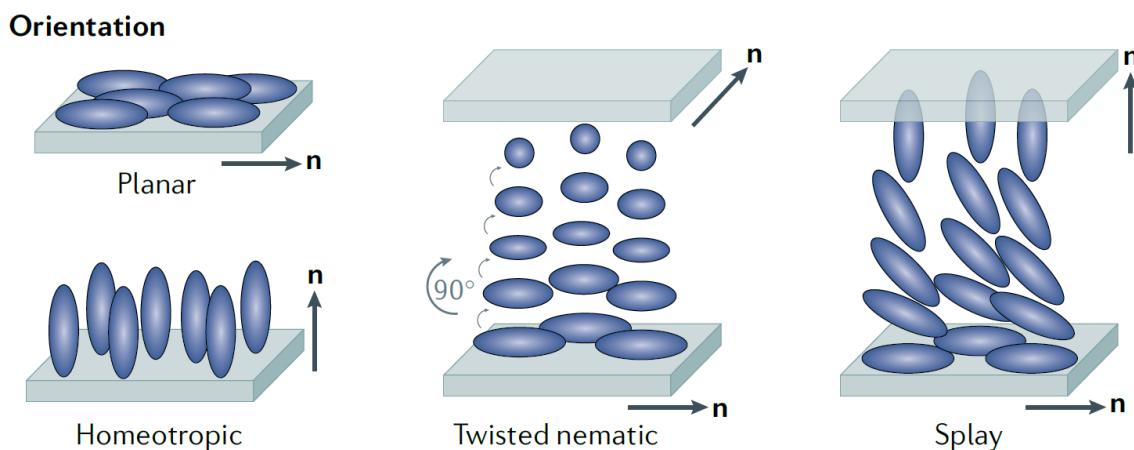


Figure 2.8 By using surface alignment approach, the alignment of mesogens within the cell is determined by the type of surface treatment, resulting in either anchoring parallelly or perpendicularly to the alignment surface. These orientations can continue through the thickness of the cell, creating uniform alignment. Alternatively, twisted nematic or splay orientations can be achieved between surfaces with different anchoring orientations, as depicted. Figure adapted from reference [86]. Permission by Springer Nature.

### **Polyimide**

To serve as LC alignment layer materials, some properties are required because of their production processes and usage environment. (1) High-heat resistance (2) Stability of the LC alignment performance under high temperature (3) High purification without ionized contamination (4) Enhanced adhesiveness and wettability to glass substrates or electrodes (5) High transparency.<sup>[91]</sup> Based on these conditions, several materials such as, polyvinyl alcohol (PVA),<sup>[92]</sup> polystyrene,<sup>[93]</sup> and polyimide,<sup>[94]</sup> have been reported. Among these materials, PI has been most commonly used to align LC molecules during 2PLP due to its high resistance to organic solvent ensuring adhesion between the structure and the substrate. Because of its chemical affinity, polyimide coated glasses pristinely show vertical anchoring effects on the LC molecules and therefore those can be used to construct glass cells to induce homeotropic alignment.<sup>[95]</sup> On the other hand, a surface rubbing technique has also been employed on polyimide coating to introduce microscopic grooves on the surface in which the alignment direction of the liquid crystal follows the orientation of these grooves and shows a planar anchoring effect.

Despite showing promising alignment performance for 2PLP, polyimide coatings have plenty of disadvantages which haven't been conquered so far: (1) The procedure for preparing polyimide coated glass cell requires multiple steps and therefore highly elongate the fabrication time for massive printing on individual substrates. (2) If a rubbing procedure is applied, dust particle generation, electrostatic discharges, and substrate damages are inevitable, which would result in microexplosions during 2PLP. (3) Since localized surface rubbing has not been extensively explored, alignment would be implemented in the glass cell globally therefore this approach has highly limited the versatility on alignment programming, especially for microprinting.

### **Photoalignment**

Photoalignment is a technique for surface-enforced alignment that utilizes the reversibility in polarization photochemistry.<sup>[96]</sup> When photoreactive molecules in polymer matrices or solid surfaces are exposed to linearly polarized light, axis-selective light absorption occurs, resulting in dichroism due to the preferential consumption of molecules whose transition moment is parallel to the electric vector of the light. For aligning typical nematic liquid crystal, this method

is generally applied by modifying the substrate surface with a photoswitchable group. Such photoresponsive alignment layers are often referred to as command layers. Azobenzenes have been extensively employed as phototriggers in this regard due to their mesogenic nature and excellent reversibility upon photoisomerization. Usually, irradiation with blue light is used to give a photostationary state containing the mesogenic *E* isomer as a major component therefore the hydrophobic alkyl substituent of the azobenzenes orientate the LC molecules homeotropically. Once the *Z*-isomer, which is a nonmesogenic structure, is induced by the polarized UV light, it acts as an impurity to deteriorate mesophases, subsequently alter the molecular axis of the mesophase into a planar fashion (Figure 2.9). Such photoreorientation approach not only offers flexibility on altering the LC alignment reversibly and spatially but also the induced orientation can be simply determined by the vector of the polarization within three dimensions, even in a slantwise angle. This technique has been used to prepare LCEs with complex director profiles and high-resolution voxels.<sup>[97]</sup>

Despite the photoalignment approach can avoid the drawbacks of rubbing treatment from the conventional methods, as known as generating static electricity or attracting dust particles, there are other limitations, especially for the applicability in 3D printing. First is the possible contamination as a result of photodegradation while using the UV laser to generate the *cis*-isomer. Second is the challenge of light competition between the photoalignment and photopolymerization as if the 3D printing technique is based on vat polymerization. Last but not least, the irradiation equipment is not only high costing, technically challenging, but also could not be volumetrically compatible with the 3D printers.

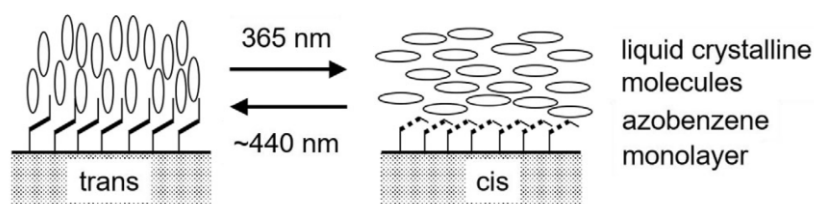


Figure 2.9. Illustrative representation of the reversible alteration of the photoaligned liquid crystals, which is induced by the photoisomerization of azobenzene units. These units are functionalized on the glass substrate. Image is adapted from reference [91]. Permission by Wiley-VCH.

## PDMS

As an intermediate approach, highly hydrophobic polymers, such as polydimethylsiloxane (PDMS), have also been observed the ability of aligning LC materials by either act as an alignment layer or used to fabricate alignment patterns. PDMS is an organosilicon-based elastomer, characterized by high transmittance in a wide spectral range (240 to 1100 nm)<sup>[98]</sup> and rubbery behavior with low elastic modulus (0.57 MPa to 3.7 MP)<sup>[99]</sup> varied by its crosslinking density. Therefore, the physicochemical properties allow the use of PDMS for fabricating surface microstructure<sup>[100]</sup> which leads to a wide range of applications, including microfluidic systems,<sup>[101]</sup> biomedical applications,<sup>[102]</sup> optical,<sup>[103]</sup> and wearable sensing devices<sup>[104]</sup>.

The highly hydrophobic PDMS has a surface contact angle of 115° with a DI water droplet and a low surface free energy (22-24 mJ/m<sup>2</sup>) at room temperature. These values are lower than that of polyimide (e.g., 31 mJ/m<sup>2</sup> of SE-4881, Nissan Chemical).<sup>[105]</sup> Therefore, these surface properties exhibit an anchoring effect on the LC mesogens, by having the director almost 90° to the PDMS surfaces.<sup>[105b]</sup> This phenomenon has been observed in most of the liquid crystal molecules, since, based on up-to-date studies, there is no chemical interaction indicated between the PDMS and liquid crystalline materials.<sup>[106]</sup> An additional beneficial feature of PDMS is the negligible birefringence (refractive index ~ 1.41). Therefore, much attention has been paid on exploiting the use of PDMS on engineering LC alignment in the past few years.

PDMS was first used to fabricate micro-grooves on a substrate via soft lithography method as a replication of rubbed polyimide substrate.<sup>[107]</sup> Besides from using PDMS to fabricate alignment pattern, it was also directly served as a substrate to simplify the process. In this case, alignment defects resulted from dust or charges generated while rubbing the substrate can be avoided.<sup>[108]</sup> Besides from directing the LC molecules with the micro-grooves, homeotropic alignment (90°) of LC was achieved within a sandwich-cell composed PDMS as alignment layers by propagating the vertical orientation from the surfaces through the bulk of LC.<sup>[105]</sup> In addition, once PDMS surfaces are perpendicular to the substrate, the director of LC would be converted accordingly. Therefore, with the optimization on the dimensions of the PDMS microchannels or microwells, planar alignment<sup>[109]</sup> or radial alignment<sup>[110]</sup> could be induced, respectively.

Apart from relying on the intrinsic vertical anchoring effect of the PDMS surfaces, various surface modification methods allowed to adjust the LC pre-tilt angle. For example, PDMS surface functionalization with silanol group carried out by air plasma treatment would highly improve the hydrophilicity and therefore alter the LC director to be parallel to the modified surface<sup>[111]</sup>. Similar planar anchoring effects of LC molecules can be achieved by coating a thin layer of poly(2-hydroxyethyl methacrylate) (PHEMA) on top of the surface of a PDMS well to form a more homogeneous alignment texture and also better actuating performance with the fabricated LC pillars.<sup>[112]</sup> Furthermore, finely adjusted LC pre-tilt angles from 0 to 90° were allowed by formation of PDMS copolymers with varied portion of poly(vinyl cinnamate), which favors planar alignment.<sup>[113]</sup> Multiple advanced devices and applications have benefited from the great flexibility of using PDMS for LC alignment, such as electrically or optically controlled microfluidics.<sup>[106, 114]</sup> However, with the promising performance on achieving LC alignment, PDMS has yet been applied in 3D/4D printing LC network.

Despite phenomenal and reliable LC alignment can be achieved by using these polymer-coated substrates, the fabrication of microrobotics has been facing challenges in terms of expanding the versatility and complexity of robotic movements. In detail, the microchannels generated by rubbing the coated polymer are unidirectional, which means that the actuation of the LC structures resulting from this technique is directionally restricted along with the aligned director. Consequently, multiple writing steps or post-manipulation are necessary to create a robotic structure that exhibits a multi-dimensional response. For example, Wiersma and coworkers had to manually manipulate the orientation of the printed microfingers or realign the LC ink within different aligning substrate stepwisely to build an autonomous microhand which contracted and expanded in both X- and Y- directions.<sup>[115]</sup> In another example reported by Guo *et al.*, LCE structures were manually assembled post-printing with heterogeneous LCE microblocks, which were printed independently with different orientation in the alignment cell.<sup>[116]</sup>

### 2.4.3 Mechanical alignment

One common approach for producing oriented liquid crystal elastomers (LCEs) films is mechanical alignment. In general, the process of mechanical alignment involves a two-step reaction. First, LC compositions are partially polymerized and subjected to a load in order to enforce the mesogen conformation along the loading axis. Next, the remaining polymerizable

groups react fully by photopolymerization while still under load to maintain the aligned configuration. This method is often applied on main-chain LCEs synthesized by chain-extension reactions, which involve aza-Michael addition of diacrylate liquid crystalline monomers with primary amines or thiol-Michael addition of diacrylate liquid crystalline monomers with thiols. This alignment technique is reliable and the resulted LCEs have shown remarkable actuating behavior, however, the scalability may be limited and the induced LC alignment is restricted to the mechanical force. Therefore, the possibility of aligning 3D printed LCE structures mechanically is scarce, especially for microprinted structures which are simply limited by the complexity of micromanipulation.

Recently, in one of my collaborating works with Philipp Mainik, we have demonstrated a facial approach of fabricating a DLP printed multi-photoresponsive structure, which was composed of mechanical aligned LCE modular blocks and passive elastomeric scaffolds. In this work, we have proposed an alternative approach to unlock the limitation of aligning LCE 3D printed structures unidirectionally.<sup>[117]</sup>

#### 2.4.4 Electromagnetic alignment

##### Electric field

Another technique for controlling the alignment of LC molecules involves applying an external field because LC molecules have the ability to align to both electric and magnetic fields. Since the molecular design of liquid crystalline materials includes polar functional groups such as esters, nitriles or halogens, a mixture consists of acrylate LC monomer and diacrylate LC crosslinker with the right composition shows dielectric anisotropy. This allows electric field alignment of these materials to orientate into the direction parallel to the applied electric field. Such properties frequently employed in display applications in real life for light intensity modulation.<sup>[118]</sup>

As if external electric field offers a solution to program LC alignment for 3D fabrication, however, there are several critical points which have to be considered. First, achieving electrical reorientation of highly viscous mesogens in polymerized LCEs requires higher voltages that might exceed the dielectric breakdown voltage of many compositions. Therefore, having a considerable amount of LC molecules with low viscosity and low molar mass has to be taken

into account for LC ink optimization. Moreover, the use of electric field necessitates the modification of the pristine printing configuration as customizing a compatible electric field setup to the 3D printer, which would highly complicate the fabrication process.

In recent collaborating works of our group, Münchinger *et al.* presented a novel method for printing LCE structures with a spatially varying director.<sup>[88b, 119]</sup> The method is based on a self-built LC cell, consisting of an ITO-coated substrate as a counter-electrode and a fixed ITO electrode above the objective lens, allowing for the application of quasistatic electric fields. Depending on the applied electric field vectors within three dimensions, the corresponding alignments of the LC ink was fixed by the laser focus *in situ*. Through the rearrangement of the electric field vector along the printing process, LCE microactuators with complex alignment design were fabricated. This method allowed for the fabrication of arbitrary microstructures with freely varied directors, breaking the barrier of surface alignment approaches.

### **Magnetic field**

Similarly, liquid crystals can be aligned using a magnetic field due to its diamagnetic susceptibility which endows the alignment of their long axis parallel to the applied magnetic field. These properties have been utilized to produce uniaxial, homeotropic, radial, or even more complicated director patterns by having the LC mixture exposed to multiple magnetic sources. This method so far has only been successfully adapted to DLP printing by having a reorientable magnetic set up around the printing platform and afforded the fabrication of 3D macro LCE structures where segments were programmed with different alignment vectors.<sup>[120]</sup>

### **2.4.5 Rheological alignment**

Rheological alignment of LCEs has been well-established within extrusion-based 3D printing techniques, such as direct ink writing (DIW), for introducing and directing LC orientation. The alignment is achieved by extruding the LCE inks through a cylindrical printhead wherein shear forces are generated. The degree of alignment of the shear flow generated LC layer contributes to velocity, as well as viscosity, residence time, and tip geometry. In addition, by designing the writing pathway, this approach gives the flexibility to customize the actuation pattern of an arbitrary geometry within mesoscale. Since this alignment method relies on a material jetting process, combining with vat polymerization techniques particularly with 2PLP is challenging.

## 2.5 Stimuli-responsive properties toward 4D microprinted LCE

The development of LC ink formulations has led to improvements in creating more complex and versatile stimuli-responsive behaviors. Employing one of the advanced alignment methods mentioned, the predetermined anisotropy confers printed structures the ability to exhibit mechanical and optical responses to various stimuli due to disruption of the mesogen order. The range of stimuli that can cause these responses include thermal-mechanical, electric-mechanical, magnetic-mechanical, photo-mechanical, physical/chemical-mechanical, and mechano-chromic responses.<sup>[85a]</sup> In the scope of microprinted LCE, the use of heat has been typically applied due to their nature of phase transitioning properties. Besides from thermal stimulus, using light or solvent have also achieved on activating LCE microstructures by advancing the LC ink with functional material. Examples of 4D microprinted LCE will be introduced in the following according to use of stimuli for activation.

### **Photoresponsive LCE microstructure**

The integration of photoresponsiveness into 2PP printed LCE microstructures enables remote tunability of small optical or mechanical systems with great spatial and temporal precision.<sup>[121]</sup> Fabricating optically controllable microactuators based on thermotropic LCEs has been mostly achieved by the incorporation of photoresponsive dopant into the LC ink.<sup>[122]</sup> Thermal-mechanical response is a result of photothermal effects, meaning that the order-disorder transition of LCE is induced by the conversion of absorbed light energy into heat.

To achieve this, a light absorbing photoswitch, e.g., azobenzene (azo) which shows great compatible with mesogens, has been most commonly employed in ink formulations to introduce photoresponsive property. This was first introduced by Wiersma and coworker at 2015, by incorporating an acrylate-functionalized azo benzene into the LC ink (Figure 2.10A). On this basis, various smart systems which was driven by green light irradiation had been developed. For example, light-fueled microscopic walkers were fabricated by printing the body of the walker ( $60 \times 30 \times 10 \mu\text{m}^3$ ) with the azo-modified LCE resist via 2PP within PVA and polyimide-coated glass cell. Upon laser illumination (532 nm), the LCE-based body undergoes a reversible and anisotropic contraction/expansion, leading to locomotion of the printed

microwalker remotely (Figure 2.10B).<sup>[95]</sup> This azo-modified ink was also utilized on constructing a light-powered 3D microhand which was capable of grabbing microscopic objects by external or autonomous control in both water and air (Figure 2.10C).<sup>[115]</sup> Similarly, LCEs have been employed for the creation of microscale optical systems that can be adjusted by their reshaping capabilities. A demonstrated example is the use of LCEs for optically controllable whispering gallery mode resonators (WGM) to fabricate tunable microoptic devices.<sup>[88a, 123]</sup>

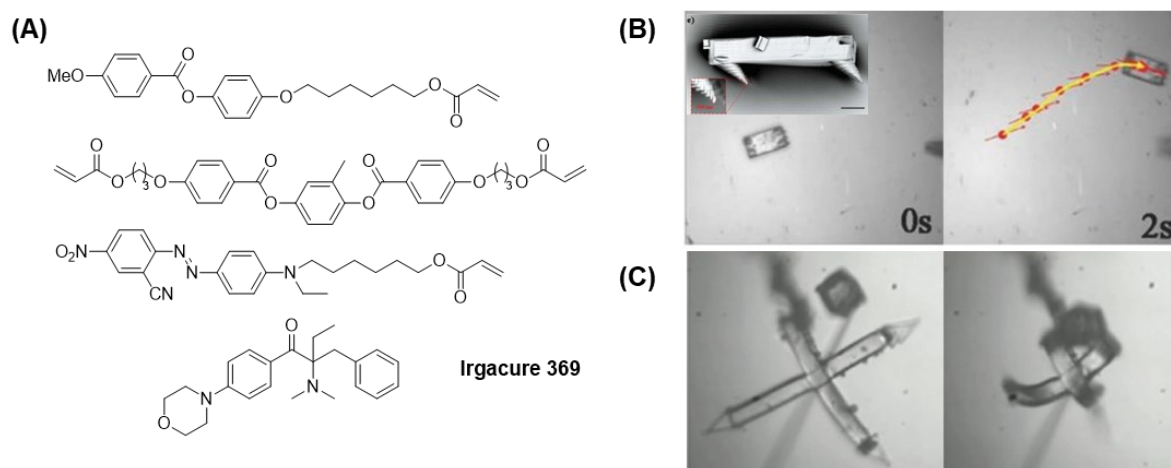


Figure 2.10 (A) LC formulation used to fabricate photoresponsive microactuators via 2PLP. Demonstrated as (B) the locomotion of a microwalker (inset, 60  $\mu\text{m}$  in length)<sup>[95]</sup> and (C) the capture of a polymeric microblock by a microhand (200  $\times$  200  $\times$  20  $\mu\text{m}^3$ )<sup>[115]</sup>, whose actuating patterns were modulated with a green laser (532 nm). Permission by Wiley-VCH.

In addition to the photothermal effect, it is worth mentioning that azobenzenes can also trigger contractile photo-mechanical responses of the incorporated LCEs based on a photomechanical effect. Apart from photothermal effect relied on a thermal diffusion process from randomly incorporated light absorbers, the photomechanical effect relies on the transduced strain along the director resulted from significant volume change during the *trans-cis* photo-isomerization when the azobenzene dyes is covalently incorporation into the main LC polymer chain. This approach has been proven in thin film that offered higher degree of actuation amplitude, faster response time, and no limitation in a thermal diffusing medium (i.e., water). However, this necessitates on the synthesis of difunctionalized acrylate azobenzene dyes.<sup>[89, 124]</sup> The other approach to activate LCE photo-mechanical response is photoreorientation, also known as the Weigert effect, arising from the more efficient isomerization dynamics of azobenzene molecules excited with light polarized along the direction of the transition dipole, which is oriented along the molecular main axis of the *trans* isomer. The excited azobenzene molecules become randomly oriented in the direction

perpendicular to the light polarization direction. As only azobenzenes will be stimulated under the linearly polarized light, this approach offers even a higher precision on special activation.<sup>[125]</sup> These two principles have been thoroughly studied in macroscopic LCE films, however, not been demonstrated in 2PLP based microstructures yet.

Except of harnessing organic dyes to trigger photothermal effects, composite materials have also been employed to serve the same purpose. For example, Chen *et al.* developed printable gold nanorod/LCE composite resins and demonstrated the light-controlled anisotropic actuating deformation of an LCE micro-woodpile with significant improvement on mechanical stability.<sup>[126]</sup> They also investigated the printing parameters and printability of LCE nanocomposite resins containing photothermal CNTs and graphene oxide for fabricating functional structures via the 2PP technique. Despite LCE structures incorporated with dopant offer the controllability via NIR light, which is a novel feature in terms of the potential adaptability on biology or sensing applications, the inhomogeneity of the ink also often leads to microexplosions during 2PP process due to accumulation of laser power resulting inconsistent printability.

### **Solvent-responsive LCE structure**

LCEs can be designed to exhibit mechanical responses to specific solvents. One way is by using an isotropic solvent where LCEs show large swelling deformation along the director due to a higher solvent uptake in the disordered state. As reported by Guo *et al.*, they used IP-S patterned glass to locally encode nematic alignment voxel-by-voxel and created helical LCE microstructures showing complex deformation upon swelling in *N,N'*-dimethylformamide based on their specialized topographical feature.<sup>[127]</sup> Alternately, one can incorporate mesogens with functional groups that are sensitive to specific solvents or chemical analytes. In another study, del Pozo *et al.* introduced the first example of a supramolecular cholesteric liquid crystalline (CLC) incorporated 4D microactuator that responded to humidity or temperature changes. During the printing process, hydrogen bonds formed by carboxylic acid-functionalized molecules acted as crosslinkers, which were subsequently cleaved in the development process and resulted in a hygroscopic LC network with reduced crosslinking density. A color change was observed in the swollen cholesteric structure after the uptake of water vapor, and variations of humidity or temperature enabled reversible actuation.<sup>[128]</sup>

## Chapter 3.

# 4D Microprinting of Multi-Photoresponsive Liquid Crystalline Actuators

### 3.1 Motivation and aims

Despite the growing interest by the 3D printing community in the remarkable works demonstrated by the Wiersma groups in 2015<sup>[95]</sup>, especially in 2PLP fabricated light responsive LCE microactuators, merely any other materials have been reported to achieve this 4D behavior on a microscale ever since. Except for responsive hydrogels which rely on an aqueous environment and the use of heat as a stimulus, impressive actuating behavior exhibited by the micro LCEs, including high level of contracting actuation, repeatability and response rate, had been overlooked. From the material perspective, not much additional achievement had been reached in the fabrication of photoresponsive micro LCEs, until the start of my PhD in 2019. In fact, the development of light driven LCE microstructures had reached its bottleneck, limited by the absence of other options for functional photoabsorbers inducing photomechanical response than azobenzenes. Therefore, the actuation wavelength was restricted to the short visible regime (i.e., 400-500 nm). These limitations have suppressed the development of light-driven LCE microstructures in terms of complexity, versatility, and their potential particularly in biomedical applications.

Hence, the aim of the first project of my PhD was to expand the library of functional LC inks for photo-responsive microstructures fabricated via 2PLP and as a consequence further the development and range of applications. Particularly for the biomedical field, activation with longer wavelength is critical to ensure good penetration depth in biological tissues or cells without damage. Moreover, to endow systems with the ability to offer more flexible actuation patterns, the possibility of implementing dual-light responsiveness into LCEs by incorporating a second photoabsorber together with the established azobenzene for allowing actuation on demand by using different wavelengths of light was exploited.

To achieve this, strategical planning and design of a pair of ideal photoresponsive molecules are necessary in order to fit two essential requirements: (1) It is important for the two functional molecules to have no overlapping absorption regions and no undesirable energy transfer between the two to be selectively activated with different colors of light. (2) As 2PLP is a light-based printing technology carried out with a 780 nm laser, additional absorption at this wavelength and its corresponding 1PP at 390 nm are preferably avoided. This ensures that no photodegradation of the photo-responsive molecules occurs through the high intensity laser

beam and that only the PI absorb at these wavelengths the photopolymerization is not affected, as the PI and the photoabsorbers do not compete with each other.

Inspired by an orthogonal system reported by Feringa and coworkers, azobenzene (Azo) in combination with another photoswitch, donor-acceptor Stenhouse adduct (DASA), were the selected candidates for fabricating systems with dual functionalities.<sup>[130]</sup> In the report, the azobenzene was functionalized with electron donating and withdrawing groups, driving the absorbance of Azo from the UV to the blue light region (~435 nm). Complementarily, an emerging class of T-type photoswitch DASA,<sup>[131]</sup> equipped with a secondary amine as an electron donor and heterocyclic acid (i.e., methylbarbituric acid or meldrum's acid) as an acceptor, absorbs light at the green-to-yellow regime (~570-620 nm), which optimally fits into the limited wavelength window between 390–780 nm and barely absorbs within the absorption region of azobenzene.<sup>[132]</sup> Upon the irradiation of the visible light, DASAs undergoes photoisomerization into a cyclized form, accompanied with decoloration, described as negative photochromism. Since the reverse switching of DASAs is thermally driven,<sup>[133]</sup> wavelength-selective control over four photoisomers was achieved with the use of three colors of light. Azobenzenes have been widely implied into a well aligned LCE matrix to generate mechanical movements, owing to either their high absorbance and/or their reversible shape changes upon light irradiation which induces the photothermal effect or photomechanical effect, respectively. Therefore, having comparable characteristics under light stimuli as azobenzenes, DASAs were anticipated to actuate the incorporated LCE through either one of the mechanisms despite this had not been demonstrated yet.

Aiming for multi-functionalized light driven LCEs, three sequential steps were performed: First, the synthesis and characterization of both Azo and DASA photoswitches were carried out. The substituents on both chromophores were determined based on their spectral regions, extinction coefficients, thermal half-lives, photoswitching efficiency and quantum yields.<sup>[130, 134]</sup> Their synthetic pathways were adapted to allow the acrylate functionalization. In addition, chromophores without polymerizable groups were also synthesized to compare the difference on triggering the mechanical effect of the embedded polymer networks between the polymerizable and non-polymerizable chromophores. Next, the development of LC ink formulation would be carried out by incorporating the synthesized photoswitches to serve as photoabsorbers ("dyes" would be used as synonym in the following). Last, the method for microprinting multi-photoresponsive LCEs based on 2PLP by employing the dyes was

developed. The resulted actuating behaviors by shining different colors of light on LCEs with varied functionalizations were studied and analyzed in depth.

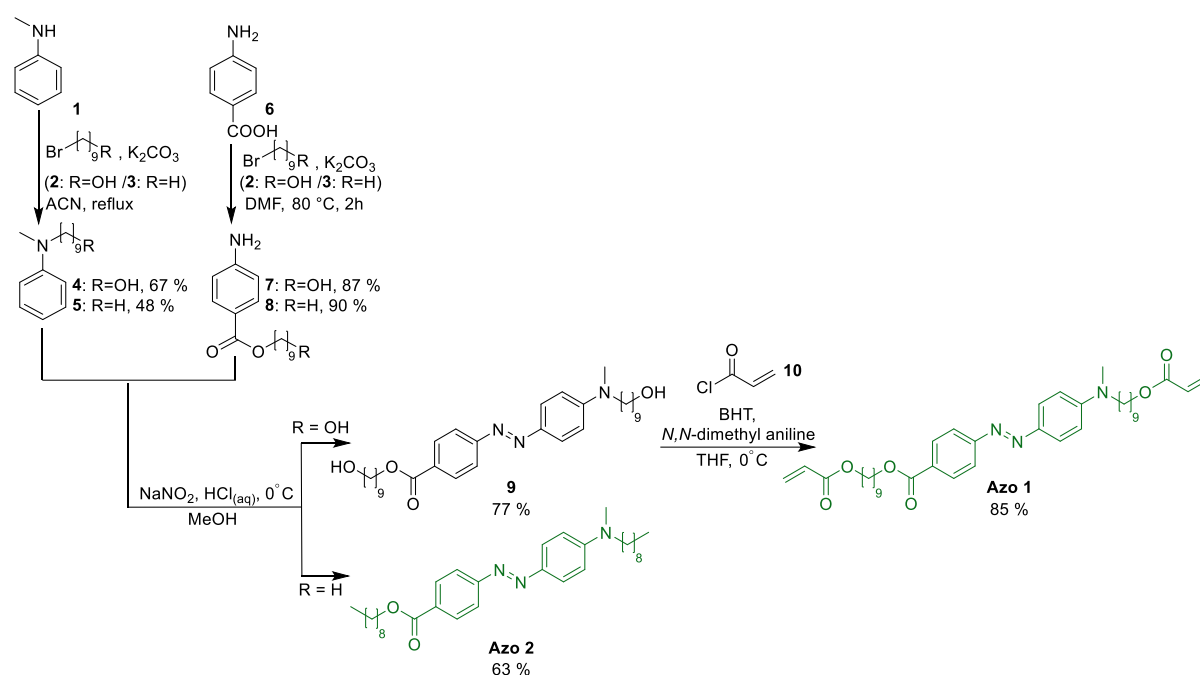
## 3.2 Results and discussion

### 3.2.1 Synthesis of photoabsorbers

To enable the incorporation of photoswitches in the photopolymerized network, particularly in the main polymer chain, the chemical structures of the targeted photoswitches were modified with two acrylate groups, which were attached at the end of long alkyl spacers (C9). This ensures the chromophores with good solubility and sufficient free volume within the later embedded polymer network for efficient photoisomerization. The synthesis of the selected orthogonal photoswitches and their unfunctionalized analogs is described in the following.

#### Azobenzenes (Azo)

The targeted azobenzene is equipped with an amino- and a carboxylate group in the para position as electron-donor and acceptor, respectively. To synthesize this, *N*-methylaniline **1** and aminobenzyl acid **6** were employed to undergo a substitution reaction and esterification respectively by using 9-bromo-1-nonanol **2**. Azo-coupling between the resulted nonanoxyl aniline **4** and aminobenzoate **7** formed the azobenzene derivative **9** equipped with two hydroxyl groups. Subsequent esterification with acryloyl chloride afforded the target product diacrylate **Azo 1**. Similar strategy was used on the synthesis of the analog **Azo 2** without polymerizable groups by using 1-bromononane **3** instead of bromo-1-nonanol **2**. (Scheme 2.1) (See the synthetic procedures and NMR spectra in Chapter 5.)

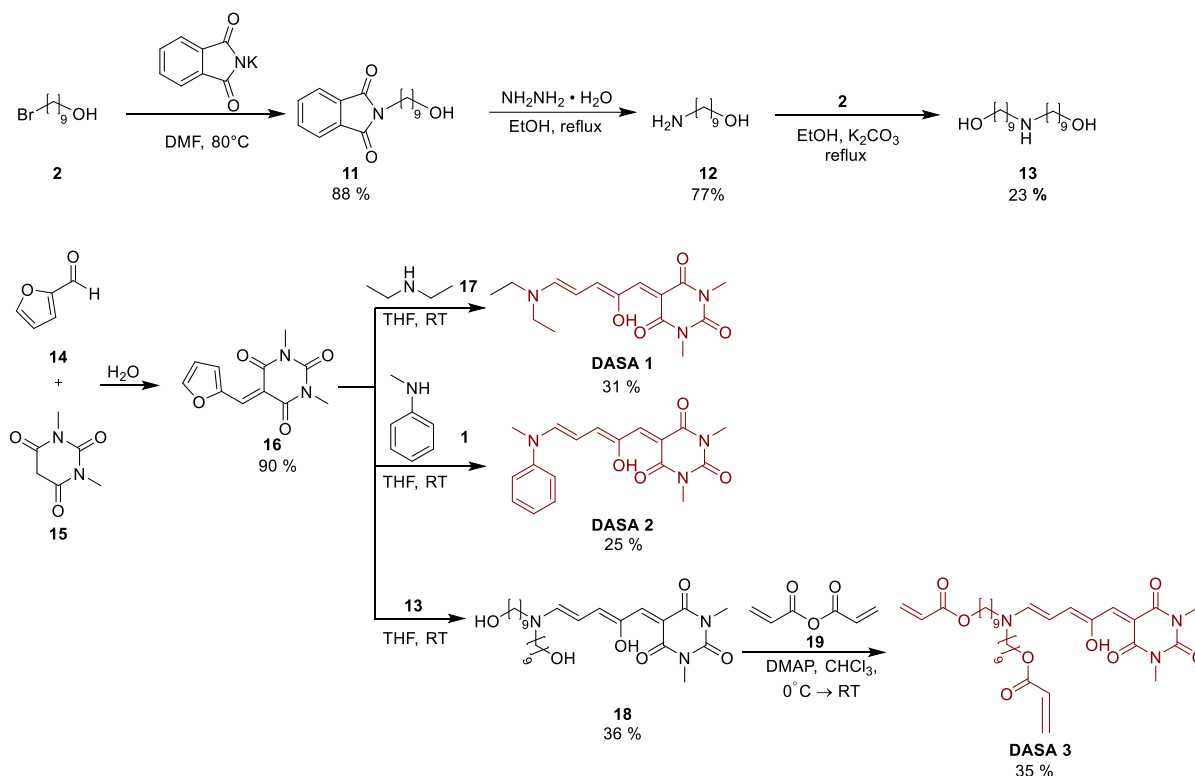
Scheme 3.1 Synthesis scheme of Azo **1** and Azo **2**.

### Donor–acceptor Stenhouse adduct (DASA)

The synthesis of DASA derivatives consisted of the ring opening reaction of an activated furan core (the acceptor) and a secondary amine as a nucleophile (the donor). On this basis, the terminal sites of the secondary amine seemed to be the most reasonable position for acrylate functionalization. For this, a secondary aminodiol (9-(9-hydroxynonylamino)nonan-1-ol) **13** was first synthesized through sequential substitution and reduction of naphthalimide from 9-bromo-1-nonanol **2**, forming the primary alkoxy amine **12**, and then followed by a nucleophilic addition. Once barbituric furan **16** was prepared by Knoevenagel condensation of furanaldehyde **14** and barbituric acid **15**, adding it into a THF solution of particular secondary amine immediately resulted into a drastic color change from pale yellow to vibrant magenta or violet accompanied with the appearance of a precipitate, indicating the formation of the DASA product.

Two targeted DASA derivatives (**DASA 1** and **DASA 2**) without polymerizable units were synthesized with diethylamine **17** and *N*-methylaniline **1** to serve as reference compounds. On the other hand, the functionalization of DASA was completed with the reaction of aminodiol **13** with acryloyl anhydride in the presence of 4-dimethylaminopyridine (DMAP) to afford the target product **DASA 3**. (Scheme 3.2) It is worth mentioning that finding the optimized

condition for the final step was particularly challenging. It was observed that the triene bridge of DASA was sensitive to either acidic and basic conditions and therefore often resulted in decomposition or creating various side products, which highly increased the difficulty of purification and hindered achieving a higher yield.



Scheme 3.2 Synthesis scheme of DASA 1 DASA 2 and DASA 3.

### Orthogonal control of photoswitches with different color of light

Prior to developing the functional ink for 3D printing, the photoresponse of each synthesized photoswitch was first investigated (Figure 3.1). The absorption spectra of **Azo 1** measured in a dilute toluene solution showed that the push-pull configuration resulted in a bathochromic  $\pi \rightarrow \pi^*$  absorption band at 438 nm, which was almost identical to its analog **Azo 2**. Reversible switching between the *trans*- and *cis*- isomers were efficiently achieved within a second for both **Azo 1** and **Azo 2**, by using light with 458 nm to switch and 365 nm to recover. On the other hand, the synthesized DASAs in toluene solutions exhibited a charge transfer absorption in the green light regime. While **DASA 1** and **DASA 3** had a sharp absorption band at 570 nm and remained transparent below 500 nm, **DASA 2** showed strong absorbance at 585 nm as well as in the UV region (295 nm) due to its secondary aniline moiety. With the irradiation of a 592

nm LED lamp, the absorption band obviously declined for all DASAs, accompanied with the color change of the solution from magenta/violet to transparent. This indicates the formation of the cyclized form of DASAs. Short thermal lifetimes of all cyclized forms were observed after switching off the LED light, while the cyclized-DASAs recovered back to the linear form immediately in dark.

Notably, both Azo and DASAs were unaffected under irradiation at wavelengths outside of their absorption regions. In detail, the absorbance of *trans*-**Azo 1** and **2** remained in the same level under the 592 nm LED, and similar observation was noticed for DASAs under the irradiation at UV (395 nm) and short visible light (433 nm). The orthogonal switching between the azobenzenes and DASA was examined by using a mixed solution of **Azo 2** and **DASA 1** under the irradiation with different wavelengths of light: 595, 433 and 385 nm. The absorption spectrum of the mixed solution was comparable to the superposition of their individual spectra. Importantly, the selective control among each photo-isomers of Azo and DASA was achieved by using three colors of light, as shown in Figure 3.1C. In a collaboration with the group of Prof. Petra Tegeder, a more detailed investigation was carried out with transient absorption spectroscopy, proving the orthogonality between the two photoswitches and that no energy transferring effect occurred even within the solid-state films.<sup>[135]</sup>

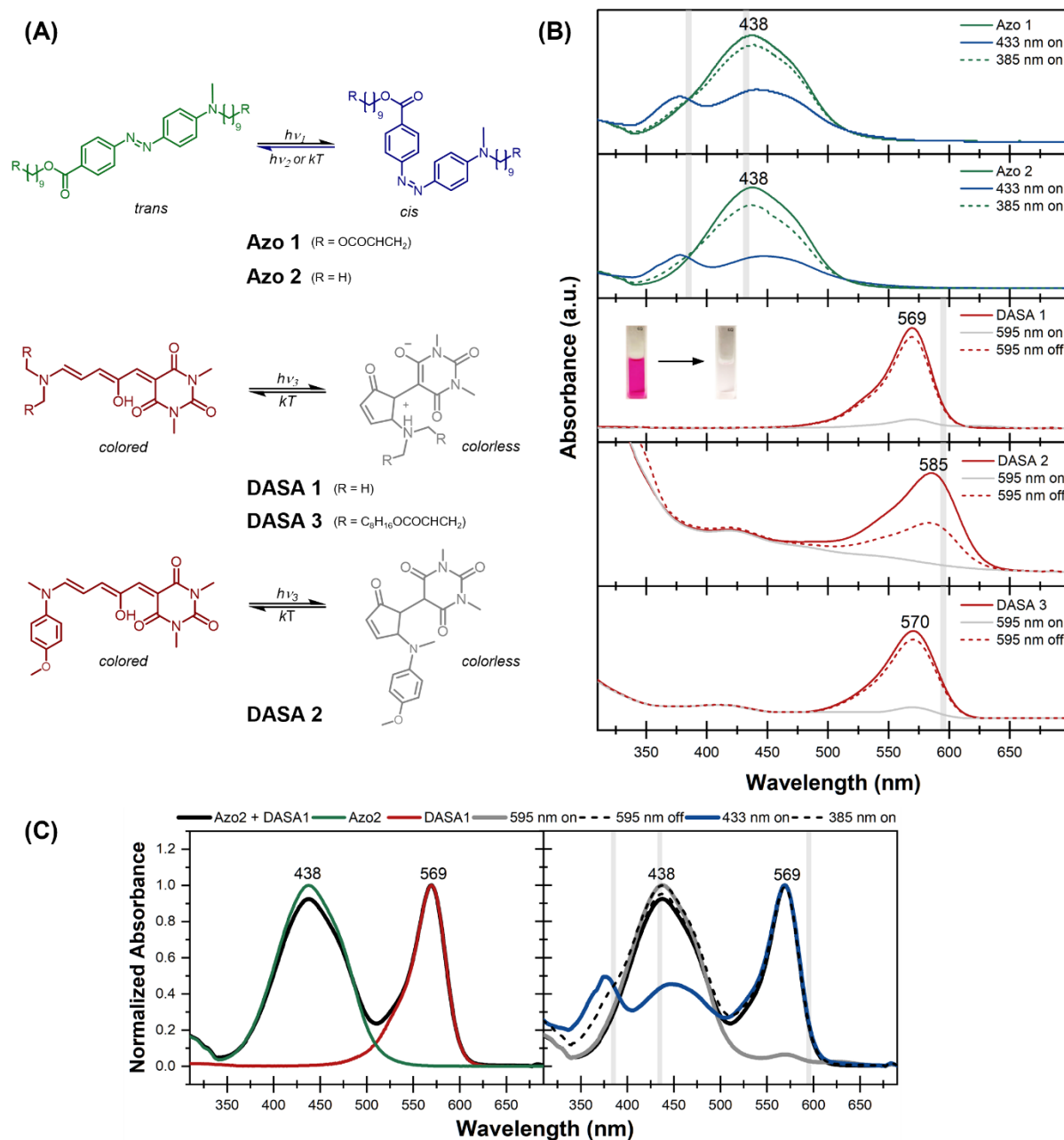


Figure 3.1 (A) Chemical structures and (B) absorption spectra of the synthesized photoswitches and their photoisomers. (C) Absorption spectra of a mixture of photoswitches (**Azo 2** + **DASA 1**, left) and orthogonally control their isomers using LEDs with three different wavelengths (385, 433, and 595 nm, right). The gray reference lines indicate the irradiation wavelengths. All absorption spectra were measured with dilute toluene solutions ( $10^{-5}$  M).

### 3.2.2 Incorporation of the dyes in the LC ink

The next steps are the examination of the compatibility of the synthesized photoswitches with a LC ink formulation, in which the solubility would be tested and the crystallinity within an alignment cell would be investigated. For this purpose, an optimized LC mixture consisted of a mixture of LCs, including bifunctional-acrylate crosslinker (RM257, 13 wt%), an acrylic monomer (C6BP, 36.2 wt%), a photoinitiator (Irg 819, 0.8 wt%) and an unreactive liquid crystalline solvent (E7, 50 wt%) was used as a starting point. In order to induce homogeneous alignment, cells coated with unidirectionally rubbed PVA films, which could form a planar alignment, were prepared (Figure 3.2A). A mixture of the described LC ink and each photoresponsive dye (**Azo1-2** and **DASA 1-3**) was filled into the cell via capillary forces at the temperature above the nematic-to-isotropic transition temperature ( $T_{ni}$ ) of the ink at around 60 °C followed by gradually cooling (1°C/min) back to room temperature (Figure 3.2B). The degree of alignment was observed by POM, where the images were dark when the aligning director was parallel to the polarizer and birefringent after rotating the polarizer in the case of planar alignment (Figure 3.2C).

Both **Azo 1** and **2** showed good solubility until 6 wt% blended into the LC mixture homogeneously. The good miscibility with the LC ink was indicated by the high degree of alignment within the glass cell confirmed by their POM images (Figure 3.2C). On the contrary, all DASAs exhibited poor solubility and miscibility in the LC mixture. For example, in the **DASA 3** incorporated mixture particles and precipitates were visible until the concentration was even lowered down to 1.3 wt%. while the immiscibility was observed in the alignment cell through phase separation, which intensively disrupted the order of LC molecules. To overcome the insolubility, attempts such as including non-mesogenic high polar crosslinkers (i.e., PEGDA, Mn = 250) into the formulation were pursued, however, despite the homogeneity of the modified mixture was highly improved, the critical balance between certain degree of DASA incorporation (>1 wt%) and LC anisotropy was not successfully reached. Moreover, in a preliminary test of 2PLP with the **DASA 3** incorporated ink, no DASA incorporation was observed in the printed structure, for two potential reasons: (1) The kinetics of the acrylate groups in **DASA 3** reacting were not in the same order of magnitude as the other LC crosslinkers. (2) The lability of the DASA chromophore led to photodecomposition under the radical environment.

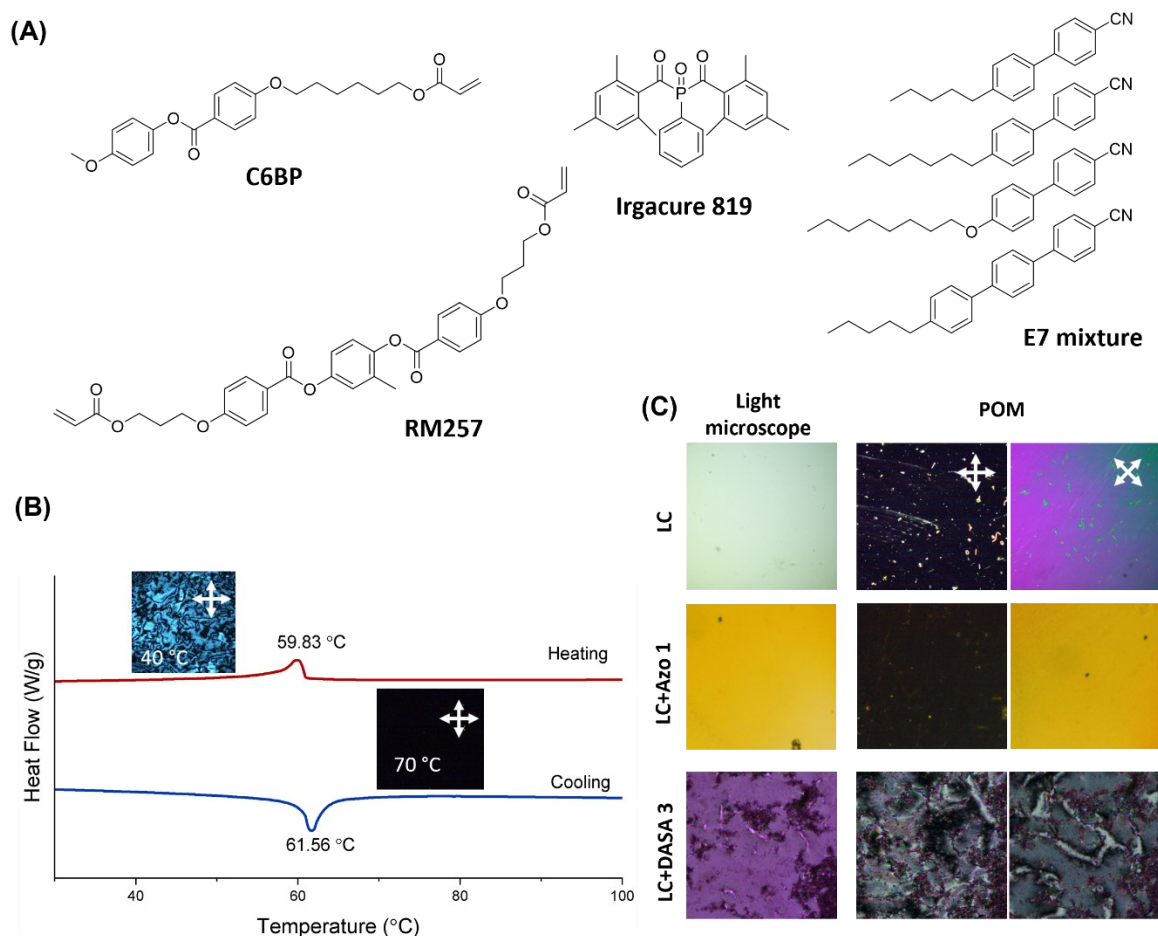


Figure 3.2 (A) Chemical structures of LCs used for film fabrication. (B) DSC traces for determining nematic-to-isotropic transition temperature ( $T_{ni}$ ) of the unpolymerized LC ink. The temperature gradient was set by the heating-cooling cycle between room temperature and 120°C (10.0°C/min). The phase transition of the ink was also verified under polarized optical microscope (inset), while no birefringence signal remained above 65°C. (C) Light and polarized microscopic images of the LC films fabricated with the parent LC link and the **Azo 1** or **DASA 3** incorporated mixtures (4 wt% in regards to the LC ink). Their planar alignment was indicated by the switch-on of birefringent signal once the director was not parallel to the polarizer. The reflective particles shown in the POM images of the pure LC and **Azo 1** embedded films were attributed to dust generated from the rubbing treatment on the PVA layers.

These experiments have highlighted the challenges on exploring other LC compatible photoresponsive molecules for 2PLP and also revealed the possible unstated reasons for the limited choice within the range of azobenzenes in this regard. At this point, it was clear that relying on conventional method, meaning the long process including synthesis of acrylate-functionalized photoabsorbers and then attempting to blend them into a LC ink, wasn't the

most efficient approach. As a result, developing an emerging strategy to overcome these limitations was in demand.

### 3.2.3 From conventional approach to post-modification approach: demonstration with photoresponsive LCE films

The possibility of incorporating the desired functional molecules after crosslinking a polymeric network as an alternative method was first explored by using LCE films. As depicted in Figure 3.3A, the parent LC mixture was aligned in the glass cell and an LED with weak illumination intensity (440-450 nm, 5.3mW/cm<sup>2</sup>) with a short irradiation time (60 s) was used to predetermine the orientation of the LC molecules by partially photopolymerizing the film. Subsequently, the film was immersed in a concentrated IPA/DCM (v/v = 10:1) solution of a dye (~20 mM) to undergo diffusion exchange of the dopant with the uncrosslinked E7 in the LCE matrix. Finally, a longer irradiation time (380-390 nm, 12.3mW/cm<sup>2</sup>, 10 min) was used to crosslink the acrylate groups of the dye with the residual monomers in the film and followed by a development step in IPA for 5 min.

As first demonstrated with **Azo 1**, the great penetration of the dye through the film was indicated by the strong coloration, while POM confirmed that the established LC alignment was preserved. Equally, the successful functionalization was also observed when applying the same post-modification procedure to **DASA 3**. For this case, for the first time there is no phase separation or irregular particles visible in the functionalized film (Figure 3.3B). Surprisingly, dyes without photopolymerizable groups, such as **Azo 2**, **DASA 1** and **DASA 2**, were also observed to be retained in the LC films respectively. This can possibly be attributed to the encapsulating effect, meaning the penetrated dye molecules were physically trapped by a further crosslinked polymer network after post-curing. The potentials of using these three chromophores to stimulate LCE activation were confirmed by bending actuations of LC strips (10 mm×2 mm×0.03mm) fabricated with Azo or DASAs functionalized film under illuminations of their absorbing light with either a 438 nm LED (3.5 W/cm<sup>2</sup>), 520nm LED (9.6 W/cm<sup>2</sup>) or a white halogen light (50 mW/cm<sup>2</sup>) (Figure 3.3C).

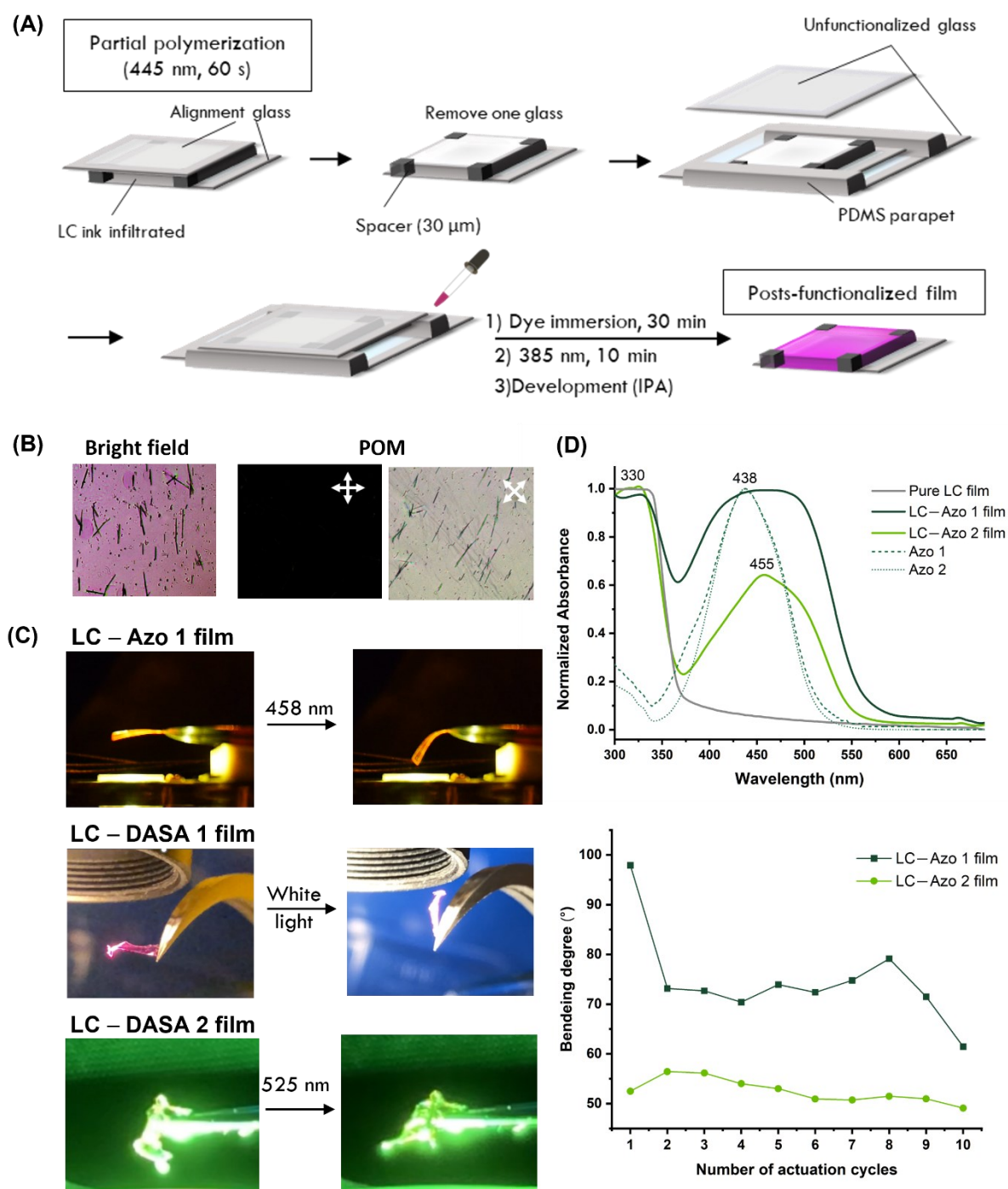


Figure 3.3 (A) Schematic illustration of the procedure to post-functionalize a LC film with a dye solution. (B) Microscopic images of a **DASA 3** post-functionalized film, indicating the planar alignment of the film was retained. (C) Photoactuation of the post-functionalized films, fabricated with **Azo 1**, **DASA 1** and **DASA 2**, respectively. (D) Top: Absorption spectra of the **Azo1**, **Azo 2** post-functionalized films and the parent LC film before functionalization, averaged from three measurements at different position of the film, and then normalized to the  $\lambda_{\text{max}}$  of the parent LC film at 330 nm. The spectra measured with the azobenzene toluene solutions were included for comparison. Bottom: Bending angles measured for the **Azo 1** and **Azo 2** functionalized films for each 10 actuating cycles.

In addition, the degree of dye penetration and the bending angle of the actuating films were compared between the films functionalized with **Azo 1** and **Azo 2**. According to their absorption spectra, **Azo 1** had a significantly higher degree of dye penetration, with an averaged absorbance ratio of dye ( $A_{455}$ ) to LC ( $A_{330}$ ) equivalent of 1, while the ratio value for **Azo 2** was 0.64. This indicated that the crosslinkable groups of **Azo 1** offered an advantage for being retained in the network due to their covalent bonding. Hence, the larger amount of the embedded **Azo 1** also consequently resulted in a higher amplitude of film actuation than **Azo 2** (Figure 3.3D).

### 3.2.4 2PLP of LCE microstructures

To transfer the successful post-modification approach from LCE films to microprinted structures, 2PLP was selected as printing technique. To facilitate two-photon polymerization, the composition of the LC ink was modified with a higher crosslinker content, consisting of RM257 (16.4 wt%), C6BP (32.8 wt%), E7 mixture, (49.2 wt%), and a photoinitiator Irg 819 (1.2 wt%), to where butylated hydroxytoluene (BHT, 0.4 wt%) was included as a radical scavenger to increase thermal stability and improve the printing resolution. For the 2PLP experiments, cells coated with polyimide layers, which enabled LC homeotropic alignment, were used for the alignment instead of PVA due to their higher thermal stability and chemical resistance avoiding detachment of the printed structure during the development step. Being processed with the same realignment method mentioned, the homeotropic alignment of the LC cell was then verified through POM by observing a black and monochromatic image irrespective of the cell orientation to the crossed polarizers. Subsequently, the aligned LC cells were used for 3D laser printing using a commercial two-photon lithography setup (PPGT2, Nanoscribe GmbH) (Figure 3.4A).

The optimized LC ink formulation allowed for a wide fabrication window but resulted in varied printing outcomes (Figure 3.4B). To gain a more in-depth understanding of the 3D printed microstructures at different printing conditions, confocal Raman spectroscopy was employed to monitor the conversion of 2PP. For this purposes, first simple 3D printed blocks with dimensions  $50 \times 50 \times 10 \mu\text{m}^3$  were printed by varying the laser power from 22.5–35 mW and the scanning speed from 3–9  $\text{mm s}^{-1}$ . Specifically, Raman spectra collected with  $1 \mu\text{m}$  resolution from an area of  $10 \times 10 \mu\text{m}^2$  at the center of the upper surface of the block was averaged. The double-bond stretching band of the acrylate group at  $1635 \text{ cm}^{-1}$  was observed

to vary in intensity as the double bonds were consumed during polymerization while the stretching signal of the carbonyl groups C=O (1726 cm<sup>-1</sup>) served as a reference peak as it was not affected by the photopolymerization. The polymerization degree of the blocks of each printing condition was indicated by the double bond conversion (DOC)<sup>[136]</sup> according to **Equation 1**:

$$DOC = 1 - \frac{A'_{(C=C)} / A'_{(C=O)}}{A_{Ink(C=C)} / A_{Ink(C=O)}} \quad \text{(Equation 1)}$$

The analysis indicated that the DOC was significantly affected by the laser dose, meaning higher laser power or slower scanning speed resulted in a higher degree of polymerization. The analyzed results agreed well with the shrinkage degree observed for the printed structures (Figure 3.4B, C). In detail, at a constant scanning speed of 5 mm s<sup>-1</sup>, an increase in laser power from 22.5 to 30 mW resulted in a rise in DOC from 0.68 to 0.80 (blue dashed line). Interestingly, the effect on DOC was less pronounced for different scanning speeds at a certain laser power (red dashed line). The measured samples were thereafter irradiated with a 385 nm LED for 30 min to simulate the post-modification treatment. The post-curing resulted in a more densely crosslinked network, verified by significant increases in DOC for all samples (solid lines), particularly for those with low conversion in the first stage. For example, the DOC of the 3D printed microtritic block with laser power of 27.5 mW and scanning speed of 6 mm s<sup>-1</sup> considerably increased from 0.71 to 0.79 after the exposure to UV light.

The relationship between the polymerization degree and the mechanical properties were studied through the measurements of nanoindentation (Figure 3.4D). Similarly, the effective Young's modulus ( $E_{eff}$ ) only varied within a small range when the scanning speed was changed, but a significant increase in  $E_{eff}$  was observed when a higher laser power was used. These observations confirmed the previous assumption that the mechanical stiffness of the LCEs is closely related and positively dependent on their polymerization degree, providing valuable insights for optimizing the 3D printing process of LCE microstructures.

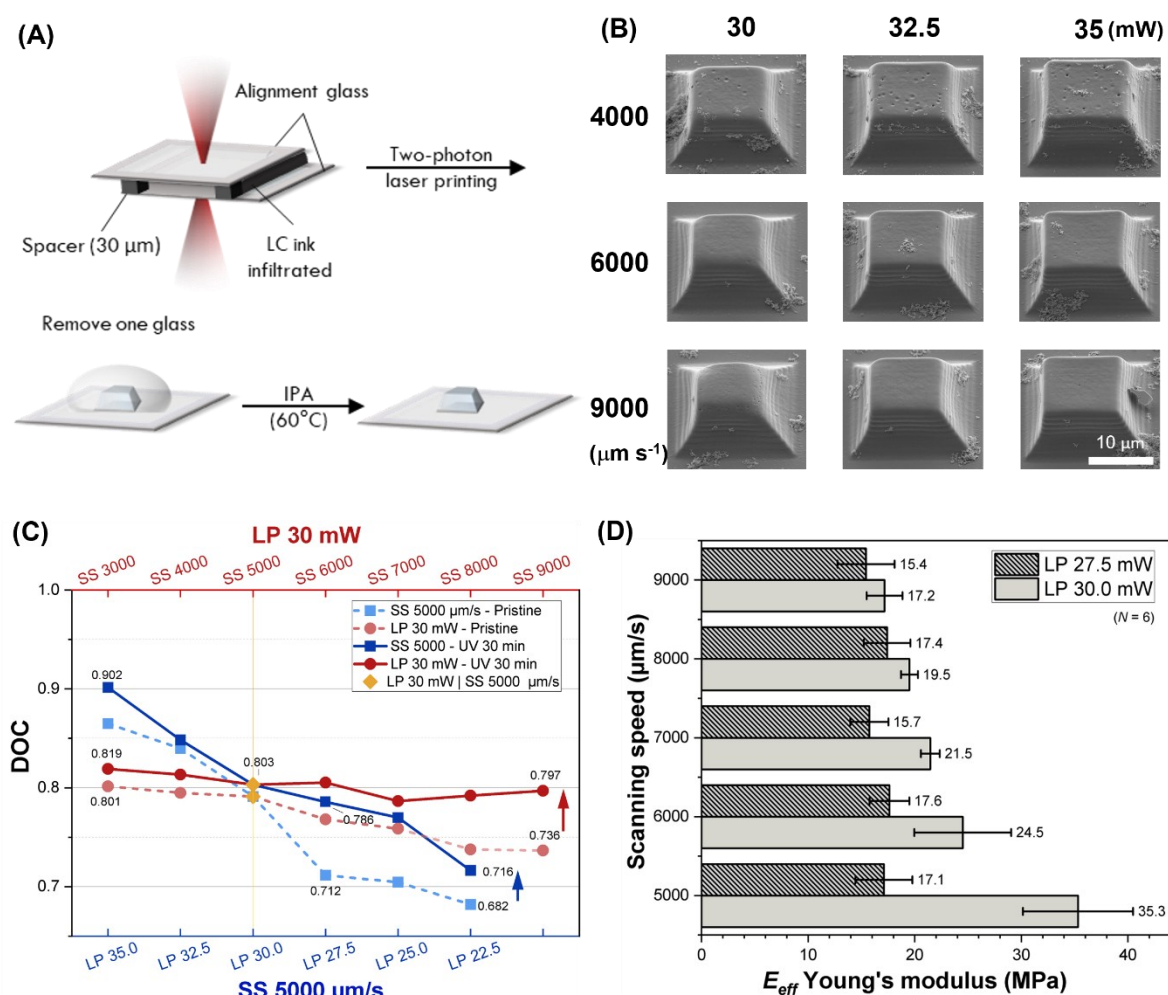


Figure 3.4 (A) Schematic presentation of LC microstructure fabricated via 2PLP. First, a LC ink was filled in an alignment cell, which was assembled with polyimide functionalized glasses. Next, 2PP was carried out with a femtosecond laser and the LC microstructure was afforded after development in IPA solvent. (B) SEM images of LC cubic microstructures (20 × 20 × 20 μm<sup>3</sup>) printed with varied laser powers (30–35 mW) and scanning speeds (4–9 mm s<sup>-1</sup>). (C) Double bond conversion (DOC) for 3D microblocks, printed with varied laser powers and scanning speeds, before and after a UV (385 nm) post-curing step. DOC was calculated with the characteristic peaks of  $\nu(\text{C}=\text{O})$  (1727 cm<sup>-1</sup>) and  $\nu(\text{C}=\text{C})_{\text{acrylates}}$  (1635 cm<sup>-1</sup>). (D) Mechanical characterization of LC microblocks printed at different laser powers and scanning speeds via nanoindentation. The standard deviation was represented with the error bars based on 6 measurements. Figures adapted from Ref [129].

### 3.2.5 Implementation of photoresponsive properties into LCE microstructures

As a next step, the post-modification process for implementing photoabsorbers into LC films was adapted for 2PLP fabricated LC microstructure. The optimized procedure is depicted in Figure 3.5, in comparison with the conventional approach. In the process described for post-modifying LCE films, a dye solvent prepared with IPA was deposited on the film directly after

the photopolymerization at the first stage leading to a diffusion exchange between the unreacted E7 and the dye molecules. Differently, in 2PLP only a volume in the range of cubic micrometers is polymerized, therefore a subsequent development process within the solvent bath is required to remove the excessive amount of unpolymerized ink. This would result in subtracting also the E7 and leaving the voids between the network collapsed. As a result, using the dye/IPA solvent to functionalize the developed structure was not always successful.

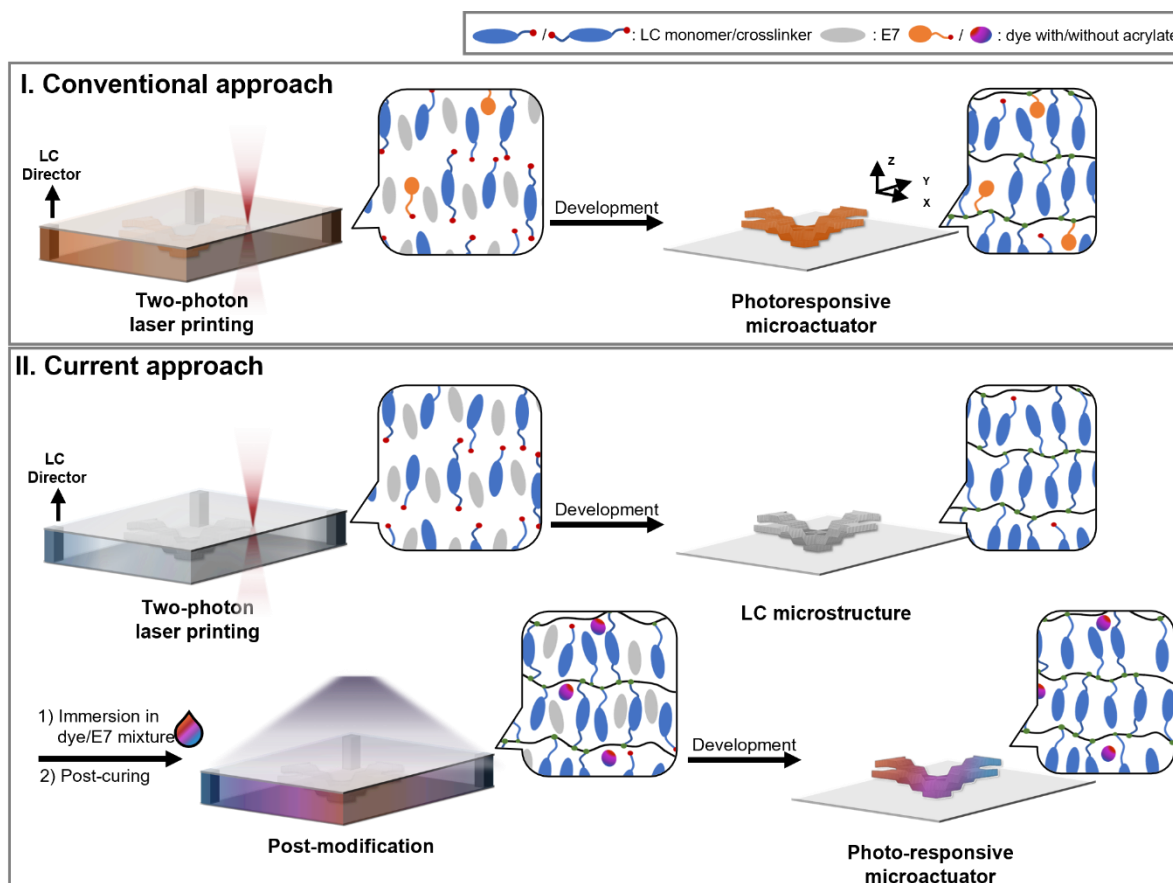


Figure 3.5 Schematic illustration of two different approaches for fabricating photoresponsive 3D microstructures via 2PLP. The conventional approach (I) involves using a LC ink containing acrylate-functionalized photoresponsive units, which is aligned in a glass cell and used for two-photon 3D laser printing. The post-modification approach (II) developed here utilizes the use of dye/E7 mixture to reswell the printed structure and afford the dye penetration. Exposure of UV light was used to further photocrosslink and encapsulated the incorporated dye molecules. With this approach, the dye molecules are not required for functionalization of polymerizable groups. Figures adapted from Ref [129].

It was discovered that E7 played a critical role in this case. First of all, a large fraction of unreactive E7 mixture in the ink formulation was necessary, which not only assisted the high degree of LC alignment by improving the miscibility of the solid mesogens, but also afforded

the formation of a flexible network from printing. However, E7 also led to a significant shrinkage of the printed microstructures ( $\sim 49\%$ ) after development (Figure 3.6A). When using standard organic solvents, the resulting compacted LC network highly compressed the diffusion channels for the dye solution leading to an unsuccessful functionalization. Interestingly, it was noticed that immersing the shrunken structure into E7 for 12 hours could “reswell” the developed structure and the subsequent post-curing (385 nm, 30 min) led to a partial (16 %) recovery by enhancing the crosslinking density (Figure 3.6B), as confirmed with  $\sim 10\%$  increase in DOC as previously shown in Figure 3.4C. Thus, these observations revealed an alternative pathway to establish the post-modification procedure for functionalizing the LCE microstructure, by utilizing an E7/dye mixture to reswell the LC matrix and allow the penetration of the dye molecules into the network. The photocrosslinking step ensured that the dyes are stably embedded in the LC network, avoiding leaching out or being washed away in the second development step. With this modification in the post-functionalization procedure, embedding the functional dye molecules was successfully achieved indicated by a drastic color change of the microstructures.

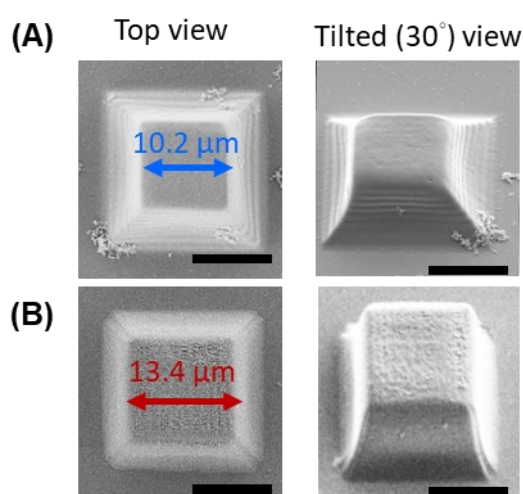


Figure 3.6 (A) SEM images of a LC cubic microstructure printed with the dimension ( $20 \times 20 \times 10 \mu\text{m}^3$ ) at a laser power of 30 mW and scanning speed of  $5 \text{ mm s}^{-1}$ . Close to 50 % of shrinkage of the top layer was observed after the development in IPA at  $60^\circ\text{C}$  for 5 min. (B) 16 % of recovery was observed after immersing the block in E7 mixture for 12 h and treated with post-curing by a 385 nm LED for 30 min. Figures adapted from Ref [129].

The dye incorporation into the LC microstructures from the previously described adapted post-modification approach was investigated in detail through various characterization methods. First, Raman spectroscopy was used to monitor the process of preparing functionalized cubic

microstructures (Figure 3.7A). It was first observed that no E7 was retained neither in the developed LC structures, nor in the functionalized structure, confirmed by the absence of  $\nu(\text{C}\equiv\text{N})$  at  $2226\text{ cm}^{-1}$ . Next, the characteristic C-N stretching signal of azobenzenes  $\nu(\text{C}-\text{N})_{\text{Azo}}$  at  $1137\text{ cm}^{-1}$  was used to indicate the incorporation of dye within block structures prepared with dispersions consisting of azo dyes and an E7 mixture, denoted as LC  $\supset$  Azo (Figure 3.7B). For LC  $\supset$  **Azo 1**, the signal at  $1137\text{ cm}^{-1}$  with high intensity was unambiguously observed. Equally the azobenzene signal was presented for **Azo 2** proving that dyes without crosslinkable group could also successfully embed into the structure. (Figure 3.7A) Furthermore, for the comparison of this new approach with the traditional one, 3D blocks printed from formulations with **Azo 1** and **Azo 2** incorporated respectively were also prepared (denoted as LC+**Azo 1** and LC+**Azo 2**). The results showed that while the  $\nu(\text{C}-\text{N})_{\text{Azo}}$  signal was detected for LC+**Azo 1** no signal was found for LC+**Azo 2** indicating that **Azo 2** was washed away during the development process.

In the next step, the degree of incorporation of the two azobenzene dyes in the microstructures was defined by the integral ratio between the azobenzene signal area and the LC moieties peak area ( $\nu(\text{C}=\text{O})_{\text{Azo}}/\nu(\text{C}=\text{O})_{\text{LC}}$ , see details in Chapter 5). The effects of the printing conditions on the dye penetration for both azobenzenes mentioned in Figure 3.7C were noted. For example, in the 3D micrometric blocks printed with a scanning speed of  $10\text{ mm s}^{-1}$  and  $5\text{ mm s}^{-1}$ , higher quantities of dye were trapped in the ones printed at  $10\text{ mm s}^{-1}$  compared to those made at  $5\text{ mm s}^{-1}$ , indicating that the crosslinking density of the polymer is critical for dye penetration. In general, when using the same concentration of the azo dyes in the E7 mixture a higher degree of functionalization of **Azo 1** compared to **Azo 2** was observed after the post-curing step due to its covalent attachment to the LC polymeric network. This had also been the case for film functionalization.

Furthermore, the use of a variety of concentrations of dyes in an E7 mixture could adjust the functionalization degree. For instance, LC  $\supset$  **Azo 2** functionalized with a mixture up to 20 wt% of dye afforded a higher integral ratio of **Azo 2** than those immersed in mixture with only 5 wt% of dye. On the other hand, it must be noted that in order to prevent crystallization, disruption of alignment and "microexplosions" during printing in the conventional fabrication approach, the concentration of **Azo 1** was limited to 2.5 wt%. By employing this new approach with a 20 wt% dye mixture, a higher degree of functionalization in LC  $\supset$  **Azo 1** than LC+**Azo 1** was observed. As demonstrated in these experiments, the benefits of this new post-

modification approach include the fact that the possibility to embedded nonacrylate dyes without modification and the flexibility of controlling the dye incorporation without adjustments to the printing parameters.

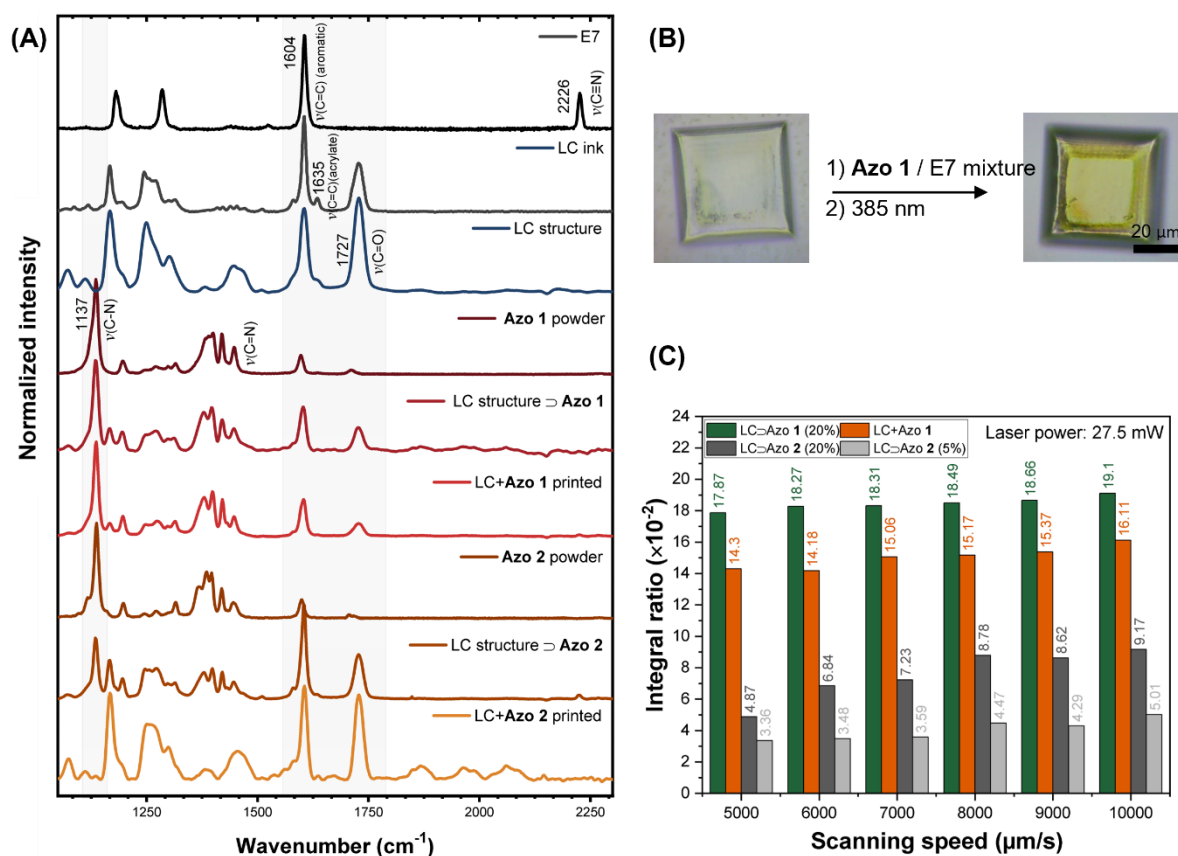


Figure 3.7 (A) Raman spectra measured for the unpolymerized ink, pristine LC microstructure, and functional microstructures prepared via conventional approach (LC+Azo) and post-modification approach (LC  $\supset$  Azo) with the employ of **Azo 1** and **Azo 2**. (B) LC cubic microstructures (50 × 50 × 10 μm<sup>3</sup>) printed and post-functionalized with **Azo 1** (LC  $\supset$  **Azo 1**) for Raman measurements. (C) Comparison of dye incorporation of blocks between two employed approaches, define by the integral ratio based on the value of  $\nu(\text{C}=\text{O})_{\text{Azo}} / \nu(\text{C}=\text{O})_{\text{LC}}$  obtained from Raman spectra. Figures adapted from Ref [129].

With this methodology developed, employing other classes of dyes to expand the functionalization of the LC structures was allowed. As one of the targeted classes, **DASA 1** and **2** without polymerizable group was more preferable to use for this purpose than **DASA 3**, which is synthetically demanding and has poor photostability. This approach also offered another major advantage: dyes used for incorporation into the microstructures are no longer restricted to have the absorption region located between the wavelengths of printing

(390-780 nm) as in the conventional method. As a result, to further explore light responsive properties in the range with even longer wavelengths, anthraquinone derivatives as a third class of photoabsorber, Sudan Blue II (**SBII**), which exhibits absorption maximum at 650 nm were also exploited for the fabrication of functional structures (Figure 3.8A). The successful appliance of incorporating dyes in the LC  $\supset$  **DASA 1**, LC  $\supset$  **DASA 2**, and LC  $\supset$  **SBII** have been confirmed by optical microscopy that produces colorful 3D microstructures in magenta, dark violet, and indigo blue, respectively. Importantly, this functionalization did not affect the alignment of the LC network, enabling LC microstructures which are compatible to dyes other than azobenzene for the first time.

Further analysis was conducted to investigate the distribution of dyes within the LC microstructure after post-functionalization using confocal laser scanning microscopy and Time-of-Flight Secondary Ion Mass Spectrometry (ToF-SIMS). First, the fluorescence intensity profiles of **DASA 1** ( $\lambda_{em} = 595$  nm) in X-Y and Y-Z slices of a functionalized LC microblock ( $75 \times 75 \times 10 \mu\text{m}^3$ ) were found to be comparable, suggesting that the dye penetrated evenly within the structure, rather than being limited to just the surfaces, as shown in Figure 3.8B. ToF-SIMS analysis further supported this observation, as the m/z signals at 371.10 ( $\text{C}_{19}\text{H}_{20}\text{N}_3\text{O}_5^-$ ) and 349.18 ( $\text{C}_{22}\text{H}_{26}\text{N}_2\text{O}_2^+$ ), which are characteristic for **DASA 2** and **SBII**, respectively, were detected with consistent signal intensity throughout the entire 3D microblock ( $40 \times 40 \times 10 \mu\text{m}^3$ ), proving that the other two classes of functional molecules, both DASA and anthraquinone derivatives, can achieve homogeneous functionalization of LC 3D structure with the utilization of E7 as a medium (Figure 3.8C, D).

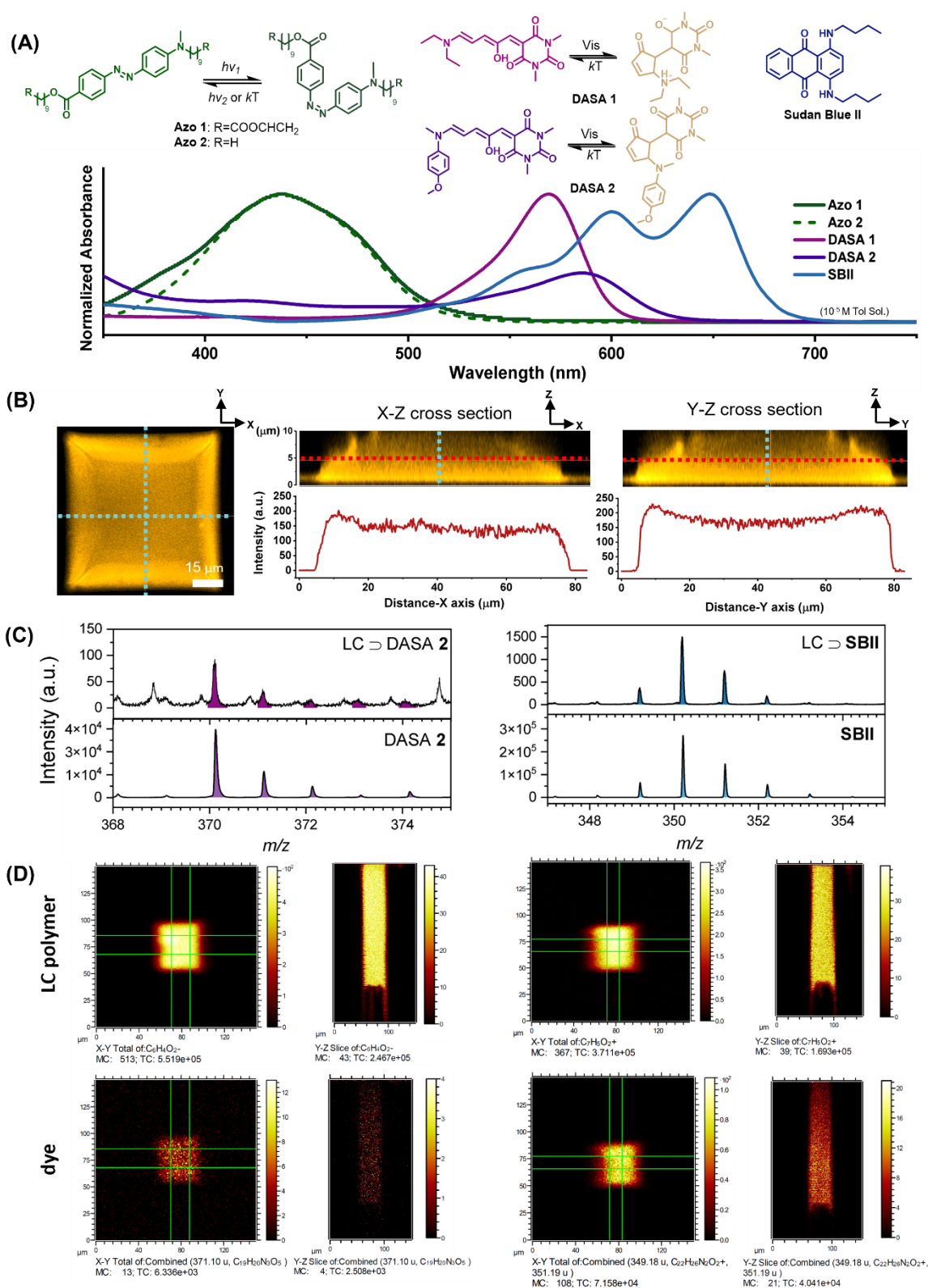


Figure 3.8 (A) Chemical structures of the photoabsorbers employed in the LC structure functionalization, that their absorption region covers the whole visible region. The UV-vis spectra were measured in solution (concentration =  $10^{-5}$  M in toluene). Characterization of dye distribution within the LC microstructure after post-functionalization, including the use of confocal microscopy and Time-of-Flight Secondary Ion Mass Spectrometry (ToF-SIMS) analysis. (C) Fluorescence images detected at 595 nm

displaying X-Y, X-Z, and Y-Z cross-sections of an LC  $\supset$  **DASA 1** 3D microblock ( $75 \times 75 \times 10 \mu\text{m}^3$ ). The fluorescence intensity profiles of each slice were measured at the red dashed lines. (C) Secondary ion mass spectra of LC  $\supset$  **DASA 2** (left), and LC  $\supset$  **SBII** microblocks (right) ( $40 \times 40 \times 10 \mu\text{m}^3$ ). The upper spectra were from dynamic SIMS analysis of a dye loaded polymer block, and lower ones were from a pure dye drop cast as reference. (D) Cross sections and depth profiling images (field of view  $x=y=150 \mu\text{m}$ ,  $z$  not to scale) of LC  $\supset$  **DASA 2** (left), and LC  $\supset$  **SBII** microblocks. The render in the upper row was based on the polymeric signal of  $\text{C}_6\text{H}_4\text{O}_2^-$  signal (left) or  $\text{C}_7\text{H}_5\text{O}_2^+$  (right). The lower row was rendered with the dye signal, which are  $\text{C}_{19}\text{H}_{20}\text{N}_3\text{O}_5^-$  (plus isotope distribution) or  $\text{C}_{22}\text{H}_{26}\text{N}_2\text{O}_2^+$  (in positive secondary ion polarity), corresponding to **DASA 2** and **SBII**, respectively. Figures adapted from Ref [129].

### 3.2.6 Two-photo laser printing of light-driven LCE microstructures

#### Single-color light actuation

As a next step after the successful incorporation of dyes into LC microstructures, fabrication of more complex geometries and the investigation of the photoactuation was pursued. In this respect, a four-arm gripper was designed, with each arm measuring  $65 \mu\text{m}$  in length and ending in a broader edge at the arm tip to facilitate image analysis during actuation characterization. To maximize the printed volume within the height of the alignment cell, the arms were not designed straight but with a "staircase" feature (Figure 3.9A). The fabrication process took place in a  $30 \mu\text{m}$  thick cell with homeotropic alignment of the LC ink.

After the 3D printed microstructures underwent the development and dye incorporation, an up-bending deformation of the arms along the director was observed, resulting in the arm tips being closer to each other than programmed and at an elevated height of around  $55\text{-}65 \mu\text{m}$  beyond the glass cell where they were originally printed in (Figure 3.9B, C). Interestingly, shrinkage perpendicular to the alignment direction did not just result in shortening of the arms within the X-Y plane, but induced clear bending, leading to a pristine "closed state". This degree of bending was highly dependent on the crosslinking density of the printed structures, and therefore could be determined by altering printing conditions such as laser power and scanning speed. As shown in Figure 3.9D, lowering the laser power or increasing the scanning speed would result in a looser and softer network and the severer shrinkage led to a more dramatic arm bending effect. Due to the thermotropic behavior of LCE, it was expected that inducing the nematic-to-isotropic transition would transform the gripper into an "open state" once their arms were elongated. Before diving into the light-driven actuation studies, a reference sample without dye was tested to ensure the actuation pattern by using heat as a

stimulus. As predicted, the 3D microactuators unfold gradually and reaching their maximum expansion at 270 °C. Afterwards, a complete recovery to the initial state was reached by cooling back to room temperature (Figure 3.9E).

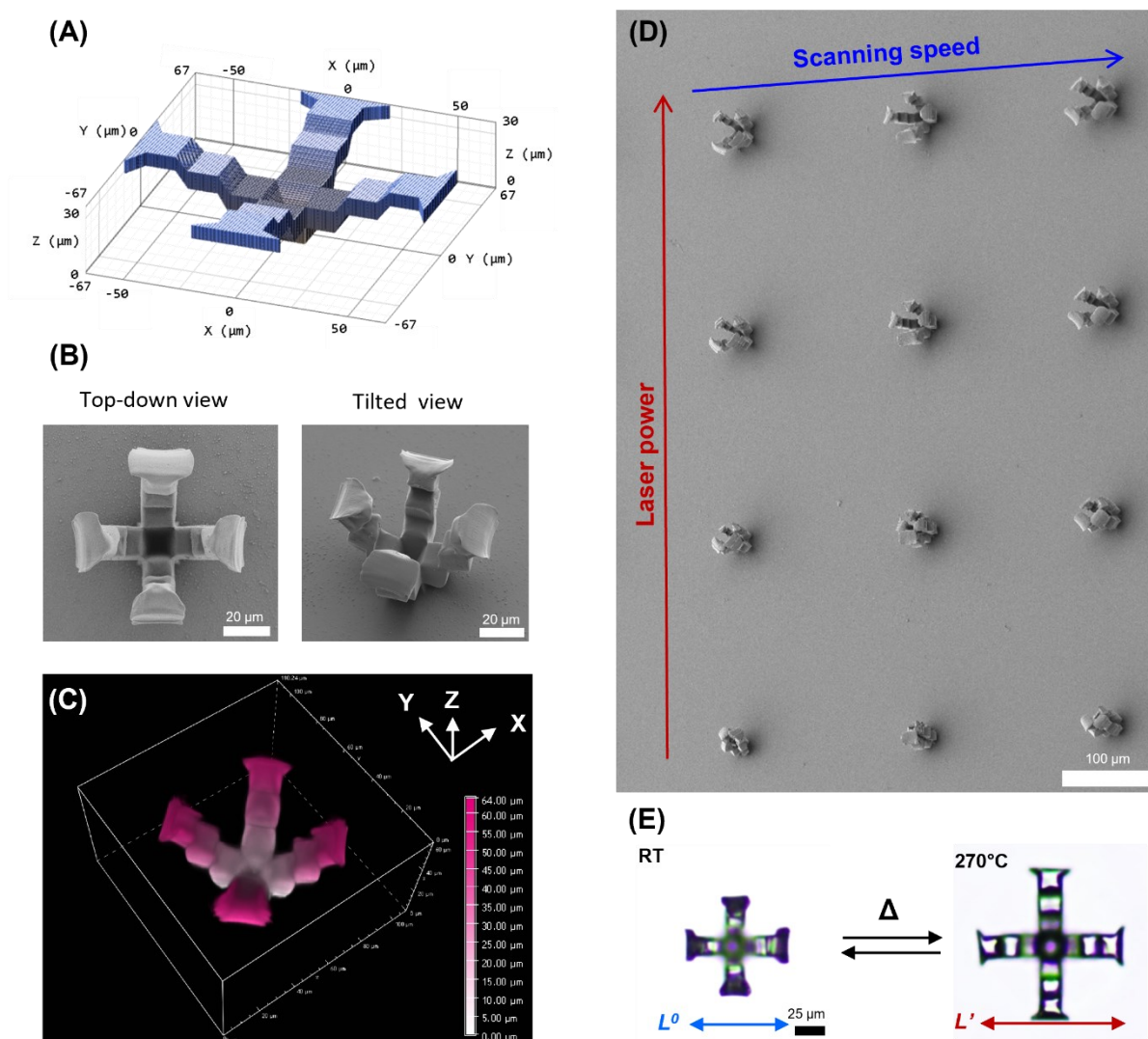


Figure 3.9 (A) 3D model design of the microactuator. (B) Scanning electron microscopic (SEM) images of a single LC microactuators from a top view (left) and a tilted view (right). (C) 3D reconstruction of LC  $\square$  **DASA 1** microactuator presenting the height profile. The images were collected by exciting the **DASA 1** molecule with 561 nm laser and detecting the fluorescence at 595 nm. The step size of the Z-stack is 1 μm. (D) An array of LC microactuators printed at different laser power (27.5–35 mW) and scanning speed (5–9 mm s<sup>-1</sup>). (E) Thermal actuation of a pristine microactuator. The structure reached maximum expansion at 270 °C and recovered to the original “closed” state after cooling back to room temperature. Figures adapted from Ref [129].

The photoresponse of the dye-incorporated LC microactuators with respect to the corresponding wavelengths of light was evaluated in the next step. For comparison, one LC+**Azo 1** was fabricated with the conventional method along with other five actuators embedded with one of the five dyes (LC  $\supset$  **Azo 1**, **Azo 2**, **DASA 1**, **DASA 2** or **SBII**) through the new approach while having the predetermined alignment remained (Figure 3.10A, B). A self-built irradiation setup, where LEDs were constructed to irradiate the structures orthogonally to the light path of an optical microscope, was used to image the photoactuation either from a top or a side view. LED emitting at 459 nm was employed for 3D microactuators containing **Azo 1** or **Azo 2** as photoabsorber (LC  $\supset$  **Azo 1** or **Azo 2**, LC+**Azo 1**), at 520 nm for LC  $\supset$  **DASA 1** or **DASA 2**, and at 622 nm for LC  $\supset$  **SBII**. All the functionalized actuators exhibited an unfolding motion similar to the reference sample under light irradiation with the respective wavelength (Figure 3.10C). The amplitude of the expanding motion could be controlled by regulating the light intensity of the LEDs. As an example, the angle between the arms and the substrate of a 3D gripper containing **Azo 1** gradually decreased from 51° to 10° by increasing the electrical current from  $I = 0$  A, 3 A to 5A (corresponding to 1.4 to 2.0 W/cm<sup>2</sup> for the blue LED), as illustrated in Figure 3.10D.

For a more detailed analysis, the actuation of the photoresponsive 3D microactuators was monitored over 50 cycles of on-off light irradiation by recording the distance changes ( $\Delta L$ ) between two opposing arm tips ( $L'$ ) compared to the initial configuration ( $L^0$ ), and the maximum distance ( $L_{max}$ ) reached by each microactuator was determined (Figure 3.10E). It was found that  $L_{max}$  differed among the microactuators, with the LC  $\supset$  **Azo 1** gripper showing the largest effect with a 65% extension in  $L$ , compared to a 27% increase for the reference LC+**Azo 1** microactuator. Such extent of actuation prominently surpassed the performance of previous reported LCE microactuators based on surface alignment. This observation correlates to the characterization results from Raman spectroscopy, highlighting the advantage of the new method which allows for an enhancement of dopant concentration, leading to larger actuation amplitudes. It is worth mentioning that LC  $\supset$  **Azo 2** showed a comparable actuation to the reference LC+**Azo 1**, despite being non-covalently attached to the polymer network. Furthermore, under irradiation at 520 nm LC  $\supset$  **DASA 1** and **DASA 2** exhibited  $L$  increases of 11% and 22%, respectively, while LC  $\supset$  **DASA 2** showed less fatigue over 50 actuation cycles and better photostability. LC  $\supset$  **SBII** microstructures enabled actuation driven by red light (622 nm, 3.5 W/cm<sup>2</sup>), with an increase in  $L$  of 18%. Notably, these new light-driven microactuators incorporating DASA and SBII dyes offered responsive structures in a previously unexplored

regime of the visible spectrum for actuation. The temporal response among each actuator was also evaluated, defined as the time required to reach 50% of recovery after the light switched off ( $t_{1/2}$ ). Under the specified irradiation conditions, LC  $\supset$  **Azo 1** exhibited the shortest  $t_{1/2}$  with 35 ms, followed by 70 ms for LC  $\supset$  **Azo 2** and LC+**Azo 1**. LC  $\supset$  **DASA 2** and **SBII** showed longer responses time of 400-500 ms, while LC  $\supset$  **DASA 1** had the slowest response of around 1 s.

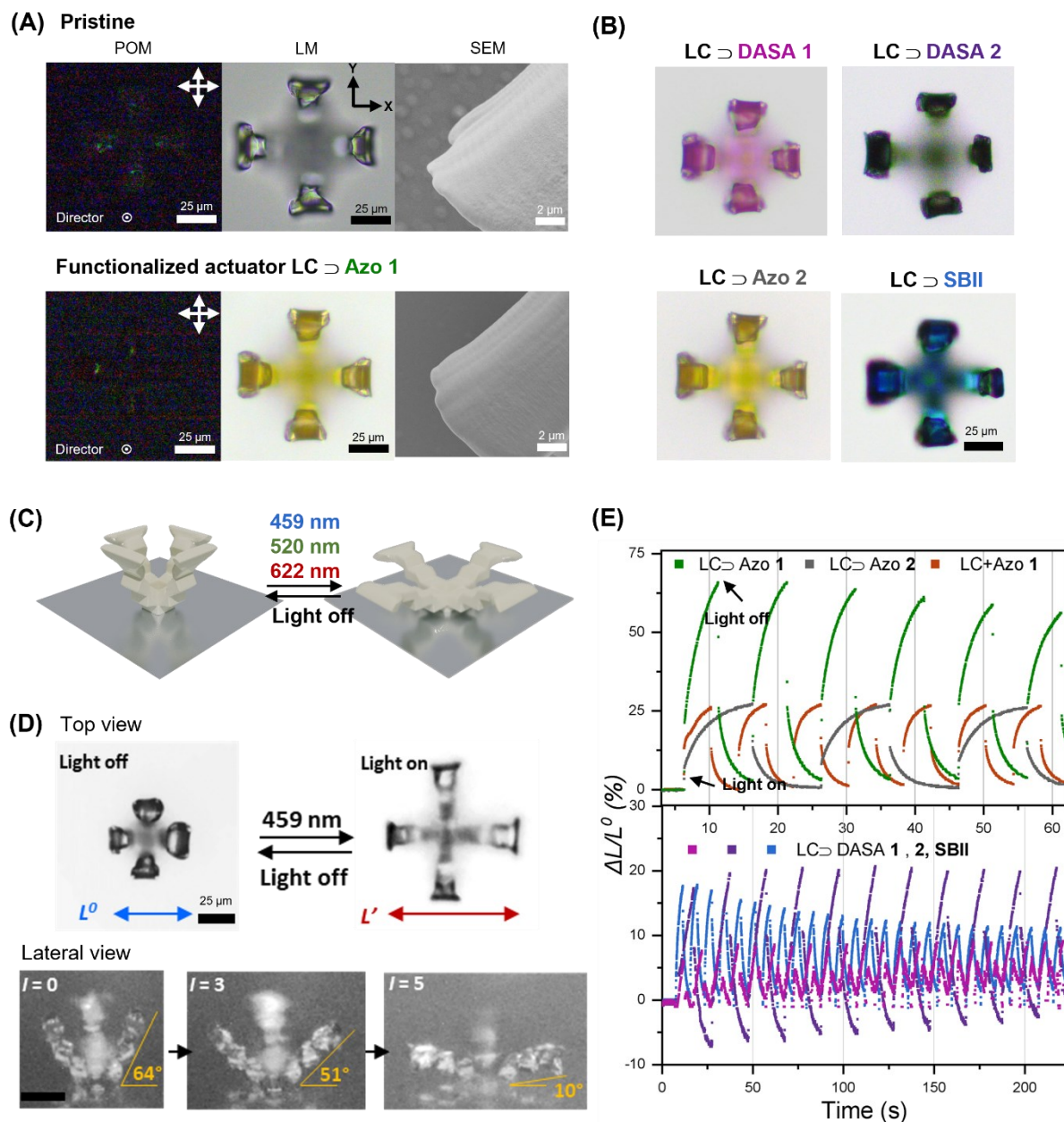


Figure 3.10 (A)(B) POM, light microscope (LM) and SEM images of the pristine microactuators in comparison with the ones functionalized with different dyes: LC  $\supset$  **Azo1/2**, **DASA 1/2**, and **SBII**. (C) 3D representation of the reversible photoactuation process. (D) Optical images of the photoactuation of LC  $\supset$  **Azo 1** microactuator from top and side views, where the bending degree can be tuned by the light intensity of the irradiated light. (E) Responses of the light-driven actuators by switching the light on and

off, according to the lateral expansion (%) from the top view. The red, green, and blue LEDs were all set at  $I = 10$  A (corresponding to 3.5, 9.6 and 3.1 W/cm<sup>2</sup>, respectively) for the LC  $\supset$  **Azo1/2**, **DASA 1/2**, and **SB II** microactuators, respectively. Figures adapted from Ref [129].

### Multiple-color light actuation

The newly developed approach provides various options to tailor the photoresponsive properties of LC microstructures. In the final step, the fabrication of complex light-driven actuators which exhibits wavelength-dependent behavior was ultimately targeted. The possibility of this was explored by incorporating two types of photoabsorbers with distinct absorption profiles into the LC structure at the same time enabling selectivity. Specifically, demonstrated by two potential combinations of dyes, the light-responding behaviors of microactuator functionalized with the mixture of **Azo 1+DASA 2** or **Azo 1+ SBII** were examined by two kinds of LEDs emitting at different wavelengths, namely 459 and 520 nm for **Azo 1 + DASA 2**, and 459 and 622 nm for **Azo 1 + SBII**. Meanwhile, as a reference, mono-functionalized microstructures (LC  $\supset$  **DASA 2** and LC  $\supset$  **SBII**) were also fabricated and irradiated under the same conditions. The responsive behaviors under each irradiation condition were imaged from the side view with the distance between two opposing tips defined as  $d$  and the differences ( $\Delta d$ ) compared to the initial state ( $d^0$ ) evaluated as depicted in Figure 3.11.

For the first case of the bifunctional microactuator LC  $\supset$  **Azo 1 + DASA 2**, only a “half expansion” with an amplitude of 84.8%, was observed under the green emitting light, analogous to the motion of LC  $\supset$  **DASA 2**. On the other hand, when only blue light was switched on, a full expansion of the bifunctional microactuator was observed due to the activation of **Azo 1**, while the reference sample LC  $\supset$  **DASA 2** was not stimulated at this wavelength. A similar wavelength selective response of the dual-functionalized microactuator was also observed among LC  $\supset$  **Azo 1 + SBII** and LC  $\supset$  **SBII**, while only the bifunctional one was activated reaching the full expansion by irradiating it with blue light (459 nm) but both structures actuated mildly under red light (622 nm) due to the absorption of **SBII**, which was embedded in both. Employing this new developed approach, LC microsystems showing a selective response at different wavelengths was achieved for the first time.

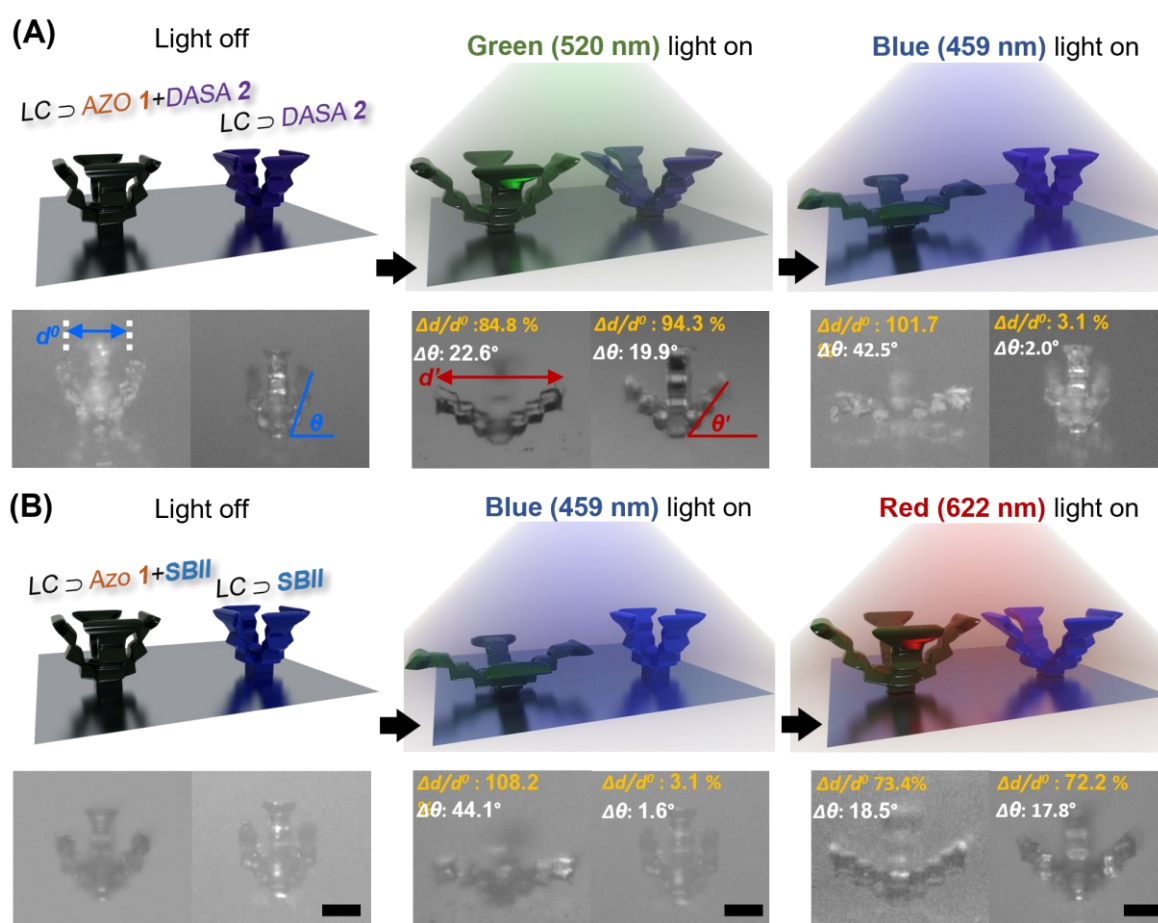


Figure 3.11 Wavelength-selective actuations among the LC bifunctionalized microstructures and the monofunctionalized ones, including LC  $\supset$  **Azo 1+DASA 2** and LC  $\supset$  **DASA 2**, as well as LC  $\supset$  **Azo 1+SBII** and LC  $\supset$  **SBII**, depicted in both 3D models and microscope images. The lateral expansion and bending angle differences from the pristine “closed” state (light off) to the actuated “opened” state (red/green/blue light on) were measured from the side view for each actuated structure ( $N = 3$ ). All scale bars represent 25  $\mu\text{m}$ . Figures adapted from Ref [129].

### 3.3 Summary

In this chapter, two strategies for expanding the variety of light-driven LC microstructures were explored. In particular, special attention was paid to the implementation of photoresponsive properties into the 3D printed LC matrix that are distinct from the class of azobenzenes, allowing the tunability of the structure by light in a longer wavelength regime. Multifunctional structures whose properties could be selectively tuned with different colors of light were also generated in this chapter.

The first approach followed the conventional strategy of utilizing exemplary azobenzenes in 2PLP, meaning that the implementation of photoresponsiveness relies on the incorporation of acrylate-functionalized dyes into a printable LC ink. However, by incorporating new photoabsorbing materials (dyes) for use in 2PLP, two major challenges were faced: (1) When light was used for two purposes of achieving microprinting and triggering the responsive properties, competition between the dye and photopolymerization has to be avoided. (2) Selection of the emerging material fitting into multiple conditions, including the compatibility with the LC ink, the ease of synthesis, and absorption in a regime outside the range of azobenzenes, was limited. To address these challenges, a new class of photoswitch, donor-acceptor Stenhouse adduct (DASA), which attractively has strong absorption band solely located in a narrow green light regime (570-590 nm), was considered as a good complementary role to azobenzene. The synthesis of two differently substituted DASAs (**DASA 1/2**) was pursued, with one of them also modified with acrylate groups (**DASA 3**). Meanwhile, with the substitution of electron donating and withdrawing groups, azobenzenes with (**Azo 1**) and without (**Azo 2**) acrylate functionalization, which absorb the blue light regime, were synthesized. Despite the great photoresponse and orthogonality between Azo and DASAs allowing for selective control of each photoisomer in solution efficiently using three different wavelengths (385, 433, and 592 nm), a severe obstacle to manipulate the LC alignment was found to be the poor miscibility between DASA molecules with the LC ink, hindering the fabrication of LC structure with DASA functionalization.

A new approach was developed to overcome these challenges on the fabrication of light-responsive 3D microstructures by post-modifying the polymerized (printed) LC network. Namely, photopolymerization was first carried out to polymerize a transparent LC formulation with a predetermined alignment profile. Thereafter, a dye solution was used to incorporate the

dye molecules into the polymer via diffusion. A secondary post-curing step with UV light (385 nm) irradiation was performed to further polymerize the network for encapsulating the deposited dye molecules. The feasibility of this approach was first proven in one-photo polymerized LC films by incorporating the synthesized dyes. In this case, not only azobenzenes but also DASAs were embedded in the film with the programmed LC alignment preserved. Importantly, it was observed that successful functionalization could be achieved by employing **Azo 2** and **DASA 1/2** without crosslinkable groups, affording photoactuators of the incorporated films under either blue (458 nm) or green (592 nm) light irradiation. This post-modification approach has been successfully applied in the fabrication of photoresponsive LC microstructures via 2PLP, by replacing the use of dye solution with a dye/E7 dispersion to reswell and penetrate the dye molecule into the printed structures. This approach overcomes the limitations and restrictions of dye use attributed to the 2PLP technique and LC formulation, providing a major advantage over the conventional approach. To demonstrate the flexibility of this new strategy, a commercially available dye, **SBII**, which absorbs red light (650 nm), was employed along with other synthesized dyes, affording the fabrication of five kinds of photoresponsive LC microstructures exhibiting absorptions extending throughout the visible spectra (400–700 nm).

The structures functionalized with dye using this new approach were characterized in detail with various techniques. Raman spectroscopy confirmed the possibility to use an uncrosslinkable dye (**Azo 2**) for functionalization, which was not the case through the conventional approach. Additionally, double bond conversion (DOC) evaluation revealed that LC structure printed with lower exposure dose (low laser power or high scanning speed) resulted in a less crosslinked network, allowing more dye molecules to penetrate. A higher increase of DOC was reached after the final UV treatment. Moreover, the analysis of the dye integral ratio pointed out another advantage of this approach, which enables the degree of functionalization to be easily tuned based on the concentration of the dye/E7 mixture, surpassing even the highest degree achieved by structures fabricated with the conventional method. Furthermore, the homogeneous distribution of dyes within the entire incorporated structures was verified with confocal microscopy and Time-of-Flight Secondary Ion Mass Spectrometry (ToF-SIMS), based on the fluorescence signal (**DASA 1**) or characteristic fragment ions (**DASA 2** and **SBII**), respectively.

With the utilization of this new approach, microactuators were printed via 2PLP and implemented with five different dyes individually. By switching their absorbing light on and off, a reversible gripper-like motion was observed for all structures, each with their own photoresponse characteristics such as amplitude of expansion and recovery time. To further demonstrated the versatility of this approach, bifunctionalized microactuators were fabricated for the first time, by implementing two dyes simultaneously– **Azo 1 + DASA 2** or **Azo 1 + SBII**. As compared to the monofunctionalized ones, it was evident that selective activation of one of the implemented features was achieved by using either red, green or blue light. The flexibility and versatility of this emerging approach have paved the way to diversify the functionalities of the 4D microprinted smart systems in the future.



## **Chapter 4.**

# **Tailoring Liquid Crystalline Alignment of 4D Microstructures via PDMS Confinement**

## 4.1 Motivation and aims

Moving forward with the design and 4D microprinting LCE structures, my next aim is to break the obstacles of LC alignment to enable straightforward programming. As mentioned in Chapter 2, the limitation on the adaptivity of the alignment approach for 2PLP hinders the versatility in complex actuation patterns. The conventional surface alignment method, which is still a dominant approach to fabricate stimuli-responsive LCE microstructures, enforces a universal alignment profile into all printed parts throughout the substrate, resulting in only single actuating pattern depending on the alignment cell. Due to this limitation, often a tedious modular fabrication process was necessary to achieve bidirectional actuation among the fabricated structures. This process involved reorienting and reassembling the printed modular blocks manually under a microscope according to the desired actuating pathway.<sup>[115-116]</sup> Although the implementation of cholesteric liquid crystal into the LC formulation assisted with self-assembly and allowed for the use of alignment surfaces to be neglected, the fact that all printed structures shared the same cholesteric phase remained unchanged.<sup>[128]</sup> The challenges of achieving high flexibility in reorienting the director three-dimensionally of the LC ink during the printing process had not been overcome, until my collaborator Alexander Münchinger reported a printing setup in 2021 using a cell containing self-built electrodes.<sup>[88b]</sup> By varying the orientation of the applied electric field, we were able to achieve high flexibility in reorienting the director three-dimensionally of the LC ink during the printing process *in situ*. Using the post-functionalization presented in Chapter 3, we reported optomechanical metamaterials that were equipped with complex three-dimensional alignment patterns. These materials allowed for the switch of their Poisson's ratio or sign of the twist per strain triggered by light.<sup>[119]</sup> Despite the custom device offered a great opportunity to fabricate emerging LCE structures in 4D, it also has some drawbacks due to the complex and high cost procedure of self-building the electrode system, and therefore, it was not user-friendly to the whole community of LCE microprinting. Other deposition-based printing technologies, such as DIW, have been employed to introduce LC alignment along the printing direction, allowing the printing pathway to determine the actuation pattern, as discussed in Chapter 2. However, these fabrication methods have a resolution limit at the meso-scale, restricting the applicability of printing high-end microactuators. As a result, my next step was to develop an approach that enable to manipulate the LC orientation easily and diversely for 2PLP, not necessarily with high precision in each slicing layer, but with the ability to adapt the actuating direction of the printed LCE actuators freely in "one go" without relying on alignment surfaces.

Among all the alignment methods, the PDMS confinement method is particularly attractive due to its low cost and ease preparation. As mentioned in Chapter 2, using PDMS micro-molds has been a promising LC alignment method that can achieve homogeneous LC alignment based on the geometry of the mold. This is due to the unique properties of PDMS, including its high hydrophobicity and low surface free energy, which make it a reliable material for anchoring the vector of LC molecules. Although this alignment method has been extensively studied in soft lithographic techniques, it has yet to be exploited in fabricating LC 3D structures. On this basis, the aim of this project was to achieve various liquid crystal alignments within the micrometer range. The investigation was started with creating the PDMS confinement cavities. Unlike the conventional micro-replica molding method, in this project, 2PLP was utilized to customize PDMS with various geometries on a substrate. Next, a liquid crystalline material, E7 mixture (also used as "solvent" in the printable LC inks), was employed to proof the effect of the fabricated PDMS structures. POM was used to evaluate the PDMS-induced alignment effect. After achieving alignment modulation within the X-Y plane of the substrate, the possibility of programming the LC alignment at arbitrary positions within 3D was explored. Last, the applicability of this alignment approach was demonstrated by replacing E7 by polymerizable LC inks, so that the fabricated LC microstructures and their responsive behaviors within distinct PDMS environment were analyzed.

## 4.2 Results and discussion

### 4.2.1 Fabrication of PDMS microcavities

In a first step, the fabrication of PDMS 3D microcavities was investigated and optimized. In contrast to the conventional micro-replica molding method, the use of 2PLP technique for customized 3D micropartitions was pursued. 2PLP offers the advantages not only on avoiding multiple complex and time-consuming procedures of the conventional approach, including mixing the PDMS based resin and the curing resin, fabricating master mold, handling fragile PDMS micro-molds and suffering from the surface inhomogeneity, but also allows for spontaneous fabrication of microstructures with arbitrary geometry. In fact, multiple PDMS microstructures printed via 2PLP, including microfluidics,<sup>[137]</sup> microelectromechanical systems (MEMS),<sup>[138]</sup> soft robotics,<sup>[139]</sup> and superhydrophobic surface,<sup>[140]</sup> have been reported with high structural precision, low shrinkage ratio (<10%) and great surface smoothness by using the a commercially available photoresist, IP-PDMS (Nanoscribe GmbH).<sup>[137]</sup> Due to the soft elastomeric properties of PDMS, successful printing by using a 25× oil objective (NA = 0.8; WD = 380 μm; Zeiss) was achieved by using two sets of printing parameters: densely crosslinked contour layers were first printed as a “shell” of the designed model with a slow scan speed (20 mm s<sup>-1</sup>, 30 mW), followed by filling the interior with a higher printing scan speed (100 mm s<sup>-1</sup>, 40mW). This printing protocol ensured a good structural stability and adhesion during the development step in isopropanol. The printable dimensions of a solid PDMS block ranged between 10 and 100 μm in width or height. It is noteworthy that printing either solid and bulky structures (e.g., length > 100 μm) or delicate overhanging structure (e.g., width < 10 μm) was challenging. This is due to the swelling properties and softness of PDMS resulting in structures possessing high surface tension between the substrate or the lack of mechanical stability, and hence detached from the substrate or collapsed. As a result, optimizing the surface-to-volume ratio was a critical aspect to perform successful microprinting PDMS structures.

### 4.2.2 LC alignment based on PDMS confinement

After optimizing IP-PDMS for microcavity fabrication, the next step was infiltrating a LC material into the PDMS structures to investigate the LC alignment effect. For this, the classic liquid crystal, E7, was used as a reference to prove this concept. In addition, few adaptations to

the microprinting procedure were made for this purpose as well as for achieving PDMS/LCE multi-material printing thereafter. In detail, the samples for PDMS microprinting and alignment investigation were conducted with a procedure including the following steps: first, a glass slide which can introduce LC homeotropic alignment was prepared by spin coating a polyimide layer (SE-5661, Nissan Chemicals, see Experimental section). The purpose of having the majority of LC molecules pointed out of the surface is to generate a dark, non-birefringent background under the POM regardless the sample orientation, so that once the aligning vector was disturbed by the PDMS and no longer perpendicular to the substrate, the resulting light leakage would be clearly identified. Next, a drop of IP-PDMS was used to print PDMS structures on this functionalized glass slide via 2PLP. A sandwich glass cell was soon fabricated together with another piece of polyimide coated glass after the development step with the PDMS-printed substrate. Afterwards, the liquid crystal mixture E7 was infiltrated into this glass cell at 65 °C which was above its glass transition temperature and then the cell was cooled down to 35°C gradually with a cooling rate of 0.5 °C/min. The liquid crystal alignment was then observed under POM.

Herein, attempts to induce two typical of LC alignment, the planar alignment and radial alignment, by utilizing the PDMS structures were investigated. For this purpose, the geometry of the PDMS structures was optimized as "PDMS channels", mimicked by two parallel PDMS partitions, or "PDMS wells", where a cubic structure contains a cylinder cavity, to respectively induce these alignment patterns. The alignment effect in regard to the dimensions of these geometries is addressed in the following section (Figure 4.1).

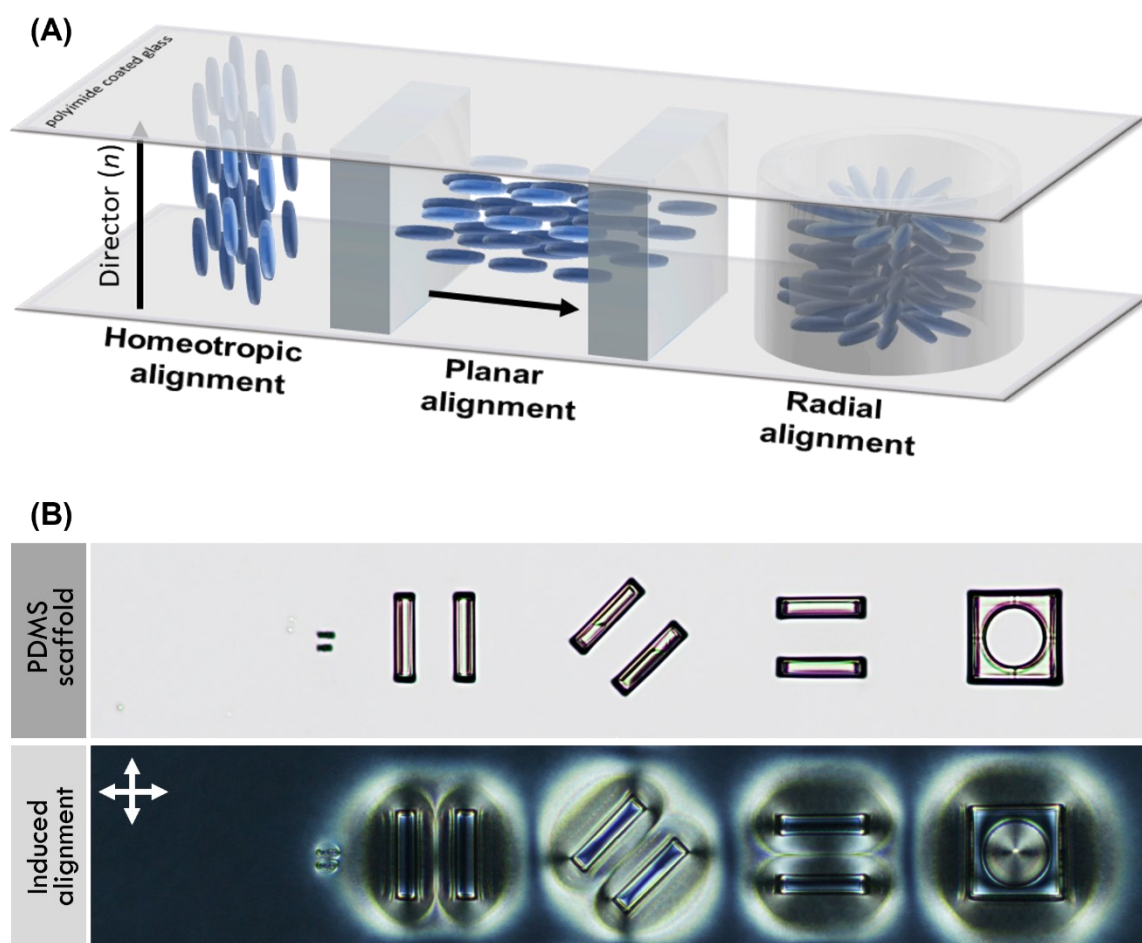


Figure 4.1 (A) Schematic illustration of using PDMS confinements to induce LC domains. (B) Microscopic image of the PDMS scaffold used for LC confinement printed on a polyimide coated glass (top) and POM images of their aligning effect with the infiltrated E7 (bottom).

### Planar alignment

A first attempt of using PDMS microstructure to modulate the LC alignment was carried out by printing two PDMS partitions mimicking “PDMS channels”. For this, E7 was infiltrated and temperature programming was carried out for realignment. Under the POM, when the PDMS partitions were parallel to the polarizer, the overall image appeared black, due to the homeotropic alignment layer of the glass cell, but concentric patterns were observed surrounding the PDMS structures in dark shade. This was attributed to the low surface energy of PDMS showing a repelling effect to the LC molecules. On the other hand, once the sample was rotated 45°, bright colors of the birefringent bands around the PDMS partition were observed, evidently showed that the orientation of the liquid crystal molecules around the

PDMS was no longer perpendicular but parallel to the glass substrate. This observation revealed that the PDMS surfaces which were perpendicular to the substrate were able to interfere with the LC director. Despite the coexistence of the polyimide alignment layer, the lower surface energy of PDMS than the polyimide layer led the LC molecule favorably redirect into the anchoring vector of the PDMS.<sup>[105]</sup>

To further investigate the relationship between the range of alteration to the PDMS geometry, pairs of PDMS microchannels along the Y-axis with constant partition thickness (20  $\mu\text{m}$ ) and length (100  $\mu\text{m}$ ), varied either in height ( $H$ ) or the channel width ( $W$ ) were printed (Figure 4.2A). Liquid crystalline solvent E7 mixture was infiltrated into these PDMS microchannels and POM images were taken while having the channels placed 45° to the crossed polarizers (Figure 4.2B). The optical density ( $OD$ ) within the microchannels was obtained by using the image processing software ImageJ and then plotted against the aspect ratio  $\eta = H/W$ <sup>[109]</sup> of the PDMS channel microchannels as shown in Figure 4.2C. When width ( $W$ ) remained constant, the analysis reflected that the aspect ratio  $\eta$  higher than 0.67 was required to achieve a successful long-range parallel alignment within the PDMS channels. In detail, once the channels were printed with the width of 30  $\mu\text{m}$  and height of 10  $\mu\text{m}$  ( $\eta = 0.33$ ), the birefringence of the channel center remained dark due to the pristine vertical alignment and hence the high mean  $OD$  value; once the height has increased to 30  $\mu\text{m}$  ( $\eta = 1.0$ ),  $OD$  has significantly decreased from 1.5 to 0.8 due to the bright birefringence signal, indicating the disruption of homeotropic alignment. The  $OD$  value remained in a similar range even the height increased further. A similar effect was also observed in another corresponding experiment by expanding the channel while having the height ( $H$ ) consistent at 30  $\mu\text{m}$ . The mean  $OD$  remained in the same range of 0.5 to 0.6 when the width was below 50  $\mu\text{m}$  but increased by the factor of two once the width was above this. The observation in the second experiment also revealed that  $\eta > 0.60$  of the PDMS channel was necessary to induce homogeneous planar alignment.

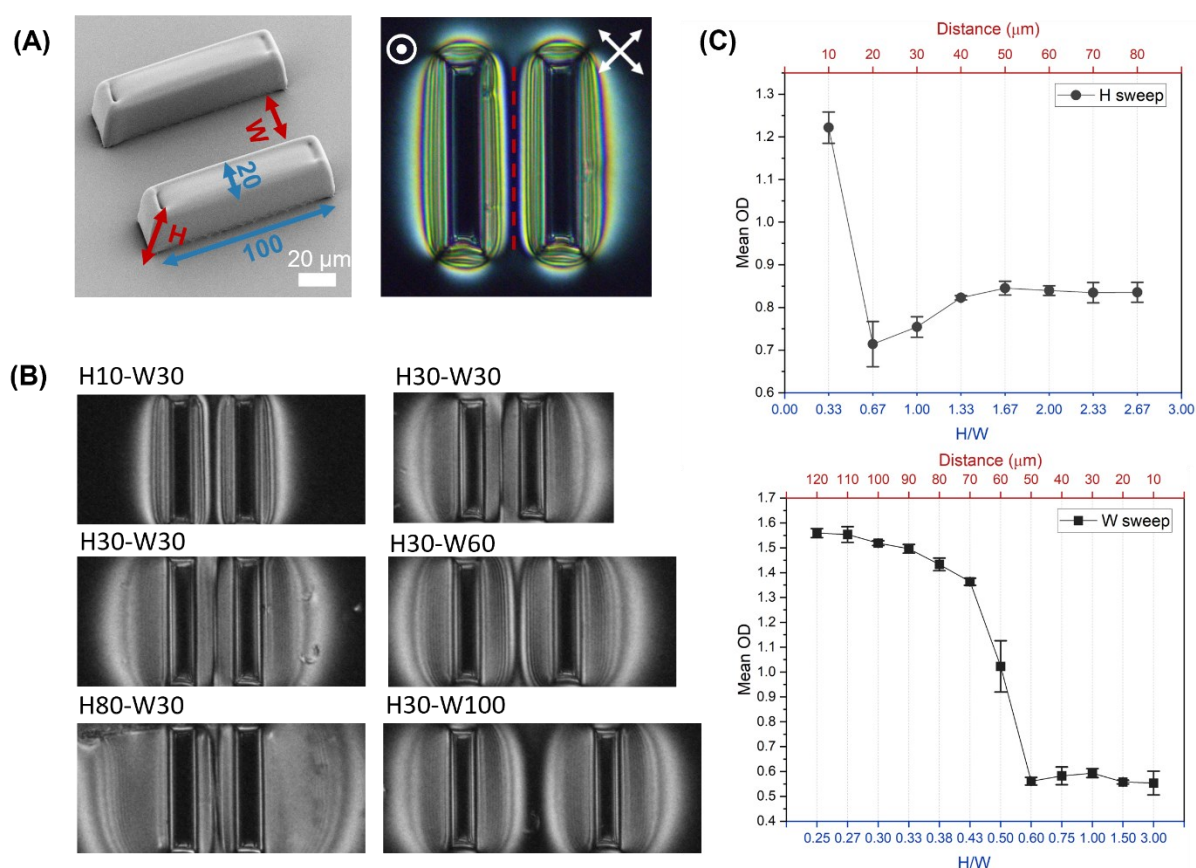


Figure 4.2 (A) SEM and POM image of a PDMS microchannel mimicked by two partitions and its alignment with E7. Red dash line indicates the position where the OD value was recorded. (B) POM images in gray scale of E7 aligned in channels with varied dimensions ( $\mu\text{m}$ ). (C)(D) Mean optical density recorded from PDMS channels plotted against their aspect ratio  $\eta$  and varied distances.

### Radial alignment

In addition to introducing planar alignment by fabricating PDMS channels, the possibility for enabling radial alignment has also been explored. For this purpose, PDMS microstructures were adapted to blocks containing cylindrical cavities (Figure 4.3A). Instead of printing a solid mesh around the well, it is worth mentioning that microtrenches, as the cross pattern along the X- and Y- axis shown in the microscopic images (Figure 4.3B), were designed at the bottom of the block for two purposes: (1) They reduced the interfacial tension between the PDMS bulk and the substrate preventing detachment due to swelling during the development and LC alignment. (2) In case of the presence of air bubble within the PDMS cavity, smooth infiltration of LC into the cylinder was ensured. With this structural adaption, the printable dimensions of

the blocks were further expanded, affording the printed cylindrical cavities had their diameter ( $D$ ) ranged from 50 to 190  $\mu\text{m}$  with a consistent height of 30  $\mu\text{m}$ , where E7 was infiltrated into.

Impressively, as shown in the POM images (Figure 4.3B), cylindrical birefringence was observed along the cavity wall. The concentric LC topography indicated that the vector of the mesogens were converted into a vertical anchoring fashion toward the PDMS surface. These birefringent areas also represented an "effective anchoring zone". Since the top and the bottom glass cell were coated with vertical alignment layers, once the intermolecular interaction with the anchored LC molecules was weaker than the one with the LC molecules which were outside of the PDMS cavity, it would preferably escape, either up or down, along the Z-axis. This phenomenon resulted into a black circle area in the POM images, which expanded larger along with the increased  $D$  of the cavity. Similar to the scenario of inducing planar alignment, converting the orientation of the LC molecules inside the cavity to homogeneous radial distribution can only be achieved within a certain aspect ratio of the PDMS cavity. To analyze this, OD profiles were acquired across the PDMS well diagonally to avoid the crisscross black brush texture. The OD values obtained at the LC-PDMS interface ( $OD_{bg}$ ) were served as background value and the differences from the OD value obtained within the cylindrical well ( $OD'$ ) were calculated ( $\Delta OD = OD' - OD_{bg}$ ). For the  $\Delta OD$  at the circular center, as if the cavity had full coverage of radial alignment, it would be a negative value; in contrast, as if an area in the cylindrical center was anchoring out the substrate with no light leakage,  $\Delta OD$  would be large above zero. As plotted in Figure 4.3C, cavities having diameter below 75  $\mu\text{m}$  were showing negative  $\Delta OD$  peak minimum at the circular center and those diameters above 100  $\mu\text{m}$  were having positive peak maximum. Thus, it could be anticipated that by using this procedure (E7 LC mixture together with IP-PDMS printed cylindrical cavity with a depth of 30  $\mu\text{m}$ ) the possible largest circular area of uniformly induced radial alignment located in the range of 4500 to 7850  $\mu\text{m}^2$  while having diameter between 75 to 100  $\mu\text{m}$ .

On the other hand, it was observed that the anchoring direction of LC molecules were highly dependent on the geometry of PDMS wall and the radial distribution was not only limited in a cylindrical fashion. For example, when the shape of the cavities was adapted into a triangular shape or even a more complicated flower shape, corresponding radial distributions were distinguished (Figure 4.3D). As a result, a sophisticated LC topography could be easily achieved by making use of the freedom on building versatile PDMS microcavities via 2PLP.

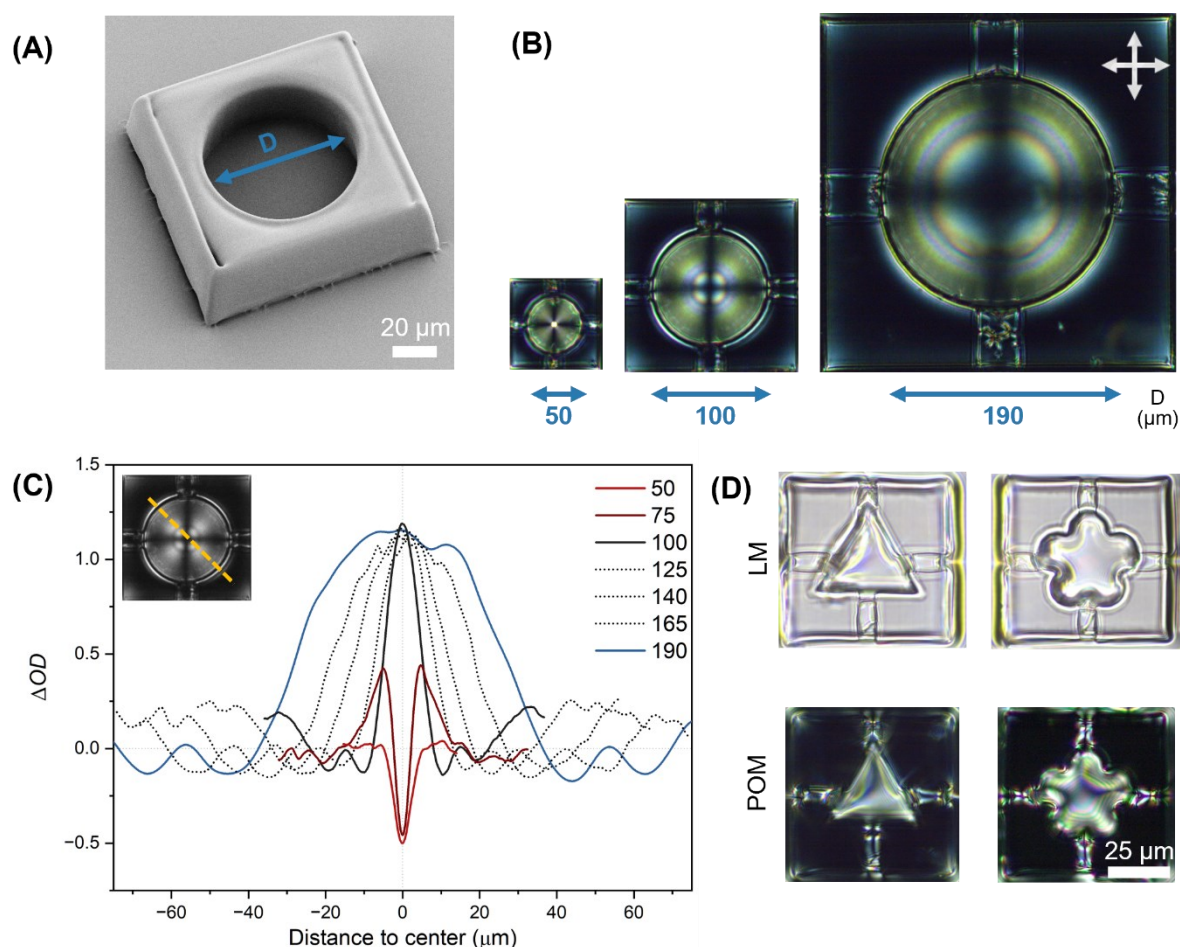


Figure 4.3 (A) SEM images of the PDMS cylindrical cavity. (B) POM images of E7 aligned in the cylindrical cavities with varied diameters ( $D$ ), where (C) the optical density ( $OD$ ) profile was recorded indicated by the inset. (D) Light microscope and POM images of PDMS cavities in triangular shape and flower shapes infiltrated with E7.

### 4.2.3 Alignment modulation along Z-axis

Having LC planar and radial alignment introduced by the PDMS cavities with geometrical difference within the X-Y plane, such alignment approach was further explored by altering the structural design in the third-dimension. For this, the height of the PDMS microchannels ( $W = 30\ \mu\text{m}$ ) and cylindrical cavities ( $D = 50\ \mu\text{m}$ ) were elevated along the Z-axis by adding supportive pillars beneath (Figure 4.4A, B). Interestingly, the radial distribution within the cylindrical cavity was still clearly observed even the cavity were  $30\ \mu\text{m}$  apart from the substrate (Figure 4.4C). For the microchannels, long-ranged planar alignment, showing black POM images when the channels were parallel to the polarizer but birefringent once rotated, was observed when they were vertically elevated less than  $7.5\ \mu\text{m}$ . However, once the altitude

increased, the POM imaging became challenging to determine due to the interference caused by the transitioning tilted LC molecules which were loosely anchored above and beneath the microchannels. Additionally, the PDMS microchannels attempt to bend toward the center when the height of the supportive pillar increased. This might be resulted from the bending of the soft pillars and hence causing uneven support to the PDMS partitions. Therefore, microscopic image for proofing the achievement of long-ranged planar alignment in higher altitude has yet been obtained.

To avoid those imaging inferences, the PDMS confining structures were adapted into a bulky block ( $90 \times 90 \times 90 \mu\text{m}^3$ ), where three kinds of PDMS confining cavities, i.e., cylindrical, triangular and floral cavities, were integrated with different altitude. As demonstrated in Figure 4.4D, the radial alignment in cylindrical was observed while the microscope was focused on the first layer. By altering the focus depth, radial alignment in triangular and floral fashions were sequentially observed. These observations revealed the novelty of this PDMS confining method, which has opened the avenue for implementing desired LC alignment freely in 3D.

#### 4.2.4 Tailoring alignment profile for LC microstructures

After demonstrating the long-ranged planar and radial alignment introduced by PDMS scaffolding microstructures, the possibility to apply this alignment method to LC microprinting for tailoring the alignment profile of the printed structure was explored. This is based on the fact that the predetermined alignment of a LC photoresist could be preserved by forming a polymeric network via 2PP as reported.<sup>[87]</sup> For this purpose, the E7 mixture was replaced with a LC ink. To characterize these induced alignment patterns based on their polarized images, it is necessary to develop a new LC ink with highly reduced shrinkage level to avoid optical interference led by structural deformation, since the LC ink used in the previous chapter for fabricating microactuators exhibited severe shrinkage due to a high content of E7 for affording soft and flexible mechanical characteristics.

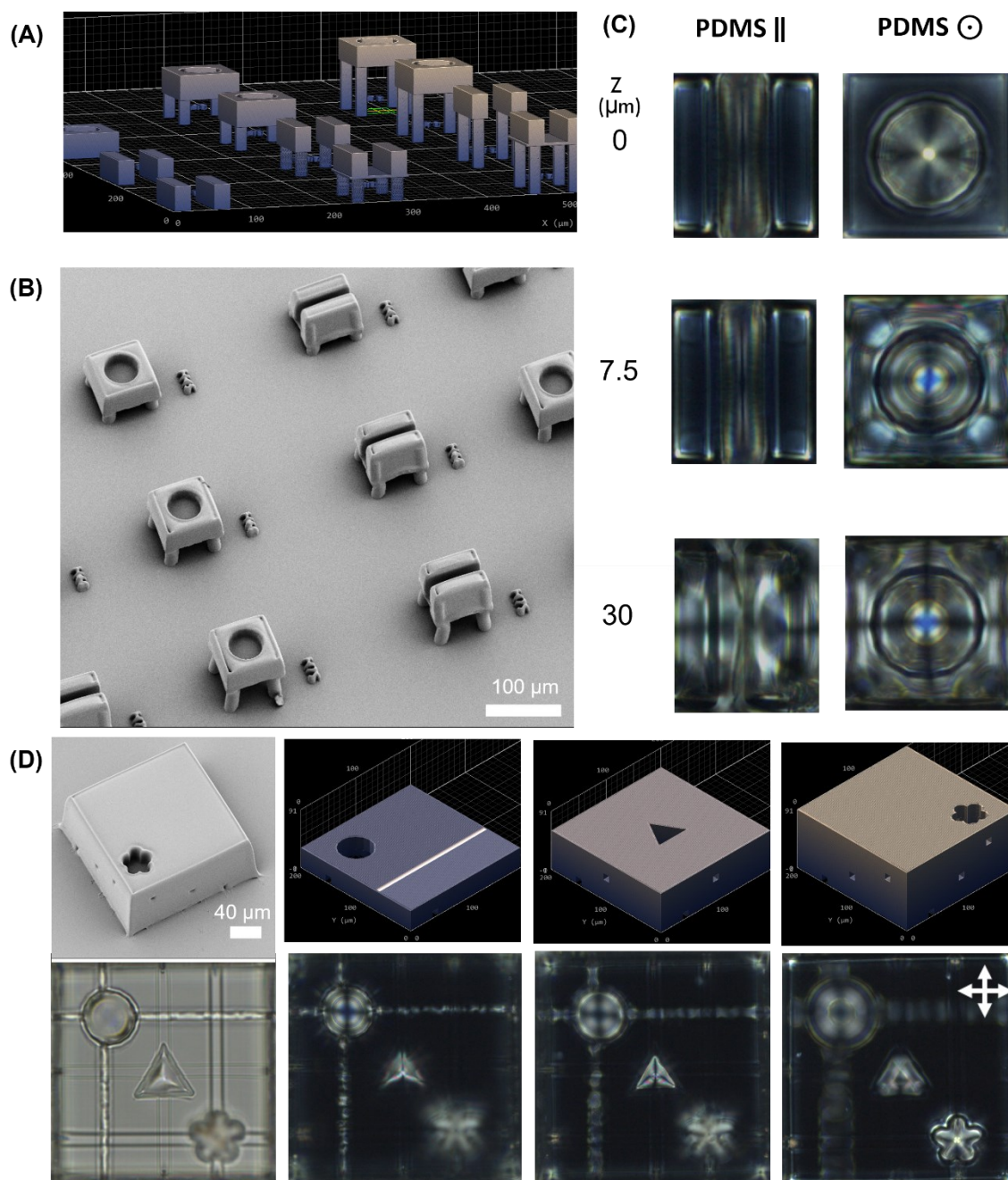


Figure 4.4 (A) 3D models and (B) SEM images of PDMS microchannels and cavities at different height. (B) POM images of PDMS microchannels (**PDMS ||**) and cavities (**PDMS ⊙**) which were printed on the substrate ( $Z = 0$ ) and in the height of  $7.5$  or  $30$   $\mu\text{m}$ . (D) SEM and light microscopic images of a PDMS block integrated with three microcavities in different altitude, shown by its 3D simulation of the printing process and its POM images taken with different focus depth.

Therefore, a new LC crosslinker, **C6BAPE**, which has high solubility in E7, was included into the formulation to reduce the usage of E7 and resulting in a negligible shrinkage level (Figure 4.5A, Table 4.1). Adapted from the previously developed two-photon printing conditions for LCE, a 63 $\times$  oil objective was continually used to create microstructures with high resolution. In comparison to the PDMS line printed with a 25 $\times$  objective, printing of accurate geometries below 10  $\mu\text{m}$  was not possible since the diameter of the voxel is three times larger than the one from 63 $\times$  objective (Figure 4.5B). The adapted LC formulation (**LC 1**) showed a great printability and wide fabrication window by altering the laser power 20–30 mW and printing speed 5–10  $\text{mm s}^{-1}$ . Moreover, it is noticeable that an increment slope of 5% on the laser power was critical to compensate the depleted laser power while printing through a birefringent structure whose thickness is more than 5  $\mu\text{m}$ , in order to keep the top surface from shrinking and causing optical interference.

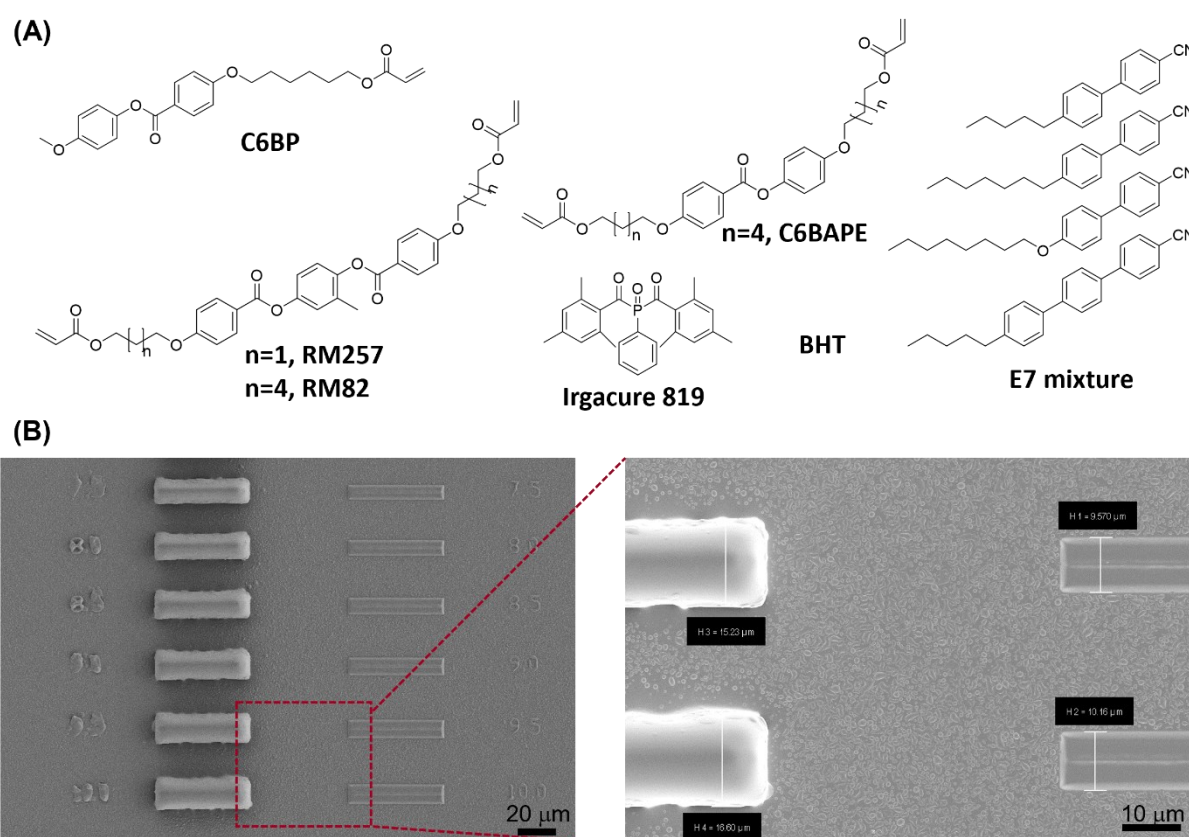


Figure 4.5 (A) Components of the new LC ink formulation. (B) Lines written with IP-PDMS (left, 25 $\times$  objective) and LCE (right, **LC 1**, 63 $\times$  objective). The line width ranges from 7.5 to 10  $\mu\text{m}$ .

Table 4.1 Compositions of LC inks.

#	%	C6BP	RM257	RM82	C6BAPE	Irg 819	E7	BHT
LC 1	wt	29.4	14.7	-	14.7	1.5	39.2	0.5
	mol <sup>†</sup>	56.0	19.0	-	20.7	2.7	-	1.7
LC 2	wt	29.4	7.4	7.4	14.7	1.5	39.2	0.5
	mol	56.7	9.6	8.4	21.0	2.7	-	1.7
LC 3	wt	29.4	-	14.7	14.7	1.5	39.2	0.5
	mol <sup>†</sup>	57.4	-	17.0	21.2	2.7	-	1.7

<sup>†</sup> Mole percentage was calculated without considering E7.

Following the same method used as before, the various alignment profiles induced by PDMS microstructures were also successfully observed at the LC microstructures printed within each confined environment. The LC microstructures demonstrated here were composed of an octagonal plate ( $50 \times 50 \mu\text{m}^2$ ) which was supported by a cylindrical post (diameter:  $10 \mu\text{m}$ ). The plate was positioned at a distance from the substrate ( $15 \mu\text{m}$ ) which corresponds to half the height ( $H$ ) of the PDMS partitions ( $H = 30 \mu\text{m}$ ). As demonstrated in Figure 4.6, from top to bottom, the degree of PDMS confinement was enhanced by adding increased number of PDMS partitions until forming an octagonal cavity. For LC structures within such confinement, the presence of the birefringence had transformed from completely black (zero degree of confinement), to rotated linear texture by having PDMS partitions side by side, and then eventually evolved into an octagonal texture radially extended from the center. Complex radial pattern of the cylindrical, triangular and flower shape observed with the E7 mixture were also transformed to the microprinted LCE structures by modify the plate geometries which fit in such PDMS cavities. This evolved alignment transition has highlighted again the emerging feature of this strategy that alignment patterning within the LCE structure can be modulated in a higher level of complexity and sophistication by the use of PDMS confinements which is not feasible in conventional alignment methods.

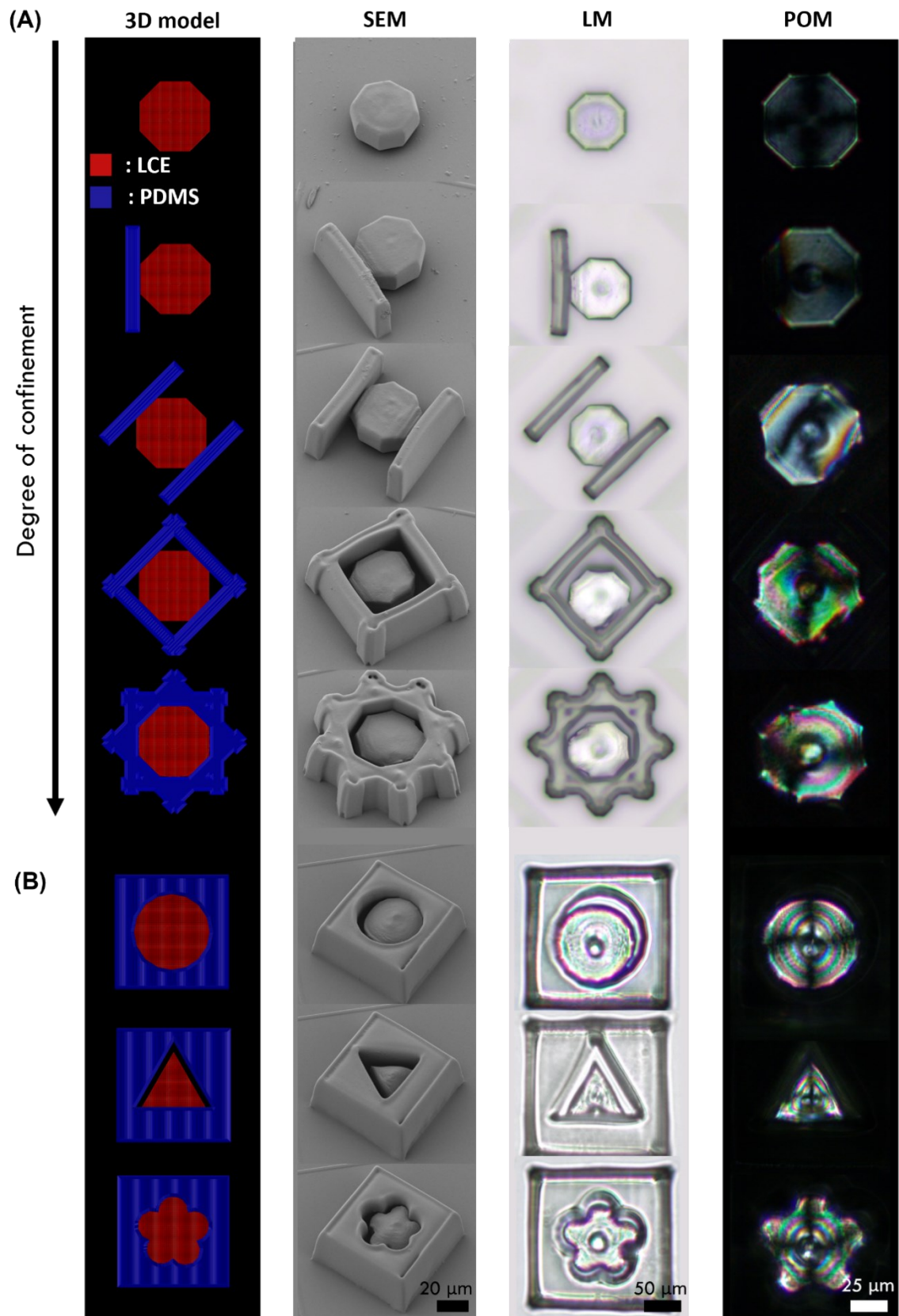


Figure 4.6 3D model (top-down view), SEM images, light microscope images (LM), and POM images (top to down) of LCE structures (**LC 1**) printed in PDMS cavities with (A) different degree of confinement or (B) cylindrical, triangular and floral geometries.

### 4.2.5 Investigating actuation behaviors based on PDMS induced alignment

Since the PDMS-induced alignment was proven with the POM images of static LCE structures, the PDMS scaffolding method had paved the way to advance the scope of 4D printing LCE microactuators. In the conventional alignment methods, the printed LCE microactuators in a same substrate were showing identical actuating behavior and direction due to the dependence of the predetermined alignment layers. Based on the observations described in the previous section, framing the PDMS scaffolds arbitrarily in space, geometry, or orientation, was anticipated to offer a flexible and versatile approach to induce planar or radial alignment to facilitate different actuating behaviors of the LCE structures printed within the scaffold. The investigation would first focus on inducing planar alignment to the actuators by fabricating the PDMS channels as shown, and then continued on the effect on radially aligned structures.

#### Planarly aligned LCE responsive microstructures

To carefully and quantitatively verify this assumption, simple and flexible pillar arrays were printed within three kinds of PDMS channels which were X-, Y-axes or diagonally orientated. The pillar arrays were constructed on a base plate with  $5 \times 5$  pillars with an optimized diameter of  $4 \mu\text{m}$  and with an overall dimension of  $20 \times 20 \times 20 \mu\text{m}^3$ . Along with this investigation, three kinds of LC ink, in varied combination of crosslinkers, were also prepared to explore the relationship between the chemical formulation and the PDMS-induced actuations. (Table 4.1) Pillar arrays were successfully printed by using all three kinds of LC inks based on the same optimized printing parameters (laser power of 22.5 mW with 3% slope increment and laser scanning speed of 7 mm/s). The actuating behavior of these pillar arrays were observed under a stereomicroscope equipped with a heating stage. Variation of the width and the length of the arrays between room temperature and at  $300 \text{ }^\circ\text{C}$  were recorded and analyzed.

The influence of the PDMS channels on the LCE pillars printed with formulation **LC 1** was clearly observed soon after the development. (Figure 4.7) For references pillars (without PDMS channels in the proximity, **PDMS x**), equally shrinkage in both X- and Y-axis occurred due to the homeotropic alignment created by the alignment surfaces on the glass cell. In contrast, pillars printed in the channel along the Y-axis (**PDMS ||**) exhibited a shorter edge along in the same direction from the top-down view. Such distinct shrinkage behavior revealed a director alteration within the channel. To be specific, LC ink within the channel reanchored between

two PDMS surfaces leading to a planar orientation between two PDMS walls and therefore resulted in a severer shrinkage perpendicularly to the adapted alignment. This phenomenon of modulating the LC ink director was ensured regardless of the orientation of the channels. Evidently, once the PDMS channel had the orientation in the X direction (**PDMS =**), the width of the arrays was much shorter in the X-axis in this case. On the other hand, when the channels were prepared in a 45° rotated configuration (**PDMS //**), the pillar array arranged in a diamond formation with the shorter diagonal paralleled to the channel. The actuation of these differently aligned LC microstructures was activated along the elevated temperature with a heating rate of 15 °C/min. After reaching 300 °C, the temperature remained constant for 30 min to ensure the actuation reaching the largest extent. Interestingly, for arrays in all three types of channels, the edges which were shorter at room temperature drastically expanded parallel to the channel orientation with a higher extent than the other sides, resulting in a rectangular or diamond shape wherein the previous longer or diagonal edge became shorter. As a result, three differently orientated channels led to three different actuating directions. By analyzing the horizontal and vertical expansion among these actuations, their behavior could be clearly differentiated. For clarity, I will first focus here on comparing the actuating differences between the pillar arrays within the vertical channels (**PDMS ||**) and the horizontal channels (**PDMS =**), followed in the end by the ones in **PDMS //**.

In case of the pillar arrays printed with formulation **LC 1**, the shape morphing behavior within and different PDMS channels were obviously distinct from the top-down view. As revealed in Figure 4.7, the vertical expansions of the pillar in **PDMS ||** were ranging from 20–50 % while the horizontal expansions were not above 20%. On the contrary, for the ones in **PDMS =**, the horizontal expansions were also much larger than the vertical ones. In comparison to the pillars without the PDMS confinement, their pristine homeotropic alignment led to actuation which was symmetric, i.e., showing same extent of vertical and horizontal expansion. These three clusters of actuating behavior were depicted in Figure 4.7C by their 90% confidence ellipses, while there were barely overlaps between these three clusters. However, when the LC ink was switched the formulation **LC 2** and **LC 3**, the difference between these three clusters significantly decreased for **LC 2** and confidence ellipses closely overlapped in the case for **LC 3**. These might be attributed to structural differences between RM257 and RM82. In other words, the steric hindrance of the longer alkyl chain of RM82 could create a larger spatial distance between each aligned mesogen within the polymerized network than in RM257. Therefore, the mesogens with converted orientation at each PDMS surface could not

effectively propagate the adapted alignment inside of the entire channel volume due to weaker intermolecular interactions. These observations revealed that a LC ink with lower steric hindrance at the polymerizing position would be more in favor for this method using PDMS scaffolds

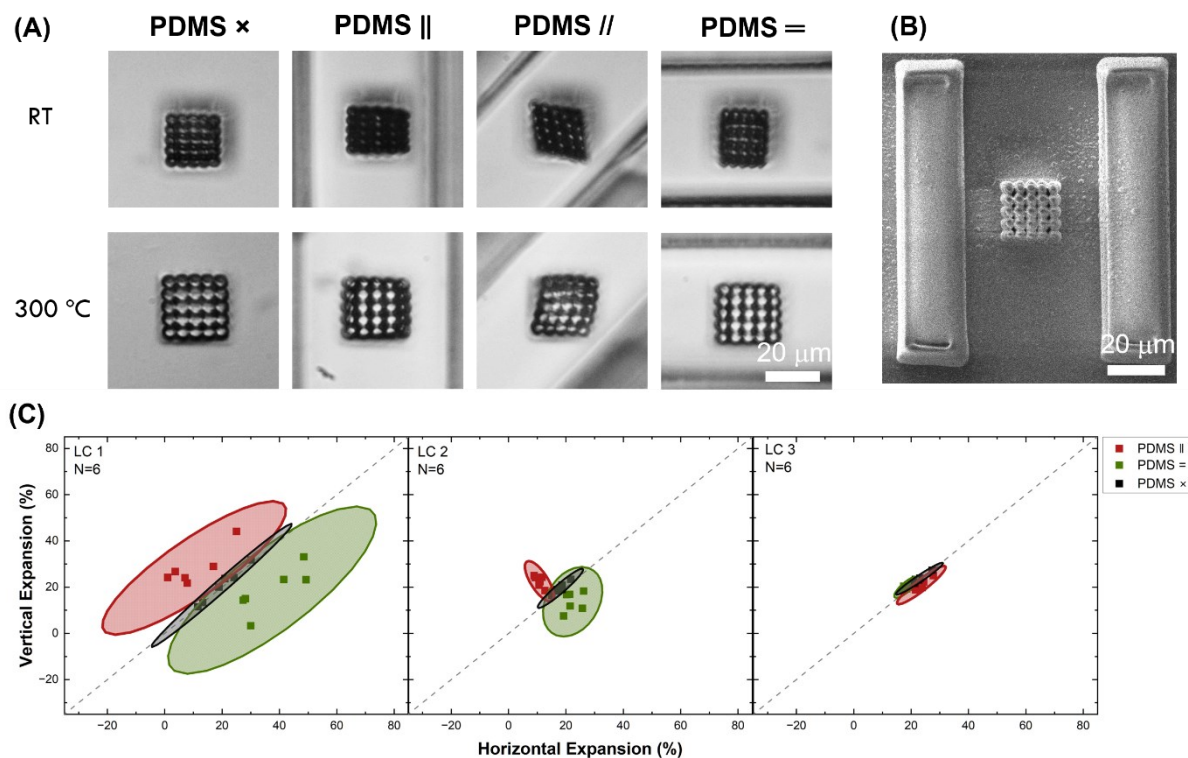


Figure 4.7 (A)(B) Actuation of the LCE pillar arrays (**LC 1**) with the pristine form and the ones in varied PDMS channels. (C) Vertical expansion of the activated LCE pillar arrays printed with varied LC inks, plotted against with their horizontal expansion. The ellipses were defined by their 90% confidence region ( $N = 6$ ).

Moving on now closely to the pillars in **PDMS //**. As mentioned before, the impact of the PDMS channels on the pillars was no longer fixed to the X- or Y- axis since the orientation was rotated. The resulting shrinkage and the expansion led to a morphing behavior between two diamond shapes for the diagonal orientation. The changes of their four corner's angles were unambiguous unlike the pillars in **PDMS ∥** and **PDMS =** which remained orthogonal during the actuation. The round shaped pillars made the angle measurements of these corners challenging. Therefore, to investigate this behavior in detail, here I designed another gripper-like LCE actuator with a dimension of  $40 \times 40 \times 30 \mu\text{m}^3$ . (Figure 4.8A) The gripper equipped with four freely rotatable arms with origami features in order to facilitate the observation of

their actuation and also provided sharp arm tips as tracking markers from the top-down view. As shown in the microscopic images in Figure 4.8B, the **PDMS //** channels also skewed the grippers diagonally. Instead of an orthogonal cross as the programmed model, the developed gripper had two arms close to each other aiming each side of the PDMS surface. This means the angles facing the wall respectively developed an acute angle while the angles toward the open ends of the channels were both obtuse. Along the heating process, the gripper showed a scissor movement having the arms pointed to the open end of the channel. At this point, the angles facing the wall became obtuse while the angles between two arms were acute. The scissor motion was observed in a reverse order and eventually recovered back to the previous state once the temperature cooled down. The level of this actuation movement was quantified by the change of the angle ( $\theta$ ) between two gripper arms, defined by two lines which were connected by the arm tips of the opposite arms respectively (Figure 4.8C). As revealed in Figure 4.8D, the grippers printed with **LC 1** showed the highest amplitude by having 24° difference before and after activation, followed by the **LC 2** printed ones with 18° difference and the **LC 3** printed ones which showed the mildest scissoring motion with only 8° difference. Their distinct level of PDMS induced motion was similarly consistent to the observation of the pillars within **PDMS ||** and **PDMS =**. Interestingly, those motions were remarkably differed from the grippers without PDMS confinement whose arms kept orthogonal during the activation cycles.

It is worth mentioning that these PDMS-induced actuations were also observed in a reference experiment in which the same PDMS/LCE bimaterial structures were printed on a glass without alignment layer coating, confirming that these PDMS-orientated actuations resulted solely from the effect of PDMS on the LC ink.

### **Radially aligned LCE responsive microstructures**

The next part of this section will move on exploring the effect of PDMS induced radial alignment. With this aim, PDMS wells were printed first thereafter LCE grippers were printed at the center of the cylinder cavities which were 75  $\mu\text{m}$  wide and 30  $\mu\text{m}$  in depth, annotated as **PDMS ⊙**. At first, while the pristine ones without confinement shown exceptional 39–57 % of area expansion upon activation, noticeable geometrical change of the grippers was not observed within **PDMS ⊙** under the stereomicroscope. Besides, not much information could be obtained due to instrumental limitation.

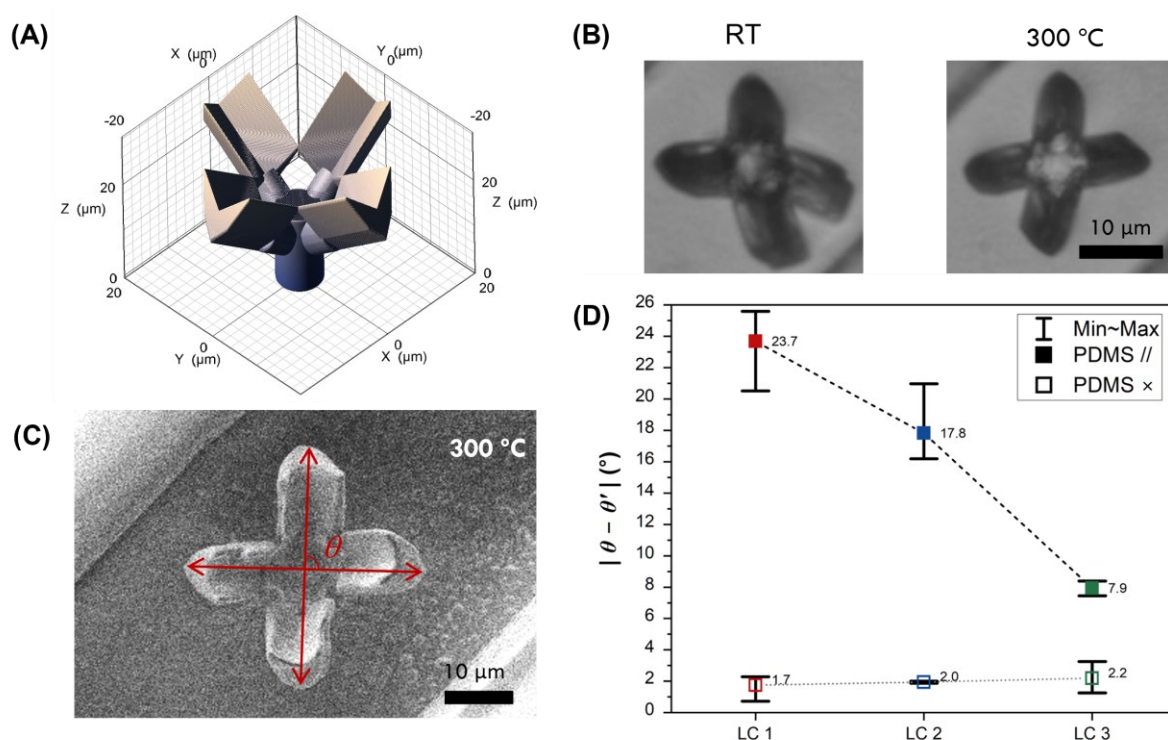


Figure 4.8 (A) 3D model, (B) SEM and (C) light microscopic images of the LCE gripper. (D) Angular difference of grippers inside the rotated PDMS channel and the ones outside printed with three kinds of LC formulation.

In order to achieve a more detailed investigation, the actuation experiments were also carried out under a scanning electron microscope which was equipped with a heating stage. For this purpose, these microstructures were not sputter coated with any metal for avoiding suppression on the actuation, and therefore, SEM images were taken in a much lower cycle time and thus lower resolution to minimize the charging effect so as the damage from the electron beam. After raising the temperature to 300 °C, this time, different motions of the gripper arms were noted between the ones in **PDMS** ⊙ and the ones outside of it (**PDMS** ×). Two parameters were determined to evaluate this: one was the width between the arm tips ( $d$ ), the other was the angle created by connecting the two angular edges next to the arm tip to the gripper center ( $\angle\alpha$ ) as depicted in Figure 4.9. For the case in **PDMS** ⊙, the SEM images showed a mild unfolding motion of the gripper arm accompanied with an 16% extended distance of  $d$ , while the angular measure  $\angle\alpha$  almost unchanged. According to the principle of similar triangle, the  $d'$  line was further away from the gripper center upon actuation, meaning the actuation pathway mainly focused on lateral expansion in X-Y plane by not having much

difference on the arm bending angle. In contrast, the parent gripper showed barely difference of their arm width upon actuation but with a narrower angle  $\angle\alpha'$ . Therefore, it suggests that the actuation pathway of the one with the parent homeotropic alignment was dominated by angular expansion, i.e., an unfolding fashion of the gripper from a "closed state" to an "opened state", as similarly observed in Chapter 3. This proves again the PDMS induce alignment flexibly to afford LCE actuators with tailored actuating behavior.

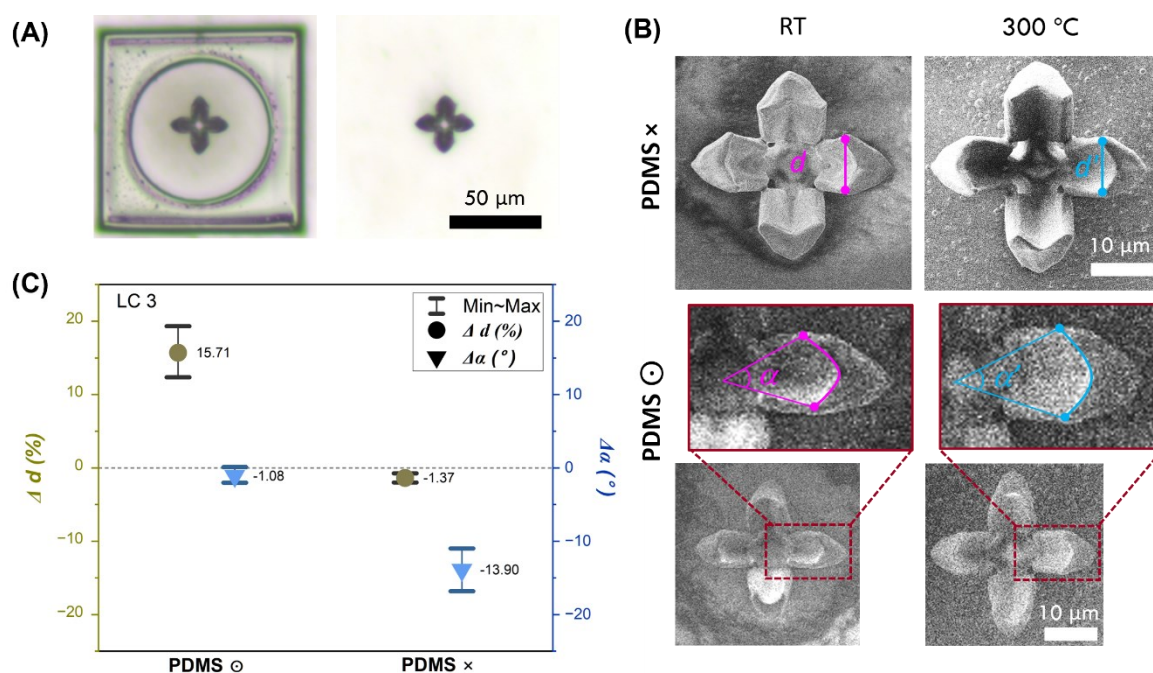


Figure 4.9 (A) Light microscopic and (B) SEM images of LCE grippers printed in or outside of a PDMS confining cylindrical cavity and (C) their parameter differences before and after actuation.

#### 4.2.6 Selective removal of PDMS scaffold

Having discussed how to construct LCE microactuators by implementing their alignment pattern and the resulted actuation behavior based on their PDMS microscaffold, the final section of this chapter addresses ways to selectively remove the PDMS structure without harming the LCE.

The structural designs of LCE actuators demonstrated in the previous section were kept in simple geometries for the purpose of image analysis but not for reaching the most impressive actuating performance, and therefore the PDMS channels had not become obstructions for

observing the actuating behavior even the pillar arrays reached a maximum  $\sim 50\%$  of lateral expansion. But one could picture that once this PDMS scaffolding method applied to a more sophisticatedly designed actuator, as the advanced gripper presented in Chapter 3 which could possibly reach a 108% of lateral expansion, optimizing the geometry of the PDMS scaffold in this case would be critical, because it has to reach both needs of fulfilling the aspect ratio  $\eta > 0.6$  and also offering enough free volume for the actuators to reach their full potential. In addition, having PDMS scaffolds tightly surrounding the actuators definitely would limit their potential on applications, while employing this method to facilitate the fabrication of 4D microrobotics is the main goal at the first place. Concluding those reasons, the removal of the PDMS scaffold definitely would be a key for improving the applicability and practicality of this alignment method in practice.

There were various methods reported on removing cured PDMS, including mechanical scraping<sup>[141]</sup>, solvent swelling<sup>[142]</sup>, dry etching<sup>[143]</sup>, or chemical treatment<sup>[141-142]</sup>. However, in order to selectively remove the PDMS microstructures, the applied etching method had to fulfill the requirement of (1) not attacking the micro-scale LCE structures or (2) the polyimide layer in order to keep the LCE part in contact to the substrate. Under this scenario, mechanical scraping and dry etching approaches were not applicable, since applying force to the PDMS channels manually with few micrometers' precision had high risk and long operational time for bulk samples, and dry etching methods, such as plasma treatment, would affect all the exposed polymeric surfaces, respectively. On the other hand, chemical removal of PDMS often relied on the use of strong alkaline solutions, such as NaOH or KOH alcohol solutions<sup>[144]</sup>, but also led to degradations of all kinds of polymer chains. As a result, since PDMS is a silicon-based polymer, the challenge here will be searching for a chemically selective organic etchant which could break down Si–O bonds but no other hydrocarbon bonds.

A quaternary ammonium fluoride, namely tetrabutylammonium fluoride (TBAF), was employed to etch out PDMS in transfer printing reported by Dahiya *et al.*<sup>[145]</sup> In detail, after PDMS acted as an intermediate carrier to transfer silicon microwires or ultra-thin chip from a bulk silicon wafer to the other flexible polyimide substrate, a dilute TBAF (1 wt%) solution was prepared with an aprotic solvent, propylene glycol methyl ether acetate (PMA), to immerse the wires at 50°C and remove the residues of PDMS with an etching rate of 1.5  $\mu\text{m}/\text{min}$ . This method of disrupting the PDMS polymer matrix was based on the breaking the Si–O bonds by forming

Si-F bonds with higher bond energy. Moreover, various evidence showed that successful removal of PDMS was achieved without damaging the polyimide substrate.

Based on this reported method, employing TBAF for etching PDMS 3D structures was exploited. In the first test, IP-PDMS was used to print 3D blocks, with dimensions ranged from  $50 \times 10 \times 10 \mu\text{m}^3$  to  $50 \times 20 \times 30 \mu\text{m}^3$ , on a polyimide coated substrate. Next, following the reported procedure, the developed PDMS blocks were immersed in the TBAF solution (1 wt%) at  $50^\circ\text{C}$  for 10 min and then shifted to pure PMA and IPA bath sequentially for 2 min each for removing the residual TBAF. The microscope images revealed that there were no PDMS block remaining attached but some dirt particles scattered around the surface (Figure 4.10A). By closely examine those dirt particles, their shapes appeared rectangular-like but bent, consisting of hard shells with partially disintegrated fillers (Figure 4.10A, inset). The dimensions indicated that they were the leftovers of the original PDMS blocks which suffered intensive shrinkage and degradation  $\sim 50\%$  from each side and their remained hard shells revealed that high density of the polymeric network afforded the contour layer a higher chemical resistance.

For a next step, the selectivity between PDMS and LCE of the TBAF etching method was examined. The same etching procedure was carried out with a polyimide coated substrate printed with PDMS and LCE lines with varied width  $0.5\text{--}10 \mu\text{m}$ . As the microscope images show in Figure 4.10B, there were no PDMS lines observed on the substrate after the TBAF treatment. In contrast, the arrays of LCE lines were retained, especially the ones with a width thicker than  $7 \mu\text{m}$  were scarcely affected. These observations revealed that LCE was not completely inert to fluoride ions but had a much slower degradation rate compared to PDMS matrix. As confirmed by the SEM images (Figure 4.10C), the LCE grippers remained in great fidelity and showed smooth surfaces even after the immersion in TBAF solution for 20 min and with an elevated temperature at  $70^\circ\text{C}$ . To this point, selectively removing the PDMS but not the LCE structures by using TBAF as etchant seemed to be a promising strategy. A preliminary examination was carried out by the same PDMS channels equipped with LCE micropillars or grippers. For etching out such a bulky PDMS mesh, it was observed that extending the immersion time or increasing the solution temperature was necessary to reach complete removal of PDMS from the substrate. However, harsher etching conditions also highly affected the structural stability of the LCE structures. The extent of influence highly depended on the geometry of the contact surface between the substrate and the structure. For example, the pillar arrays had a  $20 \times 20 \mu\text{m}^2$  base plate in contact with the substrate and no detachment was observed despite the

immersion in a heated TBAF solution at 80 °C. With the same condition, in contrast, the overhanging grippers resulted in distortion, bending, or dislodging. Since each of them were solely supported by a 10 µm wide post, such low contact surface to the substrate might resulted in a faster disruption of the posts and therefore the disruption of the grippers. As a result, while the PDMS partitions around the pillar array were fully removed successfully by etching at 80 °C, the optimized condition for the grippers was 70 °C for 10 min with the same concentrated TBAF solution. For this case, the remained PDMS parts intensively shrank and partially detached from the substrate.

Compared to the pristine stage after development, both LCE actuators appeared with a slight geometry change after the PDMS etching, transforming towards the actuated state. Besides, the extent of actuations was both drastically decreased till only 5–10%. These observations indicated that the LCE might release accumulated strain accompanied with an increase of isotropy under the heating condition in the presence of fluoride ion.

After learning from the preliminary investigation, structural modification for the PDMS partitions would be a promising approach to achieve an optimal etching result. Since one of the great advantages of fabricating microstructures based on 2PLP is the flexibility to construct geometries arbitrarily. Instead of a solid mesh demonstrated here, there are various possibilities to structurally modify the PDMS channels by (1) implementing hollow voids and breaking points or (2) reducing the contour thickness or density. By applying these methods on structural optimization, one could foresee the chance on achieving full removal of PDMS and maintaining considerable fidelity of LCE actuators under mild etching conditions.

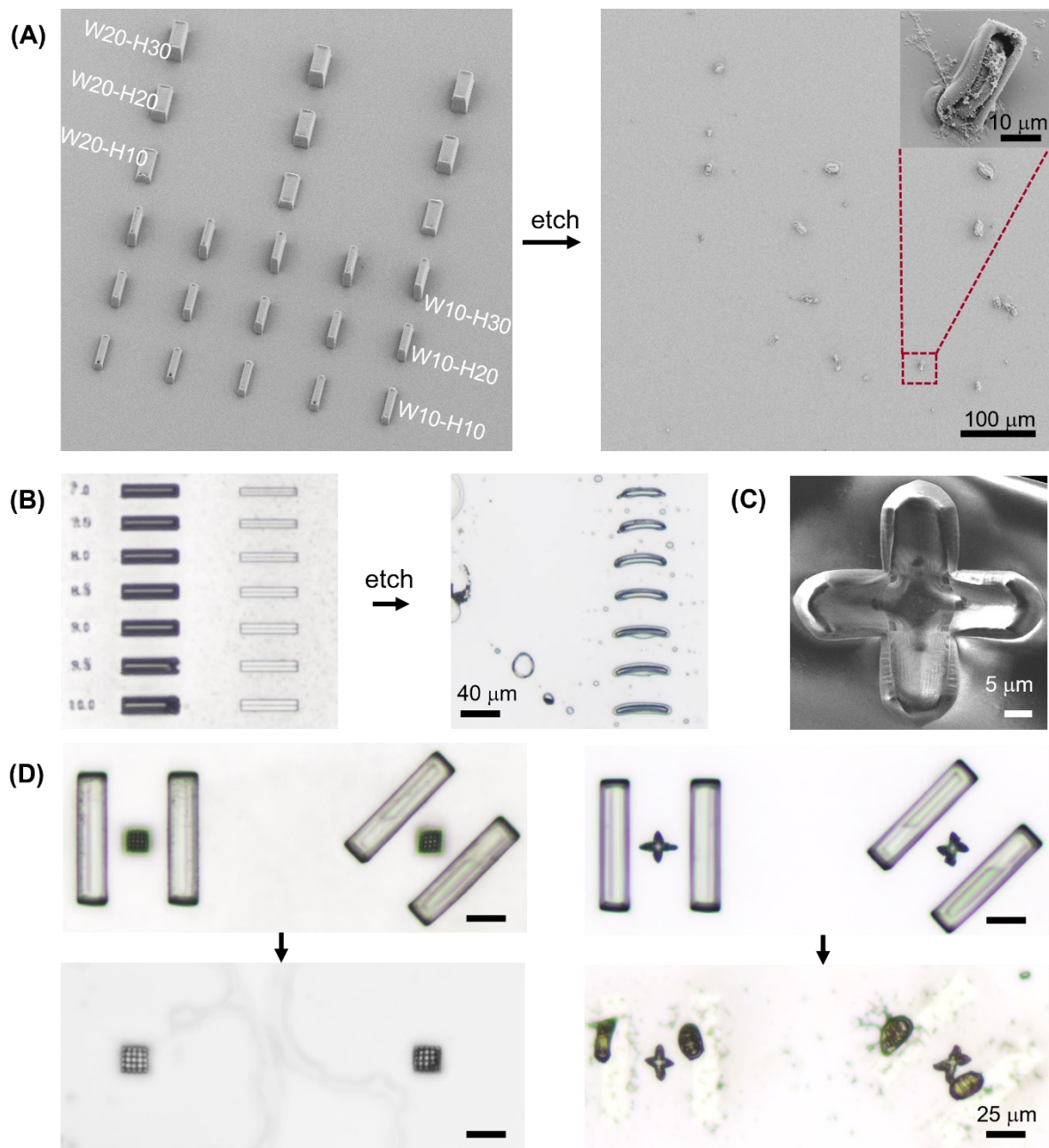


Figure 4.10 (A) PDMS blocks before and after the etching procedure by immersing in 1 wt% TBAF solution for 10 min at 50  $^{\circ}\text{C}$ . The dimension of the blocks shares the same length of 50  $\mu\text{m}$  and varied in width and height. (B) Selective removal of PDMS lines (left) against LCE lines (right) with width ranged from 7–10  $\mu\text{m}$ . (C) SEM image of a LCE gripper after the etching procedure. The structure was not sputter coated. (D) Comparison of the etching results between the LCE pillars immersed at 80  $^{\circ}\text{C}$  and the LCE grippers immersed at 70  $^{\circ}\text{C}$  for 10 min.

### 4.3 Summary

A facile approach for implementing LC alignment arbitrarily and in 3D was demonstrated. This approach was based on the utilization of the surface properties of PDMS which showed an anchoring effect to the LC molecules. In particular, the fabricated PDMS microstructures served as a confining cavity and enforced the LC director based of their geometries. This topic was investigated under two key aspects: One was the geometry dependence of PDMS structure in terms of inducing a long-range LC domain, and the other was the application of this method on 4D printing LCE microactuators based on the PDMS-induced alignment.

In the first part, the possibility of inducing planar alignment was demonstrated by constructing two paralleled PDMS partitions mimicking a channel. Those were exploited to convert the pristine homeotropically aligned LC molecules into a planar fashion, confirmed by polarized optical microscopy. To achieve a homogenous planar alignment, it was found that an aspect ratio ( $\eta$ ) between the PDMS channel width and height of  $>0.6$  was required to reach. In addition to inducing planar alignment, the focus was next shifted towards radial LC domain. For this purpose, PDMS wells were fabricated to let LC molecules anchor around the cylinder cavity to form a radial distribution. To be specific, the radial alignment was observed consistent until the diameter of the cylinder cavity was above  $75\ \mu\text{m}$  while the well depth was  $30\ \mu\text{m}$ . By keeping the dimension of the PDMS cavity with this specific ratio, the radial topology was not only limited to circular shape but also could be tailored based on the geometry of the cavity, such as a triangular or a flower shape. In addition, LC domain can also be spatially introduced in varied altitude along the Z-axis according to the height of such PDMS confinement structures. On top of inducing basic planar or radial alignment, complexity of the LC topology could be tailored based on the degree of confinement, showing a transition from the pristine homeotropic alignment, long ranged planar alignment, semi-radial alignment and finally a comprehensive radial distribution. More importantly, such alignment tuning approach of LC molecules was replicable with LC ink formulations that the PDMS-induced topology was retained in the two-photon printed structures.

The utilization of the LC anchoring effect from PDMS cavities was further exploited in the second part of this chapter in the direction of programming the alignment of the LCE microactuators and their resulted actuation. The influence of the programmed alignment was first verified with significant contrast between the LCE pillar arrays which were confined either

in a vertical PDMS channel or a horizontal channel. Particularly, these pillars exhibited a much higher degree not only of shrinkage after the development but also of actuation upon heating at 300 °C along the direction of the PDMS channel, unlike the unconfined pillars showed even degree of vertical and horizontal expansion at the activated state due to their pristine homeotropic alignment. Interestingly, the actuating motion of a freely rotatable LCE gripper confined within the PDMS channel was converted from an orthogonal contraction and expansion into a scissoring movement when the channel was rotated by 45°. These programmed actuating behavior with the use of PDMS channel were investigated with LCE actuators with three kind of ink formulation, varied in the ratio between crosslinkers with a shorter alkyl chain (RM257) or a longer chain (RM82). Higher dependence to the PDMS surrounding was observed for the ones printed with higher percentage of RM257. On the other hand, the activation of a radially aligned gripper was evaluated upon heat stimulus under a scanning electron microscope. The induced radial alignment resulted the gripper to undergo a lateral expansion in the X-Y plane instead of showing angular expansion by the parent gripper.

At the end, etching methods for selective removal of the PDMS were explored. A dilute TBAF (1 wt%) was found to be a promising candidate to remove the PDMS scaffolds after using them to manipulate the LCE printing. The degree of erosion on LCE structures depended on the etching temperature also the contact surface to the substrate. In the near future, reducing the polymer density of the PDMS scaffolds would be a key factor to achieve successful selective removal without affecting the LCE part by employing TBAF as an etchant.



## Chapter 5.

# Experimental Section

## 5.1 Materials

The chemical compounds used in this thesis were obtained from Sigma Aldrich or Fisher Scientific, unless otherwise specified. The specific liquid crystalline compounds, including 4-Methoxybenzoic acid, 4-(6-acryloyloxy-hexyloxy) phenyl ester (C6BP), 4-(6-(acryloyloxy)hexyloxy)phenyl 4-(6-(acryloyloxy)hexyloxy)benzoate (C6BAPE), 1,4-Bis[4-(3-acryloyloxypropyloxy) benzoyloxy]-2-methylbenzene (RM257), 1,4-Bis[4-(6-acryloyloxyhexyloxy)benzoyloxy]-2-methylbenzene (RM82) and the E7 mixture were supplied by SYNTHON Chemicals GmbH & Co. KG. IP-PDMS was purchased from Nanoscribe GmbH & Co. KG. No additional purification steps were performed on any of the materials prior to use.

## 5.2 Methods and procedures

### LC ink preparation

LC inks were prepared by having all LC components, a photoinitiator (phenylbis (2,4,6-trimethylbenzoyl) phosphine oxide, Irg 819) and a radical inhibitor (3,5-di-tert-4-butylhydroxytoluene, BHT) dissolved in a HPLC-grade solvent and mixed homogeneously. The solvent was continuously stirred at 80 °C under a nitrogen flow until the solvent was completely removed.

### Preparation of alignment surfaces

Prior to fabricating the alignment layer, microscope cover glasses measuring 22 × 22 mm<sup>2</sup> and with a thickness of 170 ± 5 μm (Marienfeld) were cleaned using sequential sonication in acetone and 2-propanol for 10 minutes each and then treated with a plasma cleaner (Harrick Plasma). For vertical alignment, 100 μL of polyimide (Nissan SUNEVER® SE-5661) was spin-coated on the glass surfaces at a rotation speed of 300 rpm for 5 s, followed by an acceleration to 4000 rpm for 20 s. The coated substrate was pre-baked at 80°C for 2 min and then post-baked at 220°C for 1.5 h min to allow polymerization. For planar alignment, 100 μL of 2 wt% polyvinyl alcohol (PVA) aqueous solution was spin-coated onto the glass at 4000 rpm for 1 min. The PVA film was solidified by pre-baking at 90°C for 1 min, followed by post-baking at 120°C for 1.5 h. In order to create microtrenches for planar alignment, the PVA film was rubbed unidirectionally on a velvet cloth five times by slightly applying pressure by hand. It was found

that velvet cloth served better on this purpose than cotton or silk cloth, which afforded the fabrication of parallel micortrenches without scratching off the coated layer. Nitrogen flow was used to remove particles and dust generated during the rubbing process.

### **Alignment cell construction**

The construction of the alignment cells followed previously reported methods.<sup>[89, 95]</sup> The cells were assembled with two coverslips, with each side of the alignment surfaces facing inward, and deposited with UV curable glue (Norland UV Sealant 91) at four corners. The glue was priorly mixed with soda lime solid glass microspheres (Cospheric LLC), with diameters of either 30  $\mu\text{m}$ , 50  $\mu\text{m}$ , or 100  $\mu\text{m}$  used as size standard particles to define the cell thickness. Two coverslips were pressed together and photocured for 1 min in an Asiga Flash UV chamber. To form homotropic alignment, two polyimide-coated glass coverslips were employed. On the other hand, PVA-coated ones were employed to create planar alignment by having the rubbing direction pointed in the same direction. For fabricating the splay alignment cell, both types of coated glass were used.

### **LC alignment**

To align the LC molecules, the alignment cell was heated to 80°C, where the LC mixture was filled with LC mixture using capillary force. The cell was cooled down to room temperature at a controlled rate of 1°C/min. For aligning LC ink, the cell was kept in the dark for the entire aligning process.

### **Fabrication of LC films**

The alignment cell, with a thickness of 30  $\mu\text{m}$ , was contained with aligned LC ink and placed under an LED light. Films that would be further used for post-functionalization were irradiated with a wavelength of 440-450 nm (5.3 mW/cm<sup>2</sup>) for 60 s. The cell was cut open with a razor blade, and the film was used for further experiments.

### **Two-Photon Laser Microprinting (2PLP)**

Two-photon laser writing was performed within a commercially available direct laser writing setup (Photonic Professional GT2, Nanoscribe GmbH & Co. KG).

For printing LC microstructure, a 63 $\times$  oil objective (NA = 1.4; WD = 190  $\mu\text{m}$ ; Zeiss) was used to focus a femtosecond laser ( $\lambda$  = 780 nm) at the interface between the LC ink and the bottom

glass of the alignment cell by having the laser beam pass through the immersion oil and the substrate. After printing, the cell was opened, and the unpolymerized ink was removed by immersing the substrate sequentially in two warm 2-propanol (60°C) baths for 5 min each. The printed microstructures were then gently dried with a nitrogen flow and used for the next step of post-modification.

For fabricating the PDMS microstructures, the printing was conducted with the configuration of dip-in laser lithography (DiLL). For this, a polyimide-coated glass was mounted on the sample holder with the coated side facing downward. A drop of IP-PDMS was positioned both at the center of the coated layer and at the lens of a 25× objective (NA = 0.8; WD = 380 μm; Zeiss). All PDMS microstructures were printed with a set of optimized printing parameters. While fabricating each sliced layer, a contoured shell written with 12 layers (hatching distance 0.2 μm) was first printed with a laser power of 30 mW and scanning speed of 20 mm/s, followed by the filling of the interior (laser power: 40 mW, scanning speed: 100 mm/s, slicing and hatching distance: 0.3 μm). The development of the PDMS microstructures was carried out by placing the substrate horizontally in three 2-propanol (10 mL) baths sequentially for 10 min at room temperature. The printed PDMS structures were dried with a mild nitrogen flow. For PDMS structures employed as LC alignment scaffolds, the printed substrate was soon used to fabricate an alignment cell with another piece of polyimide-coated glass after drying to prevent dust contamination. The following LC alignment step follows the general alignment procedure as mentioned.

#### **Post-functionalization of LC films**

A droplet of a concentrated (~20 mM) dye solution, prepared with a mixed solvent of IPA/DCM (v/v = 10:1), was deposited on the pristine LC film, which was attached to the alignment glass. A piece of unfunctionalized glass was used to cover the film to prevent solvent evaporation and to evenly spread the dye solution throughout the film. The film was immersed in the dye solution for at least 30 min prior to the post-curing step with a LED (380-390 nm, 12.3 mW/cm<sup>2</sup>) for 10 min, followed by the development in IPA for 5 min.

#### **Post-functionalization of LC microstructures**

The incorporation of photoresponsive dyes achieved by post-modification was carried out by using 20 wt% dye dispersions. These were prepared by respectively dissolving 20 mg of the dye and 80 mg of the E7 mixture in dichloromethane (1 mL), followed by stirring and solvent

evaporation. A dispersion with a concentration of 5 wt% was also prepared using the same procedure, and the precipitates in the dispersion were removed by syringe filtration. The resulting mixtures were then used to fill the gap in a new glass cell, which was assembled with an unfunctionalized coverslip and the previously printed substrate. The LC structures were immersed in the dispersions and kept in the dark at room temperature overnight until irradiated with UV light (380–390 nm, 14.5 mW/cm<sup>2</sup>) for 30 min. The excess dye mixture was removed with the same LC ink development method as described earlier. The resulting functionalized microstructures were used for further characterization.

### **Optical Microscopy**

LC films and all printed structures were inspected under optical microscopes, either a Leica DM2700 M (Leica Microsystems) or an Axio Imager Z1 (Carl Zeiss AG), which were run with the analytical microscope software LAS X or ZEN, respectively. For polarized images, samples were placed between crossed polarizers in both cases.

### **Stereomicroscope**

A stereomicroscope (Leica Z16 APOA) equipped with a monochrome camera (EO-5310) was employed to image the LC microstructures within the PDMS microscaffolds.

### **Heating stage**

A heating stage (LTS 420, Linkam Scientific Instruments) was flexibly coupled to the optical microscope DM2700 or stereomicroscope to be used to inspect the thermoresponsive behavior of the LC materials.

### **Scanning electron microscopy (SEM)**

#### *SEM imaging of static microstructures*

For static structures, samples were coated with a thin layer of Pt-Pd of 12 nm using a sputter coater prior to imaging. SEM images were acquired using a Zeiss Ultra 55 (Carl Zeiss AG) at 5 kV in secondary electron mode.

#### *SEM imaging of dynamic microstructures*

The PDMS-induced thermoresponse of LC microstructures was investigated in Crossbeam 540 (Carl Zeiss AG) equipped with a heating stage (module 300C, Kammrath Weiss GmbH). The

heating cycle was programmed to have the temperature first be sprint up from ambient temperature to 100°C (20°C/min), followed by a steady gradient until 300°C (10°C/min). SEM images were obtained at 1.7 kV in secondary electron mode. Structures were not sputter-coated in this case.

### **UV-Vis Absorption Spectroscopy**

The absorption spectra of the compounds were measured using a UV-Vis spectrometer (Jasco V-770 Spectrophotometer). Measurements for solution samples were conducted in a 10 mm cuvette with a concentration adjusted to reach an absorbance of approximately 1 ( $10^{-5}$  M in toluene). For solid-state samples, the films or powders were spread evenly on a quartz coverslip, which was mounted on a sample holder. For the photoresponse investigation, LEDs ( $14.5 \text{ mW/cm}^2$ ) with varied wavelengths were respectively positioned vertically above the cuvette or the coverslip to afford an orthogonal irradiating direction to the beam path of the spectrophotometer. Absorption spectra were collected while the LED was shortly switched off.

### **Differential scanning calorimetry (DSC)**

A differential scanning calorimeter (Discovery DSC 250) was used to define the nematic-to-isotropic transition temperature ( $T_{ni}$ ) of LC materials.

### **Confocal Laser scanning Microscopy**

3D reconstruction of the LC  $\supset$  **DASA 1** was achieved by composing fluorescence images captured from a Nikon A1R confocal microscope with a 20× objective (NA = 0.75). The dye molecule was excited using a 561 nm laser, and the fluorescence signal was detected at a wavelength of 595 nm with GaAsP-detectors during image acquisition.

### **Confocal Raman spectroscopy**

Raman spectra were collected by using a confocal Raman spectrometer (Renishaw InVia Reflex) in backscattering configuration equipped with a 633 nm laser and a 50× long working distance objective (Olympus, NA = 0.5). Prior to each measurement, a calibration with a silicon wafer at  $520.6 \text{ cm}^{-1}$  was performed. Each spectrum was recorded with 10 s of integration time, 2 accumulations, and an excitation density of  $2.04 \text{ mW cm}^{-2}$ . To measure LC microstructures, blocks with dimensions of  $50 \times 50 \times 10 \text{ }\mu\text{m}^3$  were printed, and measurements were performed at the center of the block with a focus point centered  $1 \text{ }\mu\text{m}$  below the surface to exclude the

influence of surface inhomogeneities. To minimize the influence of spot-to-spot variations, 100 spectra were recorded over a  $10 \times 10 \mu\text{m}^2$  area of the sample and averaged. The spectra were fitted with Voigt functions after baseline correction and normalization at the peak maximum of  $\nu(\text{C}=\text{O})$  ( $1728 \text{ cm}^{-1}$ ).

### Analysis of double bond conversion (DOC)<sup>[136]</sup>

To inspect the overall conversion of the two-photon polymerized microstructures, a total of 100 Raman spectra were acquired from a designated area measuring  $10 \times 10 \mu\text{m}^2$  on the sample. These spectra were subsequently averaged to obtain a representative spectrum. The region of interest ( $1530$  to  $1830 \text{ cm}^{-1}$ ) for the averaged spectra was normalized to the characteristic peak of  $\nu(\text{C}=\text{O})$  at  $1728 \text{ cm}^{-1}$ , and baseline corrections were applied using a spline fitting method. Notably, the  $\nu(\text{C}=\text{C})$  peaks associated with the vibrational modes of acrylate ( $1635 \text{ cm}^{-1}$ ) and aromatic group ( $1604 \text{ cm}^{-1}$ ) overlapped, hindering accurate analysis (Figure 5.1). To overcome this, curve fitting by a Voigt function was employed to deconvolute the peaks individually, enabling the determination of their respective integrals. Subsequently, the obtained peak areas were utilized in **Equation 1** (see Chapter 3) to calculate the DOC. Within this equation, the symbol  $A'$  denotes the fitted peak area of the microprinted structure, while  $A_{\text{Ink}}$  represents the area corresponding to the unpolymerized ink.

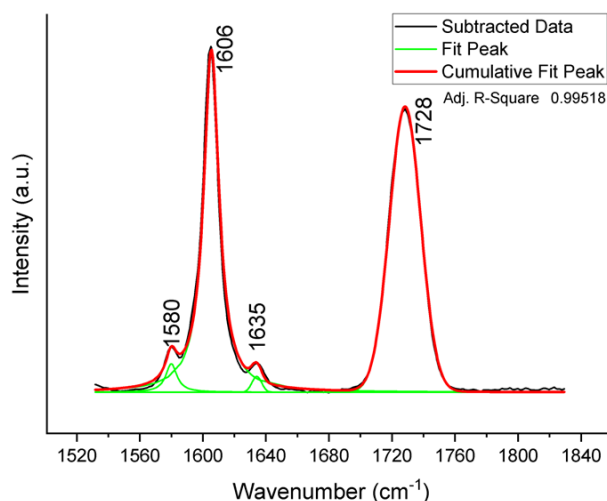


Figure 5.1 The Raman spectra of the pristine LC microprinted block revealed distinct signals at  $1635 \text{ cm}^{-1}$  and  $1728 \text{ cm}^{-1}$ , which can be attributed to the vibrational modes of  $\nu(\text{C}=\text{C})$  (acrylate) and  $\nu(\text{C}=\text{O})$ , respectively. In order to analyze these peaks more accurately, deconvolution techniques were employed. The deconvoluted peaks were then plotted on the graph, represented by a green line.

### Analysis of Azo dye integral ratio

One of the objectives was to evaluate the relative proportion of dye molecules in comparison to the LC polymer bulk within the LC  $\supset$  Azo and LC+Azo functionalized structures. For this, Raman spectra within the range of 1046-1780  $\text{cm}^{-1}$  were acquired and subjected to the aforementioned procedures of averaging and processing (Figure 5.2). In this analysis, the fitted area of the C-N peak located at 1136  $\text{cm}^{-1}$ , corresponding to azobenzene, was utilized. Specifically, the area  $A'_{\text{Azo}(C=O)}$  was determined by comparing the ratio of  $A_{\text{Azo}(C-N)}$  to  $A_{\text{Azo}(C=O)}$  observed in the pure Azo powder. Subsequently,  $A'_{\text{Azo}(C=O)}$  was divided by the total fitted area of  $A'_{(C=O)}$  measured from the functionalized LC microstructures. The calculation for this estimation is outlined in **Equation 2**:

$$\text{Integral ratio} = \frac{A'_{\text{Azo}(C-N)} \times A_{\text{Azo}(C=O)} / A_{\text{Azo}(C-N)}}{A'_{(C=O)}} \quad (\text{Equation 2})$$

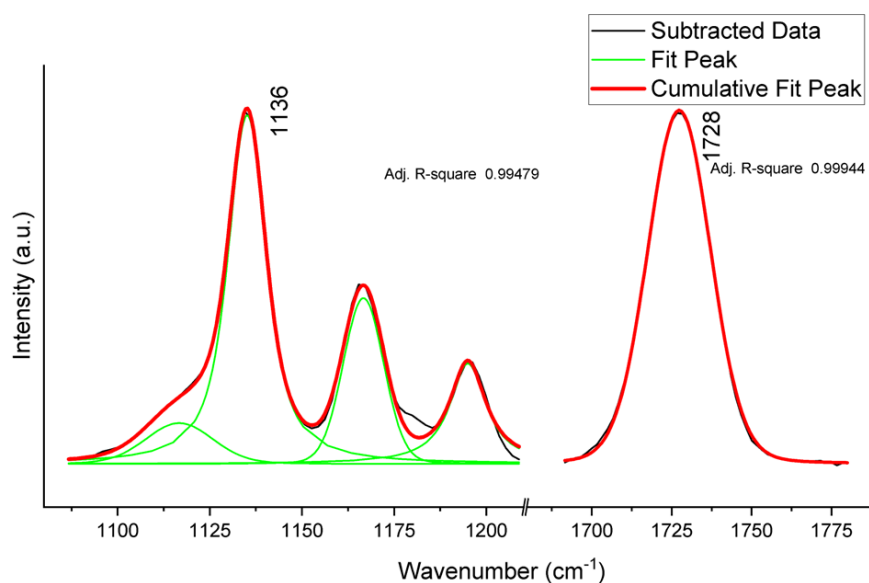


Figure 5.2 The Raman spectra of **Azo 2** post-functionalized LC microblocks (LC  $\supset$  **Azo 2**) were collected and averaged. Voigt functions were employed to fit the peaks present in the data. This fitting process aids in characterizing and quantifying the vibrational modes associated with the **Azo 2** molecules and LC polymer within the LC microblocks.

### Time-of-Flight Secondary Ion Mass Spectrometry (ToF-SIMS)

ToF-SIMS was conducted using a TOF-SIMS5 instrument (ION-TOF GmbH, Münster, Germany) equipped with a Bi-cluster primary ion source and a reflectron type time-of-flight analyzer. The ultra-high vacuum (UHV) base pressure was maintained below  $2 \times 10^{-8}$  mbar during the analysis. The Bi source was operated in "high current bunched" mode to provide short  $\text{Bi}_3^+$  primary ion pulses with an energy of 25 keV, a lateral resolution of approximately 4  $\mu\text{m}$ , and a target current of 0.35 pA, which enabled high mass resolution. To ensure high mass resolution, a short pulse length of 1 ns was used. The ion doses during reference measurements of the dyes were maintained below  $2 \times 10^{11}$  ions/ $\text{cm}^2$  (static SIMS limit). To compensate for charge, an electron flood gun was applied, providing electrons of 21 eV, and the secondary ion reflectron was tuned accordingly. The spectra were calibrated using the  $\text{C}^-$ ,  $\text{C}_2^-$ ,  $\text{C}_3^-$ , or the  $\text{C}^+$ ,  $\text{CH}^+$ ,  $\text{CH}_2^+$ , and  $\text{CH}_3^+$  peaks. For depth profiling, a dual-beam analysis was conducted in non-interlaced mode. The primary ion source was again operated in "high current bunched" mode with a scanned area of  $150 \times 150 \mu\text{m}^2$  (3 frames with  $128 \times 128$  data points, 125  $\mu\text{s}$  cycle time), and a sputter gun (operated with  $\text{Ar}_{1500}^+$  ions, 10 keV, scanned over a concentric field of  $250 \times 250 \mu\text{m}^2$ , target current 5 to 5.3 nA) was used to erode the sample for 4 s, followed by a 1 s pause until the underlying glass was reached. Cross-sections were presented as recorded, and for 3D representation, a 3D correction based on the flat underlying glass slide, based on the  $\text{Si}^+$  signal, was performed. The software used for this analysis was ION-TOF Surfacelab 7.2.129059.

### **Characterization of mechanical properties of LC microstructures**

The mechanical properties of the LC microstructures were characterized using a nanoindenter. Glass substrates printed with blocks of dimension  $100 \times 100 \times 10 \mu\text{m}^3$  were glued to a 6-well plate and immersed in DI water to prevent displacement during measurements. The indentations were carried out in a fiber-optics-based nanoindenter (Pavone, Optics11, Netherlands) using an indenter probe with a cantilever spring constant of  $k = 3.57 \text{ N/m}$  and a spherical glass tip of 3.0  $\mu\text{m}$  radius. The indentation profile was optimized with a 15  $\mu\text{N}$  indentation load, a loading rate of  $4 \mu\text{N s}^{-1}$ , and a hold time of 2 s before retraction. Indentations were repeated eight times ( $N=8$ ) at different locations within the central area ( $20 \times 20 \mu\text{m}^2$ ) of each microblock. The indentation curves were analyzed using *Data Viewer* (V2.5.0) software supplied by the device manufacturer. A curve fitting with a Hertzian contact model was applied in the range between the contact point (0 nm) and 150 nm. The Young's moduli were determined by the mean value and standard deviation of the obtained results.

### **Characterization of thermoresponse of LC microactuators**

The thermal response of the LC microstructures and microactuators was assessed using a heating stage (LTS 420, Linkam Scientific Instruments) coupled to an optical microscope, a Leica DM2700 M, or a stereomicroscope. The expansion and recovery of the structures were induced by a programmed heating cycle, where the temperature was raised from ambient temperature to 300 °C at a rate of 10 °C/min. The temperature was maintained at 300 °C for 10 min, after which the sample was cooled back to ambient temperature at the same rate. The deformation profile of each structure was obtained by analyzing the elongation and contraction between two opposing edges in the X and Y directions via image processing software ImageJ.

### Characterization of photoresponse of LC films

The fabricated LC films with splay alignment were cut into long strips along the director with a size of 10 mm×2 mm. One end was fixed with a self-closing tweezer and placed 1 cm above an LED light. The images of the bending motion of the film under light stimulus were recorded. Frames for each actuation cycle were used to create a stack image to determine the degree of actuation based on the angle formed by the tweezer tip to the highest and lowest points reached by the film (Figure 5.3). Image processing was carried out with the software ImageJ.

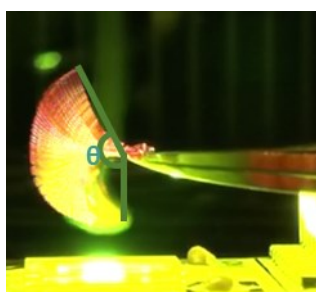


Figure 5.3 A stack image of the photoresponse of a LC-Azo1 LC film upon the stimulus of a 438 nm LED (3.5 W/cm<sup>2</sup>). "θ" denotes the measured angle for analysis.

### Characterization of photoresponse of LC microactuators

To characterize the photoactuation of the functionalized LC microactuators, they were mounted above the LEDs at a distance of 5 mm, which were attached to a high-precision stage. A monochrome camera (EO-5310) and a 10× objective (NA = 0.25) were used to image the samples from either a top or tilted view (30-45°) with a frame rate of 28.6 fps. The LED was switched on by applying an electric current of  $I = 10A$ , corresponding to light intensities of 3.5, 9.6, and 3.1 mW/cm<sup>2</sup> for red, green, and blue LEDs, respectively. A 10-second interval was

programmed for LC  $\supset$  **Azo 2** and LC  $\supset$  **DASA 2**, while 5 seconds were used for the others, based on their temporal responses. To compare the different microactuators, 50 continuous actuation cycles were performed and recorded from the top view. The amplitude of each actuation cycle was defined as the mean of the distance measurements for two opposing arm tips in the X and Y directions ( $L$ ). The measurements were performed frame by frame via ImageJ by applying an intensity threshold to improve accuracy. The temporal response was defined as the time required to reach 50% recovery after the light with maximum intensity was switched off ( $t_{1/2}$ ).

### **Analysis of LC alignment profile**

The PDMS-induced alignment profile of LC molecules within each PDMS microcavity was quantified with the value of optical density (OD) according to the polarized images. This was performed using the image analysis software ImageJ. Prior to the analysis, a calibration of optical density according to mean gray values was carried out. For this, a Kodak No. 3 Calibrated Step Tablet consisting of 21 steps with a density range of 0.05 to 3.05 OD was used. The measured mean gray value of each step was converted to its assigned OD value accordingly. The successful calibration was confirmed with a calibration curve with a  $R^2$  value of 0.99. All polarized images obtained from POM were cropped to the area of interest and converted into 8-bit grayscale for analysis.

#### *Planar alignment*

PDMS microchannels, with a length of 100  $\mu\text{m}$  and wall thickness of 20  $\mu\text{m}$ , were constructed along the Y-axis with varied channel width ( $W$ ) and height ( $H$ ) to induce planar alignment with LC molecules. A mean OD value was acquired by monitoring along a centerline (80  $\mu\text{m}$ ) along each channel. The obtained value was plotted against the channel aspect ratio  $\eta=H/W$ .

#### *Radial alignment*

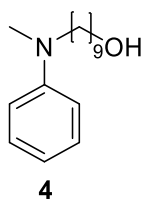
OD profiles were acquired diagonally across the PDMS well. The OD value obtained at the LC-PDMS interface served as the background value ( $OD_{bg}$ ), which was subtracted from the value measured ( $OD$ ) at each point across the well. The obtained value was plotted against the distance from the circular center.

## 5.3 Synthesis

### General

All syntheses were performed under yellow-light conditions. Reactions under anhydrous conditions were performed under an inert nitrogen atmosphere using conventional Schlenk line techniques. Purifications of the synthesized products were carried out by conducting column chromatography with silica gel (Sigma-Aldrich, particle size 40-63  $\mu\text{m}$ ) or Flash column chromatography (Interchim PuriFlash XS520Plus) equipped with high-performance spherical silica columns if necessary. The structural characterization of the synthesized compounds was carried out by performing  $^1\text{H}/^{13}\text{C}$  nuclear magnetic resonance (NMR) experiments at 295 K using a spectrometer (Bruker Ultrashield Plus-500, Bruker Avance III 400 MHz, or Bruker Avance III 300). Chemical shifts are reported in parts per million (ppm) and calibrated to the residual peaks of deuterated solvents as an internal standard (for  $^1\text{H}$  NMR,  $\text{CDCl}_3$ : 7.26 ppm;  $\text{CD}_2\text{Cl}_2$ : 5.32 ppm). Mass spectrometry was performed with MALDI-MS (Bruker AutoFlex Speed time-of-flight) or ESI-MS (Bruker ApexQe hybrid 9.4 T FT-ICR). For acrylate-functionalized products, light exposure and heating above  $25^\circ\text{C}$  under reduced pressure were limited to their minimums to avoid undesirable polymerization.

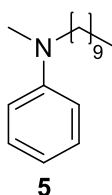
### Synthesis of *N*-(9-hydroxynonyl)-*N*-methylaniline (**4**)



A suspension of potassium carbonate (25.8 g, 187 mmol, 4.00 eq), *N*-methylaniline (**1**, 5.00 g, 46.7 mmol, 1.00 eq), and 9-bromononan-1-ol (**2**, 12.5 g, 56.1 mmol, 1.20 eq) in 90 mL acetonitrile was heated to  $90^\circ\text{C}$  and stirred at this temperature for 2 days. The reaction mixture was cooled to room temperature, and the solvent was removed under reduced pressure. After resuspending the residue in 100 mL dichloromethane, the organic phase was washed with water (2x 200 mL) and brine (200 mL). After drying over magnesium sulfate, the solvent was removed under reduced pressure. The crude product was further purified by silica gel flush column chromatography (4:1 hexane/ethyl acetate) and recrystallized in dichloromethane/hexane to yield a colorless solid. Yield: 67%, (7.73 g, 31.0 mmol).

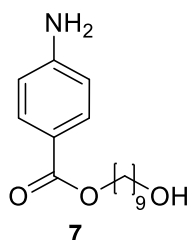
$^1\text{H}$  NMR (300 MHz,  $\text{CD}_2\text{Cl}_2$ ,  $\delta$ ): 7.18 (t,  $J = 7.7$  Hz, 2H, H3), 6.67 (d,  $J = 8.0$  Hz, 2H, H2), 6.62 (t,  $J = 7.3$  Hz, 1H, H4), 3.58 (t,  $J = 6.5$  Hz, 2H, H5), 3.29 (t,  $J = 7.6$  Hz, 2H, H6), 2.90 (s, 3H, H7), 1.32 (m, 14H,  $\text{H}_{\text{alkyl}}$ );  $^{13}\text{C}$  NMR (75 MHz,  $\text{CD}_2\text{Cl}_2$ ,  $\delta$ ): 149.9 (C1), 129.4 (C3), 116.0 (C4), 112.4 (C2), 63.2 (C5), 53.1 (C6), 38.5 (C7), 33.3 ( $\text{C}_{\text{CH}_2,\text{alkyl}}$ ), 30.0 ( $\text{C}_{\text{CH}_2,\text{alkyl}}$ ), 29.9 ( $\text{C}_{\text{CH}_2,\text{alkyl}}$ ), 29.8 ( $\text{C}_{\text{CH}_2,\text{alkyl}}$ ), 27.5 ( $\text{C}_{\text{CH}_2,\text{alkyl}}$ ), 27.0 ( $\text{C}_{\text{CH}_2,\text{alkyl}}$ ), 26.1 ( $\text{C}_{\text{CH}_2,\text{alkyl}}$ ); HRMS (EI+)  $m/z$ :  $[\text{M}]^+$  calcd for  $\text{C}_{16}\text{H}_{27}\text{NO}$ : 249.2087; found: 249.2085.

Synthesis of *N*-methyl-*N*-nonylaniline (**5**)<sup>[146]</sup>



The procedure was adapted from a previously reported method. A mixture of *N*-methylaniline (**1**, 2.14 g, 20 mmol, 1.00 eq), nonylbromide (**3**, 9.94 g, 48 mmol, 2.40 eq) and potassium carbonate (11.06 g, 80 mmol, 4.00 eq) was stirred in refluxed acetonitrile (40 mL) overnight. After cooling down to room temperature, the solvent was removed under reduced pressure. The crude was redissolved in dichloromethane (40 mL) and washed sequentially with  $\text{NaHCO}_3(\text{aq})$  (40 mL) and deionized water (40 mL), then dried with magnesium sulfate. The product was obtained after purification with silica gel flush column chromatography using a 99:1 hexane/ethyl acetate mixed solvent, with a yield of 48% (2.26 g, 9.7 mmol). All spectroscopic characterizations match the reported values.

Synthesis of 9-hydroxynonyl 4-aminobenzoate (**7**):

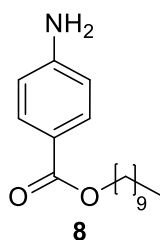


A suspension of potassium carbonate (33.4 g, 242 mmol, 5.00 eq), *p*-aminobenzoic acid (**6**, 6.62 g, 48.3 mmol, 1.00 eq), and 9-bromononan-1-ol (**2**, 11.0 g, 53.1 mmol, 1.10 eq) in 200 mL dimethylformamide was heated to 80 °C and stirred at this temperature for 3 h. The reaction mixture was cooled down to room temperature, and 500 mL water were added. The solution

was extracted with ethyl acetate (3x 100 mL) and the organic phase was dried over magnesium sulfate. The solvent was removed under reduced pressure to yield a yellowish solid. The crude product was further purified by recrystallization from toluene/hexane. (Yield: 87 %, 12.4 g, 42.1 mmol).

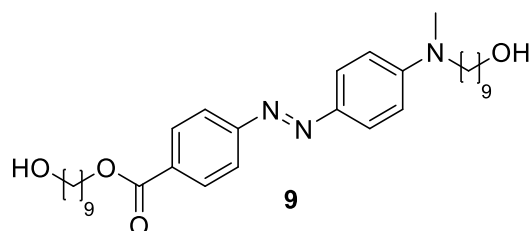
$^1\text{H}$  NMR (300 MHz,  $\text{CD}_2\text{Cl}_2$ ,  $\delta$ ): 7.81 (d,  $J$  = 8.8 Hz, 2H, H3), 6.65 (d,  $J$  = 8.8 Hz, 2H, H2), 4.22 (m, 4H, H6 +  $\text{NH}_2$ ), 3.58 (t,  $J$  = 6.7 Hz, 2H, H7), 1.72 (q,  $J$  = 7.5 Hz, 2H,  $\text{H}_{\text{alkyl}}$ ), 1.53 (q,  $J$  = 6.5 Hz, 2H,  $\text{H}_{\text{alkyl}}$ ), 1.32 (m, 10H,  $\text{H}_{\text{alkyl}}$ );  $^{13}\text{C}$  NMR (75 MHz,  $\text{CD}_2\text{Cl}_2$ ,  $\delta$ ): 166.9 (C5), 151.6 (C1), 131.7 (C3), 120.2 (C4), 114.0 (C2), 64.8 (C6), 63.1 (C7), 33.2 ( $\text{C}_{\text{CH}_2,\text{alkyl}}$ ), 29.9 ( $\text{C}_{\text{CH}_2,\text{alkyl}}$ ), 29.7 ( $\text{C}_{\text{CH}_2,\text{alkyl}}$ ), 29.6 ( $\text{C}_{\text{CH}_2,\text{alkyl}}$ ), 29.2 ( $\text{C}_{\text{CH}_2,\text{alkyl}}$ ), 26.4 ( $\text{C}_{\text{CH}_2,\text{alkyl}}$ ), 26.1 ( $\text{C}_{\text{CH}_2,\text{alkyl}}$ ); HRMS (EI+)  $m/z$ :  $[\text{M}]^+$  calcd for  $\text{C}_{16}\text{H}_{25}\text{NO}_3$ : 279.1829; found: 279.1839.

*Synthesis of nonyl p-aminobenzoate (8):*



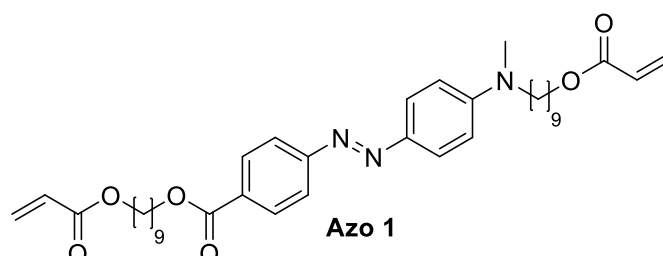
To a stirring solution of p-aminobenzoic acid (**6**, 5 g, 36.46 mmol, 1.00 eq) in DMF (200 mL), potassium carbonate (25.2 g, 182.3 mmol, 5.00 eq) was added, followed by nonylbromide (**3**, 8.31 g, 40.11 mmol, 1.10 eq). The mixture was stirred at 80 °C for 2h. After completion of the reaction, the mixture was poured into deionized water (500 mL) and extracted with ethyl acetate (3 x 200 mL), washed with brine (200 mL), and dried with magnesium sulfate. The solvent of the filtrate was removed in vacuo, and the resulting white powder was purified with silica gel flush column chromatography (2:1 hexane/ethyl acetate) to afford the product in a 90 % yield (8.62g, 32.7 mmol).

$^1\text{H}$  NMR (400 MHz,  $\text{CDCl}_3$ ,  $\delta$ ): 7.90 – 7.87 (m, 2H, H3), 6.76 – 6.73 (m, 2H, H2), 4.99 (br s, 2H,  $\text{NH}_2$ ), 4.26 (t,  $J$  = 6.7 Hz, 2H, H6), 1.74 ( $J$  = 6.7 Hz, 2H, H7), 1.46 - 1.28 (m, 14H,  $\text{CH}_2$ ), 0.88 (t,  $J$  = 6.6 Hz, 3H,  $\text{CH}_3$ );  $^{13}\text{C}$  NMR (100 MHz,  $\text{CDCl}_3$ ,  $\delta$ ): 166.6 (C5), 152.1 (C1), 130.5 (C3), 121.8 (C4), 111.7 (C2), 65.2 (C6), 31.9 ( $\text{C}_{\text{CH}_2,\text{alkyl}}$ ), 29.5 ( $\text{C}_{\text{CH}_2,\text{alkyl}}$ ), 29.3 ( $\text{C}_{\text{CH}_2,\text{alkyl}}$ ), 29.2 ( $\text{C}_{\text{CH}_2,\text{alkyl}}$ ), 28.8 ( $\text{C}_{\text{CH}_2,\text{alkyl}}$ ), 26.1 ( $\text{C}_{\text{CH}_2,\text{alkyl}}$ ), 22.7 ( $\text{C}_{\text{CH}_2,\text{alkyl}}$ ), 14.1 ( $\text{C}_{\text{CH}_3,\text{alkyl}}$ ); HRMS (ESI+)  $m/z$ :  $[\text{M}+\text{Na}]^+$  calcd for  $\text{C}_{16}\text{H}_{25}\text{NNaO}_2^+$ : 286.1778; found: 286.1777.

*Synthesis of azobenzene 9:*

A solution of sodium nitrite (150 mg, 2.17 mmol, 1.20 eq) in 6 mL of water was added dropwise to a 0 °C cool solution of 9-hydroxynonyl 4-aminobenzoate **7** (530 mg, 1.81 mmol, 1.00 eq) in 20 mL of hydrochloric acid (1.5 M). The solution was stirred for 30 min before methylaniline **4** (450 mg, 1.81 mmol, 1.00 eq) dissolved in 2 mL methanol. The reaction mixture was kept at 0 °C and stirred for 1.5 h. After removing the ice bath, it was stirred for 1 h at room temperature. The reaction mixture was added to 300 mL ice water, and the red precipitate was collected by filtration. Further purification was achieved by recrystallization of toluene/hexane. (Yield: 77 %, 765 mg, 1.39 mmol)

<sup>1</sup>H NMR (300 MHz, CDCl<sub>3</sub>, δ): 8.13 (d, *J* = 8.6 Hz, 2H, H7), 7.88 (d, *J* = 9.2 Hz, 2H, H3), 7.85 (d, *J* = 8.7 Hz, 2H, H4), 6.73 (d, *J* = 9.2 Hz, 2H, H8), 4.33 (t, *J* = 6.6 Hz, 2H, H10), 3.65 (t, *J* = 6.6 Hz, 4H, H11 + H12), 3.43 (t, *J* = 7.5 Hz, 2H, H14), 3.07 (s, 3H, H13), 1.79 (qu, 2H, *J* = 7.5 Hz, 2H, CH<sub>2</sub>), 1.63 - 1.34 (m, 26H, CH<sub>2</sub>); <sup>13</sup>C NMR (100 MHz, CDCl<sub>3</sub>, δ): 166.6 (C1), 156.2 (C5), 152.2 (C9), 143.6 (C6), 130.6 (C3), 130.6 (C2), 125.8 (C7), 122.1 (C4), 111.4 (C8), 65.3 (C10), 63.2 (C11/12), 63.2 (C11/12), 52.8 (C14), 38.8 (C13), 32.9 (C<sub>CH2,alkyl</sub>), 29.7 (C<sub>CH2,alkyl</sub>), 29.6 (C<sub>CH2,alkyl</sub>), 29.5 (C<sub>CH2,alkyl</sub>), 29.5 (C<sub>CH2,alkyl</sub>), 29.3 (C<sub>CH2,alkyl</sub>), 28.9 (C<sub>CH2,alkyl</sub>), 27.2 (C<sub>CH2,alkyl</sub>), 27.2 (C<sub>CH2,alkyl</sub>), 26.2 (C<sub>CH2,alkyl</sub>), 25.9 (C<sub>CH2,alkyl</sub>); HRMS (MALDI, DCTB) *m/z*: [M]<sup>+</sup> calcd for C<sub>32</sub>H<sub>49</sub>N<sub>3</sub>O<sub>4</sub>, 539.3718; found, 539.3724.

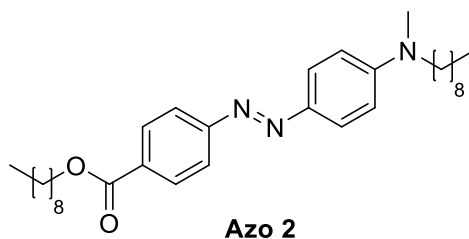
*Synthesis of compound Azo 1:*

To a solution of azobenzene **9** (70 mg, 0.13 mmol, 1.00 eq), *N,N*-dimethyl aniline (95 mg, 0.78 mol, 6.00 eq) and BHT (cat.) in 5 mL tetrahydrofuran, acryloyl chloride (26 mg, 0.27 mmol, 6 eq) was added dropwise at 0°C. The solution was heated to 60°C and stirred for 4h. Saturated

ammonium chloride solution (10 mL) was added, and the mixture was kept stirring for 15 min. The aqueous phase was extracted with ethyl acetate (3 × 20 mL) and the organic phase was dried with magnesium sulfate, followed by solvent removal under reduced pressure. Further purification of the crude product was achieved by silica gel flush column chromatography (10:1 hexane/ethyl acetate) with a yield of 85% (71 mg, 0.11 mmol).

$^1\text{H}$  NMR (300 MHz,  $\text{CDCl}_3$ ,  $\delta$ ): 8.13 (dd,  $J = 8.8, 2.0$  Hz, 2H, H3), 7.88 (dd,  $J = 9.2, 1.9$  Hz, 2H, H7), 7.85 (dd,  $J = 8.6, 1.8$  Hz, 2H, H4), 6.73 (dd,  $J = 9.2, 1.9$  Hz, 2H, H8), 6.39 (dd,  $J_{\text{trans}} = 17.3$  Hz,  $J_{\text{gem}} = 1.6$  Hz, 2H, H<sub>b</sub> + H<sub>d</sub>), 6.12 (dd,  $J_{\text{trans-vic}} = 17.2$  Hz,  $J_{\text{cis-vic}} = 10.4$  Hz, 2H, H14 + H15), 5.81 (dd,  $J_{\text{cis-vic}} = 10.4$  Hz,  $J_{\text{gem}} = 1.6$  Hz, 2H, H<sub>a</sub> + H<sub>c</sub>), 4.33 (t,  $J = 6.6$  Hz, 2H, H10), 3.72 (t,  $J = 6.6$  Hz, 4H, H11 + H12), 3.42 (t,  $J = 7.6$  Hz, 2H, H13), 3.07 (s, 3H, H18), 1.78 (qu,  $J = 7.5$  Hz, 2H, CH<sub>2</sub>), 1.69 - 1.62 (m, 6H, CH<sub>2</sub>), 1.40 - 1.33 (m, 20H, CH<sub>2</sub>);  $^{13}\text{C}$  NMR (100 MHz,  $\text{CDCl}_3$ ,  $\delta$ ): 166.4 - 166.3 (C1/19+20), 156.1 (C5), 152.0 (C9), 143.5 (C6), 130.5 (C3), 130.4 (C16/17), 130.4 (C2), 130.4 (C16/17), 128.7 (C14/15), 128.7 (C14/15), 125.7 (C7), 121.9 (C4), 111.3 (C8), 65.2 (C10), 64.7 (C11/12), 64.6 (C11/12), 52.7 (C13), 38.6 (C18), 29.5 (C<sub>CH2,alkyl</sub>), 29.4 (C<sub>CH2,alkyl</sub>), 29.2 (C<sub>CH2,alkyl</sub>), 29.2 (C<sub>CH2,alkyl</sub>), 29.2 (C<sub>CH2,alkyl</sub>), 28.7 (C<sub>CH2,alkyl</sub>), 28.6 (C<sub>CH2,alkyl</sub>), 28.6 (C<sub>CH2,alkyl</sub>), 27.0 (C<sub>CH2,alkyl</sub>), 27.0 (C<sub>CH2,alkyl</sub>), 26.0 (C<sub>CH2,alkyl</sub>), 25.9 (C<sub>CH2,alkyl</sub>), 25.9 (C<sub>CH2,alkyl</sub>); HRMS (MALDI, DCTB)  $m/z$ : [M]<sup>+</sup> calcd for C<sub>38</sub>H<sub>53</sub>N<sub>3</sub>O<sub>6</sub>, 647.3929; found, 647.3930.

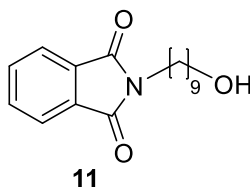
#### Synthesis of compound Azo 2:



Aminobenzoate **8** (500 mg, 1.9 mmol, 1.00 eq) was first dissolved in 1.5M  $\text{HCl}_{(\text{aq})}$  (20 mL) at 0 °C before the sodium nitrite (157.3 mg, 2.28 mmol, 1.20 eq) was slowly added. The solution was kept stirring at 0 °C for 30 min before adding the methanol (2 mL) solution of **5** (443mg, 1.9 mmol, 1.00 eq). After the reaction mixture reached room temperature it was stirred for an additional 2 h. The mixture was poured into cold deionized water, and the crude was collected by filtration. After purifying with silica gel flush column chromatography (5:1 hexane/ethyl acetate) and drying in vacuo, the product was obtained as orange powder with a yield of 63 % (611 mg, 1.2 mmol).

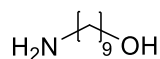
$^1\text{H}$  NMR (400 MHz,  $\text{CDCl}_3$ ,  $\delta$ ): 8.15–8.12 (d, 2H, H7), 7.95–7.91 (d, 2H, H3), 7.88 (d,  $J = 8.3$  Hz, 2H, H4), 6.77 (d,  $J = 8.9$  Hz, 2H, H8), 4.33 (t,  $J = 6.7$  Hz, 2H, H10), 3.43 (t,  $J = 7.4$  Hz, 2H, H11), 3.09 (s, 3H, H12), 1.79 (qu,  $J = 7.6$  Hz, 2H,  $\text{CH}_2$ ), 1.65 (qu,  $J = 7.3$  Hz, 2H,  $\text{CH}_2$ ), 1.46 (m, 2H,  $\text{CH}_2$ ), 1.28 (m, 22H,  $\text{CH}_2$ ), 0.89 (t,  $J = 6.6$  Hz, 6H,  $\text{CH}_3$ );  $^{13}\text{C}$  NMR (100 MHz,  $\text{CDCl}_3$ ,  $\delta$ ): 166.4 (C1), 155.5 (C5), 152.1 (C9), 143.4 (C6), 130.5 (C3), 130.5 (C2), 126.1 (C7), 121.8 (C4), 111.7 (C8), 65.2 (C10), 52.9 (C11), 38.8 (C12), 31.9 ( $\text{C}_{\text{CH}_2, \text{alkyl}}$ ), 31.8 ( $\text{C}_{\text{CH}_2, \text{alkyl}}$ ), 29.5 ( $\text{C}_{\text{CH}_2, \text{alkyl}}$ ), 29.5 ( $\text{C}_{\text{CH}_2, \text{alkyl}}$ ), 29.5 ( $\text{C}_{\text{CH}_2, \text{alkyl}}$ ), 28.8 ( $\text{C}_{\text{CH}_2, \text{alkyl}}$ ), 27.1 ( $\text{C}_{\text{CH}_2, \text{alkyl}}$ ), 27.0 ( $\text{C}_{\text{CH}_2, \text{alkyl}}$ ), 26.1 ( $\text{C}_{\text{CH}_2, \text{alkyl}}$ ), 22.7 ( $\text{C}_{\text{CH}_2, \text{alkyl}}$ ), 22.6 ( $\text{C}_{\text{CH}_2, \text{alkyl}}$ ), 14.1 ( $\text{C}_{\text{CH}_3, \text{alkyl}}$ ), 14.1 ( $\text{C}_{\text{CH}_3, \text{alkyl}}$ ), HRMS (ESI+)  $m/z$ :  $[\text{M}+\text{H}]^+$  calcd for  $\text{C}_{32}\text{H}_{50}\text{N}_3\text{O}_2$ : 508.3898; found 508.3895.

#### Synthesis of 2-(9-hydroxynonyl)isoindoline-1,3-dione (**11**)



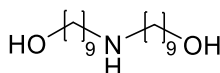
To a stirring DMF (10 mL) solution of 9-bromononan-1-ol (**2**, 844 mg, 3.78 mmol, 1.00 eq) potassium phthalimide (70 mg, 4.16 mmol, 1.10 eq) was added. The mixture was heated at 80 °C for 2 h. After cooling down to room temperature, DI water (10 mL) was added to the mixture to triturate the white precipitate, which was collected by filtration and washed with cold water (100 mL). Recrystallization in hexane/dichloromethane afforded the product a yield of 88% (964 mg, 3.33 mmol).

$^1\text{H}$  NMR (500 MHz,  $\text{CDCl}_3$ ,  $\delta$ ): 7.84 (m, 2H, H2/3), 7.70 (m, 2H, H1/4), 3.67–3.61 (m, 4H, H5/6), 1.67 (qu,  $J = 6.68$ , 2H,  $\text{CH}_2$ ), 1.57–1.52 (m, 5H,  $\text{CH}_2+\text{OH}$ ), 1.33–1.24 (m, 12H,  $\text{CH}_2$ );  $^{13}\text{C}$  NMR (125.8 MHz,  $\text{CDCl}_3$ ,  $\delta$ ): 168.5 (C9/10), 133.9 (C2/3), 132.2 (C7/8), 123.2 (C1/4), 63.1 (C6), 38.0 (C5), 32.8 ( $\text{C}_{\text{CH}_2, \text{alkyl}}$ ), 29.4 ( $\text{C}_{\text{CH}_2, \text{alkyl}}$ ), 29.3 ( $\text{C}_{\text{CH}_2, \text{alkyl}}$ ), 29.0 ( $\text{C}_{\text{CH}_2, \text{alkyl}}$ ), 28.6 ( $\text{C}_{\text{CH}_2, \text{alkyl}}$ ), 26.8 ( $\text{C}_{\text{CH}_2, \text{alkyl}}$ ), 25.7 ( $\text{C}_{\text{CH}_2, \text{alkyl}}$ ).

*Synthesis of 9-aminononan-1-ol (12)***12**

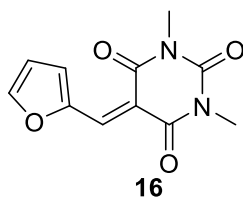
A stirred solution of isoindoline **11** (800 mg, 2.76 mmol, 1.00 eq) and hydrazine monohydrate (554 mg, 11.06 mmol, 4.00 eq) in ethanol (10 mL) was heated at reflux for 7h while a white precipitate was formed. The mixture was filtered, and the filtrate was dried in vacuo to afford the product as white solid. Yield: 77% (337 mg, 2.12 mmol).

$^1\text{H}$  NMR (500 MHz,  $\text{CDCl}_3$ ,  $\delta$ ): 3.64 (t,  $J = 6.64$ , 2H, H1), 2.68 (t,  $J = 6.94$ , 2H, H2), 1.56 (qu,  $J = 6.94$ , 2H, H3), 1.43-1.30 (m, 15H,  $\text{CH}_2 + \text{NH}_2 + \text{OH}$ );  $^{13}\text{C}$  NMR (125.8 MHz,  $\text{CDCl}_3$ ,  $\delta$ ): 63.0 (C1), 42.3 (C2), 33.9 (C3), 32.8 (C4), 29.6 ( $\text{C}_{\text{CH}_2, \text{alkyl}}$ ), 29.4 ( $\text{C}_{\text{CH}_2, \text{alkyl}}$ ), 26.9 ( $\text{C}_{\text{CH}_2, \text{alkyl}}$ ), 25.7 ( $\text{C}_{\text{CH}_2, \text{alkyl}}$ ).

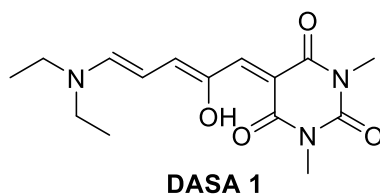
*Synthesis of 9-(9-hydroxynonylamino)nonan-1-ol (13)***13**

Amino alcohol (**12**, 1.78 g, 11.2 mmol, 1.00 eq) and 9-bromononan-1-ol (**2**, 2.5 g, 11.2 mmol, 1.00 eq) were dissolved in 17 mL ethanol, and the solution was refluxed for 24 h in the presence of potassium carbonate (4.65 g, 33.6 mmol, 3.00 eq), which was removed by filtration after the completion of the reaction. The solvent was removed under reduced pressure, and the crude was purified by column chromatography with basified silica gel (100:7.5:0.3 dichloromethane/methanol/ammonia). The product was obtained as transparent oil after drying in vacuo, with a yield of 23 % (781 mg, 2.59 mmol).

$^1\text{H}$  NMR (500 MHz,  $\text{CDCl}_3$ ,  $\delta$ ): 3.64 (t,  $J = 6.64$ , 4H, H1), 2.59 (t,  $J = 7.32$ , 4H, H2), 1.56 (qu,  $J = 6.98$ , 4H, H3), 1.48 (qu,  $J = 7.17$ , 5H, H4+NH), 1.30 (m, 22H,  $\text{CH}_2 + \text{OH}$ );  $^{13}\text{C}$  NMR (125.8 MHz,  $\text{CDCl}_3$ ,  $\delta$ ): 63.1 (C1), 50.1 (C2), 32.8 (C3), 30.1 (C4), 29.5 ( $\text{C}_{\text{CH}_2, \text{alkyl}}$ ), 29.4 ( $\text{C}_{\text{CH}_2, \text{alkyl}}$ ), 27.4 ( $\text{C}_{\text{CH}_2, \text{alkyl}}$ ), 25.7 ( $\text{C}_{\text{CH}_2, \text{alkyl}}$ ).

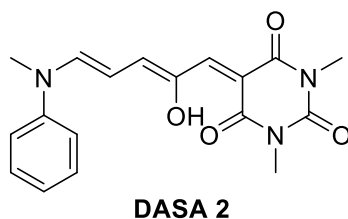
*Synthesis of 5-(furan-2-ylmethylene)-1,3-dimethylpyrimidine-2,4,6(1H,3H,5H)-trione (16)*<sup>[132a]</sup>

The procedure was adapted from a previously reported method. 2-furaldehyde (**16**) (961 mg, 10 mmol, 1.00 eq) and 1,3-dimethylbarbituric acid (1.56 g, 10 mmol, 1.00 eq) (**17**) were added to 40 mL H<sub>2</sub>O and stirred at room temperature for 2 h. The yellow precipitate was collected by filtration and washed twice with iced deionized water (30 mL). The collected solid was dissolved with dichloromethane and washed with 30 mL brine. The organic phase was dried over magnesium sulfate and the solvent was removed by rotary evaporation to give a yield of 90%. All spectroscopic characterizations match with the reported values.

*Synthesis of 5-((2Z,4E)-5-(diethylamino)-2-hydroxypenta-2,4-dien-1-ylidene)-1,3-dimethylpyrimidine-2,4,6(1H,3H,5H)-trione (DASA 1)*<sup>[133c]</sup>

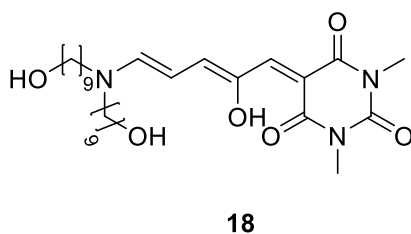
The procedure was adapted from a previously reported method. To a tetrahydrofuran (20 mL) suspension of furan adduct **16** (468 mg, 2 mmol, 1.00 eq), diethylamine (**19**, 208  $\mu$ L, 2 mmol, 1.00 eq) was added, and the mixture was stirred at room temperature for 1 h while a significant color change to magenta was observed. After the complete consumption of the starting materials, additional cold tetrahydrofuran (10 mL) was added. The precipitated dark purple solid was collected by filtration and purified with silica gel flush column chromatography using a 95:5 (vol/vol) dichloromethane/methanol mixed solvent. The collected fractions afford the product (31 %, 191.5 mg, 0.62 mmol). All spectroscopic characterizations match with the reported values.

Synthesis of compound 5-((2Z,4E)-2-hydroxy-5-(methyl(phenyl)amino)penta-2,4-dien-1-ylidene)-1,3-dimethylpyrimidine-2,4,6(1H,3H,5H)-trione (DASA 2)<sup>[133b]</sup>



The procedure was adapted from a previously reported method. To a tetrahydrofuran (12 mL) suspension of furan adduct **16** (696 mg, 2.97 mmol, 1.00 eq), N-methylaniline (**20**, 408 mg, 2.97 mmol, 1.00 eq) was added at room temperature, resulting in an immediate color change from yellow to deep blue. The precipitate was removed by filtration, and the filtrate was concentrated and purified with silica gel flush column chromatography using a 95:5 (vol/vol) dichloromethane/methanol mixed solvent. The product was precipitated from the collected fraction by adding hexane and cooling to -20 °C. The dark blue powder was collected by filtration and dried under vacuum (25%, 277 mg, 0.75 mmol). All spectroscopic characterizations match with the reported values.

Synthesis of DASA derivative **18**

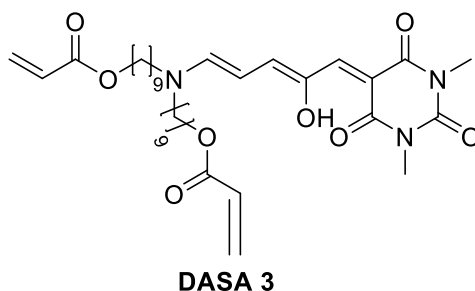


Aminodiol **13** (746 mg, 2.48 mmol, 1.00 eq) was added to a tetrahydrofuran (45 mL) suspension of furan adduct **16** (698 mg, 2.98 mmol, 1.20 eq) at room temperature, resulting in an immediate color change from yellow to magenta. After the complete consumption of aminodiol **13**, the solvent was removed by rotary evaporation. The crude was purified with silica gel flush column chromatography using a 95:5 dichloromethane/methanol mixed solvent. The collected fractions afforded the product as a dark purple paste with a yield of 36 % (484mg, 0.9 mmol).

<sup>1</sup>H NMR (500 MHz, CDCl<sub>3</sub>, δ): 12.53 (s, 1H, H1), 7.20 (d, *J* = 12.3, 1H, H5), 7.12 (s, 1H, H2), 6.75 (d, *J* = 12.4, 1H, H3), 6.06 (t, *J* = 12.4, 1H, H4), 3.63 (t, *J* = 6.5, 4H, H6), 3.38 (t, *J* = 7.48, 4H, H7),

3.35 (s, 3H, H12/13), 3.34 (s, 3H, H12/13), 1.66 (m, 5H, CH<sub>2</sub>+OH), 1.55 (m, 5H, CH<sub>2</sub>+OH), 1.35-1.31 (m, 20H, CH<sub>2</sub>). <sup>13</sup>C NMR (125.8 MHz, CDCl<sub>3</sub>, δ): 165.1 (C1), 163.4 (C8/10), 157.2 (C8/10), 152.0 (C9), 151.1 (C11), 146.5 (C2), 138.9 (C5), 102.8 (C4), 98.3 (C3), 63.0-62.9 (C6), 57.6 (C7), 49.6 (C<sub>CH2,alkyl</sub>), 32.7 (C<sub>CH2,alkyl</sub>), 29.7 (C<sub>CH2,alkyl</sub>), 29.3 (C<sub>CH2,alkyl</sub>), 29.2 (C<sub>CH2,alkyl</sub>), 29.0 (C<sub>CH2,alkyl</sub>), 28.9 (C<sub>CH2,alkyl</sub>), 28.5 (C<sub>CH2,alkyl</sub>), 28.3 (C<sub>CH2,alkyl</sub>), 27.0 (C<sub>CH2,alkyl</sub>), 26.8 (C<sub>CH2,alkyl</sub>), 26.3 (C<sub>CH2,alkyl</sub>), 25.7 (C<sub>CH2,alkyl</sub>).

### Synthesis of DASA derivative **3**



In a 100 mL round-bottom flask, DASA derivative 18 (73 mg, 0.14 mmol, 1.0 eq) and DMAP (36.7 mg, 0.30 mmol, 1.0 eq) were stirred in anhydrous chloroform under nitrogen atmosphere at 0°C for 30 min before acrylic anhydride (38 mg, 0.30 mmol, 2.2 eq) was slowly added. After the reaction mixture reached room temperature over a period of 2 h, the reaction was quenched with anhydrous methanol (10 mL) and stirred for another 30 min. The crude was obtained after the removal of solvent via rotary evaporation, followed by purification with silica gel flush column chromatography using a 95:5 dichloromethane/methanol mixed solvent. The collected fractions afforded the product as a dark purple paste with a yield of 35 % (30.3 mg, 0.047 mmol).

<sup>1</sup>H NMR (500 MHz, CDCl<sub>3</sub>, δ): 12.56 (s, 1H, H1), 7.17 (d, *J* = 12.3, 1H, H5), 7.15 (s, 1H, H2), 6.74 (d, *J* = 12.4, 1H, H3), 6.39 (d, *J* = 17.6, 2H, Ha), 6.14-6.08 (m, 2H, H7), 6.05 (t, *J* = 12.4, 1H, H4), 5.82 (d, *J* = 10.4, 2H, Hb), 4.15 (t, *J* = 6.7, 4H, H10), 3.38 (m, 4H, H9), 3.36 (s, 3H, H15/16), 3.35 (s, 3H, H15/16), 1.67 (m, 8H, CH<sub>2</sub>), 1.32 (m, 20H, CH<sub>2</sub>+OH); <sup>13</sup>C NMR (125.8 MHz, CDCl<sub>3</sub>, δ): 166.4 (C1), 165.1 (C6), 163.4 (C12/13), 156.9 (C12/13), 152.0 (C11), 150.8 (C2), 146.6 (C5), 139.3 (C8), 130.6 (C8'), 128.6 (C7), 125.5 (C7'), 102.6 (C4), 98.6 (C3), 64.6 (C10), 57.6 (C9), 49.6 (C<sub>CH2,alkyl</sub>), 30.3 (C<sub>CH2,alkyl</sub>), 29.7 (C<sub>CH2,alkyl</sub>), 29.3 (C<sub>CH2,alkyl</sub>), 29.1 (C<sub>CH2,alkyl</sub>), 29.0 (C<sub>CH2,alkyl</sub>), 28.6 (C<sub>CH2,alkyl</sub>), 28.5 (C<sub>CH2,alkyl</sub>), 28.3 (C<sub>CH2,alkyl</sub>), 27.1 (C<sub>CH2,alkyl</sub>), 26.9 (C<sub>CH2,alkyl</sub>), 26.5 (C<sub>CH2,alkyl</sub>), 25.8 (C<sub>CH2,alkyl</sub>).

## 5.4 NMR spectra

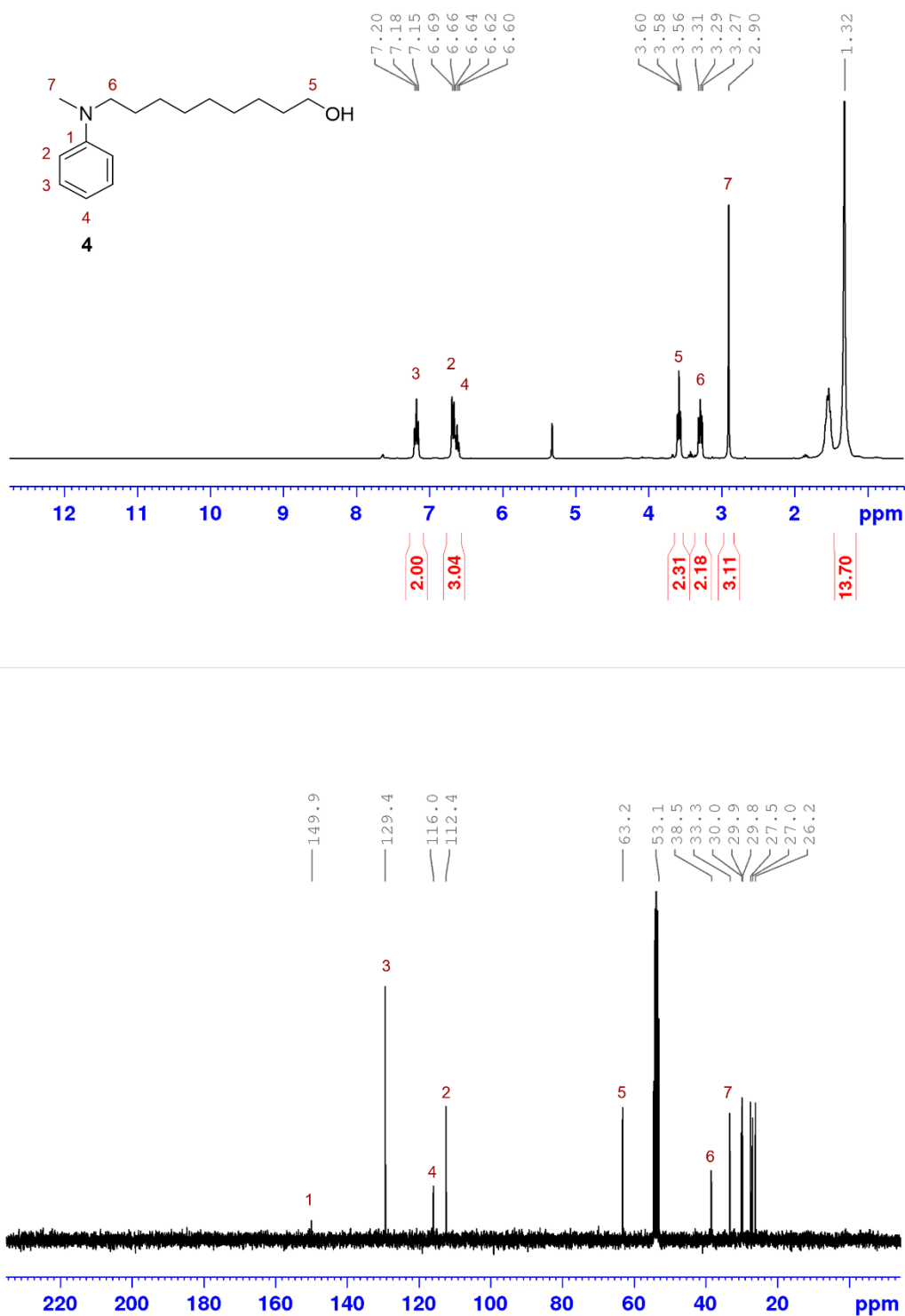


Figure 5.4  $^1\text{H}$  (300 MHz) and  $^{13}\text{C}$  (75 MHz) NMR spectra ( $\text{DCM-d}_2$ ) of *N*-(9-hydroxynonyl)-*N*-methylaniline **4**.

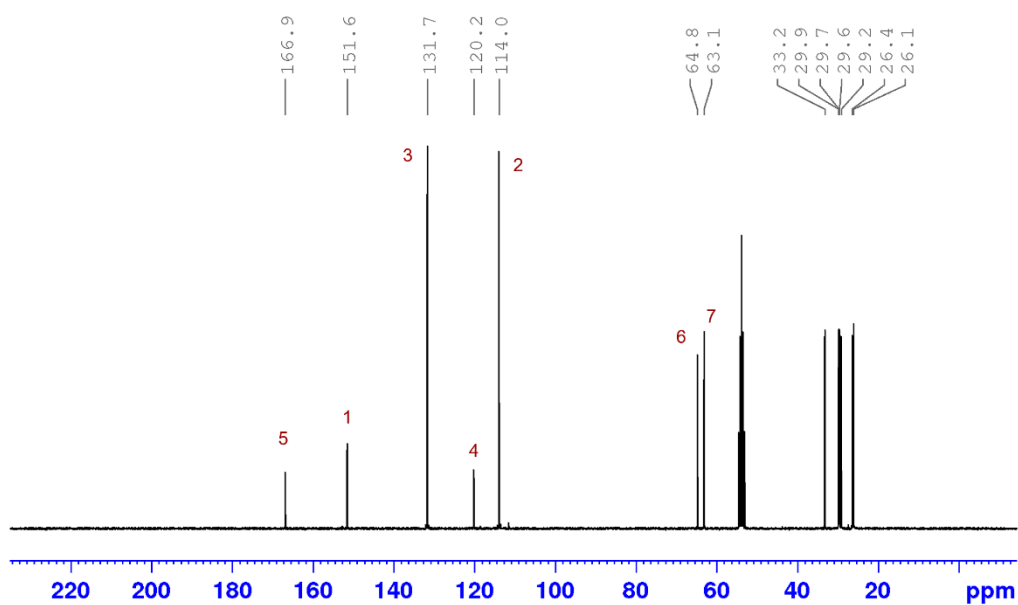
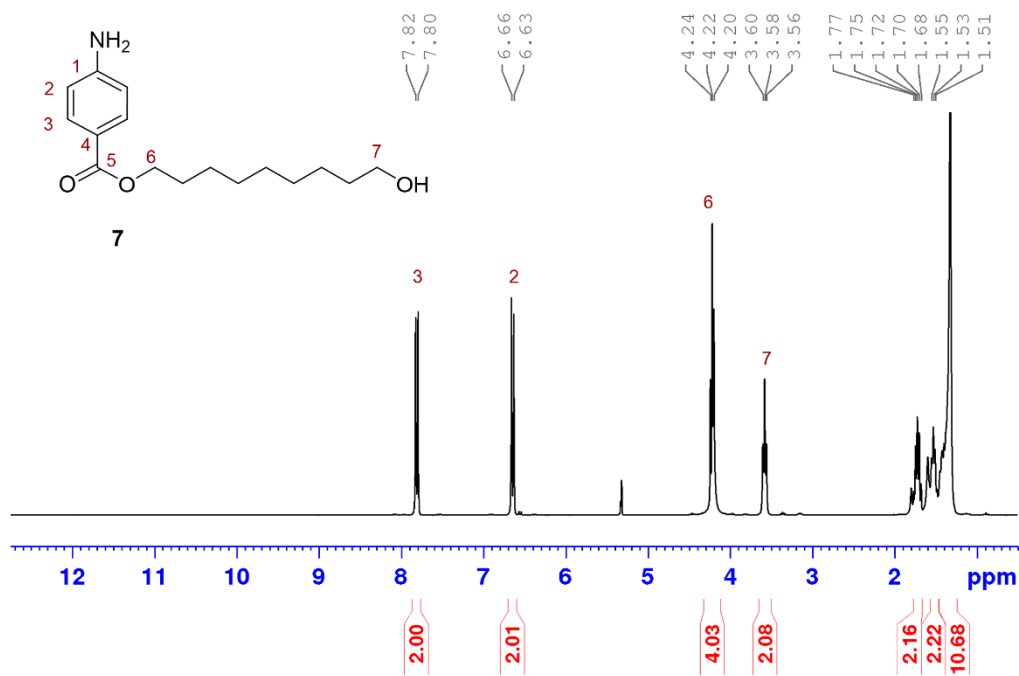
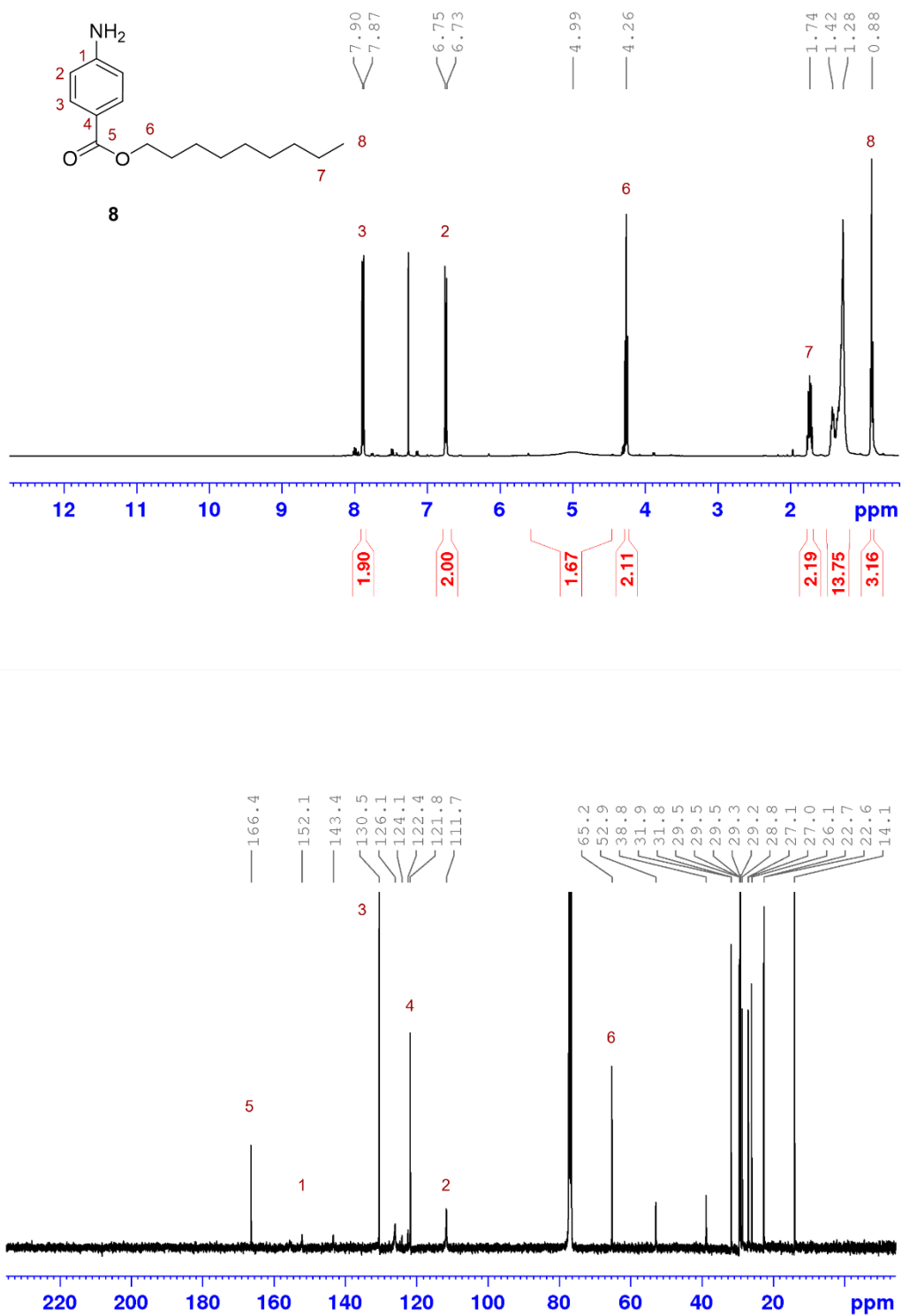
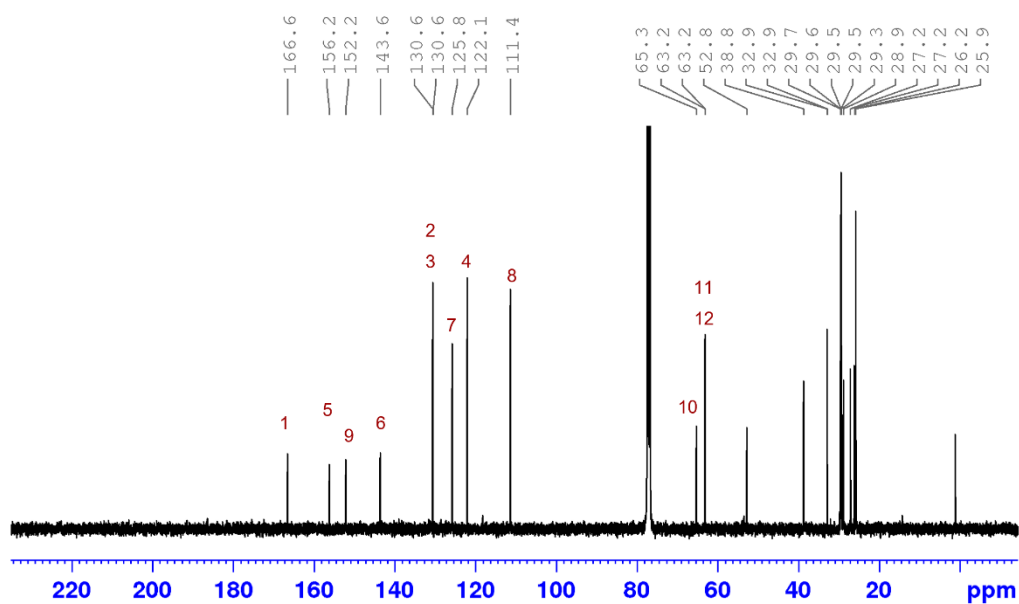
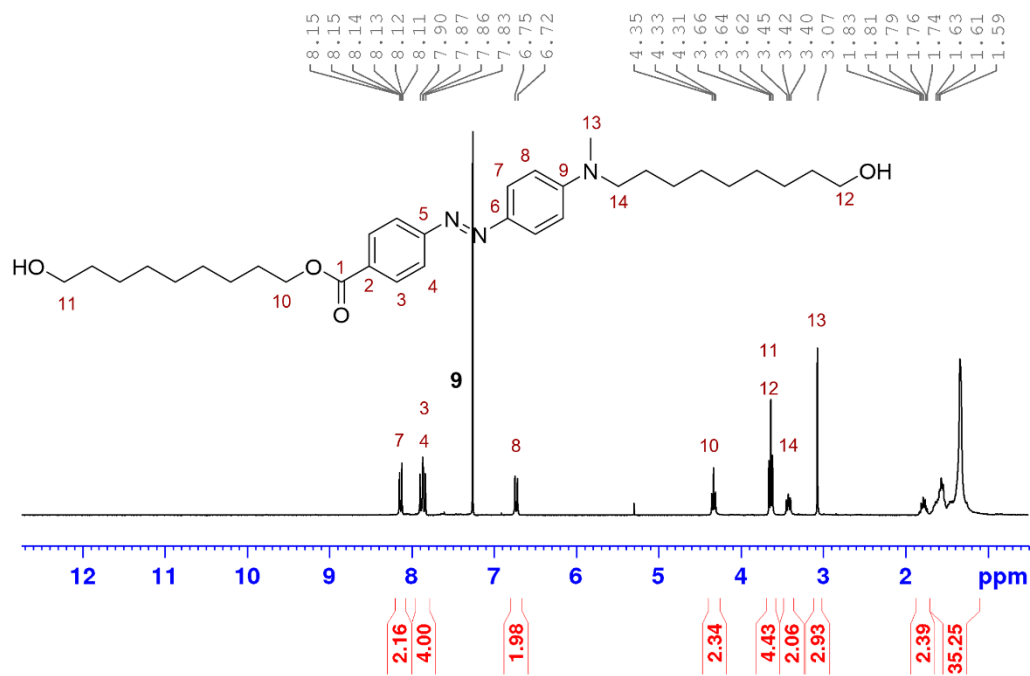
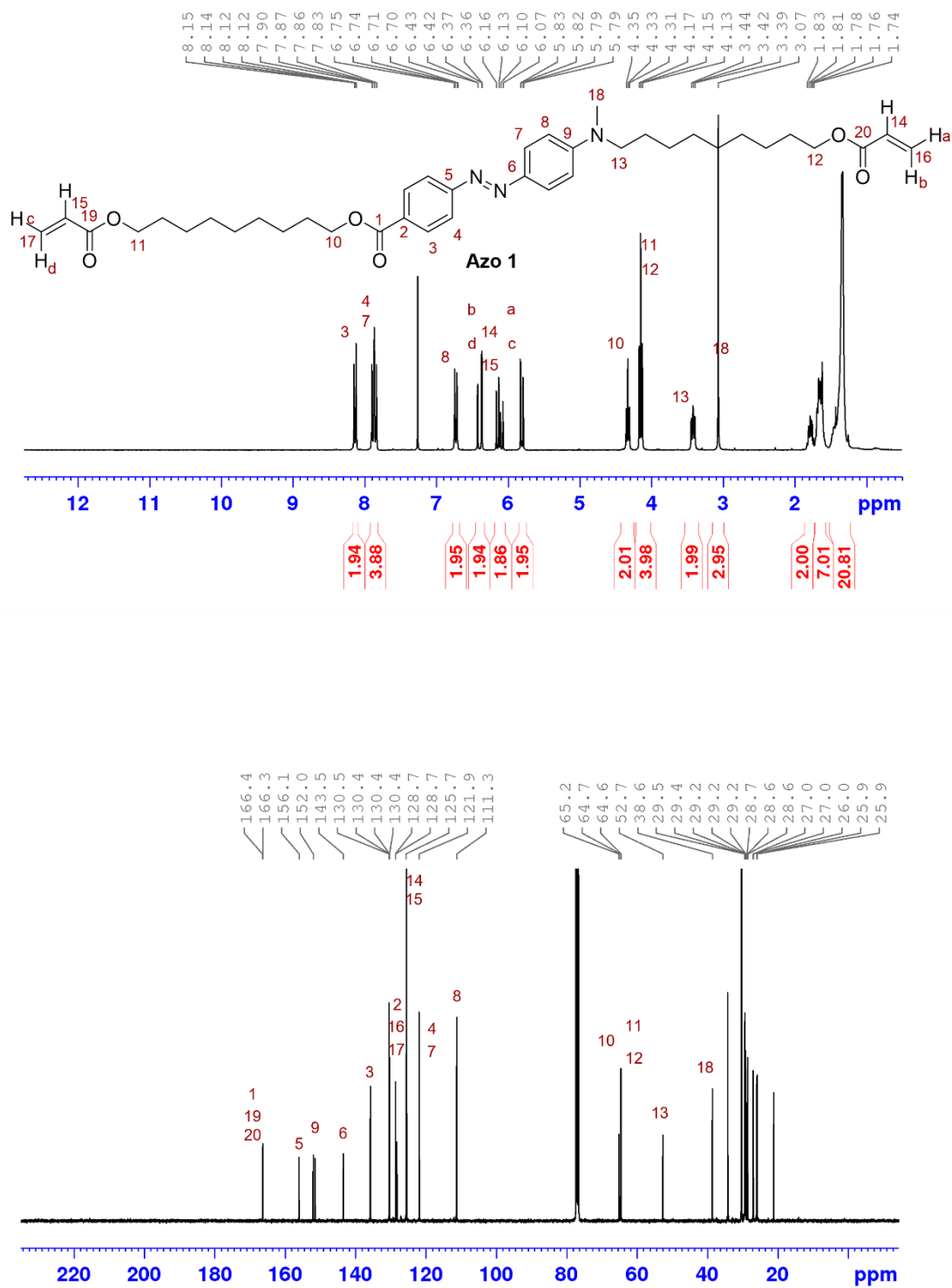
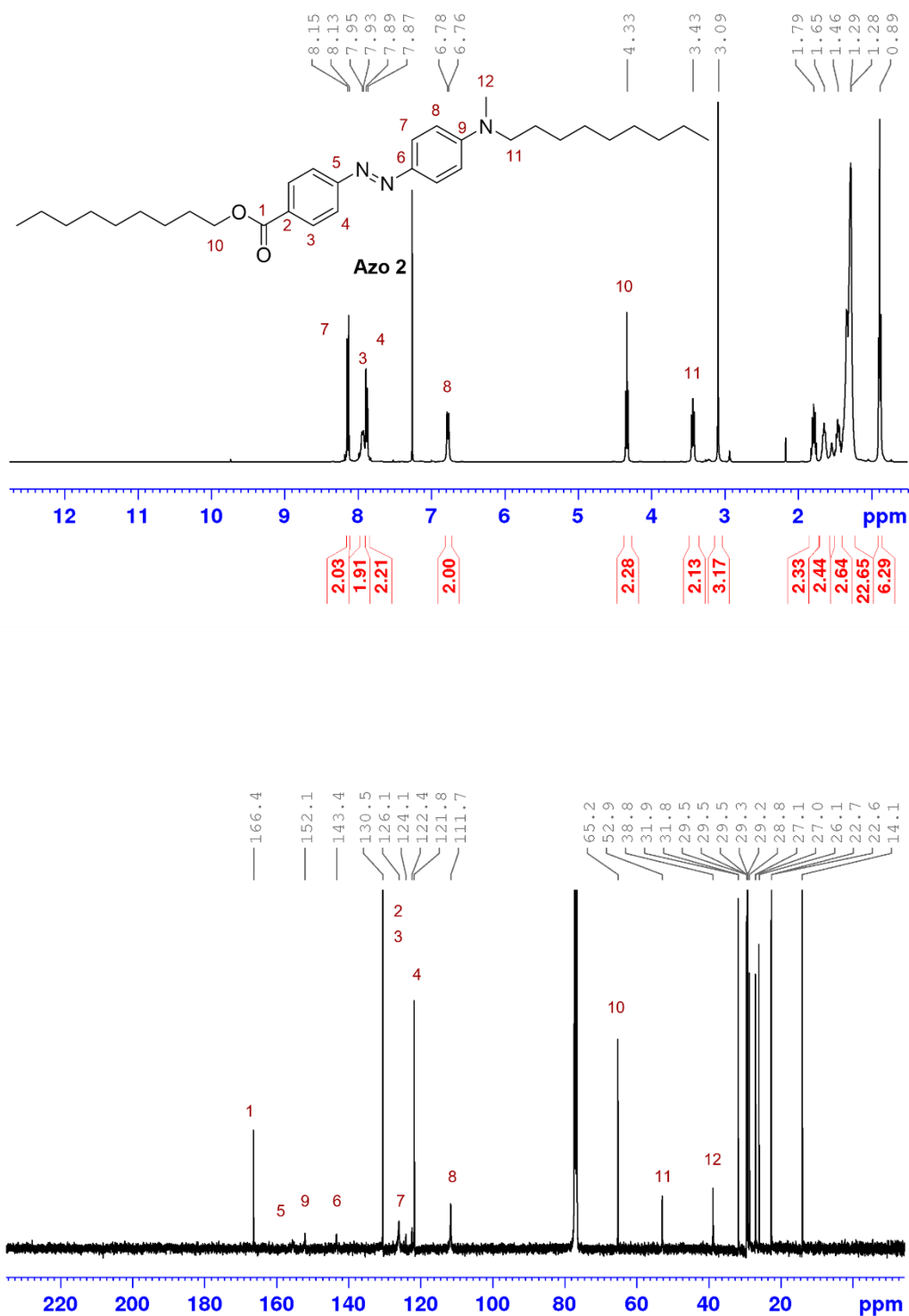


Figure 5.5 <sup>1</sup>H (300 MHz) and <sup>13</sup>C (75 MHz) NMR spectra (DCM-d<sub>2</sub>) of 9-hydroxynonyl 4-aminobenzoate 7.

Figure 5.6  $^1\text{H}$  (400 MHz) and  $^{13}\text{C}$  (100 MHz) NMR spectra ( $\text{CDCl}_3$ ) of *nonyl p-aminobenzoate* **8**.

Figure 5.7 <sup>1</sup>H (400 MHz) and <sup>13</sup>C (100 MHz) NMR spectra (CDCl<sub>3</sub>) of azobenzene 9.

Figure 5.8  $^1\text{H}$  (300 MHz) and  $^{13}\text{C}$  (75 MHz) NMR spectra ( $\text{CDCl}_3$ ) of **Azo 1**.

Figure 5.9  $^1\text{H}$  (400 MHz) and  $^{13}\text{C}$  (100 MHz) NMR spectra ( $\text{CDCl}_3$ ) of **Azo 2**.

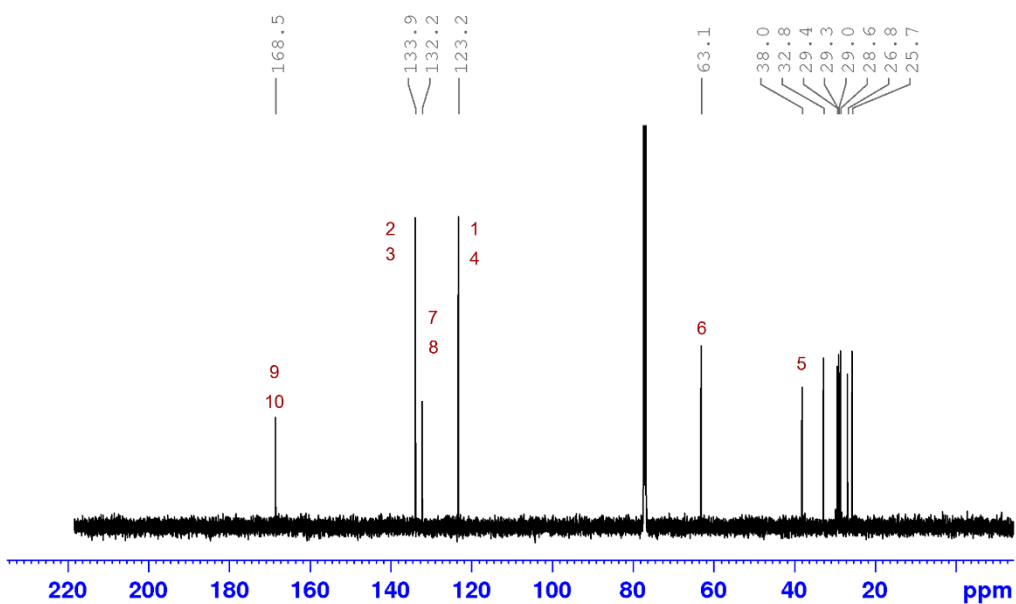
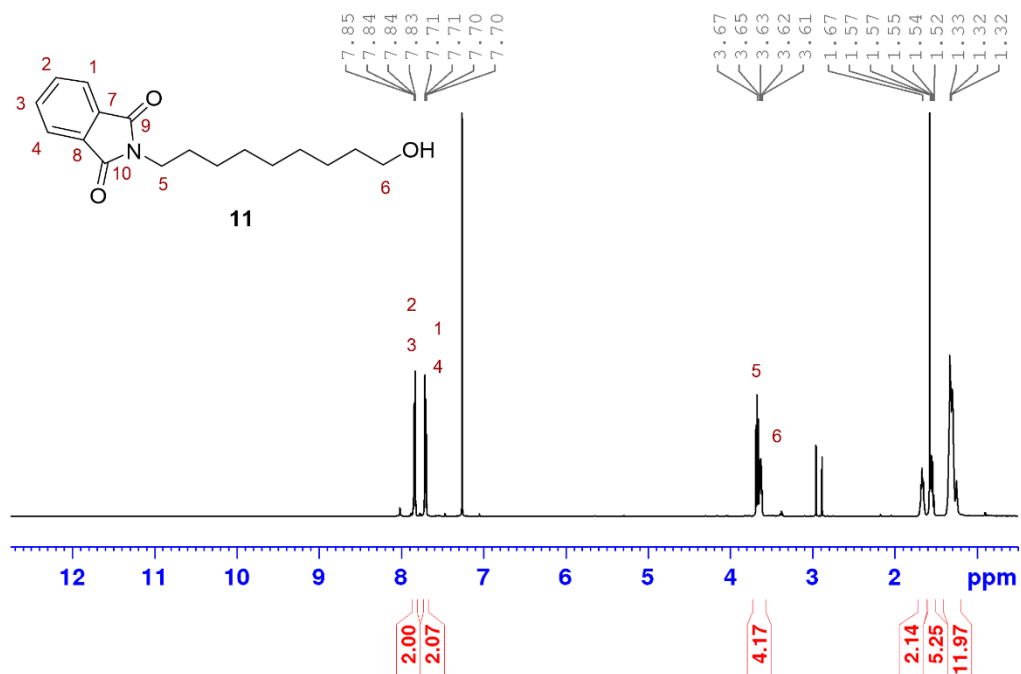
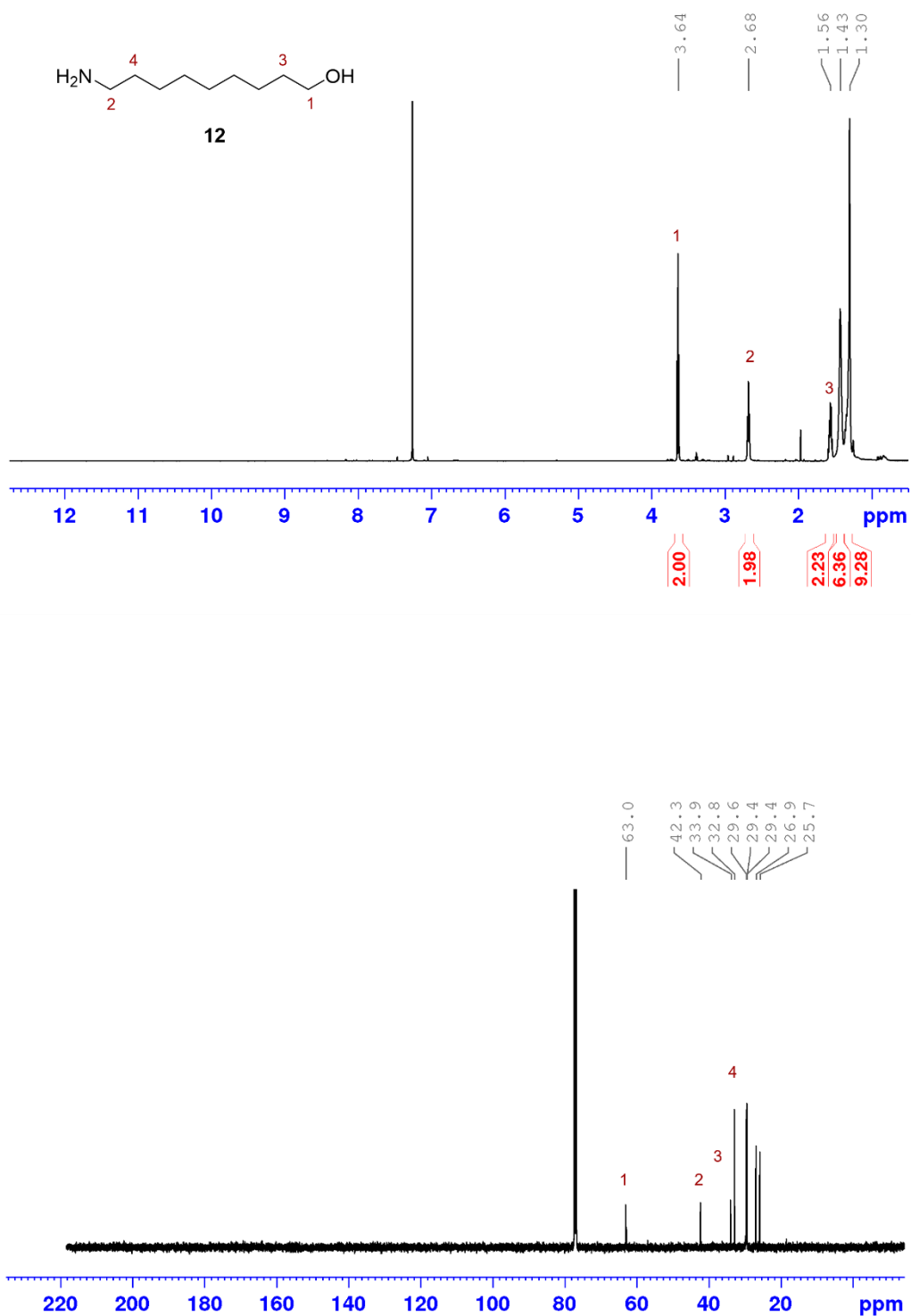


Figure 5.10 <sup>1</sup>H (500 MHz) and <sup>13</sup>C (125.8 MHz) NMR spectra (CDCl<sub>3</sub>) of 2-(9-hydroxynonyl)isoindoline-1,3-dione **11**.

Figure 5.11  $^1\text{H}$  (500 MHz) and  $^{13}\text{C}$  (125.8 MHz) NMR spectra ( $\text{CDCl}_3$ ) of 9-aminononan-1-ol **12**.

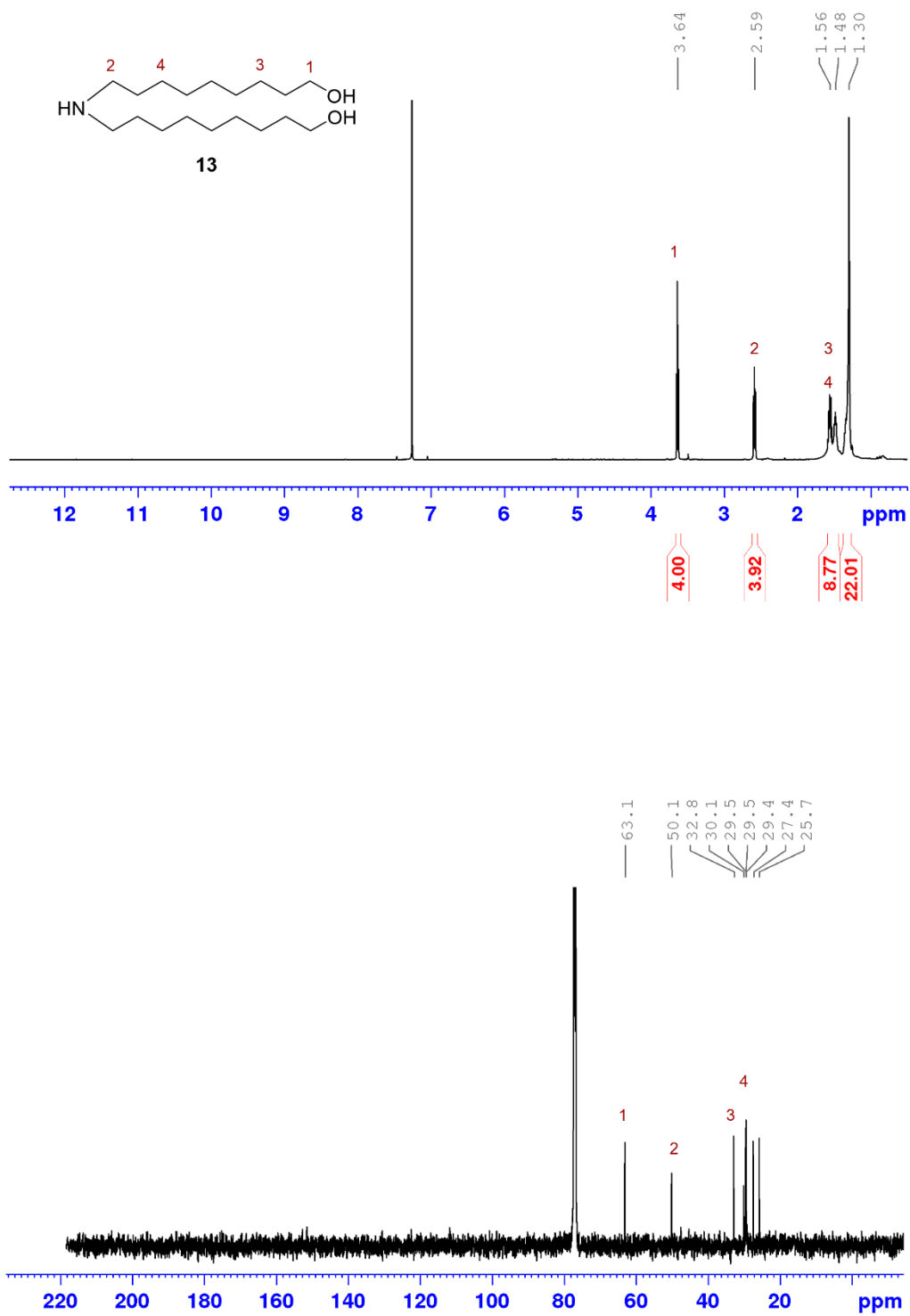
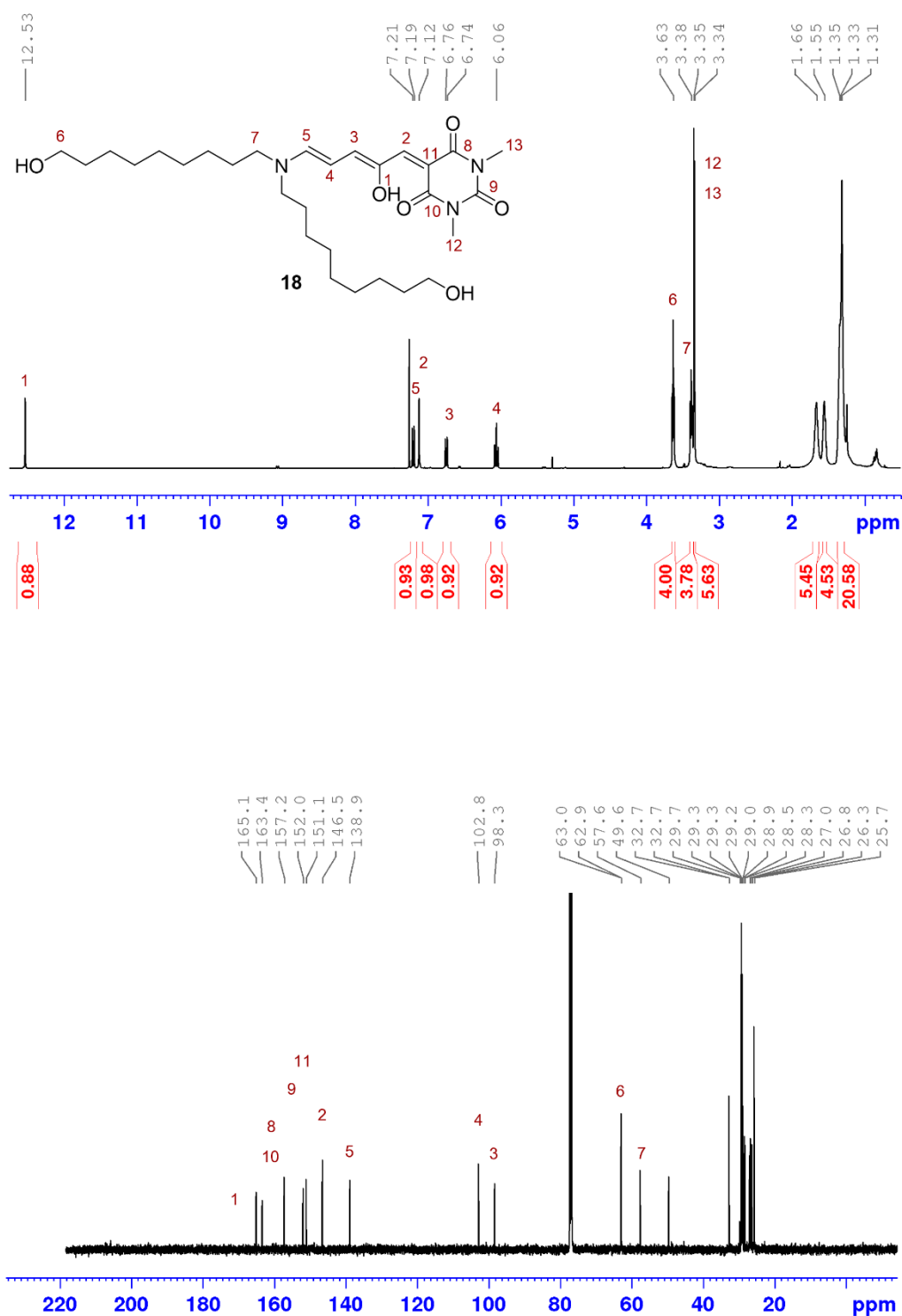
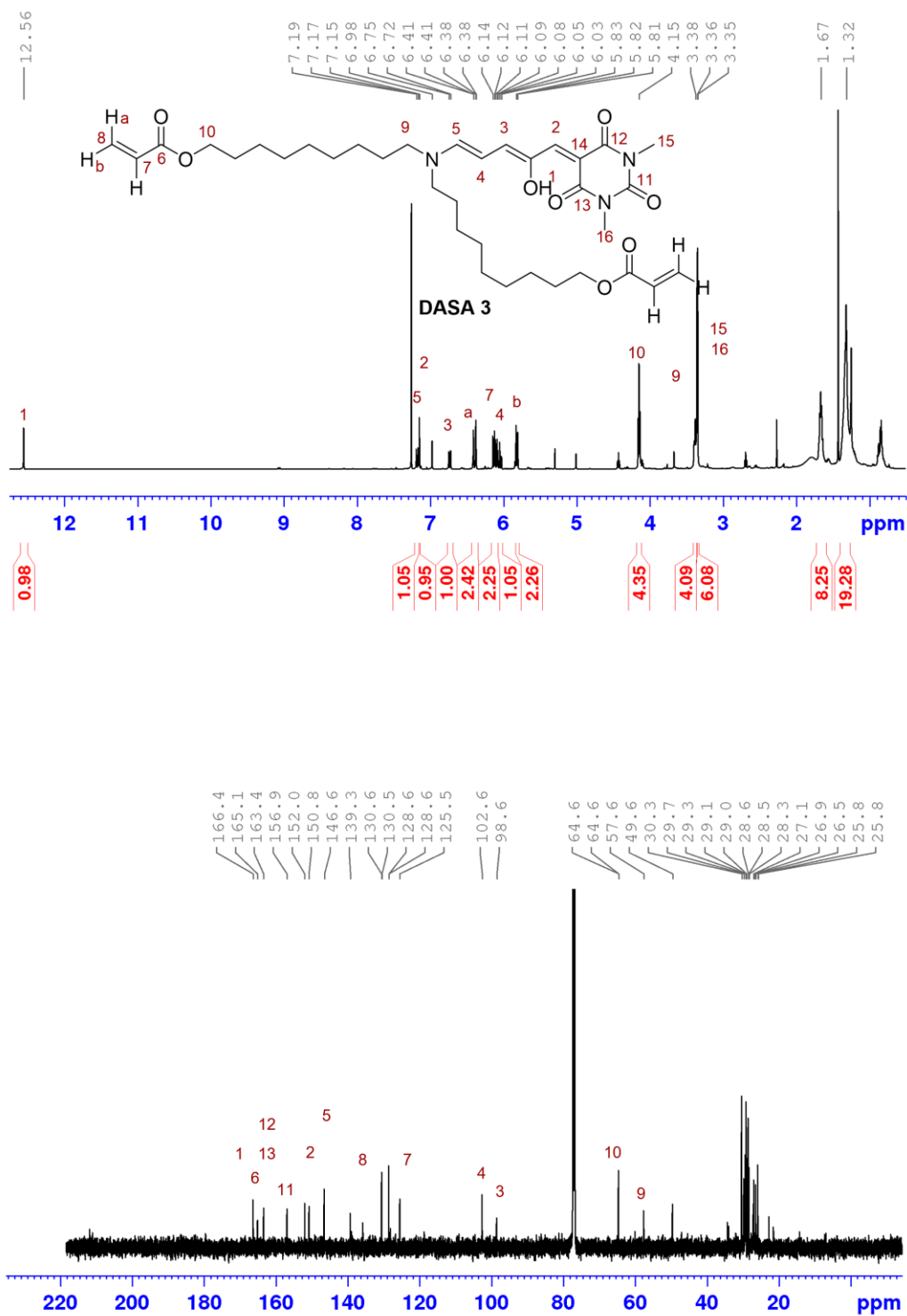


Figure 5.12 <sup>1</sup>H (500 MHz) and <sup>13</sup>C (125.8 MHz) NMR spectra (CDCl<sub>3</sub>) of 9-(9-hydroxynonylamino)nonan-1-ol **13**.

Figure 5.13  $^1\text{H}$  (500 MHz) and  $^{13}\text{C}$  (125.8 MHz) NMR spectra ( $\text{CDCl}_3$ ) of DASA derivative **18**.

Figure 5.14  $^1\text{H}$  (500 MHz) and  $^{13}\text{C}$  (125.8 MHz) NMR spectra ( $\text{CDCl}_3$ ) of DASA 3.

## **Chapter 6.**

# **Conclusions and outlook**

In the scope of this thesis, challenges that hindered the achievement of advanced 4D printed LC microsystems were overcome from two perspectives. One of the significant challenges pertained to the lack of functional LC materials, which limited the variety of stimuli-responsive properties of the fabricated microsystem. The other obstacle was related to the lack of a facile strategy to tailor the LC alignment profile in a more flexible and adaptable manner for 3D microprinting. In the following section, this thesis's work will be summarized on a per-chapter basis. The novelties of the research will be emphasized, and their potential applicability for the future will be discussed.

Chapter 3 aimed to broaden the functional material library for the fabrication of stimuli-responsive LC systems via 2PLP. Primary studies identified several challenges encountered when incorporating new classes of acrylate-functionalized photoresponsive materials into LC microstructures using conventional methods. One significant limitation arose from the fact that "light" was used for both the fabrication as well as the activation of the responsive structure. Thus, the wavelength used as a stimulus had to be non-overlapping with the printing wavelength (390 nm for one-photon printing and 780 nm for two-photon printing) to avoid competition with photopolymerization. Facing this dilemma, two classes of photoresponsive chromophores, an azobenzene (Azo) and the donor-acceptor Stenhouse adduct (DASA), were selected to serve as photoabsorbers for the incorporation of photoresponsiveness into the LC printed structures. These chromophores were customized and synthesized with specific substitutions to attain the desired absorption regions and be distinguishable from each other. The synthesis process included their functionalization towards biacrylates, which enabled covalent bonding during the polymerization process. Although the photophysical properties of the synthesized light absorbers were in line with the expected outcomes, exhibiting appropriate and narrow absorption regions, fast photoswitching efficacy, and absorption orthogonality between the two molecules, the incompatibility of DASA with the LC components in the ink impeded the formation of a LC monodomain, thereby hindering the programming of photoresponse in the printed structures.

To address the limitations encountered with conventional approaches, a novel method for incorporating functionality into LC structures was developed. The new approach was based on a post-modification strategy. By reswelling structures printed from a pure LC ink with a predetermined alignment profile using a dispersion of E7 and a functional dopant, the dopant was implemented through diffusion and encapsulation during a post-curing step. Detailed

---

characterizations have evidently confirmed the homogeneous incorporation of organic dyes via this method, irrespective of their functionalization with or without acrylate moieties. Thus, this modified approach eliminated several challenges encountered with the development of light-driven LC structures via conventional methods, such as the restricted light absorption region of the light absorber, the demanding synthesis of acrylate modification, and the optimization of the incorporated formulation and printing conditions. As a result, the high flexibility of this approach allowed for the implementation of versatile functionality into the printed LC structures, as demonstrated here with five photoresponsive molecules that have absorption regions covering the entire visible spectrum. Moreover, incorporating dual functionality into a single LC microactuator was achieved by employing a mixture of two functional molecules with distinct photoresponsiveness, resulting in a structure exhibiting activating behavior that switches between two patterns based on the wavelength of the irradiating light.

Overall, I believe that this novel approach will have a great impact in the way of fabricating light-responsive LC microstructures by eliminating the dependence on azobenzene and will open new avenues for realizing LC microsystems with a multitude of potential applications. For example, this approach has already been applied in one of the collaborative works, where a switchable optomechanical metamaterial flips the sign of the Poisson's ratio twist per strain upon light modulation.<sup>[119]</sup> Moreover, this approach has also facilitated the embedding of DASA, an emerging photoswitch, into LC structures for the first time. Since DASA exhibits an attractive color-changing property from magenta or violet to transparent upon stimuli, preliminary experiments have witnessed the reversible color switching behavior of the functionalized LC structures by using a spatially focused laser beam. This property could potentially be utilized in various applications, such as anti-counterfeiting microdevices that can encrypt or decrypt messages within the 3D structures or microdisplays that can be rewritten or re-patterned.

It is worth mentioning that the demonstrated flexibility of the approach with five different functionalities only scratches the surface of its potential. In fact, it is reasonable to believe that the versatility of this approach is not limited to organic dyes alone. For instance, composite materials composed of nanoparticles have been extensively used in the fabrication of functional films or 3D macrostructures. However, when it comes to 2PLP, several drawbacks are faced, including microexplosions caused by the inhomogeneous dispersion of

nanoparticles. The integration of electrothermal dopants, such as carbon nanotubes (CNTs) or liquid metals, or magnetothermal dopants, such as  $\text{Fe}_3\text{O}_4$  nanoparticles, into LC structures using this approach may provide a viable means of creating previously unreported electro- or magneto- responsive LC microsystems that utilize external fields to induce thermal effects. This work also demonstrated the first instance of a multi-stimuli responsive LC structure. It is likely that the achievement of other functionalities will facilitate the creation of sophisticated, smart LC microsystems equipped with complex functions. Furthermore, the transferability of this approach to other printing techniques is worth highlighting, since this post-modification method has been successfully adopted for macroscopic DLP-printed multi-wavelength responsive LCE actuators in another collaborative project within our group.<sup>[117]</sup>

Next, in Chapter 4 a new approach enabling a flexible and cost-efficient way to manipulate LC alignment three-dimensionally is presented. As the high amplitude of the final actuating behavior of LC materials depends heavily on their monodomain alignment, a convenient and flexible method to spatially introduce specific LC domains would be a crucial step in achieving more complex or versatile actuating patterns of LC microstructures. This new approach is based on the PDMS alignment technique used in soft lithography, which relies on the surface hydrophobicity of PDMS to induce the reanchoring effect of the LC molecules. In this work, 2PLP was utilized to fabricate PDMS confinements with various geometries at arbitrary positions, achieving the goal of tailoring the LC alignment profile in three dimensions. Two typical alignment topologies, planar and radial alignment, were successfully introduced within the optimized PDMS channel or PDMS well, respectively. By altering the geometry of the confining cavity, more complicated alignments could also be customized. Remarkably, such PDMS-induced alignment profiles were reproduced with a LC ink and retained within the two-photon printed LC microstructures. This approach enabled the determination of the alignment of each printed LC microstructure individually and simultaneously, resulting in distinct stimuli-responsive behaviors from each other. Notably, it was observed that the dependency on PDMS-induced alignment is more pronounced for structures fabricated with LC crosslinkers possessing shorter alkyl chain lengths, exhibiting lateral expansion along the X- and Y- axes, diagonally, or evenly across the X-Y plane, apart from the homeotropically aligned one, which pristinely shows angular expansion along the Z-axis. This facile method offers the opportunity to modulate the response of the printed LC structure based on the default 2PLP setup without requiring technical modifications. The patterned director configurations can be used to design soft microrobots with complex motions and shapes that can adapt to different environments

---

and tasks. Eventually, the possibility of selectively removing the PDMS scaffold after printing was investigated. Despite the incomplete optimization of the full procedure, partial removal of the PDMS scaffold was achieved without affecting the LC structure while using TBAF as an etchant. It is expected that this promising method could be further optimized by reducing the volume-to-surface ratio of the PDMS partitions, i.e., implementing hollow features within the structures.

In previous reported stimuli-responsive LC microstructures, discussions have mainly focused on the responsive properties and utilization of individual printed structures, such as the actuating behavior of a single actuator. However, examples of utilizing multiple LC printed parts, i.e., applying them to a microdevice, have not yet been reported. PDMS, being a soft, biocompatible, and chemically inert material, has been widely used in the production of various biomedical prototypes or microfluidic chips. Even without the removal of the PDMS, the bimaterial system that combines the advantages of PDMS and LCE can be utilized in device fabrication. One potential application of this approach is in the creation of dynamic microfluidic systems, where PDMS can be used to fabricate fluidic channels and LCE parts can be printed as adaptive valves that can switch the channel on and off or modulate the flow rate on demand. Such an integrated system has the potential to pave the way for a new field of application.

The thesis overall has proposed solutions to advance 4D microprinting of intricate LC systems, both in terms of functionality and microfabrication. These breakthroughs opened up new possibilities for future work in this field, continuing to expand the scope of functional LC microsystems tailored for various applications. While the development of 4D microprinting has primarily focused on hydrogels due to their biocompatibility and suitability for biomedical research, LCEs have received less attention despite their attractive properties, which are unachievable by other classes of smart materials, such as autonomous actuation, high actuating stresses and strains, and low fatigue rate. More likely due to the fact that the activation mechanism of early reported LC microstructure relied on the use of heat or lights with short wavelengths (blue or green light) to trigger activation, which is harmful to biological cells or tissues and thus makes them unsuitable for biological applications. In fact, multiple biocompatible LCE systems have been investigated for their interfacial interactions with aqueous media. Various complex biological structures have also been demonstrated both *in vivo* and *in vitro*, showing their potential in a range of biomedical applications, such as cardiac

contraction assist devices,<sup>[147]</sup> skin-repairing patches,<sup>[148]</sup> and functional cell scaffolds.<sup>[149]</sup> Employing the two approaches presented in this thesis, it is possible to create 4D LC systems not only in microscale but also in general 3D printed structures tailored for such innovative applications. Based on their programmable stimuli-induced mechanical responses, potential examples include actuators in biomedical devices and implants, being responsive to various stimuli, not only to light but also possibly to pH or magnetic fields, to trigger controlled and reversible deformations for drug delivery, tissue engineering, or other therapeutic applications. Furthermore, smart systems with integrated LCE and sensors or electronics that can sense and respond to their surroundings, can open up new opportunities for applications in sensing or information processing. The prospects and possibilities for further research and development in this field would be something to look forward to.

---

## BIBLIOGRAPHY

- [1] X. Kuang, D. J. Roach, J. Wu, C. M. Hamel, Z. Ding, T. Wang, M. L. Dunn, H. J. Qi, *Adv. Funct. Mater.* **2019**, *29*, 1805290.
- [2] Z. X. Khoo, J. E. M. Teoh, Y. Liu, C. K. Chua, S. Yang, J. An, K. F. Leong, W. Y. Yeong, *Virtual and Physical Prototyping* **2015**, *10*, 103-122.
- [3] B. Gao, Q. Yang, X. Zhao, G. Jin, Y. Ma, F. Xu, *Trends Biotechnol.* **2016**, *34*, 746-756.
- [4] A. Sydney Gladman, E. A. Matsumoto, R. G. Nuzzo, L. Mahadevan, J. A. Lewis, *Nat. Mater.* **2016**, *15*, 413-418.
- [5] Acumen Research and Consulting, 3D Printing Market Size - Global Industry, Share, Analysis, Trends and Forecast 2022 - 2030, <https://www.acumenresearchandconsulting.com/3d-printing-market>, accessed: April, **2023**.
- [6] (a) T. Grimm, *User's Guide to Rapid Prototyping*, Society of Manufacturing Engineers, **2004**; (b) B. Redwood, F. Schöffner, B. Garret, *The 3D printing handbook: technologies, design and applications*, 3D Hubs, **2017**.
- [7] (a) S. C. Ligon, R. Liska, J. Stampfl, M. Gurr, R. Mülhaupt, *Chem. Rev.* **2017**, *117*, 10212-10290; (b) A. Standard, *ASTM International F2792-12a* **2012**, 1-9; (c) M. Rafiee, R. D. Farahani, D. Therriault, *Advanced Science* **2020**, *7*, 1902307.
- [8] (a) A. Bagheri, J. Jin, *ACS Appl. Polym. Mater.* **2019**, *1*, 593; (b) M. Pagac, J. Hajnys, Q.-P. Ma, L. Jancar, J. Jansa, P. Stefek, J. Mesicek, *Polymers* **2021**, *13*, 598.
- [9] C. W. Hull (Company), *United States Patent, Appl., No. 638905, Filed*, **1984**.
- [10] (a) B. J. Lee, K. Hsiao, G. Lipkowitz, T. Samuelsen, L. Tate, J. M. DeSimone, *Additive Manufacturing* **2022**, *55*, 102800; (b) J. R. Tumbleston, D. Shirvanyants, N. Ermoshkin, R. Januszewicz, A. R. Johnson, D. Kelly, K. Chen, R. Pinschmidt, J. P. Rolland, A. Ermoshkin, E. T. Samulski, J. M. DeSimone, *Science* **2015**, *347*, 1349-1352.
- [11] F. Sommonte, N. Denora, D. A. Lamprou, *Pharmaceuticals* **2023**, *16*, 69.

- 
- [12] A. Ribas-Massonis, M. Cicujano, J. Duran, E. Besalú, A. Poater, *Polymers* **2022**, *14*, 2856.
- [13] S. O'Halloran, A. Pandit, A. Heise, A. Kellett, *Advanced Science* **2023**, *10*, 2204072.
- [14] J.-P. Fouassier, J. Lalevée, *Photoinitiators for polymer synthesis: scope, reactivity, and efficiency*, John Wiley & Sons, **2012**.
- [15] (a) N. Ballard, J. M. Asua, *Prog. Polym. Sci.* **2018**, *79*, 40-60; (b) M. Lang, S. Hirner, F. Wiesbrock, P. Fuchs, *Polymers* **2022**, *14*, 2074.
- [16] (a) J. V. Crivello, E. Reichmanis, *Chem. Mater.* **2014**, *26*, 533-548; (b) A. Ravve, *Light-associated reactions of synthetic polymers*, Springer, **2006**.
- [17] C. E. Hoyle, C. N. Bowman, *Angew. Chem. Int. Ed.* **2010**, *49*, 1540-1573.
- [18] S. C. Ligon-Auer, M. Schwentenwein, C. Gorsche, J. Stampfl, R. Liska, *Polym. Chem.* **2016**, *7*, 257-286.
- [19] (a) Y. Jia, C. A. Spiegel, A. Welle, S. Heißler, E. Sedghamiz, M. Liu, W. Wenzel, M. Hackner, J. P. Spatz, M. Tsotsalas, E. Blasco, *Adv. Funct. Mater.* **2022**, 2207826; (b) Y. Bao, N. Paunović, J. C. Leroux, *Adv. Funct. Mater.* **2022**, *32*, 2109864.
- [20] C. A. Spiegel, M. Hackner, V. P. Bothe, J. P. Spatz, E. Blasco, *Adv. Funct. Mater.* **2022**, *32*, 2110580.
- [21] Y. Sugihara, P. O'Connor, P. B. Zetterlund, F. Aldabbagh, *J. Polym. Sci., Part A: Polym. Chem.* **2011**, *49*, 1856-1864.
- [22] M. Carlotti, V. Mattoli, *Small* **2019**, *15*, 1902687.
- [23] (a) H. Wang, W. Zhang, D. Ladika, H. Yu, D. Gailevičius, H. Wang, C. F. Pan, P. N. S. Nair, Y. Ke, T. Mori, J. Y. E. Chan, Q. Ruan, M. Farsari, M. Malinauskas, S. Juodkasis, M. Gu, J. K. W. Yang, *Adv. Funct. Mater.* **2023**, 2214211; (b) Z. Faraji Rad, P. D. Prewett, G. J. Davies, *Microsystems & Nanoengineering* **2021**, *7*; (c) M. Hippler, K. Weißenbruch, K. Richler, E. D. Lemma, M. Nakahata, B. Richter, C. Barner-Kowollik, Y. Takashima, A. Harada, E. Blasco, M. Wegener, M. Tanaka, M. Bastmeyer, *Sci. Adv.* **2020**, *6*, eabc2648.
- [24] M. Göppert-Mayer, *Annalen der Physik* **1931**, *401*, 273-294.
- [25] W. Kaiser, C. G. B. Garrett, *Phys. Rev. Lett.* **1961**, *7*, 229-231.

- 
- [26] W. Denk, J. H. Strickler, W. W. Webb, *Science* **1990**, *248*, 73-76.
- [27] (a) A. Ustione, D. W. Piston, *Journal of Microscopy* **2011**, *243*, 221-226; (b) R. M. Williams, W. R. Zipfel, W. W. Webb, *Curr. Opin. Chem. Biol.* **2001**, *5*, 603-608; (c) W. R. Zipfel, R. M. Williams, W. W. Webb, *Nat. Biotechnol.* **2003**, *21*, 1369-1377.
- [28] S. Maruo, O. Nakamura, S. Kawata, *Opt. Lett.* **1997**, *22*, 132-134.
- [29] P. Kiefer, V. Hahn, M. Nardi, L. Yang, E. Blasco, C. Barner-Kowollik, M. Wegener, *Adv. Opt. Mater.* **2020**, *8*, 2000895.
- [30] J. Fischer, M. Wegener, *Laser & Photonics Reviews* **2013**, *7*, 22-44.
- [31] (a) L. Yang, A. Münchinger, M. Kadic, V. Hahn, F. Mayer, E. Blasco, C. Barner-Kowollik, M. Wegener, *Adv. Opt. Mater.* **2019**, *7*, 1901040; (b) J. B. Mueller, J. Fischer, F. Mayer, M. Kadic, M. Wegener, *Adv. Mater.* **2014**, *26*, 6566-6571.
- [32] (a) T. Baldacchini, in *Three-Dimensional Microfabrication Using Two-photon Polymerization* (Ed.: T. Baldacchini), William Andrew Publishing, Oxford, **2016**, pp. xxiii-xxvi; (b) A. Pikulin, N. Bityurin, in *Multiphoton Lithography*, **2016**, pp. 65-93.
- [33] S. K. Saha, C. Divin, J. A. Cuadra, R. M. Panas, *Journal of Micro and Nano-Manufacturing* **2017**, *5*.
- [34] C. Barner-Kowollik, M. Bastmeyer, E. Blasco, G. Delaittre, P. Müller, B. Richter, M. Wegener, *Angew. Chem. Int. Ed.* **2017**, *56*, 15828-15845.
- [35] F. Tüdős, T. Földes-Berezsich, *Prog. Polym. Sci.* **1989**, *14*, 717-761.
- [36] T. Wloka, M. Gottschaldt, U. S. Schubert, *Chemistry – A European Journal* **2022**, *28*.
- [37] M. Sheik-Bahae, A. A. Said, T. H. Wei, D. J. Hagan, E. W. Van Stryland, *IEEE J. Quantum Electron.* **1990**, *26*, 760-769.
- [38] C. Xu, W. W. Webb, *J. Opt. Soc. Am. B* **1996**, *13*, 481-491.
- [39] V. Hahn, F. Mayer, M. Thiel, M. Wegener, *Optics and Photonics News* **2019**, *30*, 28-35.
- [40] (a) S. W. Hell, J. Wichmann, *Opt. Lett.* **1994**, *19*, 780-782; (b) E. Rittweger, K. Y. Han, S. E. Irvine, C. Eggeling, S. W. Hell, *Photonics* **2009**, *3*, 144-147.

- 
- [41] P. Müller, R. Müller, L. Hammer, C. Barner-Kowollik, M. Wegener, E. Blasco, *Chem. Mater.* **2019**, *31*, 1966-1972.
- [42] V. Hahn, N. M. Bojanowski, P. Rietz, F. Feist, M. Kozłowska, W. Wenzel, E. Blasco, S. Bräse, C. Barner-Kowollik, M. Wegener, *ACS Photonics* **2022**.
- [43] N. M. Bojanowski, A. Vranic, V. Hahn, P. Rietz, T. Messer, J. Brückel, C. Barner-Kowollik, E. Blasco, S. Bräse, M. Wegener, *Adv. Funct. Mater.* **2022**, 2212482.
- [44] V. Hahn, T. Messer, N. M. Bojanowski, E. R. Curticean, I. Wacker, R. R. Schröder, E. Blasco, M. Wegener, *Photonics* **2021**, *15*, 932-938.
- [45] (a) J.-I. Kato, N. Takeyasu, Y. Adachi, H.-B. Sun, S. Kawata, *Appl. Phys. Lett.* **2005**, *86*, 044102; (b) S. Matsuo, S. Juodkazis, H. Misawa, *Appl. Phys. A* **2005**, *80*, 683-685; (c) V. Hahn, P. Kiefer, T. Frenzel, J. Qu, E. Blasco, C. Barner-Kowollik, M. Wegener, *Adv. Funct. Mater.* **2020**, *30*, 1907795.
- [46] (a) V. Hahn, P. Rietz, F. Hermann, P. Müller, C. Barner-Kowollik, T. Schlöder, W. Wenzel, E. Blasco, M. Wegener, *Photonics* **2022**, *16*, 784-791; (b) S. K. Saha, D. Wang, V. H. Nguyen, Y. Chang, J. S. Oakdale, S.-C. Chen, *Science* **2019**, *366*, 105-109; (c) D. Loterie, P. Delrot, C. Moser, *Nat. Commun.* **2020**, *11*, 852.
- [47] P. Kiefer, V. Hahn, M. Wegener, *A 7×7-foci 3D laser nanoprinter using a diffractive optical element and an aspheric-lens array made by 3D laser nanoprinting, Vol. PC12412, SPIE*, **2023**.
- [48] M. Regehly, Y. Garmshausen, M. Reuter, N. F. König, E. Israel, D. P. Kelly, C.-Y. Chou, K. Koch, B. Asfari, S. Hecht, *Nature* **2020**, *588*, 620-624.
- [49] L. Yang, F. Mayer, U. H. Bunz, E. Blasco, M. Wegener, *Light: Advanced Manufacturing* **2021**, *2*, 296-312.
- [50] L. Yang, H. Hu, A. Scholz, F. Feist, G. Cadilha Marques, S. Kraus, N. M. Bojanowski, E. Blasco, C. Barner-Kowollik, J. Aghassi-Hagmann, M. Wegener, *Nat. Commun.* **2023**, *14*.
- [51] F. Mayer, S. Richter, J. Westhauser, E. Blasco, C. Barner-Kowollik, M. Wegener, *Sci. Adv.* **2019**, *5*, eaau9160.

- 
- [52] (a) J. M. Winne, L. Leibler, F. E. Du Prez, *Polym. Chem.* **2019**, *10*, 6091-6108; (b) C. J. Kloxin, C. N. Bowman, *Chem. Soc. Rev.* **2013**, *42*, 7161-7173.
- [53] (a) Y. Jia, Y. Matt, Q. An, I. Wessely, H. Mutlu, P. Theato, S. Bräse, A. Llevot, M. Tsotsalas, *Polym. Chem.* **2020**, *11*, 2502-2510; (b) B. Zhang, K. Kowsari, A. Serjouei, M. L. Dunn, Q. Ge, *Nature Communications* **2018**, *9*.
- [54] N. Zheng, Y. Xu, Q. Zhao, T. Xie, *Chem. Rev.* **2021**, *121*, 1716-1745.
- [55] S. Tibbits, *Architectural Design* **2014**, *84*, 116-121.
- [56] (a) K. Zhou, *Additive Manufacturing Technology: Design, Optimization, and Modeling*, Wiley, **2022**; (b) H. Zeng, P. Wasylczyk, D. S. Wiersma, A. Priimagi, *Adv. Mater.* **2018**, *30*, 1703554.
- [57] (a) M. Pawlicki, H. A. Collins, R. G. Denning, H. L. Anderson, *Angew. Chem. Int. Ed.* **2009**, *48*, 3244-3266; (b) M. Rumi, S. Barlow, J. Wang, J. W. Perry, S. R. Marder, in *Two-Photon Absorbing Materials and Two-Photon-Induced Chemistry*, Vol. 213, Springer, Berlin, Heidelberg, **2008**, pp. 1-95; (c) G. S. He, L.-S. Tan, Q. Zheng, P. N. Prasad, *Chem. Rev.* **2008**, *108*, 1245-1330; (d) F. Terenziani, C. Katan, E. Badaeva, S. Tretiak, M. Blanchard-Desce, *Adv. Mater.* **2008**, *20*, 4641-4678; (e) H. Myung Kim, B. Rae Cho, *Chem. Commun.* **2009**, 153-164; (f) B. Strehmel, V. Strehmel, *Advances in Photochemistry* **2007**, *29*, 111-354; (g) L.-Y. Hsu, C. A. Spiegel, E. Blasco, in *Smart Materials in Additive Manufacturing: 4D Printing Principles and Fabrication*, Vol. 1 (Eds.: M. Bodaghi, A. Zolfagharian), Elsevier, **2022**, pp. 231-263; (h) C. A. Spiegel, M. Hippler, A. Münchinger, M. Bastmeyer, C. Barner-Kowollik, M. Wegener, E. Blasco, *Adv. Funct. Mater.* **2020**, *30*, 1907615.
- [58] (a) B. Narupai, P. T. Smith, A. Nelson, *Adv. Funct. Mater.* **2021**, 2011012; (b) T. Spratte, S. Geiger, F. Colombo, A. Mishra, M. Taale, L. Y. Hsu, E. Blasco, C. Selhuber-Unkel, *Adv. Mater. Technol.* **2023**, *8*, 2200714.
- [59] X. Kuang, J. Wu, K. Chen, Z. Zhao, Z. Ding, F. Hu, D. Fang, H. J. Qi, *Sci. Adv.* **2019**, *5*, eaav5790.
- [60] S. Fusco, M. S. Sakar, S. Kennedy, C. Peters, R. Bottani, F. Starsich, A. Mao, G. A. Sotiriou, S. Pané, S. E. Pratsinis, D. Mooney, B. J. Nelson, *Adv. Mater.* **2014**, *26*, 952-957.

- 
- [61] (a) C. D. L. H. Alarcón, S. Pennadam, C. Alexander, *Chem. Soc. Rev.* **2005**, *34*, 276; (b) M. A. C. Stuart, W. T. S. Huck, J. Genzer, M. Müller, C. Ober, M. Stamm, G. B. Sukhorukov, I. Szleifer, V. V. Tsukruk, M. Urban, F. Winnik, S. Zauscher, I. Luzinov, S. Minko, *Nat. Mater.* **2010**, *9*, 101-113.
- [62] (a) Y. Hirokawa, T. Tanaka, *AIP Conf. Proc.* **1984**, *107*, 203-208; (b) L. D. Zarzar, P. Kim, M. Kolle, C. J. Brinker, J. Aizenberg, B. Kaehr, *Angew. Chem.* **2011**, *123*, 9528-9532.
- [63] (a) X. Huang, X. Wang, Y. Zhao, *Dyes and Pigments* **2017**, *141*, 413-419; (b) Z. Li, J. Torgersen, A. Ajami, S. Mühleder, X. Qin, W. Husinsky, W. Holthöner, A. Ovsianikov, J. Stampfl, R. Liska, *RSC Advances* **2013**, *3*, 15939; (c) Y.-C. Zheng, Y.-Y. Zhao, M.-L. Zheng, S.-L. Chen, J. Liu, F. Jin, X.-Z. Dong, Z.-S. Zhao, X.-M. Duan, *ACS Appl. Mater. Interfaces.* **2019**, *11*, 1782-1789.
- [64] (a) O. A. Banda, C. R. Sabanayagam, J. H. Slater, *ACS Appl. Mater. Interfaces.* **2019**, *11*, 18233-18241; (b) W. Zhang, P. Soman, K. Meggs, X. Qu, S. Chen, *Adv. Funct. Mater.* **2013**, *23*, 3226-3232; (c) M. Hippler, E. Blasco, J. Qu, M. Tanaka, C. Barner-Kowollik, M. Wegener, M. Bastmeyer, *Nat. Commun.* **2019**, *10*.
- [65] (a) D. Jin, Q. Chen, T.-Y. Huang, J. Huang, L. Zhang, H. Duan, *Mater. Today* **2020**, *32*, 19-25; (b) Y. Hu, Z. Wang, D. Jin, C. Zhang, R. Sun, Z. Li, K. Hu, J. Ni, Z. Cai, D. Pan, X. Wang, W. Zhu, J. Li, D. Wu, L. Zhang, J. Chu, *Adv. Funct. Mater.* **2020**, *30*, 1907377.
- [66] C. Lv, X.-C. Sun, H. Xia, Y.-H. Yu, G. Wang, X.-W. Cao, S.-X. Li, Y.-S. Wang, Q.-D. Chen, Y.-D. Yu, H.-B. Sun, *Sens. Actuators B Chem.* **2018**, *259*, 736-744.
- [67] Z. Xiong, X.-Z. Dong, W.-Q. Chen, X.-M. Duan, *Appl. Phys. A* **2008**, *93*, 447-452.
- [68] D. Serien, K. Sugioka, *Opto-electron. adv.* **2018**, *1*, 18000801-18180008.
- [69] (a) B. Richter, V. Hahn, S. Bertels, T. K. Claus, M. Wegener, G. Delaittre, C. Barner-Kowollik, M. Bastmeyer, *Adv. Mater.* **2017**, *29*, 1604342; (b) J. A. Shadish, G. M. Benuska, C. A. Deforest, *Nat. Mater.* **2019**, *18*, 1005-1014.
- [70] (a) M. R. Lee, I. Y. Phang, Y. Cui, Y. H. Lee, X. Y. Ling, *Small* **2015**, *11*, 740-748; (b) Z.-C. Ma, Y.-L. Zhang, B. Han, X.-Y. Hu, C.-H. Li, Q.-D. Chen, H.-B. Sun, *Nat. Commun.* **2020**, *11*.

- 
- [71] (a) J. L. Connell, E. T. Ritschdorff, J. B. Shear, *Anal. Chem.* **2016**, *88*, 12264-12271; (b) B. Kaehr, J. B. Shear, *Proceedings of the National Academy of Sciences* **2008**, *105*, 8850-8854; (c) C. Y. Khripin, C. J. Brinker, B. Kaehr, *Soft Matter* **2010**, *6*, 2842.
- [72] Y. Yuan, P. Keller, I. I. Smalyukh, *Soft Matter* **2021**, *17*, 3037-3046.
- [73] Y. Xia, Y. He, F. Zhang, Y. Liu, J. Leng, *Adv. Mater.* **2021**, *33*, 2000713.
- [74] A. Lendlein, O. E. C. Gould, *Nat. Rev. Mater.* **2019**, *4*, 116-133.
- [75] (a) F. Li, Y. Liu, J. Leng, *Smart Mater. Struct.* **2019**, *28*, 103003; (b) Y. Zhang, Y. Li, W. Liu, *Adv. Funct. Mater.* **2015**, *25*, 471-480.
- [76] (a) H. Ramaraju, R. E. Akman, D. L. Safranski, S. J. Hollister, *Adv. Funct. Mater.* **2020**, *30*, 2002014; (b) M. Y. Khalid, Z. U. Arif, W. Ahmed, R. Umer, A. Zolfagharian, M. Bodaghi, *Sens. Actuator A Phys.* **2022**, *343*, 113670; (c) J. Delaey, P. Dubruel, S. Van Vlierberghe, *Adv. Funct. Mater.* **2020**, *30*, 1909047.
- [77] H. Gao, J. Li, F. Zhang, Y. Liu, J. Leng, *Materials Horizons* **2019**, *6*, 931-944.
- [78] (a) T. Chen, O. R. Bilal, K. Shea, C. Daraio, *Proceedings of the National Academy of Sciences* **2018**, *115*, 5698-5702; (b) A. Lendlein, *Science Robotics* **2018**, *3*, eaat9090.
- [79] (a) Y. Y. C. Choong, S. Maleksaeedi, H. Eng, J. Wei, P.-C. Su, *Materials & Design* **2017**, *126*, 219-225; (b) Q. Ge, A. H. Sakhaei, H. Lee, C. K. Dunn, N. X. Fang, M. L. Dunn, *Scientific reports* **2016**, *6*, 1-11; (c) Y.-L. Zhang, Y. Tian, H. Wang, Z.-C. Ma, D.-D. Han, L.-G. Niu, Q.-D. Chen, H.-B. Sun, *ACS Nano* **2019**, *13*, 4041-4048; (d) Q. Chen, T. Sukmanee, L. Rong, M. Yang, J. Ren, S. Ekgasit, R. Advincula, *ACS Appl. Polym. Mater.* **2020**, *2*, 5492-5500; (e) B. Peng, Y. Yang, T. Ju, K. A. Cavicchi, *ACS Appl. Mater. Interfaces.* **2021**, *13*, 12777-12788.
- [80] L. V. Elliott, E. E. Salzman, J. R. Greer, *Adv. Funct. Mater.* **2021**, *31*, 2008380.
- [81] W. Zhang, H. Wang, H. Wang, J. Y. E. Chan, H. Liu, B. Zhang, Y.-F. Zhang, K. Agarwal, X. Yang, A. S. Ranganath, H. Y. Low, Q. Ge, J. K. W. Yang, *Nat. Commun.* **2021**, *12*.
- [82] M. P. Jeske, W. Zhang, M. Anthamatten, *Adv. Mater. Technol.* **2022**, 2101725.

- 
- [83] G. Minnick, B. T. Safa, J. Rosenbohm, N. V. Lavrik, J. Brooks, A. M. Esfahani, A. Samaniego, F. Meng, B. Richter, W. Gao, R. Yang, *Adv. Funct. Mater.* **2023**, *33*, 2206739.
- [84] H. Yang, A. Buguin, J.-M. Taulemesse, K. Kaneko, S. P. MéRy, A. Bergeret, P. Keller, *J. Am. Chem. Soc.* **2009**, *131*, 15000-15004.
- [85] (a) M. Chen, M. Gao, L. Bai, H. Zheng, H. J. Qi, K. Zhou, *Adv. Mater.* **2022**, 2209566; (b) Y. Wang, J. An, H. Lee, *Molecular Systems Design & Engineering* **2022**, *7*, 1588-1601.
- [86] K. M. Herbert, H. E. Fowler, J. M. McCracken, K. R. Schlafmann, J. A. Koch, T. J. White, *Nat. Rev. Mater.* **2021**, *7*, 23.
- [87] H. Zeng, D. Martella, P. Wasylczyk, G. Cerretti, J.-C. G. Lavocat, C.-H. Ho, C. Parmeggiani, D. S. Wiersma, *Adv. Mater.* **2014**, *26*, 2319-2322.
- [88] (a) S. Woska, A. Münchinger, D. Beutel, E. Blasco, J. Hessenauer, O. Karayel, P. Rietz, S. Pfleging, R. Oberle, C. Rockstuhl, M. Wegener, H. Kalt, *Opt. Mater. Express* **2020**, *10*, 2928-2943; (b) A. Münchinger, V. Hahn, D. Beutel, S. Woska, J. Monti, C. Rockstuhl, E. Blasco, M. Wegener, *Adv. Mater. Technol.* **2021**, 2100944.
- [89] M. Del Pozo, J. A. H. P. Sol, A. P. H. J. Schenning, M. G. Debije, *Adv. Mater.* **2021**, 2104390.
- [90] P.-G. De Gennes, M. Hébert, R. Kant, *Macromolecular Symposia* **1997**, *113*, 39-49.
- [91] H. Sugiyama, S. Sato, K. Nagai, *Polym. Adv. Technol.* **2022**, *33*, 2113-2122.
- [92] T. R. N. Kutty, A. G. Fischer, *Mol. Cryst. Liq. Cryst.* **1983**, *99*, 301-318.
- [93] A. D. Schwab, D. M. G. Agra, J.-H. Kim, S. Kumar, A. Dhinojwala, *Macromolecules* **2000**, *33*, 4903-4909.
- [94] (a) S. Ishihara, H. Wakemoto, K. Nakazima, Y. Matsuo, *Liq. Cryst.* **1989**, *4*, 669-675; (b) D. S. Seo, Y. Iimura, S. Kobayashi, *Appl. Phys. Lett.* **1992**, *61*, 234-236; (c) D.-S. Seo, S. Kobayashi, D.-Y. Kang, H. Yokoyama, *Jpn. J. Appl. Phys.* **1995**, *34*, 3607.
- [95] H. Zeng, P. Wasylczyk, C. Parmeggiani, D. Martella, M. Burrese, D. S. Wiersma, *Adv. Mater.* **2015**, *27*, 3883-3887.

- 
- [96] (a) K. Ichimura, *Chem. Rev.* **2000**, *100*, 1847-1874; (b) M. O. Neill, S. M. Kelly, *J. Phys. D: Appl. Phys.* **2000**, *33*, R67.
- [97] (a) O. Yaroshchuk, Y. Reznikov, *J. Mater. Chem.* **2012**, *22*, 286-300; (b) V. G. Chigrinov, V. M. Kozenkov, H. S. Kwok, *Photoalignment of Liquid Crystalline Materials: Physics and Applications*, Wiley, **2008**.
- [98] T. D. C. Company, The Dow Chemical Company, Midland, MI, USA, **2017**.
- [99] Z. Wang, A. A. Volinsky, N. D. Gallant, *J. Appl. Polym. Sci.* **2014**, *131*, 41050.
- [100] (a) C. M. Knobler, *Nature* **1994**, *369*, 15-16; (b) M. Geissler, Y. Xia, *Adv. Mater.* **2004**, *16*, 1249-1269.
- [101] (a) J. Zhou, A. V. Ellis, N. H. Voelcker, *ELECTROPHORESIS* **2010**, *31*, 2-16; (b) J. Friend, L. Yeo, *Biomicrofluidics* **2010**, *4*, 026502; (c) K. Raj M, S. Chakraborty, *J. Appl. Polym. Sci.* **2020**, *137*, 48958.
- [102] K.-H. Jeong, J. Kim, L. P. Lee, *Science* **2006**, *312*, 557-561.
- [103] J. G. Lim, S. S. Lee, K. D. Lee, *Opt. Commun.* **2007**, *272*, 97-101.
- [104] J. Chen, J. Zheng, Q. Gao, J. Zhang, J. Zhang, O. Omisore, L. Wang, H. Li, *Appl. Sci.* **2018**, *8*, 345.
- [105] (a) W. Zheng, L. Yang, M. Lee, *Photonics Lett. Pol* **2011**, *3*, 8-10; (b) W. J. Zheng, M. H. Huang, *Thin Solid Films* **2012**, *520*, 2841-2845.
- [106] K. A. Rutkowska, P. Sobotka, M. Grom, S. Baczyński, M. Juchniewicz, K. Marchlewicz, A. Dybko, *Sensors* **2022**, *22*, 4037.
- [107] R. Lin, J. A. Rogers, *Nano Lett.* **2007**, *7*, 1613-1621.
- [108] C. Pei-Shiang, C. Han-Hsun, C. Jun-Wei, L. Tzu-Chieh, C. Chih-Yu, *Chin. J. Phys.* **2009**, *47*, 55-60.
- [109] W. Zheng, Y.-T. Hu, *Mol. Cryst. Liq. Cryst.* **2015**, *615*, 1-8.
- [110] W. Zheng, M. C. Lee, *Mol. Cryst. Liq. Cryst.* **2012**, *553*, 28-35.
- [111] H. Sakanoue, S. Yamashita, T. Murakami, H. Suzuki, K. Katayama, *Liq. Cryst.* **2022**, *49*, 580-588.

- 
- [112] Y. Xia, E. Lee, H. Hu, M. A. Gharbi, D. A. Beller, E.-K. Fleischmann, R. D. Kamien, R. Zentel, S. Yang, *ACS Appl. Mater. Interfaces* **2016**, *8*, 12466-12472.
- [113] D. Ahn, Y.-C. Jeong, S. Lee, J. Lee, Y. Heo, J.-K. Park, *Opt. Express* **2009**, *17*, 16603.
- [114] S. Baczyński, P. Sobotka, K. Marchlewicz, M. Słowikowski, M. Juchniewicz, A. Dybko, K. A. Rutkowska, *Appl. Sci.* **2021**, *11*, 11593.
- [115] D. Martella, S. Nocentini, D. Nuzhdin, C. Parmeggiani, D. S. Wiersma, *Adv. Mater.* **2017**, *29*, 1704047.
- [116] Y. Guo, J. Zhang, W. Hu, M. T. A. Khan, M. Sitti, *Nat. Commun.* **2021**, *12*.
- [117] P. Mainik, L.-Y. Hsu, C. W. Zimmer, D. Fauser, H. Steeb, E. Blasco, *Adv. Mater. Technol.* **2023**, submitted.
- [118] (a) H.-W. Chen, J.-H. Lee, B.-Y. Lin, S. Chen, S.-T. Wu, *Light: Science & Applications* **2017**, *7*, 17168-17168; (b) T. H. Ware, M. E. McConney, J. J. Wie, V. P. Tondiglia, T. J. White, *Science* **2015**, *347*, 982-984.
- [119] A. Münchinger, L.-Y. Hsu, F. Fürniß, E. Blasco, M. Wegener, *Mater. Today* **2022**, *59*, 9-17.
- [120] M. Tabrizi, T. H. Ware, M. R. Shankar, *ACS Appl. Mater. Interfaces* **2019**, *11*, 28236-28245.
- [121] H. Y. Jeong, S.-C. An, Y. C. Jun, *Nanophotonics* **2022**, *11*, 461-486.
- [122] (a) L. Qin, X. Liu, Y. Yu, *Adv. Opt. Mater.* **2021**, *9*, 2001743; (b) M. Gastaldi, F. Cardano, M. Zanetti, G. Viscardi, C. Barolo, S. Bordiga, S. Magdassi, A. Fin, I. Roppolo, *ACS Mater. Lett.* **2021**, *3*, 1-17.
- [123] (a) A. M. Flatae, M. Burrese, H. Zeng, S. Nocentini, S. Wiegele, C. Parmeggiani, H. Kalt, D. Wiersma, *Light: Science & Applications* **2015**, *4*, e282-e282; (b) S. Nocentini, F. Riboli, M. Burrese, D. Martella, C. Parmeggiani, D. S. Wiersma, *ACS Photonics* **2018**, *5*, 3222-3230.
- [124] M. Pilz Da Cunha, E. A. J. Van Thoor, M. G. Debije, D. J. Broer, A. P. H. J. Schenning, *J. Mater. Chem. C* **2019**, *7*, 13502-13509.
- [125] (a) S. L. Oscurato, M. Salvatore, P. Maddalena, A. Ambrosio, *Nanophotonics* **2018**, *7*, 1387-1422; (b) T. Ikeda, *J. Mater. Chem.* **2003**, *13*, 2037.

- 
- [126] L. Chen, Y. Dong, C.-Y. Tang, L. Zhong, W.-C. Law, G. C. P. Tsui, Y. Yang, X. Xie, *ACS Appl. Mater. Interfaces* **2019**, *11*, 19541-19553.
- [127] Y. Guo, H. Shahsavan, M. Sitti, *Adv. Mater.* **2020**, *32*, 2002753.
- [128] M. Del Pozo, C. Delaney, M. Pilz Da Cunha, M. G. Debije, L. Florea, A. P. H. J. Schenning, *Small Structures* **2022**, *3*, 2100158.
- [129] L. Y. Hsu, P. Mainik, A. Münchinger, S. Lindenthal, T. Spratte, A. Welle, J. Zaumseil, C. Selhuber-Unkel, M. Wegener, E. Blasco, *Adv. Mater. Technol.* **2022**, 2200801.
- [130] M. M. Lerch, M. J. Hansen, W. A. Velema, W. Szymanski, B. L. Feringa, *Nat. Commun.* **2016**, *7*, 12054.
- [131] B. L. Feringa, W. R. Browne, *Molecular switches*, John Wiley & Sons, **2011**.
- [132] (a) S. Helmy, F. A. Leibfarth, S. Oh, J. E. Poelma, C. J. Hawker, J. Read De Alaniz, *J. Am. Chem. Soc.* **2014**, *136*, 8169-8172; (b) S. Helmy, S. Oh, F. A. Leibfarth, C. J. Hawker, J. Read De Alaniz, *J. Org. Chem.* **2014**, *79*, 11316-11329.
- [133] (a) S. Singh, K. Friedel, M. Himmerlich, Y. Lei, G. Schlingloff, A. Schober, *ACS Macro Letters* **2015**, *4*, 1273-1277; (b) J. R. Hemmer, S. O. Poelma, N. Treat, Z. A. Page, N. D. Dolinski, Y. J. Diaz, W. Tomlinson, K. D. Clark, J. P. Hooper, C. Hawker, J. Read De Alaniz, *J. Am. Chem. Soc.* **2016**, *138*, 13960-13966; (c) J. R. Hemmer, Z. A. Page, K. D. Clark, F. Stricker, N. D. Dolinski, C. J. Hawker, J. Read De Alaniz, *J. Am. Chem. Soc.* **2018**, *140*, 10425-10429.
- [134] M. M. Lerch, W. Szymański, B. L. Feringa, *Chem. Soc. Rev.* **2018**, *47*, 1910-1937.
- [135] T. Schmitt, L. Y. Hsu, N. Oberhof, D. Rana, A. Dreuw, E. Blasco, P. Tegeder, *Adv. Funct. Mater.* **2023**.
- [136] (a) A. S. Alketbi, Y. Shi, H. Li, A. Raza, T. Zhang, *Soft Matter* **2021**, *17*, 7188; (b) Q. Hu, G. A. Rance, G. F. Trindade, D. Pervan, L. Jiang, A. Foerster, L. Turyanska, C. Tuck, D. J. Irvine, R. Hague, R. D. Wildman, *Additive Manufacturing* **2022**, *51*, 102575.
- [137] P. F. J. van Altena, A. Accardo, *Polymers* **2023**, *15*, 1816.

- 
- [138] G. L. Smith, J. B. Tyler, N. Lazarus, H. Tsang, L. Viorner, J. Shultz, S. Bergbreiter, *Adv. Funct. Mater.* **2023**, 2207435.
- [139] S. Van Kesteren, X. Shen, M. Aldeghi, L. Isa, *Adv. Mater.* **2023**, 2207101.
- [140] A.-I. Bunea, N. Szczotka, J. Navne, R. Taboryski, *Micro and Nano Engineering* **2023**, 19, 100192.
- [141] K. S. Ryu, X. Wang, K. Shaikh, C. Liu, *J. Microelectromech. Syst.* **2004**, 13, 568-575.
- [142] J. N. Lee, C. Park, G. M. Whitesides, *Anal. Chem.* **2003**, 75, 6544-6554.
- [143] (a) J. Garra, T. Long, J. Currie, T. Schneider, R. White, M. Paranjape, *Journal of Vacuum Science and Technology, Part A: Vacuum, Surfaces and Films* **2002**, 20, 975-982; (b) B. Balakrishnan, S. Patil, E. Smela, *J. Micromech. Microeng.* **2009**, 19, 047002.
- [144] S. Z. Szilasi, C. Cserháti, *Appl. Surf. Sci.* **2018**, 457, 662-669.
- [145] R. Dahiya, G. Gottardi, N. Laidani, *Microelectron. Eng.* **2015**, 136, 57-62.
- [146] S. Chaudhuri, M. Verderame, T. L. Mako, Y. M. N. D. Y. Bandara, A. I. Fernando, M. Levine, *Eur. J. Org. Chem.* **2018**, 2018, 1964-1974.
- [147] C. Ferrantini, J. M. Pioner, D. Martella, R. Coppini, N. Piroddi, P. Paoli, M. Calamai, F. S. Pavone, D. S. Wiersma, C. Tesi, E. Cerbai, C. Poggesi, L. Sacconi, C. Parmeggiani, *Circulation Research* **2019**, 124.
- [148] J. Wu, S. Yao, H. Zhang, W. Man, Z. Bai, F. Zhang, X. Wang, D. Fang, Y. Zhang, *Adv. Mater.* **2021**, 33, 2106175.
- [149] D. Martella, C. Parmeggiani, *Chem. Eur. J.* **2018**, 24, 12206-12220.